Molecular Gas in Late-stage Merging Galaxies

Junko Ueda

Department of Astronomy, Graduate School of Science, The University of Tokyo

junko.ueda@nao.ac.jp

Abstract

We reveal the distribution and kinematics of molecular gas in colliding galaxy systems near the late-stage of their coalescence, called merger remnants. We statistically analyze their properties utilizing the largest-to-date survey of cold molecular gas. This is the first step in our series of studies which put emphasis on molecular gas in merger remnants.

It has been long predicted from numerical simulations that a major merger of two disk galaxies results in the formation of a spheroid-dominated early-type galaxy. Contrary to this classical scenario of galaxy merger evolution, recent simulations that include more realistic gas physics have shown that not all of the major mergers will become early-type galaxies, but some will re-emerge as a disk-dominated late-type galaxy. However there has been no observational confirmation of this theoretical prediction. In order to verify this scenario and to investigate the evolution of galaxy after a merging event, we have conducted a ^{12}CO imaging survey of optically-selected merger remnants in the local Universe using millimeter/submillimeter interferometers including ALMA, SMA, and CARMA, and the NRO 45 m single-dish telescope.

We find that 65 % (24/37) of the sample show kinematical signatures of a rotating molecular gas disk. We reveal a high occurrence of molecular gas disks including rings in the merger remnants, and the sizes of these disks vary significantly from 1.1 kpc to 9.3 kpc. We estimate the size ratio ($R_{\rm ratio}$) of the gas disk to the stellar spheroidal component for 24 merger remnants with gas disks in order to investigate whether cold molecular gas disks are in extended form, as predicted from recent numerical simulations. The size ratios $R_{\rm ratio}$ for 54 % (13/24) of the merger remnants are less than unity. Six merger remnants which are bright at infrared wavelengths have compact molecular gas disks, which may have formed by past gas inflow that was triggered by dynamical instability following the merging. On the other hand, 46 % (11/24) of the merger remnants have gas disks which are extended relative to the stellar components. We also discover a possible positive correlation between $R_{\rm ratio}$

and the total far-infrared luminosity. This suggests that the physical activities that are responsible for increasing luminosity, namely starburst/AGN, are related to the formation of the extended molecular gas disks. The molecular gas disks in the merger remnants show various properties, and we conclude that our sample includes merger remnants at different stages of their evolution, whose progenitors have different characteristics or which have different initial conditions.

From comparisons of the merger remnants with early-type galaxies and late-type galaxies regarding their molecular gas and stellar components, overall, our conclusion is that 65 % of the merger remnants evolve into early-type galaxies, 5 % into late-type galaxies, 14 % into either early-type/late-type galaxies, and 16 % into galaxies which cannot be classified into early-type/late-type galaxies. Among the sources with observational signatures of a rotating molecular gas disk, we find that sources with compact molecular gas disks will become early-type galaxies regardless of the gas mass fraction, mainly because of the short depletion time of the molecular gas ($\lesssim 10^8$ yr) and high gas concentration in the nuclear region. On the other hand, we find that sources with extended molecular gas disks and large gas mass fractions are likely to become late-type galaxies, unless there are further mechanisms which transport the molecular gas toward the central regions thereby decreasing the sizes of the gas disks. Confirming the evolution path of the sources with extended molecular gas disks and low gas mass fractions requires further studies to investigate whether a large amount of cold gas will settle on the extended gas disks by the returning of the ejected cold gas via tidal tails and cold gas stream/accretion. For six merger remnants whose velocity fields cannot be modeled with circular motion, their clumpy morphology and complex gas structure are different from the morphology and structure of both early-type/late-type galaxies, therefore their evolution path is not clear. The seven merger remnants which were not detected in the CO line will evolve into early-type galaxies earlier than the merger remnants with compact molecular gas disks.

This study confirms, observationally, a new scenario that merging events are the crossroads of galaxy evolution, reprocessing them into a mixture of types including early-type/late-type galaxies.

Contents

List of Figures

List of Tables

Chapter 1

Introduction

1.1 Extragalactic Astronomy through Observations

There are more than 100 billion galaxies in the Universe, though we can see only four galaxies with our naked eyes. Galaxies are gravitationally bound systems composed of stars, star clusters, interstellar medium of gas and dust, and dark matter. The majority of galaxies are parts of larger associations known as groups, clusters, and superclusters of galaxies. Each individual galaxies have different size, mass, stellar population, and structure, which tell us about its evolutionary history.

Galaxies usually emit light at all wavelengths from X-rays to radio (Figure 1.1). We provide a brief summary about observations towards galaxies at different wavelengths.

- **Optical observations**: Initial observations towards galaxies were carried out using visible light, which traces mainly stars because the peak wavelength of most stars lies in the optical. Optical imaging reveals the stellar populations and the distribution of dusty regions via extinction. In addition, imaging with a narrow-band filter shows ionized HII regions in galaxies, which are usually coincident with star forming regions.

- **Infrared observations**: Infrared radiation can pass through dusty regions. Therefore infrared observations are useful for investigating objects obscured at visible wavelength by gas and dust. The infrared is divided into three spectral regions, near-, mid- and far-infrared. The near-infrared light is dominated by stars, but mainly tracing red giant stars and red dwarfs. The mid- and far-infrared light is produced by radiation from dust, which is heated by stars formed in molecular clouds. Far-infrared imaging is also used to discover high-z galaxies.

- **Radio observations**: The continuum observations are used for examining activity in galactic nuclei, in particular active galactic nuclei (AGNs), and for investigating star forming activities. The atomic and molecular line observations, such as the neutral hydrogen line (HI line) at 21 cm and the CO (1–0) line at 115 GHz, are used for investigating the properties of gaseous components, such as chemical evolution and physical state. In addition, the HI line is useful for the kinematic measurements in galaxies (e.g., galactic rotation curve).

- **Ultraviolet and X-ray observations**: Ultraviolet (UV) and X-ray telescopes can detect high energy astrophysical phenomena. UV spectroscopy is used to discern the temperature, density and chemical composition of the interstellar medium. The X-ray spectrum is a powerful tool for identifying AGNs, because their luminosities are considerably higher than those of other

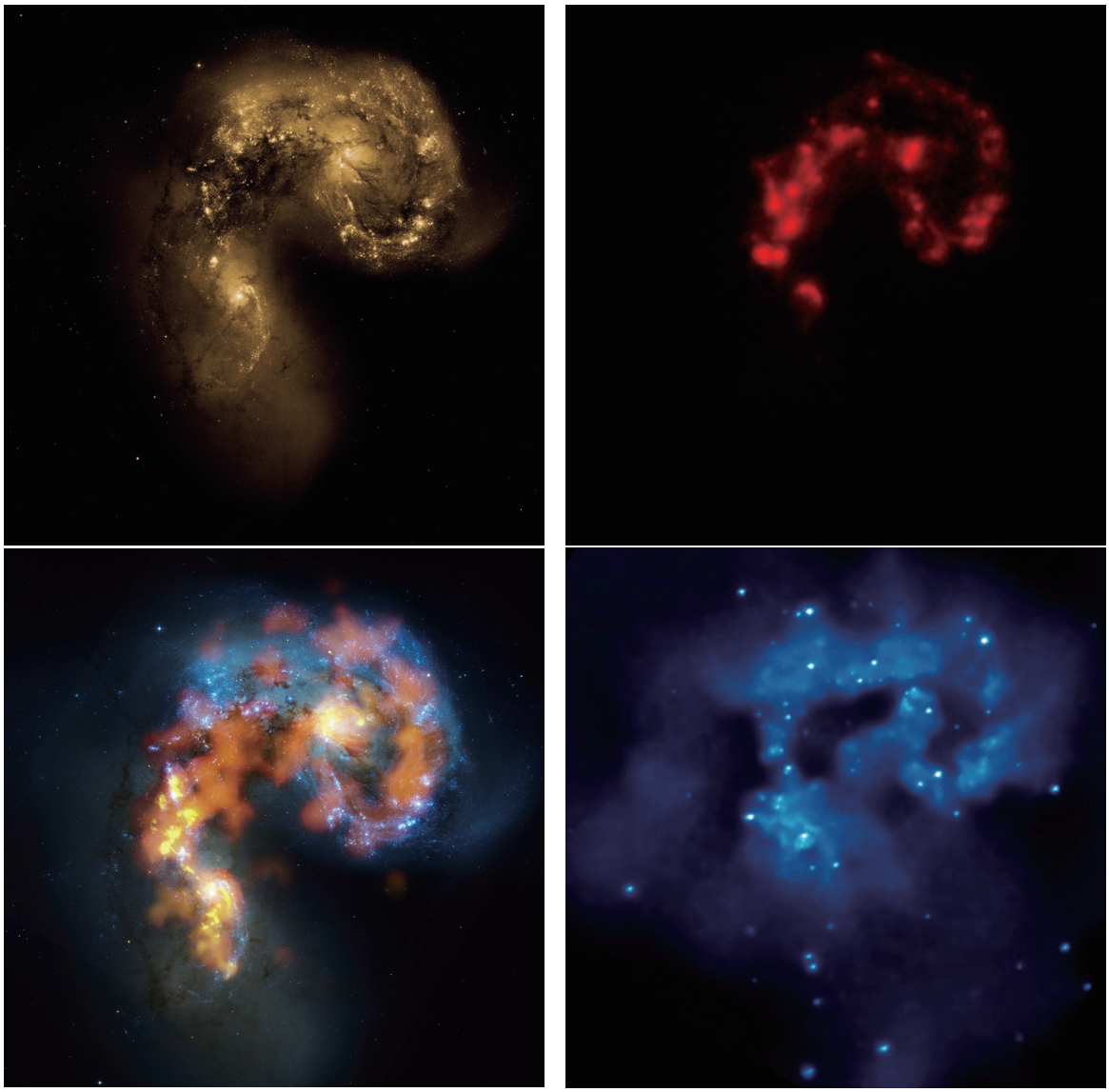

Figure 1.1: An example of multi-wavelength observations: optical (upper-left), infrared (upper-right), radio (bottom-left), and, X-ray (bottom-right). The object is the Antennae galaxies. The radio image is a multi CO line image overlaid on the optical image.

Image credit—Optical: NASA/STScI, Infrared: NASA/JPL-Caltech, Radio: B. Saxton, (NRAO/AUI/NSF), ALMA (ESO/NAOJ/NRAO) (Background optical image: the NASA/ESA Hubble Space Telescope), X-ray: NASA/CXC/SAO/J.DePasquale.

galactic X-ray sources. In addition, diffuse X-ray emission traces the galactic feedback from AGNs as well as from stars in the form of stellar winds and supernovae.

Galaxies are fundamental components of the Universe, and thus investigating galaxies leads to understanding the Universe itself. Technical improvements of observational instruments enable us to observe galaxies at redshifts up to $z \sim 7.5$ (Finkelstein et al., 2013). Sensitivity and spatial resolution of observations have been limited, however, so that we cannot directly investigate the evolutionary history of distant galaxies. Thus, as a first step, it is important to study nearby galaxies in detail, which might provide clues to an understanding of distant galaxies in the early Universe.

1.2 Galaxy Classification

The classification of galaxies is a fundamental tool in astronomy. A classification scheme usually provides new insight into extragalactic astronomy and allows us to build a deep understanding of how galaxies form and evolve. Thus classification schemes have been developed for specific purposes.

1.2.1 Morphological Classification

Galaxies have been historically classified according to their apparent morphology. The most famous morphological classification is the Hubble's "tuning fork" scheme (Hubble, 1958, Figure 1.2). Galaxies with different morphologies have evolved in different ways. Therefore morphological classification usually turns out to correlate with a difference in physical properties of galaxies. We provide a brief introduction about four main types of galaxies.

- **Elliptical galaxies** (En) have nearly elliptical isophotes without any clearly defined structure. The surface brightness profiles of elliptical galaxies are well fit by Sérsic profile (see § 2.1). They are subdivided according to their ellipticity $\epsilon \equiv (1 - \mathrm{b/a})$ ($0 \leq \epsilon \lesssim 0.7$), where a and b are the semimajor and semiminor axes, respectively. The notation En is used to classify ellipticals with respect to the ellipticity ($n = 10\epsilon$ (integer value)). They are composed of old, low-mass stars and little interstellar matter, which results in low rates of star formation. The motion of stars is predominantly random motion. Elliptical galaxies are preferentially found close to the centers of galaxy clusters. Elliptical galaxies are called "**early-type**" **galaxies**. This name does not imply any interpretation but exists only for historical reasons.

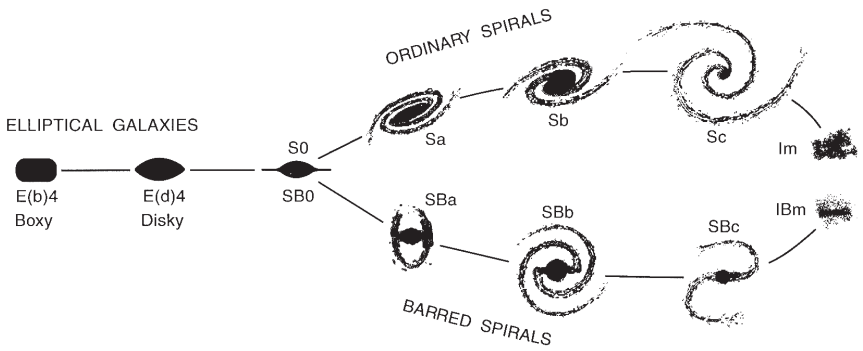

Figure 1.2: Hubble's tuning fork for galaxy classification.
Image credit—Kormendy & Bender (1996) (reproduced by permission of the AAS.)

- **S0 galaxies (lenticular galaxies)** (S0) are intermediates between ellipticals and spirals in the classification scheme. They consist of a bulge and a large enveloping region, which appears like a disk without spiral arms. They are subdivided into S0 and SB0, depending on whether or not they show a bar. S0 galaxies have used up or lost most of the interstellar matter and thus have little ongoing star formation. S0 galaxies and elliptical galaxies share common properties such as spectral features and scaling relations, and they are referred to as **early-type galaxies**.

- **Spiral galaxies** (Sx) contain a rotating disk with spiral arms and a central bulge. These structures are surrounded by a much fainter halo of stars, many of which are part of globular clusters. They are divided into two subclasses: ordinary spirals (Sx) and barred spirals (SBx). In each of these subclasses, they are further divided according to the bulge-to-disk brightness ratio, and the notation Sx presents the brightness ratio (x = a/b/c). Spiral arms are sites of ongoing star formation and young, hot OB stars inhabit them. The motion of stars is dominated by rotation in a disk, while it is predominantly random motion in a bulge. Spiral galaxies are mostly found in low-density regions and are rare in the centers of galaxy clusters. They are also called "**late-type**" **galaxies**. This name is only historical as well as early-type galaxies.

- **Irregular galaxies** (Irr) are galaxies with only weak (Irr I) or no (Irr II) regular structure. Irregular galaxies usually contain abundant amounts of gas and dust. Some of them were once spiral or elliptical galaxies, but they were deformed by gravitational interaction with neighbors. The classification between two subtypes (Irr I and Irr II) is often refined. In particular, the sequence of spirals is extended to the classes of irregular galaxies (e.g., Sdm, Sm, Im, IBm).

1.2.2 Starburst Galaxies

The light from "normal" galaxies (ellipticals and spirals) is emitted mainly by stars. Therefore, in principle, the spectral energy distribution of normal galaxies is a composite of the spectra of their stellar population. In contrast, another type of galaxy, the so-called **starburst galaxy**, has a spectral energy distribution dominated by thermal dust emission at far-infrared (FIR) and submillimeter wavelengths or by radiation from young massive stars in the blue (optical) and UV regions. Starburst galaxies are characterized by strongly enhanced star formation. The star formation rate (SFR) can be larger than normal galaxies by a factor of 10^{2-3} (SFR $\gtrsim$ 100 $M_\odot$ yr^{-1}; see also Kennicutt, 1998), whereas the Milky Way, which is a typical normal galaxy, forms star with rate of a few $M_\odot$ yr^{-1} (e.g., Murray & Rahman, 2010). The SFR in starburst galaxies is so large that these galaxies will consume their gas reservoir, from which stars are newly forming, on a short timescale after which the SFR will decrease. Thus, starburst phase is a brief period of galaxy evolution. The primary cause of starbursts is gravitational interaction between galaxies. The majority of starburst galaxies appears to be in the midst of a merger or a close encounter with other galaxies. An impressive example of starburst galaxies is an intermediate-stage merger known as the Antennae galaxies (see Figure 1.1).

1.2.3 Ultra/Luminous Infrared Galaxies

Luminous infrared galaxies (**LIRGs**) are galaxies with FIR luminosities $L_{\rm FIR}$ above 10^{11} $L_\odot$, and galaxies with $L_{\rm FIR} \geq 10^{12}$ $L_\odot$ are especially called **ultraluminous infrared galaxies** (**ULIRGs**) (Sanders & Mirabel, 1996). Many LIRGs and ULIRGs were discovered in 1984 by the $IRAS$ satellite (Neugebauer et al., 1984). The bulk of the IR luminosity for U/LIRGs comes from dust heating due to intense starbursts within giant molecular clouds. If star formation takes place in the interior of dense molecular clouds, which contain large amounts of dust, strong radiation from young luminous stars heats the surrounding dust and the dust reemits it at infrared wavelengths. In some cases, the IR luminosity of U/LIRGs comes from an **active galactic nucleus** (**AGN**), which shows significant emission in all wavelengths from a compact region at the centre of a galaxy. The majority of U/LIRGs appears to be during a process of a merger and shows strongly disrupted morphology. Therefore, U/LIRGs are closely related to gravitational interactions between galaxies (e.g., Arp 220 and NGC 6240). In addition, ULIRGs may represent an important stage in the formation of quasars and powerful radio galaxies (see also Sanders & Mirabel, 1996).

1.3 Galaxy Mergers

1.3.1 Overview

Galaxy Mergers are galaxies in the process of colliding or merging with other galaxies. Mergers are also called interacting galaxies or merging galaxies. Galaxy interactions and mergers play an important role in the formation and evolution of galaxies, as illustrated by the increasing galaxy merger rate as one goes to higher redshift (Figure 1.3; Bundy et al., 2009; Bridge et al., 2010). Gravitational interactions between galaxies have powerful effects on their morphology and physical states. The degree of the effect depends on a wide variety of parameters such as collision orbit, collision speed, and relative size. Galaxy mergers are also known to enhance star formation activities as seen in the increasing fraction of tidally distorted morphologies. Therefore, galaxy mergers are closely related to galaxy formation and evolution.

Hubble (1936) noticed the existence of galaxies whose morphologies were quite unusual and later classified them as "highly peculiar objects" (Hubble, 1958). Arp (1966) compiled a catalog of 338 peculiar galaxies from the Palomar all sky survey (Minkowski & Abell, 1963). Similar cataloging projects were carried out by Vorontsov-Velyaminov (1959, 1977) and Arp & Madore (1987). Larson & Tinsley (1978) found early observational evidence that galaxies in the Arp catalog showed a higher level of star formation activity than the control sample of normal galaxies obtained from the Hubble atlas. This was confirmed by the $IRAS$ satellite (Neugebauer et al., 1984). It discovered a new population of galaxies with high IR luminosities (U/LIRGs, see § 1.2.3), many of which showed highly disturbed morphology, indicating recent or past galaxy interactions.

Numerical simulations have provided new insights into studies of galaxy mergers. The first analog n-body simulation of galaxy interaction was carried out by Holmberg (1941). He demonstrated that the degree of tidal disturbance depended on collision orbits. Toomre & Toomre (1972) proved using the restricted three-body approximation that tidal interaction could profoundly alter the distribution and dynamics of stars in a relatively short time. In addition, they predicted that major mergers would result in elliptical galaxies and that star formation activity was enhanced by galaxy interaction, fueling gas to nuclear regions. These predictions were later confirmed by large scale numerical simulations (e.g., Barnes & Hernquist, 1992; Mihos & Hernquist, 1996; Springel et al., 2005).

There are a number of excellent reviews and papers on galaxy mergers: Schweizer (1983, 1986, 1990), Barnes & Hernquist (1992), Struck (1999), and Hopkins et al. (2009, § 1).

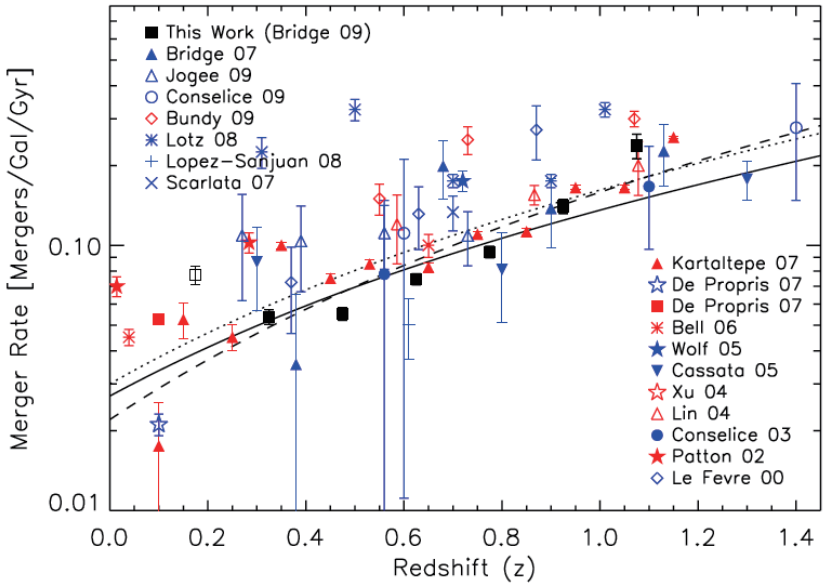

Figure 1.3: Merger rate as a function of redshift in units of mergers galaxy^{-1} Gyr^{-1} (Bridge et al., 2010). The merger rate increases with redshifts.

Image credit—Bridge et al. (2010) (reproduced by permission of the AAS.)

1.3.2 Merger Classification

Galaxy mergers are classified into distinct groups according to their properties.

- **Major/Minor mergers:** Mergers are classified into two types by the mass ratio of their progenitors. One type is major mergers with mass ratios in the range 1:1–3:1 (or 1:1–4:1), and the other is minor mergers with mass ratios below 3:1 (or 4:1). Major mergers, which can lead to significant dynamical and morphological disturbances, are strongly linked to starbursts and AGNs (e.g., Sanders & Mirabel, 1996). Minor mergers including small satellite-galaxy interactions are thought to occur more frequently than major mergers (e.g., Jogee et al., 2009).

- **Wet/Dry mergers:** Mergers are classified into two types by their gas richness. Wet mergers are gas-rich mergers which may produce a larger amount of star formation and trigger starburst, AGN and quasar activities (e.g., Hopkins et al., 2006). On the other hand, dry mergers are gas-poor mergers, most of which are formed by mergers between gas-poor early-type galaxies. These mergers may not involve dramatic changes in the star formation rate but can play an important role in the stellar mass growth (e.g., Naab et al., 2006; Lin et al., 2008).

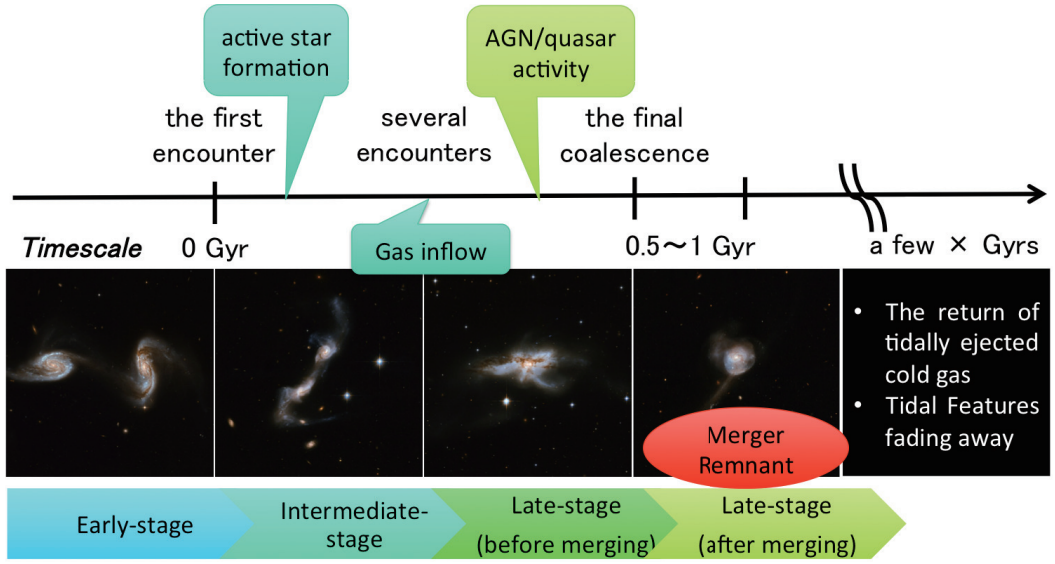

Figure 1.4: Merger sequence and timescale. A merger sequence of major mergers is divided into three stages: early-, intermediate-, and late-stage. A typical timescale of galaxy merge from the first encounter to the final coalescence is 1 Gyr, and a timescale of returning of tidally ejected material after the coalescence is estimated to extend over many Gyr.

Image credit—NASA, ESA, the Hubble Heritage (STScI/AURA)-ESA/Hubble Collaboration, and A. Evans (University of Virginia, Charlottesville/NRAO/Stony Brook University)

1.3.3 Merger Sequence and Timescale

Toomre (1977) first demonstrated that major mergers can be sequenced the so-called "Toomre Sequence". He compiled a set of 11 apparently interacting and merging galaxies from available optical images, and roughly ordered them according to the completeness of the interaction based purely on their optical morphology. The sequence of major mergers is usually divided into three stages: early-stage, intermediate-stage, and late-stage (Figure 1.4), but there is no strict definition to each stage. The typical timescale of galaxy merging from the first encounter to the final coalescence is 1 Gyr (Springel & Hernquist, 2005; Chien & Barnes, 2010), and the timescale of the returning of tidally ejected material after the coalescence is estimated to extend over many Gyr (Hibbard & Mihos, 1995), which is longer compared to the timescale from the first encounter to the final coalescence. General characteristics observed and expected from numerical simulations in each stage are below.

- **Early-stage mergers** (before the first encounter): Galaxies approach each other but are still distinct. The morphology starts to be distorted, and an optical bridge connects the galaxies.

- **Intermediate-stage mergers** (after the first encounter): The apparent morphology is strongly distorted, and tidal tails are formed. Gas inflows into the nuclei, triggering starbursts.

- **Late-stage mergers** (during merger and after merging): AGN and quasar activities are often observed in late-stage mergers, where a growth of a supermassive black hole is also expected. After merging, the system represents a single stellar body and will relax to a normal galaxy.

1.4 Galaxy Formation and Evolution

1.4.1 Galaxy Formation in the Λ-CDM model

The Cosmic Microwave Background (CMB) was discovered by Penzias & Wilson (1965), which was confirmed as the first observational evidence of the Big Bang by Dicke et al. (1965). Since the discovery of the CMB, a number of ground-based observations have been carried out to search for small anisotropies in the CMB, which are seeds of structures in the present Universe. The structures evolved out of very small density fluctuations in the early Universe. Thus these density fluctuations should be visible as small temperature fluctuations in the CMB. The NASA Cosmic Background Explorer (COBE) satellite finally confirmed temperature fluctuations in the CMB map (Smoot et al., 1992), and the Λ-CDM cosmological model came under consideration.

The Λ-CDM model is a cosmological model with the cosmological constant (Λ) and cold dark matter (CDM). Λ is the energy density in a vacuum that explains the accelerating expansion of the Universe. It is currently thought to be associated with dark energy, which constitutes about 70% of the energy density of the present Universe. CDM is necessary to account for gravitational effects observed in large-scale structures, including the rotation of galaxies and the gravitational lensing of light by galaxy clusters. These gravitational effects cannot be explained by the quantity of observable matter. The dark matter component is estimated to constitute about 25% of the mass energy density of the Universe. The remaining 5% is comprised of all baryonic matter observed as atoms and chemical elements. The Λ-CDM model is today referred to as the standard cosmological model, which is able to account for nearly all the large-scale features of the observable Universe, including the accelerating expansion of the Universe and the large-scale structure in the distribution of galaxies.

In the Λ-CDM cosmological model, structure formation in the Universe basically proceeds hierarchically. Small gravitationally bound structures such as stars and stellar clusters form first, and

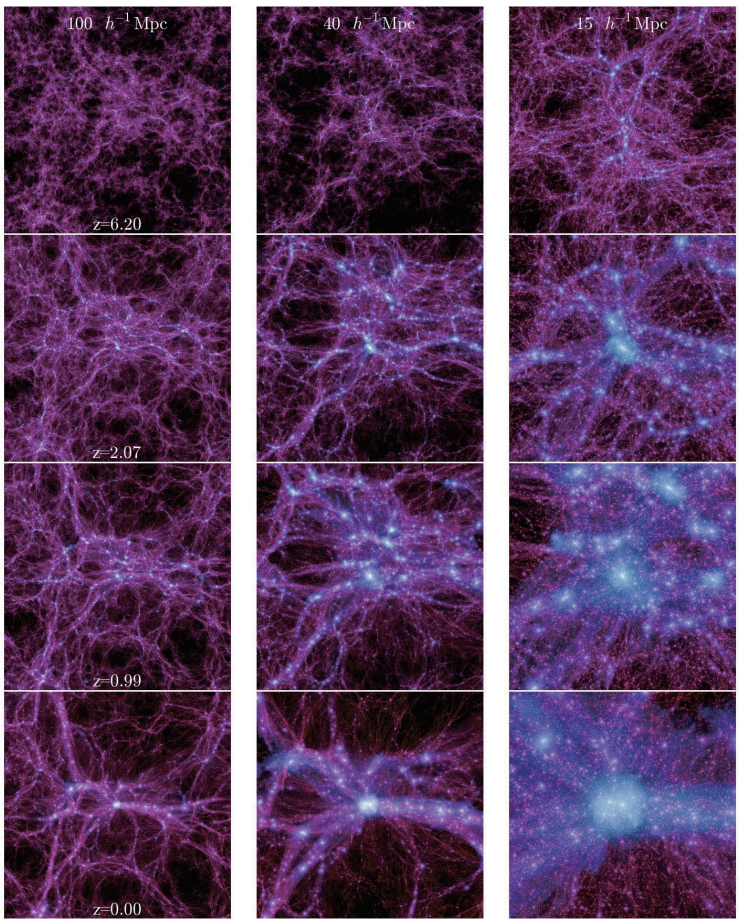

Figure 1.5: Time evolution of the formation of the most massive dark-matter halo in the Millennium-II Simulation (Boylan-Kolchin et al., 2009). The halo is shown at three comoving scales (from left to right: 100, 40 and 1 Mpc^{-1}) and at four different cosmological epochs (from top to bottom: z = 6.2, 2.07, 0.99 and 0).

Image credit—Boylan-Kolchin et al. (2009) (reproduced by permission of the AAS.)

subsequently they merge to form massive gravitationally bound systems such as galaxies, followed by groups, clusters, and superclusters of galaxies. In other words, low-mass dark matter halos form first and subsequently more massive halos form by merging of lower-mass halos (Figure 1.5; Boylan-Kolchin et al., 2009). Gas in a halo cools efficiently and then it is converted into stars. Gas initially accumulates in a disk and subsequently will form stellar disk when the density of the gas in the disk reaches a threshold for star formation. It is now understood that disk galaxies are formed in this way. However, disk galaxies can lose angular momentum during the process of galaxy collision. It is not understood whether disk galaxies will survive after galaxy collision. In contrast, it has been long predicted that the primary mechanism of the formation of early-type galaxies is major mergers (Toomre & Toomre, 1972; Barnes & Hernquist, 1992). Early-type galaxies are often found in the centers of galaxy clusters, where merging is expected to be frequent due to a high galaxy-density. In addition, observations using absorption-line indicate that a significant fraction of early-type galaxies in galaxy clusters has undergone recent star formation (Barger et al., 1996). This bottom-up formation scenario of early-type galaxies is naturally expected for structure formation processes in the Λ-CDM cosmological model.

1.4.2 Galaxy Evolution through Galaxy Mergers

In the Λ-CDM cosmological model, galaxy interactions and mergers are related to the formation and evolution of galaxies. Galaxies undergo several interactions and mergers during their lifetime, thus galaxies evolve by repeated galaxy merger events. Since the 1970's, it has been long predicted from numerical simulations that a major merger of two disk galaxies results in a formation of a spheroid-dominated early-type galaxy (e.g., Toomre, 1977; Barnes & Hernquist, 1992; Naab & Burkert, 2003). This classical scenario is supported by observations, revealing stellar structures of merger remnants (e.g., Schweizer, 1982; Rothberg & Joseph, 2006a) and signatures of mergers such as shells and tidal features around elliptical galaxies (e.g., Schweizer & Seitzer, 1992; Schweizer, 1996).

Contrary to the classical scenario of merger evolution, recent high-resolution simulations that include more realistic gas physics have shown that not all of the major mergers will become an early-type galaxy, but some will reemerge as a disk-dominated late-type galaxy (Barnes, 2002; Robertson & Bullock, 2008; Hopkins et al., 2009). Gas in mergers that do not lose significant angular momentum through stellar torque will survive the collision, reforming a gaseous (and subsequently a stellar) disk

(Figure 1.6; Springel & Hernquist, 2005), while gas that falls to the galaxy center will contribute to a nuclear starburst and subsequent formation of the spheroidal component. This merging process is a candidate for a formation scenario of cold molecular gas disks, that is otherwise not well understood. Another possibility is cosmological accretion (Kereš et al., 2005; Dekel et al., 2009) of low-angular momentum cold gas that eventually settles onto the galactic disk, but this scenario is predicted to be likely more relevant in the outskirts of the galaxies in the local Universe. In galaxy mergers, the chance of disk survival during the merging event depends on orbital parameters, mass ratio, and gas mass ratio of the progenitors (Hopkins et al., 2009), and the same simulations also suggest that increasing the gas mass fraction to the stellar mass leads to a more efficient disk survival (Figure 1.7) as there are fewer stars to lose angular momentum to. In case of pre-mergers with the gas mass fraction of 10 %, which is a typical value for late-type galaxies in the local Universe, the surviving disk fraction after merging is expected to be a few % as shown in Figure 1.7 (Hopkins et al., 2009). The new scenario of merger evolution might resolve a problem that the number of elliptical galaxies in the local Universe is much less than the theoretical value based on the classical scenario (Bournaud et al., 2007).

Minor mergers are thought to occur more frequently than major mergers. Numerical simulations have shown that minor mergers form late-type galaxies (Quinn et al., 1993; Walker et al., 1996) and hybrid systems with spiral-like morphology but elliptical-like kinematics (Bournaud et al., 2004). Such systems were observed by Jog & Chitre (2002). However other numerical simulations predict that late-type galaxies cannot have survived due to multiple minor mergers because repeated minor mergers destroy disks into spheroids (Bournaud et al., 2007), and compact high-redshift spheroids can evolve into local early-type galaxies in the process of minor mergers (Naab et al., 2009). The evolution of minor mergers is still under discussion as well as the evolution of major mergers.

1.5 Merger Remnants

Merger remnants are completely merged galaxies with a single nucleus, and still have tidal tails, shells, and loops, indicating dynamical interactions (e.g., Figure 1.4). Merger remnants are classified as late-stage mergers (see § 1.3.3), and will relax to normal galaxies over time (a few Gyr; Hibbard & Mihos, 1995), returning of tidally ejected material.

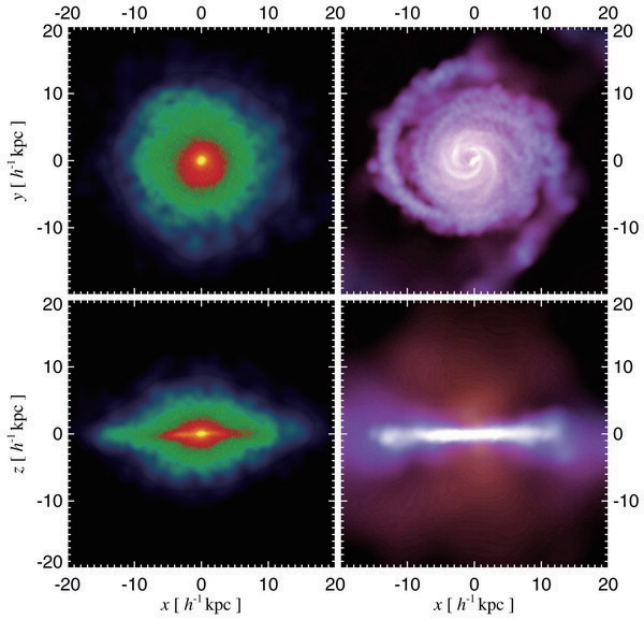

Figure 1.6: Result of a simulation of reformed extended gas disk (Springel & Hernquist, 2005), showing the diistribution of stars (left) and gas (right) in a merger remnant in 1.96 Gyr from the first encounter. The top panels show a face-on view, and the bottom panels show a edge-on view.

Image credit—Springel & Hernquist (2005) (reproduced by permission of the AAS.)

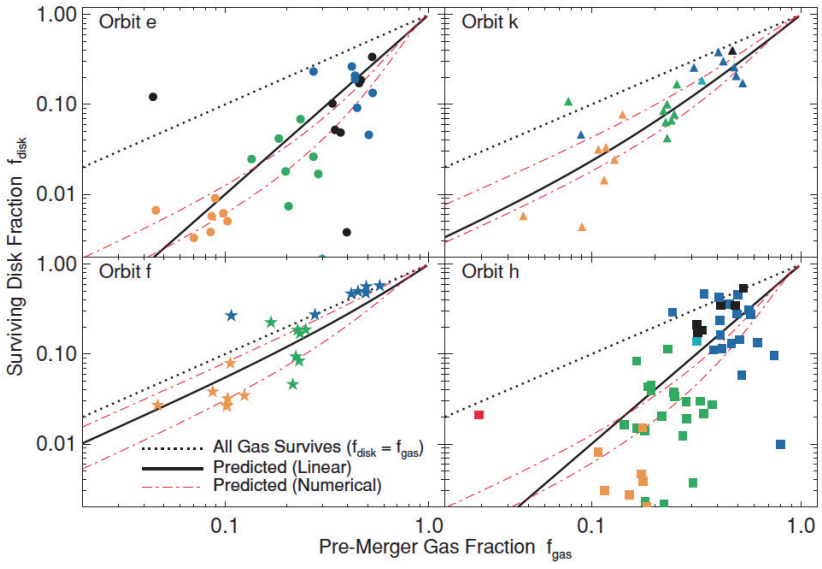

Figure 1.7: The surviving disk fraction as a fraction of gas mass fractions just before the final coalescence (pre-merger gas fraction), for 1:1 major mass-ratio mergers (Hopkins et al., 2009). The disk fraction increases with the gas mass fraction.

Image credit—Hopkins et al. (2009) (reproduced by permission of the AAS.)

1.5.1 Previous Studies on Merger Remnants

Most previous studies on merger remnants (e.g., Lake & Dressler, 1986; Shier & Fischer, 1998; James et al., 1999; Genzel et al., 2001; Dasyra et al., 2006; Rothberg & Joseph, 2004, 2006a,b) focused on the stellar properties. This is because the classical scenario, in which a major merger between two disk galaxies forms a new elliptical galaxy (see § 1.4.2), received higher attention. These studies show that the kinematic and photometric properties of the stellar components in merger remnants, including velocity dispersions, stellar masses and light profiles, are consistent with typical elliptical galaxies and have supported the classical hypothesis for the evolution of major mergers.

A large-scale observational study of the large sample of merger remnants in the local Universe was carried out by Rothberg & Joseph. They present K-band photometry for 51 candidate of merger remnants (Rothberg & Joseph, 2004). Using both the de Vaucouleurs profile and the Sérsic profile, they find that the stellar components in a majority of the sample sources have undergone violent relaxation, though seven sources show evidence for incomplete phase mixing. Their analysis also indicates the presence of "excess light" in the surface brightness profiles of nearly one-third of the sample, suggesting the effect of starbursts induced by the dissipative collapse of the gas. Two years later, they conducted a spectroscopic study for a subsample of 38 merger remnants (Rothberg & Joseph, 2006a,b) to investigate whether the merger remnants have the same stellar properties as elliptical galaxies, such as stellar luminosity and distribution, central stellar velocity dispersion, and metallicity. As a result, the merger remnants show a strong correlation among the parameters of the fundamental plane, which is embedded in a three-dimensional space comprised of the central velocity dispersion, the effective radius, and the surface brightness within the effective radius (Djorgovski & Davis, 1987). Bulges in spiral galaxies and elliptical galaxies share the fundamental plane (e.g., Bender et al., 1992). In addition, their analysis shows that 11 % of the subsample is boxy and anisotropically supported, while 47 % is disky and rotationally supported. The merger remnants show variation in shape and rotation. This may provide an observational diagnostic for discriminating among evolution scenario of merger remnants.

Observational studies of molecular gas in merger remnants have been conducted (e.g., Downes & Solomon, 1998; Wilson et al., 2008), but most of the previous samples are mergers with high FIR luminosities (U/LIRGs). In addition, these studies focused on the the physical state of molecular gas. There are few studies focusing on the morphology of molecular gas.

1.5.2 The Evolution of Merger Remnants

Although the main bodies of merger remnants become devoid of distinct structure, they show plumes and shells in the outer regions after merging (e.g., Rothberg & Joseph, 2004). These features are smoothed out over time. However, returning of tidal material can lengthen the completion of the phase-mixing process. The most tightly bound gaseous material returns to the main body rather quickly and can resettle into a warped disk (Mihos & Hernquist, 1996; Naab & Burkert, 2001; Barnes, 2002). Such a warped gaseous disk has been observed in the nearby merger remnant Centaurus A (Nicholson et al., 1992). In contrast, the loosely bound, high-angular momentum gas falls back to ever-increasing radii over longer time scales, forming a more extended disk outside several effective radii in the merger remnant. The timescale of returning of tidally ejected material is estimated to extend over many Gyr (Hibbard & Mihos, 1995), which is longer compared to the timescale from the first encounter to the final coalescence (10^{8-9} yr; Hibbard & Mihos, 1995; Chien & Barnes, 2010). Therefore, the process of phase mixing takes much longer to complete than violent relaxation.

As mentioned in the previous section (§ 1.4.2), early numerical simulations of galaxy mergers (e.g., Barnes & Hernquist, 1992) demonstrated that a major merger of two disk galaxies can produce an object with an $r^{1/4}$ stellar distribution like typical elliptical galaxies. However, in recent simulations with a gaseous component, disky and rotationally supported merger remnants also form from major mergers (e.g., Springel & Hernquist, 2005). This raises several questions: Do merger remnants with an extended gas disk really exist? and will they evolve into elliptical galaxies with properties similar to those in present-day elliptical galaxies, or into a different type of galaxy? In order to answer these questions, observational studies focusing on a gaseous component in merger remnants are required along with further advanced numerical simulations.

1.6 Radio Astronomy and Interferometry

Radio astronomy is the study of objects in the Universe by analyzing the radio waves emitted from the objects. The very first observations go back to Karl Jansky's discovery in the 1930's. He observed radiation from the Milky Way using a rotating radio antenna. Tow decades later, in 1951, Ewen and Purcell discovered the 21 cm hydrogen line from the Milky Way using a horn antenna. Subsequent observations have provided a whole new outlook on already known objects such as stars and galaxies, while revealing new types of objects, such as radio galaxies, quasars, pulsars, and masers.

1.6.1 Radio Observations in the CO line

The most abundant molecule in the Universe is molecular hydrogen (H_2), which is a symmetric homo-nuclear molecule with no permanent electric dipole moment, hence we cannot observe the H_2 line at radio wavelengths because it does not have a permitted transition. The second most abundant molecule is carbon monoxide (^{12}CO; hereafter CO), which has been used extensively as an indirect tracer of H_2 despite its low relative abundance (N_{CO}/N_{H_2} = 10^{-4} – 10^{-5}; Tielens, 2005). Collisions between CO and H_2 excite the CO to higher rotational states (to J = 2, 3,...), which subsequently returns to the lower energy level by radiating the excess energy away. Because CO has a low dipole moment, it is easily excited to higher J levels at a low critical density ($n_{\rm crit}$ = 1.1 $\times$ 10^3 cm^{-3} for CO (1–0); Tielens, 2005) and an upper energy level ($E_{\rm u}$ = 5.5 K for CO (1–0); Tielens, 2005).

The lowest J transition of CO, CO (1–0) line, is the best tracer of the diffuse extended disk and of the kinematics of the cold molecular gas. On the other hand, a high J transition of CO is a good tracers of denser and warmer molecular gas related directly to star formation, because the critical density and the upper energy level are higher than those of the CO (1–0).

In general, the CO (1-0) line is optically thick, which satisfies the optical depth $\tau_\nu > 1$. An optically thick line is one in which the average photon of frequency ν cannot traverse the entire medium without being absorbed. Thus we observe radiation emitted from the surface of molecular clouds rather than from the core of molecular clouds. In contrast, an optically thin line is less affected by absorption and thus we can investigate the core of molecular clouds using optically thin lines.

1.6.2 Radio Interferometer

Radio astronomy is conducted using radio antennas (telescopes), that are either used singularly or used with multiple linked antennas utilizing the techniques of radio interferometry and aperture synthesis. The former is a single-dish telescope and the latter is a radio interferometer. Radio interferometers achieve higher angular resolution than single-dish telescopes because the angular resolution θ is determined by approximately λ/D, where λ is the wavelength observed and D is the diameter of the single-dish telescope or the longest baseline length. Though early interferometers were used as a single baseline between two antennas for measurement, later interferometers, such as the Very Large Array (VLA), form arrays of telescopes arranged in a pattern on the ground. A limited number of baselines will result in insufficient uv-plane coverage and low-quality imaging.

There are currently-operated millimeter/submillimeter interferometers in the world (Figure 1.8):

- **Atacama Large Millimeter/submillimeter Array (ALMA)**

  ALMA is the most powerful millimeter/submillineter interferometer, which consists of up to 64 12-m antennas and a compact array (ACA; 12×7-m antennas + 4×12-m antennas). The proposed maximum baseline is 18.5 km, which provides 0.″03 angular resolution at 115 GHz. It is built in the Atacama Desert of northern Chile at an altitude of approximately 5000 m. Incoming radio waves are less susceptible to absorption by terrestrial water vapor in the ALMA site and thus we can observe radio waves at relatively shorter wavelengths (at higher frequencies).

- **Combined Array for Research in Millimeter-wave Astronomy (CARMA)**

  The CARMA is a millimeter-wave interferometer, which combines the previously independent Owens Valley Millimeter Observatory (OVRO) array and Berkeley-Illinois-Maryland Association (BIMA) array. The number of antennas is increased to 23 (6×10.4 m antennas + 9×6.1 m antennas + 8×3.5 m antennas), providing a substantial improvement in uv coverage. It is located at a high-altitude site (∼2200 m) in the Inyo Mountains of California, USA. The maximum baseline is approximately 2 km, which provides ∼0.″3 angular resolution at 115 GHz.

- **Plateau de Bure Interferometer (PdBI)**

  The PdBI is one of the most sensitive millimeter interferometers, operated by the Institut de radioastronomie millimétrique (IRAM). It is situated on the Plateau de Bure at altitude of 2550 m in the French Alps. During its history, the PdBI underwent several track extensions and received additional antennas and technical upgrades. The interferometer now consists of six 15 m antennas with powerful dual-polarisation receivers for the 3mm and 1mm observing bands. The maximum baseline is 760 m, which provides 0.″7 angular resolution at 115 GHz.

- **Submillimeter Array (SMA)**

  The SMA is the only submillimeter-wave interferometer in the north hemisphere, operated at wide-range frequencies from 180 GHz to 700 GHz. It consists of eight 6 m antennas located at an altitude of 4100 m on Mauna Kea in Hawaii, USA. The digital correlators allows flexible allocation of thousands of spectral channels. The maximum baseline is 509 m, which provides ∼0.″4 angular resolution at 345 GHz. It can be operated together with the James Clerk Maxwell Telescope (JCMT) and the Caltech Submillimeter Observatory (CSO) as eSMA.

Figure 1.8: Existing millimeter/submillimeter interferometers: ALMA (upper-left), CARMA (upper-right; ©CARMA), PdBI (bottom-left; ©IRAM), and SMA (bottom-right)

1.7 Scientific Goals and Thesis Structure

In this thesis, I statically reveal the distribution and kinematics of the molecular gas in late-stage mergers, using our own and archival observational data, which is the largest interferometric CO survey on merging galaxies to date. This is the first step in our series of studies which emphasize the cold molecular gas in merger remnants, instead of the stellar component which has been the focus of previous studies. From this new compilation of high quality CO data, I give new insights into the evolution of galaxies via galaxy mergers. This thesis opens up the possibility of additional future studies, for example comparative studies with numerical simulations, observations of the diffuse gas traced in HI, and dense gas traced in HCO^+/HCN. Initial preparation is already underway and understanding the evolution of a major merger is our ultimate scientific goal.

The key scientific goal of this thesis involves understanding the properties of molecular gas in merger remnants. We have conducted a CO survey toward 27 optically-selected merger remnants in the local Universe using millimeter/submillimeter interferometers (ALMA, SMA, and CARMA). Combined with archival data, we analyze the molecular gas in 37 optically-selected merger remnants in order to investigate the following main questions.

- **What is the distribution and kinematics of cold molecular gas in merger remnants? (Chapter 2, and Chapter 3)**
  Chapter 2 presents the CO images of 37 optically-selected merger remnants obtained at ALMA, SMA, CARMA and PdBI. Our study is the first systematic CO imaging survey of merger remnants. The distribution and kinematics of molecular gas are presented for each source to investigate the properties of the molecular gas in merger remnants in Chapter 3 and Chapter 4.

- **Do extended cold molecular gas disks form in merger remnants, as predicted from recent numerical simulations? (Chapter 2 and Chapter 3)**
  Recent numerical simulations with realistic gas physics have shown that some gas-rich major-mergers will reemerge as a disk dominated late-type galaxy, by reforming an extended cold molecular gas disk (and subsequently a stellar disk) or via survival of the progenitor disks. In order to verify this scenario and look for observational evidence of an extended molecular disk

forming in merger remnants, the presence of the molecular gas disk is confirmed using fitting and modeling programs in Chapter 3. Chapter 4 focuses on the size of the gas disk.

- **Are the properties of the molecular gas in merger remnants different from early-type and late-type galaxies? (Chapter 4)**

  Comparing the properties of the molecular gas in early-type galaxies and late-type galaxies, leads to better understanding of the nature of merger remnants. Combining with IR images, we investigate whether the global properties such as gas mass fraction and star formation activity in merger remnants are different from those of early- or late-type galaxies or not.

- **What type of galaxies will merger remnants evolve into? (Chapter 4)**

  It has been long predicted from numerical simulations that a major merger of two disk galaxies results in a formation of the spheroid-dominated early-type galaxy. In the final section of Chapter 5, the evolution of merger remnants is discussed observationally by comparing the sizes of the molecular gas disks and gas mass fractions to early-type and late-type galaxies in the field. Finally, the observational implications are compared with theoretical predictions.

- **What's next? (Chapter 5)**

  Chapter 6 begins with a summary of this thesis including answers to the questions addressed here. It is then followed by further implication and plans to better understand galaxy merging and the evolution and formation of galaxies in the local Universe through galaxy mergers.

Chapter 2

Merger Remnant CO Imaging Survey

In this chapter, we present the results of the Merger Remnant CO Imaging Survey toward 37 optically-selected merger remnants. We describe the sample selection, observational details, and data reductions. The CO maps are presented along with background information and short descriptions of the morphological and kinematical features of the molecular gas for each source. In addition, we investigate the CO velocity fields of the merger remnants using numerical calculations to quantify whether the velocity fields can be modeled by circular rotation. As a results, we find the molecular gas disks in 24/37 sources, and then determine the kinematical parameters of the molecular gas disks.

2.1 Merger Remnant Sample

Our sample is drawn from the merger remnant sample studied by Rothberg & Joseph (2004), which is selected solely based on optical morphology that suggests advanced stages of the merger, regardless of star formation or AGN activity. Specifically, their sample sources are selected primarily from four catalogs, the Atlas of Peculiar Galaxies (Arp, 1966), the Catalogue of Southern Peculiar Galaxies (Arp & Madore, 1987), the Atlas and Catalog of Interacting Galaxies (Vorontsov-Velyaminov, 1959), and the Uppsala General Catalogue (Nilson, 1973), by visually inspecting optical images according to the following criteria:

- Tidal tails, loops, and shells, which indicate strong gravitational interactions.
- Single nucleus, which marks the completion of the merger.
- The absence of nearby companions, which marks advanced stages of the merger.

Out of the 51 objects studied by Rothberg & Joseph (2004), we have obtained new and published interferometric CO maps for 37 merger remnants in the parent sample. In addition, we have obtained new single-dish CO measurements and published CO data for 26 out of 37 sources to estimate the total flux. We note that the exact fraction of how many of these sources resulted from a major or minor merger is unknown since it is difficult to reverse the chronology and disentangle the exact mass and morphology of the progenitors. The K-band images (Rothberg & Joseph, 2004) of 37 merger remnants are shown in Figure 2.1, and basic properties of the sample are summarized in Table 2.1.

We estimate the FIR luminosities, using the $IRAS$ Point Source Catalog (Beichman et al., 1988), the $IRAS$ Faint Source Catalog (Moshir et al., 1992), and the $IRAS$ Faint Source Reject Catalog (Moshir et al., 2008), according to the following equation (Helou et al., 1988):

$$L_{\rm FIR} = 1.26 \times 10^{-14} \left(2.58\, S_{60\ \mu{\rm m}} + S_{100\ \mu{\rm m}}\right), \tag{2.1}$$

where $S_{60\ \mu{\rm m}}$ and $S_{100\ \mu{\rm m}}$ are the $IRAS$ 60 μm and 100 μm band flux densities measured in Jy. The FIR luminosities of the sample sources range from 10^9 to 10^{12} $L_{\odot}$, but nine of our 37 sources are not detected in the IRAS maps and we estimate the upper limits of the FIR luminosity. One source (UGC 8058) is classified as ULIRG, and 12 sources are classified as LIRGs.

Rothberg & Joseph (2004) estimate the Sérsic index from the Sérsic profile, which is a generalized form of the de Vaucouleurs profile to probe the surface brightness profile:

$$\mu(r) = \mu_{\rm eff} + b_n \left[\left(\frac{r}{r_{\rm eff}} \right)^{1/n} - 1 \right], \tag{2.2}$$

where n is a free parameter, called the "Sérsic index", $r_{\rm eff}$ is the radius of the isophote containing half the total luminosity, and $\mu_{\rm eff}$ is the surface brightness at the effective radius. The constant b is given by b_n = 0.868n - 0.142. The Sérsic index indicates an exponential disk profile seen in typical disk galaxies when n = 1 and a de Vaucouleurs profile seen in typical elliptical galaxies when n = 4. The Sérsic index of n = 10 means that the Sérsic fitting is less accurate than the fitting toward other sources with $n \neq 10$ and introduces large errors into the Sérsic effective radii of sources with n = 10. In our sample of 37, there are 12 sources with $n < 3$, 12 sources with $3 \leqq n < 5$, three sources with $5 \leqq n < 10$, and 10 sources with n = 10).

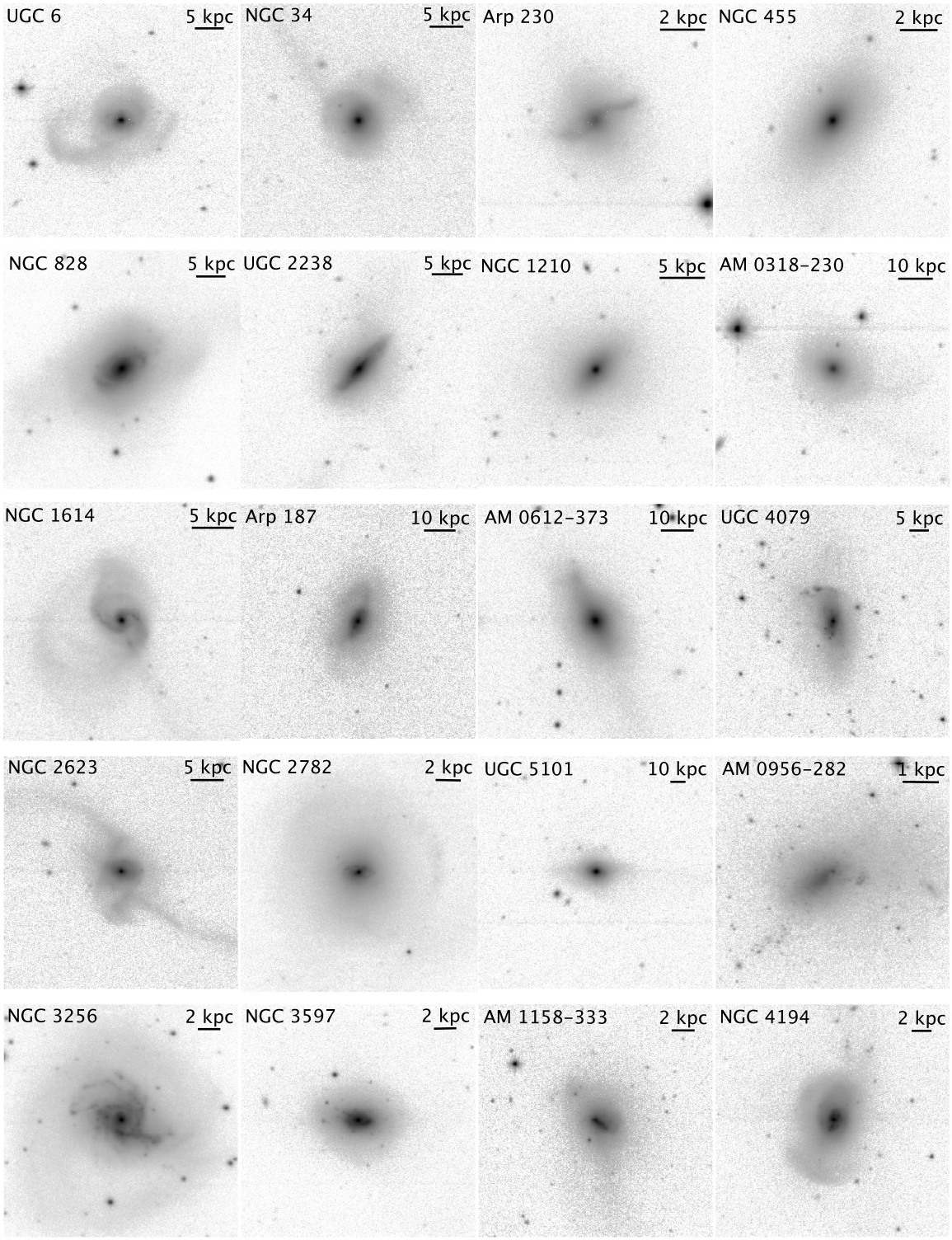

Figure 2.1: K-band images (Rothberg & Joseph, 2004) of the 37 merger remnant sample. The length of each side corresponds to 90″. The magnification is selected individually for each galaxy to clearly illustrate its individual morphological structures.

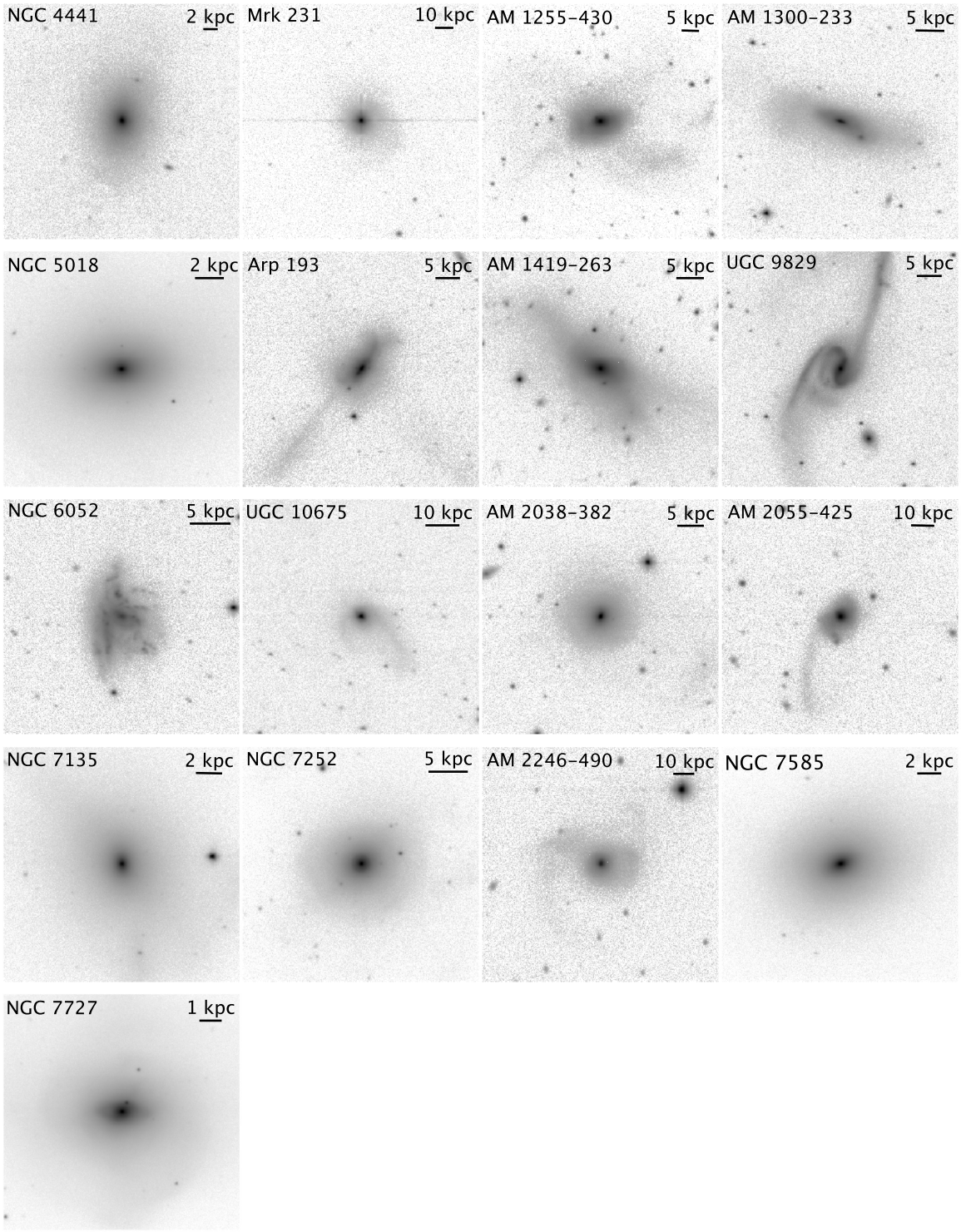

Figure 2.1: Continued. K-band images (Rothberg & Joseph, 2004) of the 37 merger remnant sample.

Table 2.1: Merger Remnant Sample

Name (1)	R.A. (J2000) (2)	Decl. (J2000) (3)	V_{sys} [km s^{-1}] (4)	D_L [Mpc] (5)	Scale [pc/1″] (6)	Log L_{FIR} [$L_\odot$] (7)	M_K [mag] (8)	Sérsic n (9)
UGC 6	00 03 09	21 57 37	6582	91.5	425	10.91	-24.01	10.00
NGC 34	00 11 06	-12 06 26	5931	82.6	385	11.41	-24.61	10.00
Arp 230	00 46 24	-13 26 32	1742	23.9	115	9.57	-21.75	1.56
NGC 455	01 15 57	05 10 43	5269	73.3	343	$<$ 9.71	-24.64	6.21
NGC 828	02 10 09	39 11 25	5374	74.6	349	11.29	-25.36	2.99
UGC 2238	02 46 17	13 05 44	6436	89.8	417	11.28	-24.58	1.46
NGC 1210	03 06 45	-25 42 59	3928	54.4	257	$<$ 9.15	-23.72	4.08
AM 0318-230	03 20 40	-22 55 53	10699	150.7	681	$<$ 10.34	-25.09	5.01
NGC 1614	04 33 59	-08 03 44	4778	66.1	311	11.51	-24.74	10.00
Arp 187	05 04 53	-10 14 51	12291	173.8	778	10.80	-25.25	4.10
AM 0612-373	06 13 47	-37 40 37	9734	136.5	621	$<$ 10.25	-25.65	3.44
UGC 4079	07 55 06	55 42 13	6108	85.1	396	10.43	-23.78	3.08
NGC 2623	08 38 24	25 45 17	5535	77.1	360	11.53	-24.22	10.00
NGC 2782	09 14 05	40 06 49	2562	35.1	168	10.44	-23.83	6.68
UGC 5101	09 35 51	61 21 11	11809	166.8	749	11.95	-25.50	10.00
AM 0956-282	09 58 46	-28 37 19	980	13.6	65.0	9.12	-20.50	2.45
NGC 3256	10 27 51	-43 54 14	2738	37.6	179	11.51	-24.72	2.17
NGC 3597	11 14 41	-23 43 39	3504	48.5	230	10.88	-23.72	1.87
AM 1158-333	12 01 20	-33 52 36	3027	41.8	199	9.96	-22.61	3.75
NGC 4194	12 14 09	54 31 36	2506	34.7	166	10.81	-23.21	4.59
NGC 4441	12 27 20	64 48 06	2674	36.8	175	9.96	-22.98	6.83
UGC 8058	12 56 14	56 52 25	12642	178.6	797	12.37	-27.55	10.00
AM 1255-430	12 58 08	-43 19 47	9026	126.6	578	$<$ 10.18	-24.93	1.87
AM 1300-233	13 02 52	-23 55 18	6446	89.8	417	11.41	-24.65	4.99
NGC 5018	13 13 00	-19 31 05	2794	38.5	183	9.61	-25.15	4.39
Arp 193	13 20 35	34 08 22	7000	97.5	451	11.59	-24.40	2.74
AM 1419-263	14 22 06	-26 51 27	6709	93.6	434	$<$ 10.19	-24.94	4.12
UGC 9829	15 23 01	-01 20 50	8492	118.8	545	10.39	-24.96	2.34
NGC 6052	16 05 12	20 32 32	4716	65.3	307	10.88	-23.55	1.13
UGC 10675	17 03 15	31 27 29	10134	142.5	646	11.03	-24.80	10.00
AM 2038-382	20 41 13	-38 11 36	6057	84.3	393	10.37	-24.70	10.00
AM 2055-425	20 58 26	-42 39 00	12840	181.7	810	11.95	-25.08	2.34
NGC 7135	21 49 46	-34 52 35	2640	36.4	173	9.05	-23.95	10.00
NGC 7252	22 20 44	-24 40 41	4688	64.9	305	10.66	-24.84	3.32
AM 2246-490	22 49 39	-48 50 58	12884	182.1	812	11.72	-25.52	10.00
NGC 7585	23 18 01	-04 39 01	3447	47.7	226	$<$ 9.34	-24.98	3.53
NGC 7727	23 39 53	-12 17 35	1855	25.6	123	$<$ 8.80	-24.23	3.41

NOTE.—Col.(1): Source name. Col.(2) & Col.(3): Right ascension and declination. The positions are defined by the K-band image (Rothberg & Joseph, 2004). Col.(4): The system velocity (Rothberg & Joseph, 2004). Col.(5): The luminosity distance. Col(6): The spatial scale. Col.(7): The FIR luminosity. The luminosities are estimated using the IRAS catalogs. Col.(8): The K-band magnitude (Rothberg & Joseph, 2004). Col.(9): The Sérsic index (Rothberg & Joseph, 2004). The Sérsic index n = 10 means that the Sérsic fitting is less accurate and introduces errors into the solution.

2.2 Observations and Data Reduction

2.2.1 Observations with ALMA

The CO (1–0) observations for 20 sources (see Table 2.2) were carried out using ALMA within the ALMA Cycle 0 period. All sources except for NGC 455 are located in the southern sky (decl. < 0). We used the compact configuration for three nearby sources (Arp 230, AM 0956-282, and NGC 7727) and the extended configuration for the other 17 sources to achieve $\leq$ 1 kpc spatial resolution. The number of 12 m antennas was 16 – 24 depending on observation. The primary beam of the array is $\sim 50''$at 115 GHz. The correlator has a 1.875 GHz bandwidth with 488 kHz frequency resolution.

We imaged the calibrated visibility data using the Common Astronomy Software Applications package (CASA). The synthesized beam size ranges between $1\farcs2$ and $6\farcs4$ by adopting briggs weighting of the visibilities (robust = 0.5), and the achieved rms noise level in 20 km s^{-1} channel maps ranges between 1.78 – 5.29 mJy $beam^{-1}$. The uncertainty of flux calibration is 5 %.

2.2.2 Observations with SMA

The CO (2–1) observations for five galaxies (NGC 828, UGC 2238, UGC 9829, NGC 6052, and UGC 10675; see Table 2.2) were carried out at the SMA in June and October 2011. The data were obtained using the compact configuration, which provides maximum baseline lengths of approximately 70 m. The primary beam of the array is $\sim 52''$at 230 GHz. The correlator was configured to cover 2 GHz with 3.25 MHz frequency resolution.

Data inspection was carried out using the IDL-based SMA calibration tool MIR, and imaging was done using the MIRIAD package. The synthesized beam size is $\sim 1\farcs6$ by adopting natural weighting of the visibilities, which gives maximum sensitivity. The achieved rms noise level in 20 km s^{-1} channel maps range between 18.5 – 27.3 mJy beam s^{-1}. The uncertainty of flux calibration is 20 %.

2.2.3 Observations with CARMA

The CO (1–0) observations for two galaxies (UGC 6 and UGC 4079; see Table 2.2) were carried out using the CARMA on January and February 2011. The data were obtained using the C configura-

tion, which provides baseline lengths of 26 – 370 m. The primary beam of the 10 m array is $\sim 60''$at 115 GHz. The correlator was composed of 10 bands, and each band consisting of 15 channels with 31.25 MHz frequency resolution.

Data inspection and imaging were carried out using the MIRIAD package. The synthesized beam sizes are $2\farcs0 \times 1\farcs5$ for UGC 6 and $1\farcs8 \times 1\farcs6$ for UGC 4079 by adopting natural weighting of the visibilities. The achieved rms noise level in 20 km s^{-1} channel maps are 7.54 mJy beam s^{-1} for UGC 6 and 4.25 mJy beam s^{-1} for UGC 4079. The uncertainty of the flux calibration is 20 %.

2.2.4 Interferometric Archival Data

We further obtained published and archived interferometric CO maps for 10 sources, out of which seven sources were observed using the SMA (Wilson et al., 2008), two sources were observed using the Plateau de Bure Interferometer (PdBI) (Hunt et al., 2008; Jütte et al., 2010), and one source (NGC 3256) was observed using ALMA for Science Verification. The basic properties of the archive data are summarized in Table 2.4. The observed CO transitions are J = 1–0 for three sources, which were observed with ALMA or PdBI, J = 2–1 for five sources, and J = 3–2 for two sources.

The synthesized beam size ranges between $0\farcs8$ and $6\farcs4$, which correspond to < 1 kpc for each source. The achieved rms noise levels in 20 km s^{-1} channel maps range between 1.38 mJy $beam^{-1}$ and 32.5 mJy $beam^{-1}$. The uncertainty of flux calibration is 5 % for NGC 3256, which was observed at ALMA, and 20 % for the rest.

2.2.5 Single-dish Observations

The CO (1–0) observations were carried out using the NRO 45 m telescope for 10 sources during 2011 – 2012. The single-beam, 2-Sideband, and dual-polarization reciever (T100; Nakajima et al., 2008) was used as the receiver front end. The analog signal from T100 is downconverted to 2–4 GHz and digitized to 3-bits before being transferred to the digital FX-type spectrometer SAM45. The 488 kHz resolution mode (2 GHz bandwidth) of SAM45 was used for the frequency resolution. A standard position switching between a source and an off-point was adopted to remove the atmospheric and instrumental effects in the bandpass. Typical system temperature was 150 – 200 K.

Table 2.2: Properties of Interferometric Observations

Name	Transition	Telescope	rms [mJy/Beam]	Norm. rms [mJy/Beam]	Spectral Res. [km/s]	Beam Size [″]
(1)	(2)	(3)	(4)	(5)	(6)	(7)
UGC 6	CO (1–0)	CARMA	3.37	7.54	100	2.00 × 1.47
Arp 230	CO (1–0)	ALMA	5.82	2.91	5	4.45 × 3.77
NGC 455	CO (2–1)	ALMA	2.07	2.07	20	1.57 × 1.23
NGC 828	CO (2–1)	SMA	22.1	24.7	25	4.23 × 3.10
UGC 2238	CO (2–1)	SMA	17.7	19.8	25	4.25 × 2.97
NGC 1210	CO (1–0)	ALMA	2.18	2.18	20	1.41 × 1.11
AM 0318-230	CO (1–0)	ALMA	3.12	3.12	20	1.98 × 1.25
Arp 187	CO (1–0)	ALMA	2.52	2.52	20	2.19 × 1.23
AM 0612-373	CO (1–0)	ALMA	2.83	2.38	20	1.93 × 1.51
UGC 4079	CO (1–0)	CARMA	1.90	4.25	100	1.80 × 1.58
AM 0956-282	CO (1–0)	ALMA	5.71	2.86	5	4.21 × 2.80
NGC 3597	CO (1–0)	ALMA	3.98	3.98	20	1.56 × 1.17
AM 1158-333	CO (1–0)	ALMA	4.60	4.60	20	1.70 × 1.14
AM 1255-430	CO (1–0)	ALMA	1.78	1.78	20	1.95 × 1.17
AM 1300-233	CO (1–0)	ALMA	2.06	2.06	20	2.24 × 1.07
NGC 5018	CO (1–0)	ALMA	5.29	5.29	20	1.98 × 1.22
AM 1419-263	CO (1–0)	ALMA	1.80	1.80	20	1.88 × 1.09
UGC 9829	CO (2–1)	SMA	24.4	27.3	25	4.11 × 2.82
NGC 6052	CO (2–1)	SMA	21.4	18.5	15	3.23 × 2.63
UGC 10675	CO (2–1)	SMA	18.0	20.1	25	3.59 × 3.04
AM 2038-382	CO (1–0)	ALMA	2.97	2.97	20	1.47 × 1.16
AM 2055-425	CO (1–0)	ALMA	2.34	2.34	20	1.35 × 1.08
NGC 7135	CO (1–0)	ALMA	3.99	3.99	20	1.72 × 1.18
NGC 7252	CO (1–0)	ALMA	3.36	3.36	20	1.87 × 1.16
AM 2246-490	CO (1–0)	ALMA	2.24	2.24	20	1.34 × 1.17
NGC 7585	CO (1–0)	ALMA	3.93	3.93	20	1.52 × 1.10
NGC 7727	CO (1–0)	ALMA	4.36	2.18	5	4.10 × 3.74

NOTE.—Col.(1): Source name. Col.(2): The CO transition. Col.(3): Telescope name. Col.(4): The noise level in the velocity resolution shown in Col. (6). Col.(5): The normalized noise level in the velocity resolution of 20 km s^{-1}. Col.(6): The spectral resolution of the channel map. Col.(7): The beam size.

Table 2.3: Properties of Archival Interferometric Data

Name	Transition	Telescope	rms [mJy/Beam]	Norm. rms [mJy/Beam]	Spectral Res. [km/s]	Beam Size [″]	Ref.
(1)	(2)	(3)	(4)	(5)	(6)	(7)	(8)
NGC 34	CO (2–1)	SMA	13.8	15.4	25	4.13×3.11	1
NGC 1614	CO (2–1)	SMA	11.2	15.8	40	3.67×3.33	2
NGC 2623	CO (2–1)	SMA	11.6	16.4	40	1.21×0.99	2
NGC 2782	CO (1–0)	PdBI	1.94	1.37	10	2.09×1.51	3
UGC 5101	CO (2–1)	SMA	11.9	16.8	40	1.20×0.96	2
NGC 3256	CO (1–0)	ALMA	1.29	1.84	40.64	7.57×5.43	4
NGC 4194	CO (2–1)	SMA	12.7	8.98	10	2.94×2.38	5
NGC 4441	CO (1–0)	PdBI	2.92	1.67	6.56	3.25×2.65	6
UGC 8058	CO (3–2)	SMA	19.8	28.0	40	0.93×0.72	2
Arp 193	CO (3–2)	SMA	23.0	32.5	40	2.22×1.98	2

NOTE.—Col.(1): Source name. Col.(2): The CO transition. Col.(3): Telescope name. Col.(4): The noise level in the velocity resolution shown in Col. (6). Col.(5): The normalized noise level in the velocity resolution of 20 km s^{-1}. Col.(6): The spectral resolution of the channel map. Col.(7): The beam size. Col(8): Reference: 1. Archive (PI: Z. Wang), 2. Wilson et al. (2008), 3. Hunt et al. (2008), 4. ALMA Science Verification, 5. Archive (PI: S. Aalto), 6.Jütte et al. (2010)

Data reduction was carried out using the AIPS-based NRO calibration tool NEWSTAR. After flagging scans with large ripples, the final spectra were made by fitting a first order baseline. The chopper wheel method was used to convert to antennae temperature ($T_{\rm A}^{*}$) scale, and the $T_{\rm A}^{*}$ was converted to the main beam temperature ($T_{\rm mb}$) using a main beam efficiency of $\eta_{\rm mb} = 0.4$ and $T_{\rm mb} = T_{\rm A}^{*}/\eta_{\rm mb}$. The final spectra are converted to Jansky using Kelvin–to–Jansky conversion factor of 2.4 Jy K^{-1} and the beam size of $\sim 15''$at this frequency. We checked the telescope pointing every 0.5 – 1.0 hour toward a nearby SiO maser. The rms noise levels range between 1 mK and 12 mK in 30 km s^{-1} velocity resolution (Table 2.2).

2.3 Distribution and Kinematics of the Molecular Gas

2.3.1 High Resolution Interferometric CO Maps

The CO emission was newly detected in 20 out of 27 sources (74 %). The final number of our sample is 37 including seven galaxies undetected in the CO line after combining with archival data. The line integrated intensities are listed in Table 2.5. The integrated intensity maps and velocity fields of 30 sources are presented in Figure 2.2 and Figure 2.3, respectively. They were made by smoothing and clipping the intensity using the AIPS task, MOMNT. The cleaned image cube was smoothed both spatially and in velocity and then this cube was clipped at the 1.5 σ level per a channel for 20 galaxies observed with ALMA (Cycle 0), 5 σ level per a channel for NGC 3256 and NGC 4194 because of high side-lobe levels which cannot be eliminated, and 2 σ level per a channel for the others.

The molecular gas in 20/30 sources is distributed in the nuclear regions and the CO emission peaks roughly correspond to the galactic centers. In the other 10 sources, the CO distribution shows multiple components or typical galactic structures such as arms and a bar. We mention remarkable CO structures here and detailed structures in § 3.5. The CO distribution shows a multiple-peak along the major axis in Arp 230 and an arm-like structure in NGC 3597, while their velocity fields appear very smooth. In NGC 4194 and NGC 6052, the CO distribution does not correlate with the stellar distribution and the CO emission is not associated with the galactic centers. Hunt et al. (2008) report that the CO emission in NGC 2782 is elongated in the nuclear region and clearly shows the diffuse spiral arms extending towards the north and south. In UGC 9829, which has two long tails, the molecular gas is distributed along one tail. The molecular gas in AM 1158-333 is distributed outside the stellar profile, but the faint structure is not clear due to the limited sensitivity.

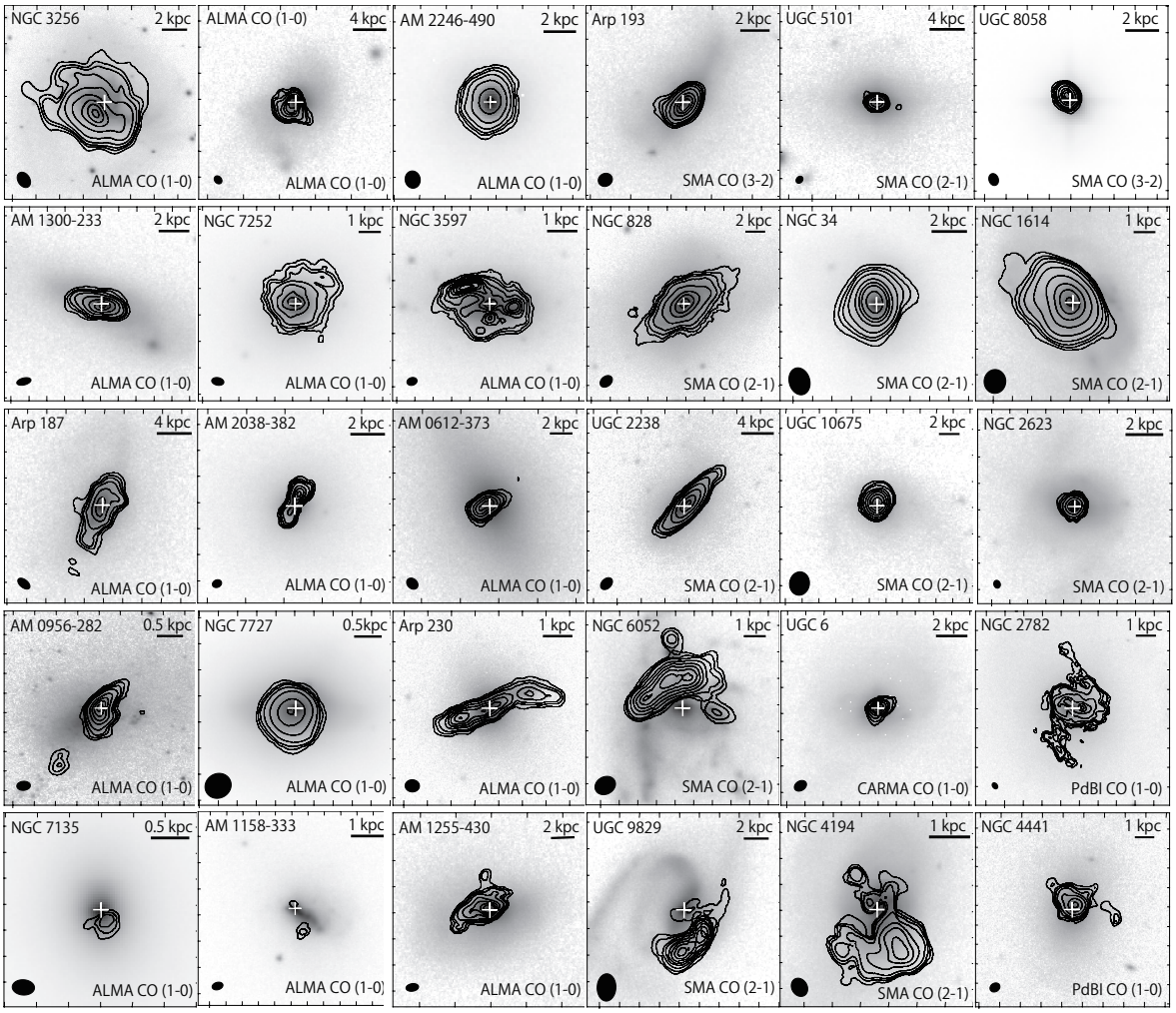

Figure 2.2: The CO integrated intensity maps of 30 merger remnants. The white plus signs show the galactic centers defined by the K-band images (Rothberg & Joseph, 2004). The black elliptical on the bottom-left corner of each map show the beam size. The FIR luminosities of the sources decreases from up to bottom.

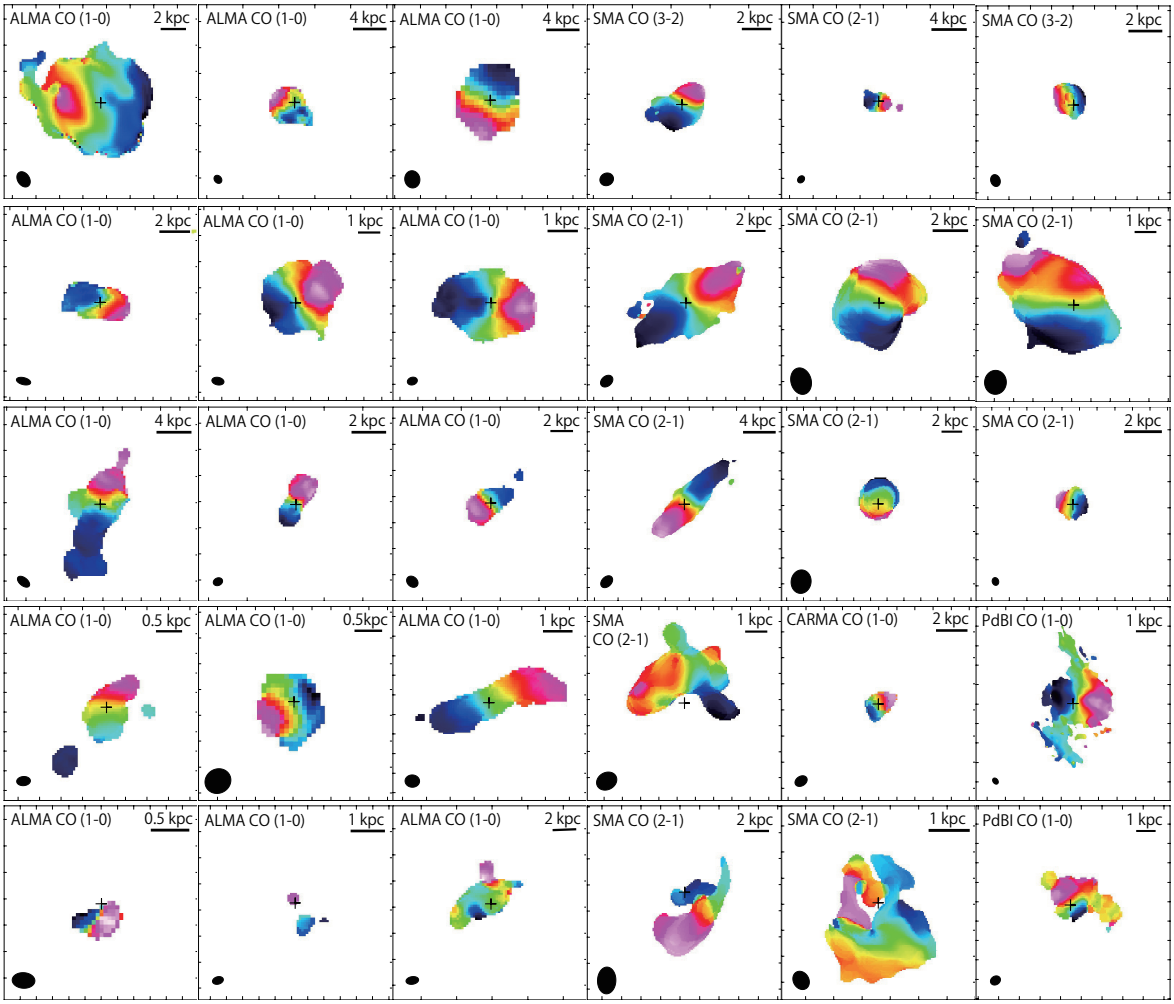

Figure 2.3: The CO velocity fields of 30 merger remnants. The black plus signs show the galactic centers defined by the K-band images (Rothberg & Joseph, 2004). The black elliptical on the bottom-left corner of each map show the beam size. The FIR luminosities of the sources decrease from up to bottom.

2.3.2 Single-dish CO (1–0) Spectra

The new CO (1–0) spectra for 10 sources observed with the NRO 45 m telescope are presented in Figure 2.2 and the properties of the observations are listed in Table 2.5. We report the first detections of the CO (1–0) line in two sources (UGC 4079 and UGC 9829). The velocity integrated line intensity of NGC 2623 and NGC 2782 are 37.44±7.49 K km s^{-1} and 23.53±1.71 K km s^{-1}, respectively. These correspond to 53 % and 25 % of those in the previous observations carried out at the Five College Radio Astronomical Observatory (FCRAO) 14 m telescope (Young et al., 1995). These differences could be explained by a difference in the beam sizes. The beam size of the NRO 45 m telescope (15″at 115 GHz) is about three times smaller than that of the FCRAO 14 m telescope. The integrated line intensities of UGC 5101, NGC 4194, and UGC 8058 are 17.41±3.48 K km s^{-1}, 47.68±9.54 K km s^{-1}, and 13.02±2.60 K km s^{-1}, respectively. These sources are observed with the IRAM 30 m telescope and the integrated intensities are 15.6±3.12 K km s^{-1} for UGC 5101 and 22.0±4.40 K km s^{-1} for UGC 8058 (Solomon et al., 1997), and 29.26±0.26 K km s^{-1} for NGC 4194 (Albrecht et al., 2004). Using the Kelvin–to–Jansky conversion factors of 4.5 for the IRAM telescope, the ratios of the total flux of the NRO to the IRAM single-dish measurements are 60 % for UGC 5101, 87% for NGC 4194, and 32 % for UGC 8058. The total flux of NGC 4441 is 65.5±13.1 Jy km s^{-1}, which corresponds 1.6 larger than that in the previous observations carried out at the Onsala Space Observatory (OSO) 20 m telescope (Jütte et al., 2010). The velocity integrated line intensity of NGC 6052 is 16.86 ± 3.37 K km s^{-1}, which corresponds to 55 % of the previous observations at the NRO (Yao et al., 2003).

We gather archival single-dish CO (1–0) data for 16 galaxies listed in Table 2.6. The velocity integrated intensity $I_{\rm CO}$ in K km s^{-1} is converted into the flux $S_{\rm CO}\Delta v$ in Jy km s^{-1} using Kelvin–to–Jansky conversion factors of 23.1 Jy K^{-1} for the FCRAO 14 m telescope, 4.95 Jy K^{-1} for the IRAM 30 m telescope, 30.4 Jy K^{-1} for the National Radio Astronomy Observatory (NRAO) 12 m telescope, and 27 Jy K^{-1} for the Swedish-ESO Submillimetre Telescope (SEST).

We estimate missing flux for 24 sources (Table 2.4), comparing the CO line flux in the same region measured from the interferometric measurements to the single-dish measurements. We obtain the CO (2–1) and CO (3–2) single-dish data from literature and compare the fluxes for seven sources. There are no available data for five sources of which we have the CO (2–1) maps. We estimate upper limits of missing flux, assuming the CO (2–1)/CO (1–0) brightness temperature ratio is 1.

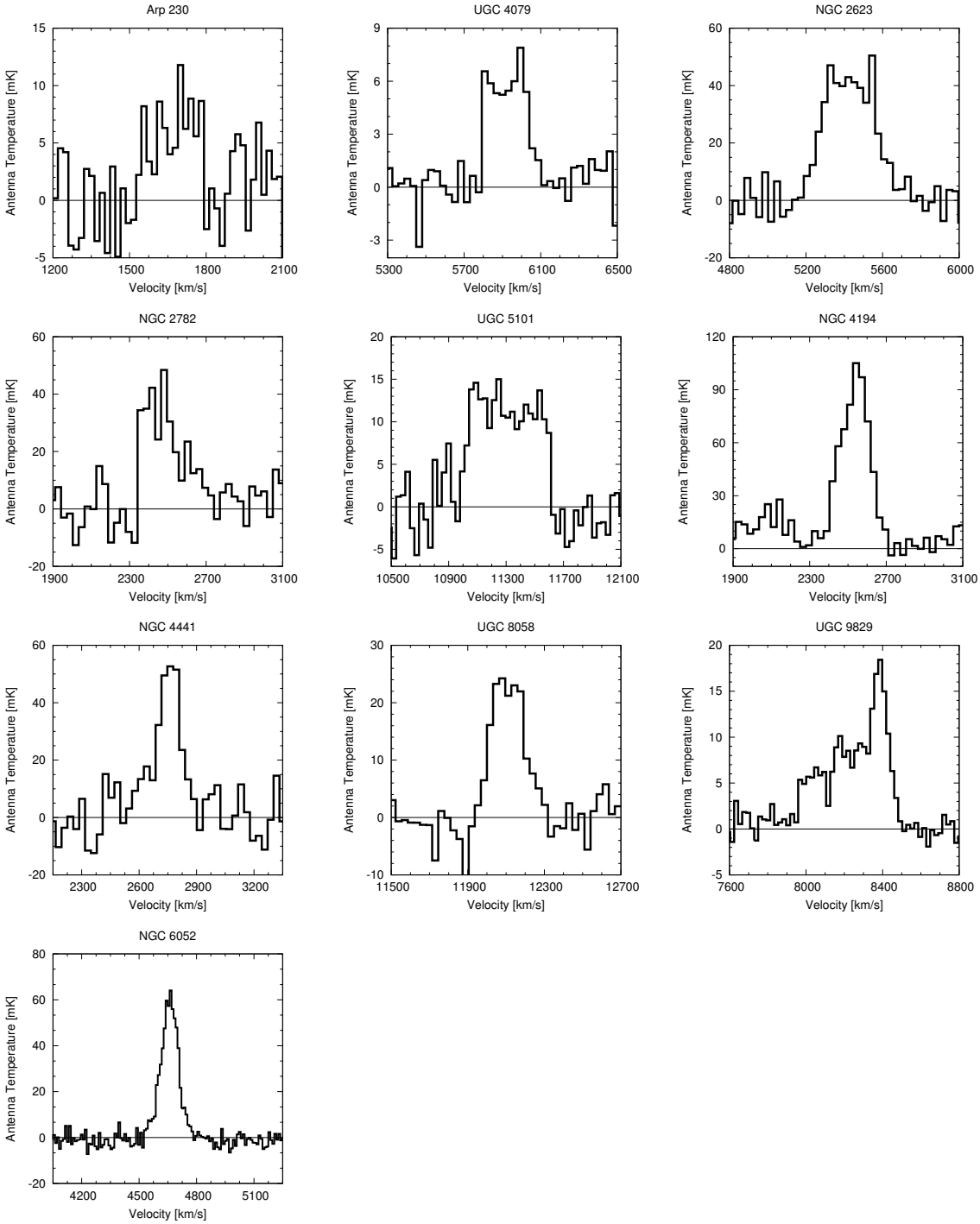

Figure 2.4: The CO (1–0) spectra for 10 merger remnants obtained with the NRO 45 m telescope. The velocity resolution is different for each galaxy.

Table 2.4: The CO Properties Derived from Interferometric Maps

Name (1)	Transition (2)	Telescope (3)	$S_{\nu,\mathrm{co}}dv$ [Jy km s^{-1}] (4)	Missing flux [%] (5)	Ref. (6)
UGC 6	CO (1–0)	CARMA	14±3	70	2
NGC 34	CO (2–1)	SMA	383±77	46	3
Arp 230	CO (1–0)	ALMA	24±1	10	1
NGC 455	CO (1–0)	ALMA	< 0.54	···	···
NGC 828	CO (2–1)	SMA	1000±200	< 35[a]	4
UGC 2238	CO (2–1)	SMA	490±98	< 33[a]	5
NGC 1210	CO (1–0)	ALMA	< 0.54	···	···
AM 0318-230	CO (1–0)	ALMA	< 0.84	···	···
NGC 1614	CO (2–1)	SMA	727±145	85	3
Arp 187	CO (1–0)	ALMA	61±3	(-12)	1
AM 0612-373	CO (1–0)	ALMA	23±1	···	···
UGC 4079	CO (1–0)	CARMA	< 1.14	···	···
NGC 2623	CO (2–1)	SMA	267±53	< 26[a]	1
NGC 2782	CO (1–0)	PdBI	124±25	(-66)	1
UGC 5101	CO (2–1)	SMA	242±48	23	6
AM 0956-282	CO (1–0)	ALMA	24±1	···	···
NGC 3256	CO (1–0)	ALMA	1589±79	21	7
NGC 3597	CO (1–0)	ALMA	140±7	25	8
AM 1158-333	CO (1–0)	ALMA	4±1	···	···
NGC 4194	CO (2–1)	SMA	420±84	< 49[a]	1
NGC 4441	CO (1–0)	PdBI	39±8	34	1
UGC 8058	CO (3–2)	SMA	381±76	90	9
AM 1255-430	CO (1–0)	ALMA	32±2	···	···
AM 1300-233	CO (1–0)	ALMA	94±5	57	10
NGC 5018	CO (1–0)	ALMA	< 1.53	···	···
Arp 193	CO (3–2)	SMA	904±181	90	9
AM 1419-263	CO (1–0)	ALMA	4±1	···	···
UGC 9829	CO (2–1)	SMA	57±11	< 46[a]	1
NGC 6052	CO (2–1)	SMA	161±32	79	3
UGC 10675	CO (2–1)	SMA	45±9	< 56[a]	11
AM 2038-382	CO (1–0)	ALMA	33±2	47	12
AM 2055-425	CO (1–0)	ALMA	51±3	57	10
NGC 7135	CO (1–0)	ALMA	3±1	···	···
NGC 7252	CO (1–0)	ALMA	87±4	44	13
AM 2246-490	CO (1–0)	ALMA	39±2	53	10
NGC 7585	CO (1–0)	ALMA	< 1.41	···	···
NGC 7727	CO (1–0)	ALMA	13±1	···	···

NOTE.—Col.(1): Source name. Col.(2) The CO transition. Col.(3): Telescope name. Col (4): The CO velocity integrated line intensity. Col.(5): The percentage of missing flux derived by comparing the CO line flux in the same region estimated from the interferometric and single-dish measurements. Col.(6): Reference of the single-dish measurements used to calculate the missing flux: 1: this work, 2: Maiolino et al. (1997), 3: Albrecht et al. (2007), 4: Bertram et al. (2006), 5: Sanders et al. (1991), 6: (Rigopoulou et al., 1996), 7: Casoli et al. (1992), 8: Wiklind et al. (1995), 9: Mao et al. (2010), 10: Mirabel et al. (1990), 11: Zhu et al. (1999), 12: Horellou & Booth (1997), 13: Andreani et al. (1995)

[a]The missing flux is estimated using the CO (1–0) single-dish measurements, assuming that the CO (2–1)/CO (1–0) brightness temperature ratio is 0.5.

Table 2.5: Properties of Single-dish Observations and Archival Data

Name (1)	Telescope (2)	rms [mK] (3)	T_{A^*} [mK] (4)	I_{CO} [K km s^{-1}] (5)	Ref. (6)
UGC 6	NRAO 12 m	···	···	1.57±0.18	2
NGC 34	NRAO 12 m	···	···	3.89±0.32	2
Arp 230	NRO 45 m	4.24 (20)	11.79±2.36	4.12±0.82	1
NGC 828	IRAM 30 m	···	···	71.13±0.65	3
UGC 2238	NRAO 12 m	···	···	6.0±1.2:	4
NGC 1614	FCRAO 14 m	···	···	5.75±0.75	5
Arp 187	NRAO 12 m	···	···	1.8±0.09	6
UGC 4079	NRO 45 m	1.23 (30)	7.89±1.58	4.01±0.80	1
NGC 2623	NRO 45 m	5.49 (30)	50.46±10.09	37.44±7.49	1
NGC 2782	NRO 45 m	7.59 (30)	48.43±9.69	23.53±4.71	1
UGC 5101	NRO 45 m	2.84 (30)	15.00±3.00	17.41±3.48	1
NGC 3256	SEST 15 m	···	···	71±2	7
NGC 3597	SEST 15 m	···	···	6.9±1.4	8
NGC 4194	NRO 45 m	7.70 (30)	105.04±21.01	47.68±9.54	1
NGC 4441	NRO 45 m	8.75 (30)	52.65±10.53	21.98±4.40	1
UGC 8058	NRO 45 m	3.08 (30)	24.23±4.85	13.02±2.60	1
AM 1300-233	SEST 15 m	···	···	8.2±1.6:	9
NGC 5018	SEST 15 m	···	···	$<$ 1.35±0.27:	10
Arp 193	NRAO 12 m	···	···	7.0±0.3	6
UGC 9829	NRO 45 m	1.27 (20)	18.42±3.68	11.04±2.21	1
NGC 6052	NRO 45 m	2.85 (10)	64.09±12.82	16.86±3.37	1
UGC 10675	IRAM 30 m	···	···	3.74±0.18	11
AM 2038-382	SEST 15 m	···	···	2.29±0.43	12
AM 2055-425	SEST 15 m	···	···	4.4±0.88:	9
NGC 7252	SEST 15 m	···	···	5.8±0.5	13
AM 2246-490	SEST 15 m	···	···	3.1±0.62:	9

NOTE.—Col.(1): Source name. Col. (2) Telescope. Col.(3): The noise level in the velocity resolution shown in (). Col.(4): The antenna temperature corrected for atmospheric attenuation. Col.(5) The CO (1–0) line flux in K km s^{-1}. Col (6) Reference: 1: this work, 2: Maiolino et al. (1997), 3: Bertram et al. (2006), 4: Sanders et al. (1991), 5: Young et al. (1995), 6: Evans et al. (2005), 7: Casoli et al. (1992), 8: Wiklind et al. (1995), 9: Mirabel et al. (1990), 10: Huchtmeier & Tammann (1992), 11: Zhu et al. (1999), 12: Horellou & Booth (1997), 13: Andreani et al. (1995)

2.3.3 The Molecular Gas Disks in Merger Remnants

Most of the merger remnants show disk-like rotation in their velocity field (Figure 2.3). In order to quantify the geometry of the rotating molecular gas and the rotation curve, we apply a fitting program (AIPS's task GAL) to the CO velocity fields of the 30 merger remnants detected in the CO line. The galactic center is assumed to be coincident with the galactic center in the K-band image (Rothberg & Joseph, 2004), assuming that the molecular gas rotates around the galactic center if the molecular gas disk is formed. We fit tilted concentric ring models with constant velocities to the velocity field using a least-squares fitting values of the kinematical parameters. As a result, the velocity fields of 24 out of 30 sources were modeled by circular rotation. We consider that molecular gas disks form in these 24 merger remnants. The estimated position angle, inclination, systemic velocity, and maximum rotational velocity are listed in Table 2.6.

The CO velocity fields of the remaining six galaxies (AM 1158-333, NGC 4194, AM 1255-430, UGC 9829, NGC 6052, and NGC 7135) cannot be modeled with purely circular motion due to the clumpy CO distribution or the complicated velocity distribution. The CO distribution is strongly distorted in the six sources, and the CO emission is not associated with the galactic center in half of them (NGC 4194, NGC 6052 and NGC 7135). The characteristics of their CO distribution and the most likely cause that the CO velocity field cannot be modeled with circular motion are as follows.

- **AM 1158-333:** The CO emission is very faint. There are two molecular gas components. One component is associated with the galactic center, and the other is distributed below the main body blue-shifted by 80 $\mathrm{km\ s^{-1}}$ from the systemic velocity. It is likely that the fitting programs are not successful due to the faint clumpy structures.

- **NGC 4194:** The majority of the CO emission comes form the southern part of the galaxy, though the CO emission is associated with the galactic center. The velocity gradient is seen over the whole galaxy. However, the gradient is not continuous near the nucleus, which may cause the failure of the modeling.

- **AM 1255-430:** The CO emitting gas is elliptically distributed around the galactic center. The velocity gradient is not seen over the whole galaxy, and the components with various velocities coexist in the whole galaxy. This complicated velocity structure cannot be modeled with circular motion.

- **UGC 9829:** The majority of the CO emission comes form the root of the northern tail, with only weak emission seen in the nucleus. The velocity gradient is seen along the tail. However, the gradient is not continuous near the nucleus, which may cause the failure of modeling.
- **NGC 6052:** The distribution of the CO emitting gas is strongly distorted. The majority of the CO emission comes form the northern part of the galaxy, and the CO emission is not associated with the galactic center. The components with various velocities coexist in the whole galaxy. This complicated velocity structure cannot be modeled with circular motion.
- **NGC 7135:** The CO emitting gas is distributed in the south region of the main body and not associated with the nucleus. The detailed structure and kinematics of the molecular gas are not clear due to the weak CO emission, and thus the fitting is not successful.

In addition, we present the Position-Velocity (PV) diagrams along the kinematical major axes of 24 sources with molecular gas disks in Appendix B. The PV diagrams reveal that the emission peaks are clearly shifted from the galactic centers in 18/24 sources (Table 2.6), suggesting the presence of a ring and/or a bar, while the peaks of the integrated intensities roughly corresponds to the galactic centers as shown in Figure 2.2. Assuming that these 18 sources have rings, the radii of the rings range between 72.0 pc and 1.25 kpc. The PV diagrams of NGC 828 and UGC 2238 show a double peak located at the connecting point between rigid rotation and flat rotation, which may signify spiral or bar structures rather than ring structures. It is likely that the molecular gas in the merger remnants are forming various structures, although it is difficult to identify their structure using only molecular gas data. In this thesis, we identify merger remnants whose the velocity fields can be modeled by circular rotation as sources with molecular gas disks.

Table 2.6: Kinematical Parameters of the CO Velocity Field

Name	Position angle [°]	Inclination [°]	$V_{\rm sys}$ [km s^{-1}]	$V_{\rm max}$ [km s^{-1}]	Ring Structure
(1)	(2)	(3)	(4)	(5)	(6)
UGC 6	303	28	6473	212	◯
NGC 34	346	29	5701	225	◯
Arp 230	294	65	1696	136	◯
NGC 455	···	···	Non-detection	···	···
NGC 828	308	61	5231	269	◯
UGC 2238	137	67	6383	249	◯
NGC 1210	···	···	Non-detection	···	···
AM 0318-230	···	···	Non-detection	···	···
NGC 1614	357	46	4747	470	◯
Arp 187	345	50	11467	321	×
AM 0612-373	122	53	947	347	◯
UGC 4079	···	···	Non-detection	···	···
NGC 2623	75	22	55340	539	◯
NGC 2782	260	25	2564	250	◯
UGC 5101	257	33	11800	427	◯
AM 0956-282	353	29	987	216	×
NGC 3256	82	40	2757	150	×
NGC 3597	264	55	3475	159	◯
AM 1158-333	···	···	···	···	···
NGC 4194	···	···	···	···	···
NGC 4441	26	23	2718	179	◯
UGC 8058	99	17	12640	389	×
AM 1255-430	···	···	···	···	···
AM 1300-233	54	27	6303	406	◯
NGC 5018	···	···	Non-detection	···	···
Arp 193	331	29	6994	359	◯
AM 1419-263	···	···	Non-detection	···	···
UGC 9829	···	···	···	···	···
NGC 6052	···	···	···	···	···
UGC 10675	172	14	9810	403	◯
AM 2038-382	149	27	5964	264	◯
AM 2055-425	34	8	12360	423	×
NGC 7135	···	···	···	···	···
NGC 7252	298	24	4695	259	◯
AM 2246-490	156	30	12440	435	◯
NGC 7585	···	···	Non-detection	···	···
NGC 7727	119	59	1818	131	×

NOTE.—Col.(1): Source name. Col.(2) The position angle of the galaxy. Col.(3): The inclination of the galactic plane. Col.(4): The systemic velocity. Col.(5): The maximum rotational velocity. Col.(6): The Position-velocity diagram shows a ring-like structure (◯) or not (×). These kinematical parameters (Col.(2) – Col.(5)) are estimated by fitting toward the CO velocity field.

Chapter 3

Global Properties of the Molecular Gas in Merger Remnants

In this chapter, we present the results of the CO data analysis and discuss the global properties of the molecular gas in the merger remnants. We investigate the extent, structure, and mass of the molecular gas. We also investigate the degree of star formation and AGN activities. The merger remnants show various properties, hence it is not easy to categorize the source by their properties. This may signify that our sample includes merger remnants on different timescales, from progenitors with different characteristics, or from different initial conditions.

3.1 The Extent of the Molecular Gas

According to the interferometric imaging, 30/37 (81 %) merger remnants were detected in the CO lines. We find that the molecular gas disks are formed in 24/37 (65 %) merger remnants. As the next step, we estimate two types of radii ($R_{\rm CO}$ and R_{80}) using the integrated intensity maps (Figure 2.2) to specify the size of the molecular gas disk. $R_{\rm CO}$ is the radius that encloses the maximum extent of the molecular gas disk, and R_{80} is the radius which contains 80 % of the total CO flux. For 24 sources that were identified to have molecular gas disks, we take into account the position angle and inclination of the gas disk estimated by the fitting procedure described in Appendix C when we measure the size of the molecular gas disk. We define these 24 sources as "Type A". For six sources in which the CO velocity field cannot be modeled by circular motion, we define them as "Type B" and estimate $R_{\rm CO}$ and R_{80} without correcting for the geometry of the galaxy. The $R_{\rm CO}$ and R_{80} of 30 (24 (Type A) + 6 (Type B)) sources are listed in Table 3.1.

The histogram of $R_{\rm CO}$ is shown in Figure 3.1 (left). The dark-gray bars show Type A and the light-gray bars show Type B. For three sources (NGC 2782, NGC 3256, and NGC 4441), we measure $R_{\rm CO}$ after excluding the CO extensions which clearly exist outside the molecular gas disk (see Figure 2.2 and Figure 2.3). The average $R_{\rm CO}$ of Type A is 3.54$\pm$2.33 kpc. Arp 187 has the largest molecular gas disk with a radius of 9.25$\pm$0.32 kpc, which corresponds approximately to 85 % of the size of the molecular gas disk in the Milky Way ($R_{\rm CO,MW} \sim 11$ kpc; Nakanishi & Sofue, 2006). In order to examine the effect of observation sensitivities on the estimated radii, we investigate the relation between 1 σ mass sensitivity and $R_{\rm CO}$ (Figure 3.2 (left)). Type A and Type B are plotted with filled squares and open circles, respectively. The colors represent different CO transitions. Because of the absence of obvious trends in this figure, we argue that the observational sensitivity does not strongly affect the observed size of the molecular gas.

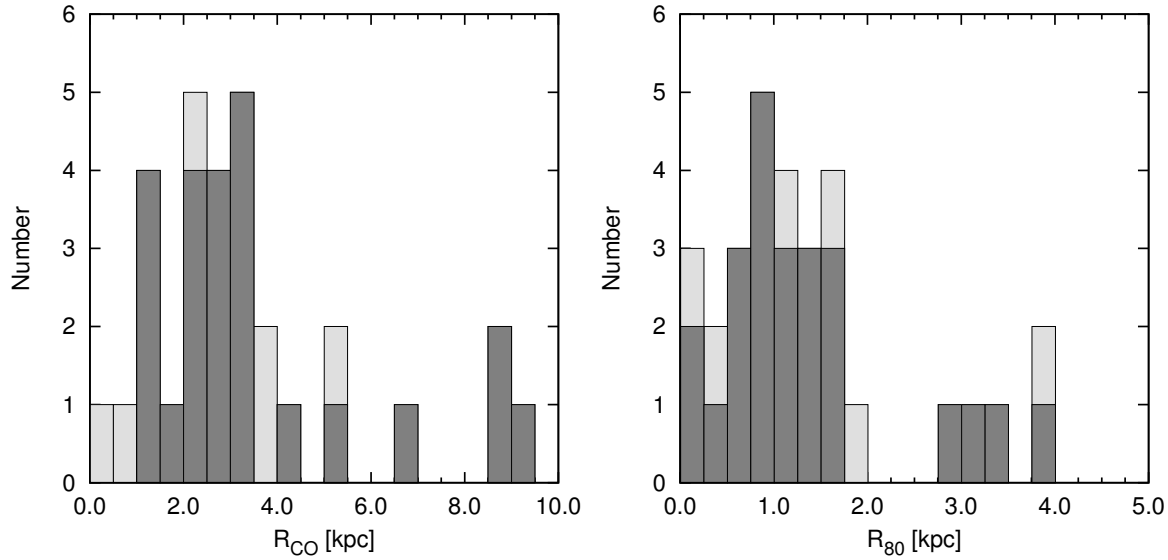

Figure 3.1: Histogram of the molecular gas extent. $R_{\rm CO}$ is the maximum size of the molecular gas extent (left) and R_{80} is the radius which contains 80 % of the total CO flux (right). The dark-gray and light-gray bars show the number of Type A and Type B, respectively.

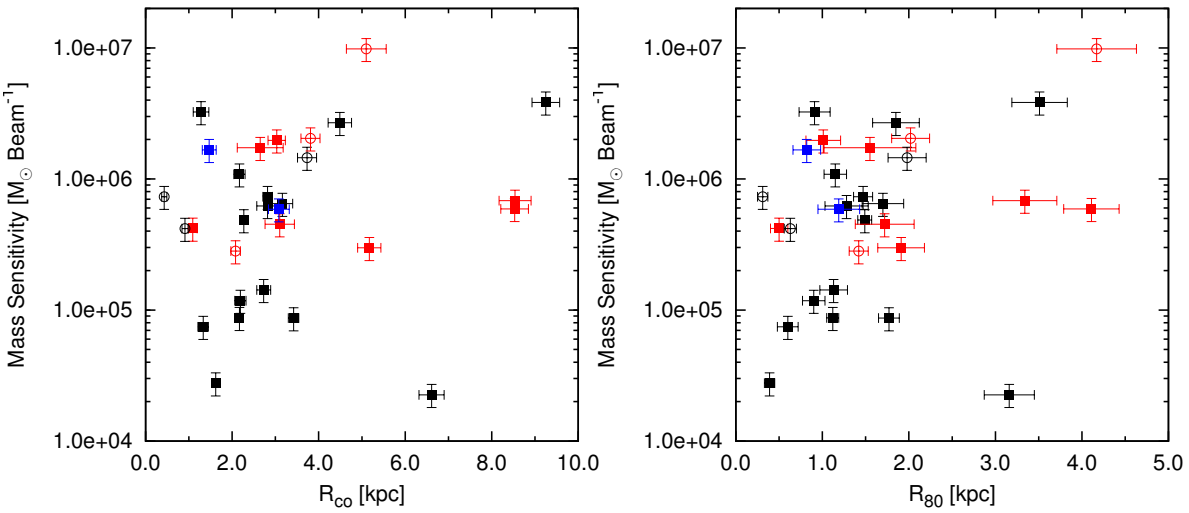

Figure 3.2: Relation between the molecular gas extent and 1 σ mass sensitivity. $R_{\rm CO}$ is the maximum size (left) and R_{80} is the radius which contains 80 % of the total CO flux (right). The filled squares show Type A, and the open squares show Type B. The colors represent different CO transitions. The black, red, and blue show the CO (1–0), CO (2–1), and CO (3–2) transition, respectively.

Table 3.1: Structure Parameters of the CO Extent

Name	$R_{\rm CO}$ [kpc]	R_{80} [kpc]	$\frac{R_{80}}{R_{\rm eff}}$	A	C
(1)	(2)	(3)	(4)	(5)	(6)
UGC 6	1.28±0.18	0.91±0.18	1.79±0.36[a]	0.17	0.20
NGC 34	3.10±0.34	1.72±0.34	4.54±0.91[a]	0.16	0.20
Arp 230	3.42±0.12	1.77±0.12	2.56±0.17	0.14	0.33
NGC 828	8.53±0.32	4.11±0.32	1.54±0.12	0.04	0.23
UGC 2238	9.53±0.37	3.34±0.37	1.57±0.17	0.09	0.33
NGC 1614	5.17±0.27	1.91±0.27	0.55±0.08[a]	0.26	0.43
Arp 187	9.25±0.32	3.51±0.32	0.50±0.05	0.21	0.27
AM 0612-373	4.49±0.27	1.85±0.27	0.26±0.04	0.36	0.43
NGC 2623	1.09±0.10	0.50±0.10	0.18±0.04[a]	0.15	0.20
NGC 2782	2.17±0.07	1.12±0.07	0.18±0.01	0.24	0.33
UGC 5101	3.03±0.20	1.01±0.20	4.04±0.80[a]	0.23	0.20
AM 0956-282	1.62±0.06	0.39±0.06	0.18±0.03	0.29	0.43
NGC 3256	6.61±0.29	3.16±0.29	1.72±0.16	0.69	0.27
NGC 3597	2.27±0.08	1.49±0.08	1.16±0.06	0.36	0.47
AM 1158-333	0.91±0.07	0.63±0.07	0.39±0.04	···	0.56[b]
NGC 4194	2.08±0.11	1.42±0.11	1.41±0.11	···	0.54[b]
NGC 4441	2.19±0.13	0.90±0.13	0.24±0.03	0.73	0.43
UGC 8058	1.47±0.16	0.82±0.16	16.4±3.26[a]	0.65	0.20
AM 1255-430	3.73±0.22	1.98±0.22	0.66±007	···	0.33[b]
AM 1300-233	2.73±0.16	1.13±0.16	0.08±0.01	0.46	0.43
Arp 193	3.08±0.24	1.19±0.24	0.40±0.08	0.39	0.20
UGC 9829	5.10±0.46	4.17±0.46	0.49±0.05	···	0.33[b]
NGC 6052	3.81±0.22	2.02±0.22	0.49±0.05	···	0.56[b]
UGC 10675	2.65±0.53	1.55±0.53	3.10±1.07[a]	0.38	0.35
AM 2038-382	2.17±0.13	1.15±0.13	1.19±0.13[a]	0.39	0.33
AM 2055-425	3.16±0.23	1.70±0.24	0.57±0.08	0.67	0.43
NGC 7135	0.43±0.06	0.31±0.06	0.01±0.01	···	0.60[b]
NGC 7252	2.82±0.11	1.47±0.11	0.60±0.05	0.29	0.38
AM 2246-490	2.82±0.25	1.28±0.25	0.15±0.03[a]	0.17	0.60
NGC 7727	1.33±0.12	0.60±0.12	0.25±0.05	0.28	0.60

NOTE.—Col.(1): Source name. Col.(2): The maximum size of the molecular gas extent. Col.(3): The radius enclosing 80% of the total CO flux. Col.(4): The ratio between R_{80} and the K-band effective radius ($R_{\rm eff}$). Col.(5) & (6): The asymmetry parameter and concentration parameter for the molecular gas extent.

[a] The ratios are uncertain because the effective radius of the stellar component ($R_{\rm eff}$) may have a large error.

[b] The concentration parameter is estimated without regard for the position angle and inclination of the galaxy.

The histogram of R_{80} is shown in Figure 3.1 (right). The representation of the color is the same as in Figure 3.1 (left). We investigate the relation between the mass sensitivity and R_{80}, and again find no correlation between them (Figure 3.2 (right)). The average R_{80} of the detected molecular gas disks is 1.61$\pm$0.87 kpc. NGC 828 has the molecular gas disk with the largest R_{80} of 4.11$\pm$0.32 kpc. Its maximum radius is $R_{\rm CO}$ = 8.53$\pm$0.32 kpc, which is the third largest in our sample. On the other hand, AM 0956-282 has a molecular gas disk with the smallest R_{80} of 0.39$\pm$0.06 kpc. The $R_{\rm CO}$ of the gas disk in AM 0956-282 is smaller than the average, but it is not the smallest in the merger remnant sample. We estimate R_{80} of the molecular gas disk in the Milky Way (hereafter, $R_{80,\rm MW}$) from the radial average surface brightness (Nakanishi & Sofue, 2006). As a result, $R_{80,\rm MW}$ is 8.5$\pm$0.5 kpc, which is about five times larger than the average R_{80} in our sample. There is no sample source which has a larger molecular gas disk than the gas disk in the Milky Way.

3.2 The Relative Size of the Molecular Gas Extent

We estimate the ratio of R_{80} to the K-band effective radius ($R_{\rm eff}$) to investigate the relative size of the molecular gas extent to the stellar spheroidal component. $R_{\rm eff}$ is the radius of the isophote containing half of the total K-band luminosity. We adjust $R_{\rm eff}$ of the merger remnants estimated by Rothberg & Joseph (2004) to account for the differences in the assumed distances to the source. The ratios between R_{80} and $R_{\rm eff}$ ($R_{\rm ratio}$, hereafter) are listed in Table 3.1. The $R_{\rm ratio}$ of UGC 8058 is extremely large ($R_{\rm ratio}$ = 16). The distance to UGC 8058 is approximately 180 Mpc (1$''$= 800 pc), hence the CO distribution is only marginally resolved and R_{80} is likely overestimated due to the large beam, leading to an overestimation of $R_{\rm ratio}$.

We investigate the relative size of the molecular gas extent for 29 sources, excluding UGC 8058. The $R_{\rm ratio}$ of the 29 sources range between 0.01 and 4.5 The histogram of $R_{\rm ratio}$ is shown in Figure 3.3. The $R_{\rm ratio}$ of more than half of the sources are less than unity, while 11/29 (38 %) sources have extended molecular gas disks compared to the stellar spheroidal component. The source with the largest $R_{\rm ratio}$ is NGC 34 ($R_{\rm ratio}$ = 4.54), followed by UGC 5101 ($R_{\rm ratio}$ = 4.04) and UGC 10675 ($R_{\rm ratio}$ = 3.10). These three sources have relatively high FIR luminosities (LIRGs; Log $L_{\rm FIR} > 11$), and thus the large gas disk with respect to the size of the stellar spheroid may be correlated to the physical activity that boosts the FIR luminosity. Thus we examine whether the relative size of the molecular gas extent increases with the FIR luminosity in what follows.

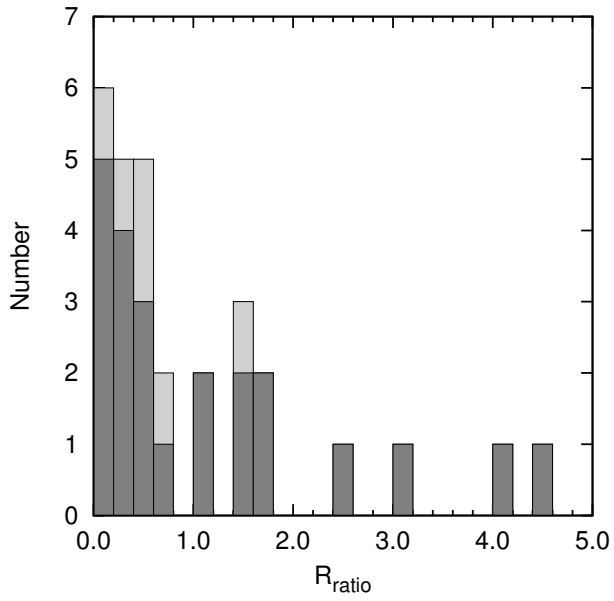

Figure 3.3: Histogram of the relative size of the molecular gas extent to the stellar spheroidal component in 29 merger remnants. R_{80} is the radius which contains 80 % of the total CO flux and $R_{\rm eff}$ is the radius of the isophote containing half of the total K-band luminosity. The dark-gray and light-gray bars show the number of Type A and Type B, respectively.

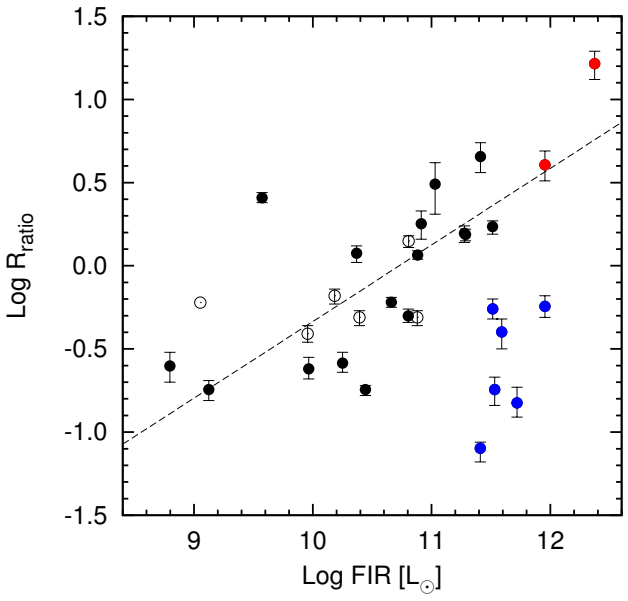

Figure 3.4: Relation between the FIR luminosity and the relative size of the molecular gas extent to the stellar spheroidal component. The filled circles show Type A, and the open circles show Type B. The dashed line is the best fit to the correlation between the FIR luminosity and $R_{\rm ratio}$. The blue color show sources shifted from the correlation, and the red color shows sources with an AGN.

The relation between the FIR luminosity and the relative size of the molecular gas extent for 30 sources shows two sequences (Figure 3.4). One sequence is that the relative disk size increases with the FIR luminosity. We estimate the best fit of this sequence using a least-squares fitting and show the result (Log $R_{\rm ratio}$ = (0.46 $\pm$ 0.07) Log $L_{\rm FIR}$ - (4.94 $\pm$ 0.77)) with a dashed line in the plot. The correlation coefficient (R^2) is 0.70. Sources with an extended molecular gas disk have high FIR luminosities, suggesting that active star formation takes place in the molecular gas disks which may subsequently form stellar disks. However, the timescale for stellar disk formation is related to the complex interplay among gravitational compression, residual gas inflow, shear motion, stellar feedback, and the gas dynamics in the non-axisymmetric potential, and it may not be easy to determine. In order to confirm the formation of stellar disks, we will have to observe these sources using dense gas tracers and stellar formation tracers in high angular resolution as our future work.

It is strongly suggested from multi-wavelength observations that an AGN exists in UGC 5101 (e.g., Imanishi et al., 2003; Armus et al., 2007) and UGC 8058 (Mrk 231; e.g., Smith et al., 1998; Lonsdale et al., 2003). These two sources with an AGN, which are shown with red symbols in Figure 3.4, have higher FIR luminosities and larger gas disks. It is possible that these sources are dynamically stable despite the existence of AGNs because of the evidence of an extended gas disk. This is in contrast to the traditional picture where central inflow of gas triggers starburst/AGN at $<$ 1 kpc scales (Downes & Solomon, 1998).

The other sequence consists of six sources with a high FIR luminosity and a compact molecular gas disk, which are shown with blue symbols in Figure 3.4. These compact gas disk could be formed by past dynamical instability during the merging process (Barnes, 2002). Dynamical instability leads to the formation of a very strong bar (Hernquist, 1989) which can efficiently drive gas inflow (Bournaud & Combes, 2002; Berentzen et al., 2007), and then results in nuclear gas concentration (Barnes & Hernquist, 1991). The detailed distribution of the molecular gas in five of six sources show ring-like structures (see the PV-diagram in Appendix B) inhibiting further immediate gas flow toward the nucleus (Iono et al., 2004).

We note about one source, Arp 230, with an extended molecular gas disk ($R_{\rm ratio}$ = 2.56) and a low FIR luminosity (Log $L_{\rm FIR}$ = 9.57). Arp 230 is a candidate of a polar ring galaxy (Whitmore et al., 1990). A polar ring galaxy has a large-scale ring structure outside the main body. In Arp 230, the molecular gas is distributed along the polar ring. Thus it is likely that the molecular gas shows an extended distribution in comparison with the stellar main body.

3.3 The Structural Parameters of the Molecular Disks

In order to systematically quantify the galaxy morphology, we adapt two structural parameters, the asymmetry parameter and the concentration parameter (Iono et al., 2004). The asymmetry parameter (A) is defined as

$$A = \frac{|I - I_{\rm rot}|}{2I_{\rm tot}}, \tag{3.1}$$

where I is the face-on image, $I_{\rm rot}$ is I rotated 180°around the galactic center, and $I_{\rm tot}$ is the total integrated intensity. According to this definition, A = 0 means complete asymmetry and A = 1 means total antisymmetry. The concentration parameter (C) is defined as the ratio between the outer and inner regions represented by the radii enclosing 20% and 80% of the total flux,

$$C = \frac{r_{20}}{r_{80}}. \tag{3.2}$$

We measure the two parameters of Type A after correcting for the position angles and inclinations derived by the model fitting. We also estimate the C-parameter of Type B without correcting for the geometry of the galaxy. The estimated A- and C-parameters are summarized in Table 3.1, and the histogram of the parameters are shown in Figure 3.5 and Figure 3.6.

The asymmetry parameters range from 0.04 to 0.73 and the mean value of 24 sources is 0.33 $\pm$ 0.19. The histogram shows two peaks, i.e., one is around 0.2–0.4 and the other is around 0.7 (Figure 3.5). NGC 828 has the most nearly symmetric molecular gas disk in our sample (A = 0.04). On the other hand, sources with relatively antisymmetric molecular gas disks are NGC 3256, NGC 4441, UGC 8058, and AM 2055-425 ($A > 0.6$). These sources except for UGC 8058 have the CO extensions outside the main disk components and the extensions are not symmetric structures (see the integrated intensity maps in Figure 2.2). The CO integrated intensity map of UGC 8058 shows nearly symmetric distribution and no extension (Figure 2.2), however the A-parameter of UGC 8058 is relatively large because the rotational center of the CO emission is different from the galactic center defined by the K-band image. We suggest three possibilities of this large asymmetry: (1) non-circular motion is dominated due to gas inflow or outflow as seen in a similar object, Mrk 273 (Cicone et al., 2013) (2) there is a double nucleus because the merging is not completed and the CO emission is associated with one nucleus. and, (3) the CO emission is significantly nonuniformly-distributed.

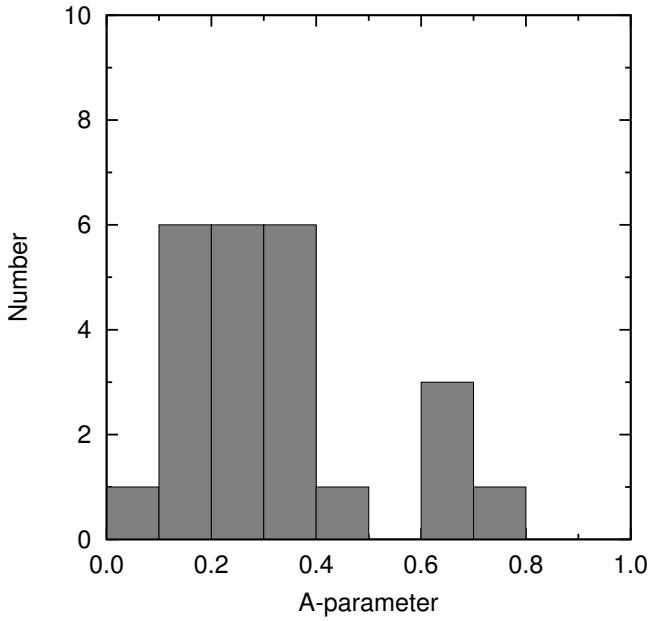

Figure 3.5: Histogram of the asymmetry parameter (A-parameter) $A = 0$ means complete asymmetry and $A = 1$ means total antisymmetry. The asymmetry parameter is estimated toward only Type A.

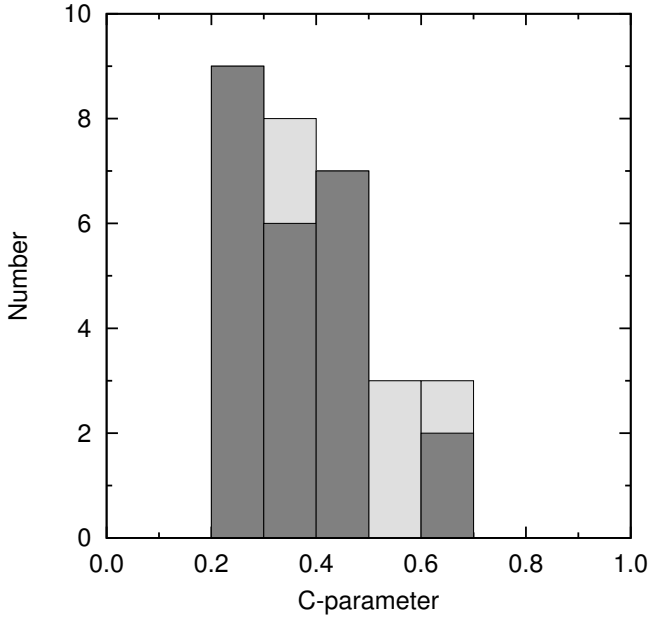

Figure 3.6: Histogram of the concentration parameter (C-parameter). The gas concentration becomes high as C-parameter is small. The dark-gray and light-gray bars show Type A and Type B, respectively.

The concentration parameters range from 0.20 to 0.60 and the mean value of 30 sources is 0.37 $\pm$ 0.13. Type B sources have relatively large values of the C-parameters. We estimate the C-parameter for the molecular gas disk in the Milky Way using the radial average surface brightness (Nakanishi & Sofue, 2006). The C-parameter for the Milky Way is 0.4, which is similar to the mean C-parameter of the merger remnant sample.

The two structure parameters will be used in § 3.6 to explain the morphological and kinematical features of the molecular gas and in § 4.6 to discuss the evolution of the merger remnants.

3.4 Molecular Gas Mass in Merger Remnants

The molecular gas mass ($M_{\rm CO}$) is estimated from the CO integrated intensity using the following two equations (Solomon & Vanden Bout, 2005);

$$\frac{L_{\rm CO}}{\rm L_\odot} = 3.25\times10^7\Big(\frac{S_{\rm CO}\Delta v}{\rm Jy\ km\ s^{-1}}\Big)\Big(\frac{\nu_{\rm obs}}{\rm GHz}\Big)^{-2}\Big(\frac{D_{\rm L}}{\rm Mpc}\Big)^2(1+z)^{-3}, \tag{3.3}$$

where $L_{\rm CO}$ is the CO luminosity, $S_{\rm CO}\Delta v$ is the CO integrated intensity, $\nu_{\rm obs}$ is the observing frequency, $D_{\rm L}$ is the luminosity distance, and z is the redshift. Then the molecular gas mass is derived by;

$$\frac{M_{\rm CO}}{\rm M_\odot} = \alpha_{\rm CO}\frac{L_{\rm CO}}{\rm L_\odot}, \tag{3.4}$$

where $\alpha_{\rm CO}$ is the CO luminosity-to-H_2 mass conversion factor in $\rm M_\odot\ pc^{-2}\ (K\ km\ s^{-1})^{-1}$. The conversion factor has been a controversial issue for a long time. Solomon & Barrett (1991) find that the conversion factor is roughly constant in the Galaxy and nearby spiral galaxies and suggest that the conversion factor is $X_{\rm CO}$ = 2.2 $\times$ 10^{20} $\rm cm^{-2}\ (K\ km\ s^{-1})^{-1}$, corresponding to $\alpha_{\rm CO}$ = 4.8 $\rm M_\odot\ pc^{-2}\ (K\ km\ s^{-1})^{-1}$. However, the conversion factor, in gas-rich galaxies at high redshift and local U/LIRGs, is lower than the standard value in the Galaxy (e.g., $\alpha_{\rm CO} \sim$ 0.6–0.8; Papadopoulos et al., 2012; Downes & Solomon, 1998). Furthermore, Narayanan et al. (2012b) suggest from numerical models that the conversion factors in mergers, on average, are lower than those in high-redshift disk galaxies which may have gravitationally unstable clumps. Indeed, the low $\alpha_{\rm CO}$ values are found in mergers such as the Antennae galaxies ($\alpha_{\rm CO} \sim$ 0.2–1; Zhu et al., 2003) and Arp 299 ($\alpha_{\rm CO} \sim$ 0.2–0.6; Sliwa et al., 2012).

Table 3.2: Global Properties of the Merger Remnant Sample (1)

Name	$M_{\rm H_2,SD}$	$M_{\rm H_2,INT}$	SFR	$t_{\rm dep}$
	[10^8 $M_\odot$]	[10^8 $M_\odot$]	[$M_\odot$ yr^{-1}]	[Gyr]
(1)	(2)	(3)	(4)	(5)
UGC 6	46 ± 5	···	14	0.32
NGC 34	···	25 ± 5	45	0.056
Arp 230	···	1.6 ± 0.3	0.65	2.5
NGC 455	···	$< 0.33 \pm 0.07$	< 0.089	···
NGC 828	···	54 ± 11	33	0.16
UGC 2238	···	38 ± 8	33	0.12
NGC 1210	···	$< 0.19 \pm 0.01$	< 3.2	$<$ -3.23
AM 0318-230	···	$< 2.2 \pm 0.4$	< 11	$<$ -2.71
NGC 1614	···	31 ± 6	57	0.054
Arp 187	···	210 ± 40	11	1.9
AM 0612-373	···	50 ± 20	< 3.1	> 1.6
UGC 4079	8.0 ± 1.6	···	4.7	0.17
NGC 2623	···	15 ± 3	59	0.026
NGC 2782	···	18 ± 4	4.8	0.37
UGC 5101	···	63 ± 13	160	0.041
AM 0956-282	···	0.51 ± 0.10	< 0.23	> 0.22
NGC 3256	53 ± 1	···	56	0.093
NGC 3597	51 ± 10	···	13	0.39
AM 1158-333	···	0.78 ± 0.16	1.6	0.050
NGC 4194	···	29 ± 6	11	0.27
NGC 4441	8.3 ± 1.7	···	1.6	0.52
UGC 8058	···	51 ± 10	410	0.012
AM 1255-430	···	58 ± 12	< 2.6	> 2.2
AM 1300-233	34 ± 7	7.4	44	0.077
NGC 5018	$< 0.26 \pm 0.05$	···	0.70	< 0.037
Arp 193	39 ± 2	···	67	0.058
AM 1419-263	···	3.8 ± 0.8	< 2.7	> 0.14
UGC 9829	···	46 ± 9	4.3	1.1
NGC 6052	···	40 ± 8	13	0.30
UGC 10675	9.8 ± 0.5	···	19	0.053
AM 2038-382	51 ± 9	···	4.1	1.3
AM 2055-425	74 ± 15	···	160	0.047
NGC 7135	···	0.48 ± 0.10	0.20	0.24
NGC 7252	76 ± 7	···	7.9	0.96
AM 2246-490	52 ± 10	···	91	0.057
NGC 7585	···	$< 0.37 \pm 0.07$	< 0.038	···
NGC 7727	···	1.0 ± 0.2	< 0.11	> 0.93

NOTE.—Col.(1): Source name. Col.(2): The molecular gas mass estimated using the single-dish data. Col.(3): The molecular gas mass estimated using the interferometric data. Col.(4): The star formation rate estimated from the FIR luminosity. Col.(5): The depletion time of the molecular gas, assuming that the gas reservoir is not replenished.

We estimate molecular gas masses of 18 sources with the FIR luminosity less than 10^{11} $L_{\odot}$, using the conversion factor of $\alpha_{\rm CO}$ = 4.8 (Solomon & Barrett, 1991), and we use a different conversion factor of $\alpha_{\rm CO}$ = 0.8 (Downes & Solomon, 1998) for 14 U/LIRGs. In estimating the molecular gas mass from the CO (3–2) and the CO (2–1) luminosity, we convert the high-J CO luminosity into the CO (1–0) luminosity, assuming that the CO (3–2)/CO (1–0) and the CO (2–1)/CO (1–0) brightness temperature ratio is 0.5, which is similar to the average CO (3–2)/CO (1–0) ratio in local U/LIRGs estimated by Iono et al. (2009). We estimate the total molecular gas masses ($M_{\rm H_2,SD}$) of 32 sources including additional sample for single-dish observations (NGC 2655, NGC 3656, NGC 3921, UGC 11905, and IC 5298), using the single-dish CO data (see Table 2.5). In addition, we estimate the molecular gas masses ($M_{\rm H_2,INT}$) detected in the interferometric maps of 30 sources (see Table 2.4). The molecular gas masses in the merger remnant sample range between 10^7 $M_{\odot}$ and 10^{11} $M_{\odot}$. In general, $M_{\rm H_2,INT}$ is less than $M_{\rm H_2,SD}$ due to missing flux. However, for some sources, $M_{\rm H_2,INT}$ is larger than $M_{\rm CO,SD}$ because a primary beam size of a single-dish telescope is significantly smaller than that of an interferometer and the CO extent. We use $M_{\rm H_2,INT}$ as the total molecular gas mass for 12 sources with $M_{\rm CO,INT} > M_{\rm CO,SD}$ in the following discussions.

3.5 Star Formation Activity

3.5.1 The Integrated Star-Formation Rate

The star formation rate (SFR) in a galaxy is one of the indicators of galaxy evolution because the amount of star formation can strongly influence the future stellar population. Variations in star formation activity and stellar population can be related to morphological classifications like the Hubble sequence (§ 1.2.1; Hubble, 1958). For example, blue galaxies or galaxies with signs of recent star formation tend to be late-type galaxies.

The SFR spatially integrated over a galaxy (the integrated SFR) is often used for investigating star formation properties of extra-galaxies, because young stars which have just formed are unresolved in all but the closest galaxies. Diagnostics of SFR have been in development for over four decades. The more commonly-used relations to determine SFR are based on measurements using the continuum in UV, FIR, and radio as well as emission lines in optical and NIR. In this study, we use the SFR estimated from the FIR luminosity. The FIR emission provides an excellent measurement of the SFR

in dusty starbursts. The relation between SFR and FIR luminosity (Kennicutt, 1998) is given by

$$\left(\frac{SFR}{\mathrm{M}_{\odot}\ \mathrm{yr}^{-1}}\right) = 4.5 \times 10^{-44} \left(\frac{L_{\mathrm{FIR}}}{\mathrm{ergs\ s}^{-1}}\right). \tag{3.5}$$

This relation is based on a simple assumption that all of the UV and much of the blue radiation from massive stars is absorbed by grains, with the associated thermal re-radiation appearing as emission in the 40–120 μm (FIR) wavelengths. Strictly speaking, this assumption applies only to starbursts with ages less than 10^8 yrs (Kennicutt, 1998). In more quiescent, normal galaxies, the assumption is not valid because the contribution of dust heating from old stars cannot be disregarded, and the SFR is overestimated using this correlation.

We estimate SFRs of 37 sources using their FIR luminosities (Table 3.2). The SFRs of 24/37 sources are larger than that of the Milky Way (a few $\mathrm{M}_{\odot}\ \mathrm{yr}^{-1}$; e.g., Murray & Rahman, 2010), and three sources (UGC 5101, UGC 8058, and AM 2055-425) have significantly large SFRs (> 100 $\mathrm{M}_{\odot}\ \mathrm{yr}^{-1}$). The SFRs of 13/37 sources are similar to or less than that of the Milky way. These SFRs may be smaller, because SFRs of sources with active star formation are overestimated. We find that star formation activities with large SFRs continue in $\sim$60 % of the sample after a completion of merging, while the star formation activities in $\sim$30 % of the sample have already faded.

3.5.2 The Depletion Time of the Molecular Gas

We make a simple assumption on star formation, in which the SFR estimated from the FIR luminosity is constant until the molecular gas in a galaxy is consumed completely, assuming that the gas reservoir is not replenished and that all of the molecular gas is used for star formation. Under this assumption, the depletion time of the molecular gas in a galaxy ($t_{\mathrm{dep}}(\mathrm{H}_2)$) is given by

$$t_{\mathrm{dep}}(\mathrm{H}_2) = \frac{M_{\mathrm{H}_2}\ [\mathrm{M}_{\odot}]}{\mathrm{SFR}\ [\mathrm{M}_{\odot}\ \mathrm{yr}^{-1}]}, \tag{3.6}$$

where M_{H_2} is the molecular gas mass. The depletion time describes how long a galaxy could sustain star formation at the current SFR before running out of fuel. This parameter is also used as the star formation efficiency defined by the inverse of $t_{\mathrm{dep}}(\mathrm{H}_2)$.

We estimate the depletion time of the molecular gas for 33/37 merger remnants (Table 4.1). It is difficult to estimate the depletion time of the other four sources because we know only upper limits

of both molecular gas mass and FIR luminosity. The depletion times range between 10 Myr and 2 Gyr, although 28/33 are < 1 Gyr. A typical timescale of galaxy merger from the first encounter to coalescence is 1 Gyr, and an additional few Gyrs until tidal tails disappear (Hibbard & Mihos, 1995). Comparing the depletion timescale to the typical timescale of a galaxy merger, we expect the molecular gas in our merger remnant sample to run out before the outer phase mixing are completed. Therefore, if gas reservoir is not replenished, the merger remnants with compact gas disks will result in gas-poor early-type galaxies, and some gas reservoir is required to transform the merger remnants into late-type galaxies. At least some gas is expected to remain, however, because here we assume that all of the molecular gas is used for star formation. In fact, all of the molecular gas cannot be used for star formation and the molecular gas is supplied by feedback from star formation and gas streaming via tidal tails. In order to check the effect of gas streaming via tidal tails, we will have to investigate the evidence of returning diffuse gas using the HI line observation, and this is deferred to our future work.

3.6 Possibility of Active Galactic Nuclei

Mergers between gas-rich progenitor galaxies trigger starburst activities in the nuclear region and throughout the extended disk (e.g., Mihos & Hernquist, 1996) that heats the surrounding dust and produces strong FIR radiation. In some cases, radial streaming motions can efficiently feed gas to a central black hole, and trigger an AGN in late-stage mergers (e.g., Narayanan et al., 2008). However, it is not well understood when an AGN phase becomes prominent and how long it will last. We look for the presence of an AGN in the merger remnant sample to investigate whether an AGN phase continues after the completion of the merger.

The correlation between radio continuum and FIR luminosities in galaxies has been studied well. Helou et al. (1985) define the logarithmic FIR–radio flux ratio:

$$q \equiv \log\left(\frac{L_{\rm FIR}}{3.75 \times 10^{12}\ {\rm W\ m^{-2}}}\right) - \log\left(\frac{S_{1.4\ {\rm GHz}}}{{\rm W\ m^{-2}\ Hz^{-1}}}\right), \tag{3.7}$$

where $L_{\rm FIR}$ is the FIR luminosity in unit of $\mathrm{W\ m^{-2}}$ and $S_{1.4\ \mathrm{GHz}}$ is the observed 1.4 GHz flux density in units of $\mathrm{W\ m^{-2}\ Hz^{-1}}$. Most galaxies with a wide range of bolometric luminosities, from dwarf galaxies to ULIRGs, obey a linear correlation between radio and FIR luminosity (Condon

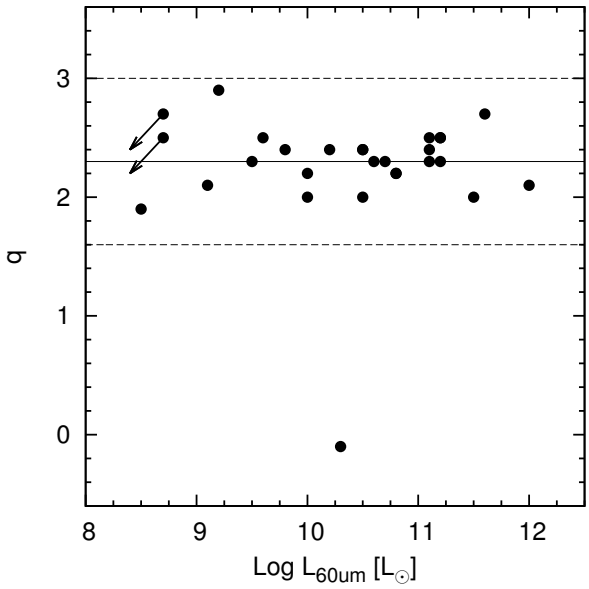

Figure 3.7: The logarithmic FIR–radio flux ratio, "q-values", plotted as a function of the $IRAS$ 60 μm luminosity. The solid line marks the average value of q = 2.2, while the dotted lines delineate the "radio-excess" (below) and "IR-excess" (above) objects, which have five times larger radio or IR flux density than the expected values from the linear radio–FIR relation, respectively.

et al., 1991). Its correlation, so-called the radio–FIR correlation, is one of the most powerful tools for distinguishing between an AGN and a starburst dominated source. AGN dominated sources show small q-values (radio-excess), wheareas starburst dominated sources show large q-value (IR-excess).

We estimate the q-value for 28 merger remnants, for which the 1.4 GHz radio continuum data is available (Brown et al., 2011; Condon et al., 2002, 1998, 1996), in order to investigate their deviation from the linear radio–FIR correlation. The resultant q-value are summarized in Table 4.2 and plotted as a function of the $IRAS$ 60 μm luminosity in Figure 4.8. The median q-value in 28 sources is 2.3, which is similar to the median q-value among spiral galaxies in Virgo (Helou et al., 1985). In Figure 4.8, all of the sample except for Arp 187 are found between the two dotted lines, which mark the five-fold excess and deficit of the radio emission with respect to the median (q = 2.3). Therefore, most of the merger remnants in our sample do not show the presence of an AGN. This might suggest that AGN activity fades or becomes weak after the completion of the merger. We note that a galaxy with a heavily obscured AGN does not show a radio-excess. In fact, it is strongly suggested from multi-wavelength observations that an AGN exists in UGC 5101 (e.g., Armus et al., 2007; Imanishi et al., 2003) and UGC 8058 (Mrk 231; e.g., Lonsdale et al., 2003; Smith et al., 1998), however these

galaxies do not show a radio-excess, which is consistent with a previous study ($q \sim 2$; Yun et al., 2001). Thus it remains a possibility that obscured AGNs host in other merger remnants.

Arp 187 shows a radio-excess (q = -0.1), suggesting the presence of an AGN, while other wavelength data does not show evidence of an AGN in this galaxy. We also investigate the radio spectral index at a few GHz ($f_\nu \propto \nu^\alpha$) using radio data from the literature (Wright & Otrupcek, 1992, at 5 GHz and 8.4 GHz). A steep radio spectra ($\alpha \lesssim$ -0.4) indicates sources with non-thermal emission. We find a spectra index of α = -1.0 for Arp 187, which also indicates AGN activity.

3.7 Summary of the Global Properties of the Merger Remnants

In this chapter, we investigate the global properties of the molecular gas and star formation activity in the merger remnants. Main summaries are as follows:

- The large molecular gas disk with respect to the size of the stellar spheroid may be correlated to the physical activity that boosts the FIR luminosity, namely starburst/AGN. However, 6 out of 14 U/LIRGs have compact molecular gas disk compared to the average size, where gas might inflow to the nuclear region efficiently by dynamical instability during the merging process. Additional studies are required to investigate the obvious reasons to distinguish between sources with extended gas disk and with compact gas disk.

- Star formation activities with large SFRs continue in $\sim$60 % of the sample, while the star formation activities in $\sim$30 % of the sample have already faded. Under an assumption that the SFR estimated from the FIR luminosity is constant and the gas reservoir is not replenished, the molecular gas in the merger remnant sample is expected to run out before the phase mixing is completed. Unless gas reservers are supplied, the merger remnants with compact disks will results in gas-poor early-type galaxies rather than gas-rich late-type galaxies.

- Most of the merger remnants show no presence of an AGN according to the correlation between radio continuum and FIR luminosity. This might suggest that AGN activity fades or becomes weak after the completion of merging, though it remains possible that obscured AGNs exists.

- The merger remnants show various properties, hence it is not easy to categorize the source by their properties. This may signify that our sample includes merger remnants on different timescales, from progenitors with different characteristics, or from different initial conditions.

Table 3.3: The Radio–FIR Correlation

Name (1)	$S_{1.4\ \mathrm{GHz}}$ [mJy] (2)	q (3)	Ref. (4)
UGC 6	28.4±1.0	2.3	1
NGC 34	67.5±2.5	2.5	1
Arp 230	26.3±1.6	2.1	1
NGC 828	104.7±3.7	2.2	1
UGC 2238	72.2	2.2	2
NGC 1614	138.2±4.9	2.5	1
Arp 187	1482.7±44.5	-0.1	1
UGC 4079	12.3±0.9	2.2	1
NGC 2623	96.2±2.9	2.5	1
NGC 2782	125.5±5.0	2.0	1
UGC 5101	170.9±5.9	2.0	1
AM 0956-282	6.9±1.3	< 2.7	1
NGC 3256	661	2.3	3
NGC 3597	76.3±2.3	2.4	1
AM 1158-333	14.3±0.6	2.3	1
NGC 4194	101.1±3.1	2.4	1
NGC 4441	11.5±0.6	2.5	1
UGC 8058	309.9±12.1	2.1	1
AM 1300-233	76.3±3.1	2.4	1
NGC 5018	2.0±0.5	2.9	4
Arp 193	104.9±3.2	2.3	1
UGC 9829	4.3±0.6	2.4	1
NGC 6052	105.3±4.2	2.0	1
UGC 10675	15.1±0.6	2.3	1
AM 2055-425	31	2.7	3
NGC 7135	5.9±0.5	1.9	1
NGC 7252	25.3±1.2	2.4	1
NGC 7585	1.5±0.5	< 2.5	4

NOTE.—Col.(1): Source name. Col.(2) The 1.4 GHz radio continuum flux. Col.(3): The q-value. This is the logarithmic radio–FIR flux ratio. Col.(4) Reference: 1. Condon et al. (1998), 2. Condon et al. (2002), 3. Brown et al. (2011), 4. Condon et al. (1996)

3.8 Individual Sources

We provide background information regarding each source revealed from previous observations and studies at all available wavelengths, and from numerical simulations. In addition, we give a short description of the morphological and kinematical features of the molecular gas seen in the integrated intensity maps (Figure 2.2 in § 2.3.1), velocity field (Figure 2.3 in § 2.3.1), channel maps (Appendix A), and PV diagram (Appendix B).

3.8.1 UGC 6 (VV 806, Mrk 334)

This galaxy has several loops and shells seen in the optical, suggesting a galaxy interactions. The HST/WFPC2 V-band image clearly shows circumnuclear spiral structures (see Figure A.1; Martini et al., 2003). The Hα emission is concentrated in the 3 kpc nuclear region and the velocity field seems to be in good agreement with a rotating disk model (Smirnova & Moiseev, 2010). The rotational velocity is almost constant (210–220 km s^{-1}) over radial distance range of 4″– 12″. The HI spectra show a double-horn profile, which is characteristic of a rotating disk (Mirabel & Sanders, 1988). Optical spectroscopy classifies the galaxy as a Seyfert 1.8 (e.g., Nagao et al., 2000; Osterbrock & Martel, 1993). Deo et al. (2007) detect strong polycyclic aromatic hydrocarbon (PAH) emission features at 6–15 μm, as seen in the spectra of starburst galaxies.

The CO (1–0) emitting gas is distributed along a optical dust lane. The detailed distribution of the molecular gas is not clear due to the limited velocity resolution, but a velocity gradient is seen in the velocity field. The emission peak in channel maps is slightly offset from the galactic center, but it is not clear whether this offset is real or not due to a large velocity resolution (ΔV = 100 km s^{-1}).

3.8.2 NGC 34 (NGC 17, VV 850, Mrk 938)

This galaxy is classified as a LIRG. The galaxy has several ripple-like patterns and two linear tidal tails extending towards the northeast and the southwest of the main body seen in the optical. The projected length of the longer tail is over 20 kpc. The high-resolution HST/ACS B-band image clearly shows a bluish central disk with spirals (Figure A.2). Its optical light is dominated by a $\sim$400 Myr old poststarburst population (Schweizer & Seitzer, 2007). The nature of its optical spectra is controversial. Some authors classify the galaxy as a Seyfert 2 based on the optical spectra (e.g., Brightman & Nandra, 2011; Yuan et al., 2010; Veilleux et al., 1995), while others suggest a com-

posite spectrum (e.g., Gonçalves et al., 1999; Mulchaey et al., 1996). However, strong Hα emission distributed over the entire galaxy indicates that the galaxy is more properly classified as a starburst galaxy rather than a Seyfert galaxy (Mulchaey et al., 1996). The kinematics of the HI emitting gas suggests that the galaxy is forming an outer disk (Fernández et al., 2010). A broad HI absorption (ΔV = 514$\pm$21 km s^{-1}) is also found in the inner region. In addition, a diffuse radio component is in the shape of two radio lobes, spanning 390 kpc (Fernández et al., 2010). This emission could be a signature of an AGN or a starburst-driven superwind.

The galaxy has an extended CO distribution in comparison with the stellar spheroidal component ($R_{80}/R_{\rm eff} \sim 6$), but the absolute size of the CO distribution is approximately equal to the average size in our sample. The detailed CO structure is not clear due to low spatial resolution of 1.4 kpc. The velocity field shows a velocity gradient of $\sim$300 km s^{-1} kpc^{-1}. The PV diagram along the kinematic major axis reveals nearly symmetric isophotes and two emission peaks on opposite sides of the nucleus, indicating the presence of a ring or a disk with non-uniform distribution.

3.8.3 Arp 230 (IC 51)

This galaxy is well known as a shell galaxy and listed as a candidate of a polar ring galaxy (Whitmore et al., 1990), which has a ring of gas, stars, and dust that orbit perpendicular to the apparent major axis of the stellar body. The HST/WFPC2 V-band image shows strong dust lanes along the polar ring (Figure A.3). Stellar shells are clearly visible in the northeast and southeast. The outermost shell has a color that would have resulted from a strong starburst 1–2 Gyr ago, and the color of the intermediate shell implies an age of 0.5–0.7 Gyr. Furthermore the color of the inner shells shows weaker bursts at a younger age ($\leq$ 0.3 Gyr), implying that the strength of starburst decreased with time (McGaugh & Bothun, 1990). The majority of the 6 cm radio continuum and HI emission is aligned with the optical dust lane (Schiminovich et al., 2013; Cox & Sparke, 2004). Two HI peaks are seen in strongly obscured regions along the polar ring, which suggests that the atomic gas rotates with the polar ring.

The CO (1–0) emitting gas is seen along a optical dust lane and distributed in three main components. One component is associated with the nucleus and the others are located at both ends, corresponding to the edge of the polar ring. The symmetry of the CO distribution is the third highest in our sample (A-parameter = 0.14). The velocity field shows a very shallow gradient of $\sim$50 km s^{-1} kpc^{-1}. These signatures suggest the presence of a slow-rotating ring/disk.

3.8.4 NGC 455 (Arp 164, UGC 815)

This galaxy has been relatively poorly studied. Optical imaging reveals two diffuse tails extending towards the northwest and the southeast. While the galaxy is undetected in the IRAS Sky Survey Atlas, it can be detected in the AKARI All-Sky Survey. We estimate the FIR luminosity of 3.0 $\times$ 10^9 $L_\odot$ by using of the AKARI data (Yamamura et al., 2010) and a formula defined by Takeuchi et al. (2010). This galaxy is undetected in the CO (1–0) line. The 3 σ upper limit on the molecular gas mass is 3.3×10^7 $M_\odot$.

3.8.5 NGC 828 (UGC 1655)

This galaxy is classified as a LIRG. The NIR image shows several filaments surrounding the main body and spiral features within 10″of the galactic center. The small 3.3 μm PAH equivalent width ($\leq$ 20 nm) suggests that a powerful buried AGN is present in the galaxy (Imanishi, 2006). In the Hα emission, there are three sources with comparable surface brightness (Hattori et al., 2004). One diffuse source is associated with the nucleus and the others are located nearly symmetrically along the major axis of the galaxy. Furthermore, the rotation curve measured from the Hα emission shows flat rotation with a constant velocity of 200 km s^{-1} at $\geq$ 8″ from the galactic center (Márquez et al., 2002). The distribution and the characteristics of molecular gas have been investigated using millimeter/submillimeter telescopes. Multiple CO lines show double horn profiles, suggesting the presence of a rotating disk (Narayanan et al., 2005; Casoli et al., 1992; Sanders et al., 1991). The ^{12}CO (1–0)/^{13}CO (1–0) line ratio is 10.6$\pm$1.3, which are only slightly larger than in normal spiral galaxies (Aalto et al., 1991). The reason of the nearly normal line ratio is probably that the galaxy has not undergone strong perturbations of the gas component.

Our new CO (2–1) observations confirm the presence of a large molecular gas disk with a radius of 8.5 kpc. The rotation curve of the molecular gas disk shows flat rotation at $\geq$ 8″ from the galactic center with a velocity of about 290 km s^{-1}, which has been corrected using an estimated inclination of 61°. This rotational velocity is larger than that measured form the Hα emission (Hattori et al., 2004) by 90 km s^{-1}. Previous CO (1–0) observations provid a rotation curve (Wang et al., 1991), which is in agreement with the rotation curve measured from the Hα emission (Epinat et al., 2008), but the disk size is limited to a 3.5 kpc radius. In addition, the symmetry of the CO distribution in the

molecular gas disk is the highest in our sample (A-parameter = 0.04), while Wang et al. (1991) report a significant asymmetrric distribution. The PV diagram along the kinematical major axis reveals a double peak located at the connecting point between rigid rotation and flat rotation.

3.8.6 UGC 2238

This galaxy is classified as a LIRG. According to optical spectroscopy, Veilleux et al. (1995) classify the galaxy as a LINER, while Yuan et al. (2010) suggest that the galaxy is a starburst–AGN composite. The SFR derived from the combination of the IR luminosity and the FUV measurement is 37.70 $M_\odot$ yr^{-1} (Howell et al., 2010), which is much larger than the SFR measured from the Hα luminosity (0.24 $M_\odot$ yr^{-1}; Poggianti & Wu, 2000). The radio continuum emission is elongated in the northeast and southwest, corresponding to the optical morphology (Condon et al., 1990).

We find a large molecular gas disk in the galaxy for the first time with a radius of 8.5 kpc. The CO (2–1) emitting gas is elongated in the direction of the morphological major axis of the stellar component. The rotation curve shows flat rotation at $\geq 6''$ from the galactic center with a velocity of about 220 km s^{-1}, which has been corrected using an estimated inclination of 67°. In addition, the symmetry of the CO distribution in the molecular gas disk is the second highest in our sample (A-parameter = 0.09). The PV diagram along the kinematic major axis reveals three emission peaks. One peak is associated with the nuclear region. The others are located at the connecting point between rigid rotation and flat rotation.

3.8.7 NGC 1210 (AM 0304–255)

This galaxy presents shells in optical images (Malin & Carter, 1983). The UV imaging reveals a tidal tail extending toward the north and a diffuse debris structure on the south region (Marino et al., 2009). Furthermore, several UV knots with a luminosity similar to that of the nucleus are seen along the tidal tail. The HI emission obtained by Schiminovich (2001) corresponds to the tidal tail visible in the UV images. The PV diagram measured from the [OII] line at 4959 Å shows a rigid rotation, suggesting a rotating stellar component (Longhetti et al., 1998). This galaxy is undetected in the CO (1–0) line. The 3 σ upper limit on the molecular gas mass is 1.9×10^7 $M_\odot$.

3.8.8 AM 0318–230

There are few studies focusing on this galaxy. The K-band isophotal shape clearly shows a rectangular core, even though the overall shape is dominated by disky isophotes (Rothberg & Joseph, 2004; Chitre & Jog, 2002). This galaxy is undetected in the CO (1–0) line. The 3 σ upper limit on the molecular gas mass is 2.1×10^8 $M_\odot$.

3.8.9 Arp 187

This galaxy is well known as a radio galaxy. Many radio continuum surveys including the galaxy have been conducted, but there are few studies focusing on the galaxy at all available wavelengths. Optical imaging shows two diffuse tails running in the north and south directions. Evans et al. (2005) suggest that the massive star formation rate is low because the galaxy has a low $L_{\rm IR}/L_{\rm CO}$, which is similar to the global $L_{\rm IR}/L_{\rm CO}$ of local spiral galaxies, and the dust temperature is lower (30–45 K) than the typical value of radio galaxies. Assuming that the IR luminosity is entirely due to star formation, the SFR derived from the FIR luminosity is a few solar masses per year.

3.8.10 AM 0612–373

There are few studies focusing on this galaxy. Optical imaging shows a long tail extending over 30 kpc toward the south and a dust lane running along the photometric minor axis of the stellar body (Smith & Hintzen, 1991). The rotation curve measured from the Ca II triplet absorption line ($\lambda \sim$ 0.85 μm) reveals a velocity gradient ($V = \pm$ 160 km s^{-1}; Rothberg & Fischer, 2010), which cannot be fully explained by rigid rotation or flat rotation.

Most of the CO (1–0) emitting gas is distributed within a radius of 2.5 kpc from the galactic center. We note that the kinematical major axis of the CO distribution is perpendicular to the apparent morphological major axis of the stellar body. The PV diagram along the kinematic major axis shows a velocity gradient of $\sim$200 km s^{-1} kpc^{-1} and two peaks located at a distance of 1 kpc from the galactic center, suggesting a ring-like structure.

3.8.11 UGC 4079 (Mrk 84)

There are few studies focusing on this galaxy. The HST/WFPC2 B-band imaging shows clumpy structures in the main body and a faint tail with several blobs. The HI spectra show a double-horn

profile with a FWHM of 234 km s^{-1} (Springob et al., 2005). The new CO (1–0) spectra obtained using the NRO 45 m telescope show a double-horn profile bwith the FWHM of 240 km s^{-1}, suggesting the presence of a rotating gas disk. However, the galaxy is undetected in the interferometric maps due to the limited sensitivity. Thus the rotating molecular gas disk is not confirmed.

3.8.12 AM 0956–282 (VV 592)

There are few studies focusing on this galaxy. Optical imaging shows a diffuse core with patchy structures. Rothberg & Joseph (2004) cannot determine structure parameters of the K-band surface brightness due to its disturbed structure. It is possible that the uncertainty of the position the nucleus defined in the K-band peak is a large. The HI spectrum shows a single peaked profile with the FWHM of 75 km s^{-1} (Koribalski et al., 2004).

The CO (1–0) emitting gas is distributed in three main components. The largest component is associated with the main body of the galaxy and shows a velocity gradient. The position angle of the kinematic major axis is almost 0°, which is not aligned with the apparent isophotal major axis of the stellar body. The PV diagram along the kinematic major axis reveals a velocity gradient, which is steeper in the northern region than the souther region. The intermediate component located in the southeast of the largest component seem to share the same velocity component. A diffuse optical counterpart, possibly a short tidal tail is seen in the same region. Thus this component seems to have been ejected from the main body due to the interaction. The smallest component is located in the west of the main body. This component has a stellar counterpart, with a weak 3 mm continuum emission associated to it. This component may be a star cluster or a dwarf galaxy.

3.8.13 AM 1158–333

There are few studies focusing on this galaxy. Optical imaging shows a diffuse extension toward the south of the main stellar body. The main body is elongated in the northeast and southwest. The brightest peak, which we define as the nucleus, is located at the northeast edge. Arp & Madore (1987) classify the galaxy as an elliptical galaxy with jets. The HI spectra show a double peaked profile with a FWHM of $\sim$ 100 km s^{-1} (Theureau et al., 1998).

We detect two molecular gas components traced by the CO (1–0) line. One component is associated with the nucleus. This cannot be resolved due to the limited spatial resolution. The other is

distributed below the main body blue-shifted 80 km s^{-1} from the systemic velocity (V_{sys} = 3027 km s^{-1}). The molecular gas mass of the component associated with the nucleus is 8.4×10^6 $M_\odot$, which is three times smaller than that of the other component.

3.8.14 NGC 4441 (UGC 7572)

Optical imaging shows one tidal tail extending toward the north and two stellar shells in the southwest of the main body. Manthey et al. (2008) investigate the large-scale HI distribution and kinematics using the Westerbork Radio Synthesis Telescope. The total mass of the atomic gas is 1.46×10^9 $M_\odot$. The distribution of the HI emission shows two prominent tidal tails extending more than 40 kpc towards the north and south. The northern tail follows the optical tail closely. In contrast, the southern tail is not aligned with the shell structure. The HI velocity field shows a regular rotation pattern in the inner region, indicating that the gas settled after the merger. Its velocity gradient continues into the tidal tails.

Jütte et al. (2010) investigate the CO (1–0) distribution and kinematics with high spatial and velocity resolution. Most of the CO emission comes from a central rotating disk with a radius of about 2 kpc. The molecular gas in the disk shows a regular rotation pattern whose kinematic major axis is nearly perpendicular to the rotation of large-scale HI structure, indicating a kinematically decoupled core. Jütte et al. (2010) suggest that the molecular gas disk is stable and cannot be responsible for star formation related to galaxy evolution. In addition, there are CO extensions on the outer side of the molecular disk, which seem to be kinematically decoupled from the molecular disk.

This galaxy is a candidate of a merger remnant between a spiral and an elliptical galaxy (Jütte et al., 2010; Manthey et al., 2008). One reason is the large difference in the stellar and atomic gas distribution, which is unlikely to occur in merges between two disk galaxies. The other reason is the presence of a large amount of atomic and molecular gas, and signs of a strong past star formation activity. These properties are not expected in mergers between two elliptical galaxies. Thus, it is most likely that the galaxy is a merger remnant between a spiral and an elliptical galaxy.

3.8.15 AM 1255–430

There are few studies focusing on this galaxy. The optical morphology is X-shaped with tails and plumes, the longest of which extends over 20 kpc. Optical imaging reveals a dust lane running

north-south in the nuclear region and extending over 2 kpc (Smith & Hintzen, 1991).

The distribution of the CO (1–0) emitting gas is significantly disturbed. The kinematical parameters of the molecular gas cannot be determined. A high-velocity component (V = 8680 – 8960 km s^{-1}) appears to inflow into the nuclear region. A low-velocity component (V = 8560 – 8660 km s^{-1}) is seen at the north of the nucleus. The velocity fields of these two components are discontiguous.

3.8.16 NGC 5018

The galaxy has several shells seen in the NUV (Rampazzo et al., 2007) and the optical (Malin & Carter, 1983), and it presents a prominent linear dust lane extending toward the northwest (Fort et al., 1986). The Hα+[NII] imaging reveals the presence of extended emission-line gas distributed like a strongly warped disk with a projected radius of $\sim 20''$ (Goudfrooij et al., 1994). A rotation curve measured from the Ca II triplet absorption line ($\lambda \sim 0.85$ μm) and the CO stellar absorption line (λ = 2.29 μm) shows flat rotation (Rothberg & Fischer, 2010). The HI emission is not associated to the nuclear region, however it is distributed along a filamentary structure stretching across its main body and connecting two neighbors, NGC 5022 and MCG 03-34-013 (Kim et al., 1988). The HI filament is a sign of interaction between these galaxies.

This galaxy is undetected in the CO (1–0) line. The 3 σ upper limit on the molecular gas mass is 2.64 $\times$ 10^7 $M_\odot$. In previous CO (2–1) observations at the Caltech Submillimeter Observatory, Lees et al. (1991) reports a non-detection.

3.8.17 AM 1419–263

There are few studies focusing on this galaxy. Optical imaging presents a $\sim$20 kpc plume elongated in the southwest and northeast and a 4 kpc tail extending towards the south (Smith & Hintzen, 1991). Even though the optical structure is strongly distorted, the K-band surface brightness profile is almost perfectly fitted by the de Vaucouleur's $r^{1/4}$ law (Sérsic n = 4.12; Rothberg & Joseph, 2004). The rotation curve measured from the Ca II triplet absorption line ($\lambda \sim 0.85$ μm) shows a shallow velocity gradient (Rothberg & Fischer, 2010), which cannot be fully explained by rigid rotation flat rotation. The galaxy is tentatively detected in the CO (1–0) line only in the channel maps. The detailed distribution and kinematics of the molecular gas is not clear due to the limited sensitivity.

3.8.18 UGC 9829 (VV 847)

There are few studies focusing on this galaxy. Optical imaging shows two long tidal tails running north-south. The projected length of the northern tail is longer than 30 kpc. The K-band image shows a bar structure across the nucleus (Rothberg & Joseph, 2004). The HI emission is distributed in the same velocity range as the CO emission (8000 – 8500 km s^{-1}; Bottinelli et al., 1993), but the HI spectral shape is not similar to the CO spectra.

The galaxy is an unusual case in that most of the CO (2–1) emission comes form the root of the northern tail, with only weak emission seen in the nucleus. The molecular gas shows a kinematic signature of gas streaming along the northern tail, but it does not appear to inflow into the nuclear region because the velocity of the molecular gas in the nucleus is about 250 km s^{-1} smaller than that in the tail leading to the nucleus.

3.8.19 NGC 6052 (Arp 209, UGC 10182, VV 86, Mrk 297)

The optical morphology is dominated by a larger number of clumpy features, which appears to be young massive clusters according to their colors and brightnesses (Holtzman et al., 1996). Alloin & Duflot (1979) interpret the galaxy as the collision of two late-type galaxies, which might have produced the bursts of star formation in clumps. Taniguchi & Noguchi (1991) report on numerical N-body simulations of the collision of two disk galaxies that the evolutionary phase of this galaxy corresponds to about 1.5×10^8 yr after the first impact. The peak of the radio continuum emission are shifted from the emission peak in optical images, suggesting the presence of off-nuclear starbursts (e.g., Deeg et al., 1993; Condon et al., 1990). The most of the CO and HI spectra obtained using single-dish telescopes shows a single peak profile (e.g., Garland et al., 2004, 2005).

The CO (2–1) emitting gas comes from the northern part of the galaxy and is not associate with the nucleus and bright knots in optical. The velocity field is significantly disturbed and shows complex structures. The majority of the molecular gas appears not to circularly rotate around the nucleus, while the velocity of the Hα and [NII] emissions shows galaxy rotation (Smith et al., 1996). The timescale estimated from numerical simulation (Taniguchi & Noguchi, 1991) is shorter than a typical merger timescale. Therefore, it seems that the galaxy has not undergone violent relaxation, according to the kinematics of the molecular gas and the apparent morphology.

3.8.20 UGC 10675 (VV 805, Mrk700)

Optical imaging shows a plume extending towards the southwest of the main body. Optical spectroscopy classifies the galaxy as a Seyfert 1 (Gallego et al., 1996; Denisiuk et al., 1976). However, Gonçalves et al. (1999) suggest that the galaxy is a LINER because the line strengths are weaker than those in classical AGNs. Furthermore, there is no evidence of an AGN from the radio–FIR correlation (Ji et al., 2000).

The CO (2–1) emitting gas appears to form a disk overall, but it is extremely disturbed. The velocity field shows a velocity gradient of ~ 150 km s^{-1}. The PV diagram along the kinematic major axis reveals three peaks, two of which overlap along the line of sight. There are only resolution elements along the radial direction due to limited sensitivity and low angular resolution. Thus it is possible that radial properties have large errors.

3.8.21 AM 2038–382

Optical imaging shows a plume extending towards the east and a prominent southwest loop. Optical spectroscopy reveals a dominance of A–F type stars, while lacking strong HII region type emission lines, suggesting that the burst of star formation ended less than a few $\times$ 10^8 yr ago (Sekiguchi & Wolstencroft, 1993). The HI spectrum is roughly a double-horn profile (Richter et al., 1994), which is typical for a rotating disk. However the PV diagram measured from the CO stellar absorption line at 2.29 μm shows no sign of a rotating disk (Rothberg & Fischer, 2010).

The CO (2–1) moment 0 map is shaped like a peanut. A peanut-shaped gas distribution is often seen in barred galaxies because gas piles up in the bar ends. The size of the northern concentration is larger than the southern one. The PV diagram along the kinematic major axis shows two emission peaks, which are offset by $2''(\sim 0.8$ kpc) offset from the galactic center. A velocity gradient of ~ 210 km s^{-1} is present in the moment 1 map. These signatures imply the presence of a ring or a bar, but a bar structure is not identified in optical images.

3.8.22 AM 2055–425

This galaxy is classified as a LIRG or an ULIRG depending to the assumed distance. The SFR derived from the combination of the IR luminosity and the FUV measurement is larger than 200 M$_\odot$ yr^{-1} (Howell et al., 2010). The HST/ACS B-band image shows two tidal tails and knotty

structures in the main body. The velocity field of the Hα emission shows simple circular motion with a velocity width of 150 km s^{-1} (Mihos & Bothun, 1998). Optical spectroscopy classifies the galaxy as a starburst-AGN composite (Brightman & Nandra, 2011; Yuan et al., 2010). The IR spectroscopy reveals the presence of a buried AGN (Imanishi et al., 2010; Risaliti et al., 2006). Similarly, the X-ray emission is clearly dominated by a hidden AGN (Franceschini et al., 2003).

The CO (1–0) emitting gas is distributed along an optical dust lane. Most of the CO emission comes from the southeast region of the main body, but the emission peaks seen in all channel maps are located at the nucleus. The PV-diagram also shows gas concentration in the nucleus. In addition, an extension of the molecular gas is seen in the southwest region of the main body, which does not correspond to the stellar arm structure. The symmetry of the CO distribution is the lowest (A-parameter = 0.67) in our sample mainly due to the nonuniform distribution as mentioned above. The velocity field shows a velocity gradient of $\sim$100 km s^{-1} kpc^{-1}. An inclination of an expected disk was estimated to be 6°, in which case, the maximum rotational velocity exceeds 600 km s^{-1}. We note possibilities that the inclination has a large error or the fitting algorithm did not work well.

3.8.23 NGC 7135 (AM 2146–350, IC 5136)

This galaxy has shell structures seen in the optical (Malin & Carter, 1983) as well as in the UV (Rampazzo et al., 2007). The distribution of warm ionized gas shows an asymmetric structure relative to the stellar body, elongated in the southwest direction (Rampazzo et al., 2003), which corresponds to the FUV distribution. A velocity field of warn ionized gas indicates rotational motion with the maxim rotation velocity of 78 km s^{-1} (Rampazzo et al., 2003). The galaxy is classified as a LINER using optical line-strength indices (Annibali et al., 2007). In addition, Rampazzo et al. (2007) suggests, using the relation between optical line-strength indices and UV colors, that the galaxy experienced recent nuclear star formation likely triggered by the interaction/accretion that formed the shells. The VLA HI emission is mostly detected outside the main body (Schiminovich, 2001).

The CO (1–0) emitting gas is distributed in the southern region of the main body and not associated with the nucleus. The detailed structure and kinematics of the molecular gas are not clear due to the weak CO emission.

3.8.24 NGC 7252 (Arp 226, AM 2217-245)

This galaxy is a well-known merger, called the "Atoms for Peace". The galaxy has remarkable loops and two long tidal tails seen in the optical. High-resolution optical observations conducted using the HST reveal spiral arms within $3\farcs5$ of the galactic center and weak spiral features out to about $9''$ (Whitmore et al., 1993). The Hα emission largely follows the spiral arms (Laine et al., 2003), suggesting that most of the star formation is strongly concentrated in the nuclear region. Miller et al. (1997) detect 499 cluster candidates, whose mean age is 0.6$\pm$0.2 Gyr (Whitmore et al., 1997). The HI emission is associated with the optical tidal tails, whose projected length are $520''$and $270''$(Hibbard et al., 1994), corresponding to 160 kpc and 270 kpc, respectively ($1''$= 305 kpc). Blue star-forming dwarf galaxies host at the end of the tidal tails (Boquien et al., 2009). The HI line width of 200 km s^{-1} seems surprisingly low given the disturbed optical morphology of the system (Richter et al., 1994) The molecular gas is associated with the 2.5 kpc radius disk of ionized gas (Wang et al., 1992).

Numerical simulations focusing on this galaxy have been conducted (e.g., Chien & Barnes, 2010; Hibbard & Mihos, 1995; Borne & Richstone, 1991). They conclude that the galaxy is a merger between two disk galaxies and will result in an elliptical galaxy. The merger age is estimated to be about 0.5–1 Gyr from numerical simulations (Chien & Barnes, 2010; Hibbard & Mihos, 1995) as well as observations (Schweizer, 1982). This is in good agreement with the mean age of the star clusters (Whitmore et al., 1997). Mihos et al. (1993) suggest that the SFR has fallen to one third of its peak according their simulation.

3.8.25 AM 2246–490

This galaxy is classified as a LIRG or an ULIRG depending on the assumed distance. The HST/ACS B-band image shows a single nucleus with long prominent tails (Figure A.29). The galaxy has a significant core light excess in the HST/NICMOS H-band image (Haan et al., 2011). The 6.2 μm PAH equivalent width is relatively large, suggesting that the galaxy built up a concentrated stellar cusp in the center due to luminous nuclear starbursts (Haan et al., 2011). Optical spectroscopy classifies the galaxy as an ambiguous class between a star-forming galaxy and Seyfert 2 galaxy (Yuan et al., 2010; Kewley et al., 2001). There is no signature of an AGN according to a selection by the hard X-ray color and the 6.4 keV iron line (Iwasawa et al., 2011).

The CO (1–0) emitting gas is concentrated in the nuclear region (C-parameter = 0.60) and shows

a velocity gradient of 120 km s^{-1} kpc^{-1}. It is expected from the CO velocity field and optical images that an inclination of the galactic plane is relatively low. As a result of fitting to the velocity field, the inclination is estimated to be 26°. The PV diagram along the kinematic major axis reveals rigid rotation and a double peak located off-center, suggesting the possibility of a ring structure, otherwise the molecular gas is non-uniformly distributed in a disk.

3.8.26 NGC 7585 (Arp 223)

This galaxy has shells seen in the optical (Malin & Carter, 1983). Multicolor optical imaging reveals that the shells are bluer than the main body, and that the timescale between multiple interactions is typically $\sim$ 1 Gyr (McGaugh & Bothun, 1990). The upper mass limit of the atomic gas is 7.5 $\times$ 10^9 $M_\odot$ (Balick et al., 1976). The galaxy is undetected in the CO (1–0) line. The 3 σ upper limit on the molecular gas mass is 1.64 $\times$ 10^8 $M_\odot$. Georgakakis et al. (2001) also report non-detection in the CO observations with the OSO 20 m telescope.

3.8.27 NGC 7727 (Arp 222, VV 67)

The HST/WFPC2 B-band image reveals spiral structures (Figure A.30; Peeples & Martini, 2006), while the K-band surface brightness profile roughly follows the de Vaucouleurs law, suggesting that violent relaxation has taken place since the progenitors merged (Rothberg & Joseph, 2004; Chitre & Jog, 2002). There is diffuse gas traced in the X-ray in the nuclear region, but this emission is not extended (Brassington et al., 2007). Optical spectroscopy reveals an absorption profile corresponding to the rotational velocity (V = $\pm$ 150 km s^{-1}; Simien & Prugniel, 1997). The Hα emission is associated with the central body (Knapen, 2005), where the mean stellar color is slightly bluer than the outer envelopes (Schombert et al., 1990). The HI line spectrum shows an asymmetric double-horn profile (Bottinelli et al., 1990).

The CO (1–0) emitting gas is concentrated in the nuclear region (C-parameter = 0.60) and shows a steep velocity gradient of 380 km s^{-1} kpc^{-1}. Its global morphology and kinematics suggest that the molecular gas forms a disk. The PV diagram along the kinematic major axis shows two velocity components with several peaks. The low-velocity component (V = 1665 – 1735 km s^{-1}) is associated with the nucleus and the high-velocity component (V = 1740 – 1990 km s^{-1}) is distributed along the optical dust lane. The molecular gas mass in the high-velocity component is nearly right times larger

than that in the low-velocity component. The total molecular gas mass measured from the CO (2–1) observations with a single-dish telescope is 1×10^8 $M_\odot$ (Crabtree & Smecker-Hane, 1994). We do not use this gas mass for the discussion because the conversion factor is unknown.

Chapter 4

The Evolution of the Merger Remnants

In this chapter, we discuss the evolution of merger remnants (hereafter, MRs) by comparing the properties of molecular gas and stellar components in the MRs with early-type galaxies (ETGs) and late-type galaxies (LTGs). According to these comparisons, the majority of the MRs shows a compact molecular gas disk relative to the stellar spheroidal component. Unless the disks grow significantly, for example from the return of ejected molecular gas or tidal HI gas, these MRs will likely evolve into ETGs. We also find that sources (5 %) with extended molecular gas disks and large gas mass fractions are likely to become late-type galaxies, unless there are further mechanisms which transport the molecular gas toward the central regions thereby decreasing the sizes of the gas disks.

4.1 Control Sample

The main motivation of this study is to investigate whether mergers can produce disk-dominated LTGs, or mergers all result in spheroid-dominated ETGs. The important next step is to investigate whether MRs share the global properties of molecular gas and stellar components with ETGs or LTGs. We expect MRs to show properties similar to ETG/LTGs, depending on which galaxy type they evolve into. We thus compare the derived parameters in the MRs to those for ETG/LTGs, using control samples. We use published radio and NIR data of ETGs in the $\mathrm{ATLAS^{3D}}$ project (Cappellari et al., 2011) and LTGs in the BIMA-SONG project (Regan et al., 2001; Helfer et al., 2003).

4.1.1 Early-type Galaxies in the $\mathrm{ATLAS^{3D}}$ sample

The $\mathrm{ATLAS^{3D}}$ Project combines a multi-wavelength survey of 260 ETGs in the local Universe (< 43 Mpc) with numerical simulations and semi-analytic modeling of galaxy formation. Alatalo et al. (2013) and Davis et al. (2013) present CO interferometric data of 38 ETGs in the $\mathrm{ATLAS^{3D}}$ sample. We use published radial surface brightness profiles of the molecular gas for the 38 ETGs (Davis et al., 2013) and refer to the CO velocity fields and PV diagrams of these sources (Alatalo et al., 2013). In addition, we use the total molecular gas mass derived from single-dish CO measurements by Young et al. (2011) and the effective radius of the stellar component estimated by Cappellari et al. (2011). The various data of the $\mathrm{ATLAS^{3D}}$ sample is available from the website[a].

[a] http://www-astro.physics.ox.ac.uk/atlas3d/

4.1.2 Late-type Galaxies in the BIMA SONG sample

The BIMA Survey of Nearby Galaxies (BIMA SONG) project is the first systematic imaging survey of the CO (1–0) emission in 44 nearby LTGs using the BIMA millimeterwave interferometer. Regan et al. (2001) present initial results for a subsample of 15 LTGs, and then Helfer et al. (2003) present the data from the full survey of 44 LTGs. The interferometric maps show the distribution and kinematics of the CO emission at resolutions of a few hundred parsec. Twenty-nine out of 44 LTGs show clearly a disk-like rotation in their velocity fields, while the remaining 15 LTGs show clumpy or complex structures. We use the CO integrated intensity maps and velocity fields of the 29 LTGs with molecular gas disks in the BIMA SONG sample for our comparative study. The CO moment maps of 24/29 sources are made by combining the data obtained using the NRAO 12 m single-dish telescope with the interferometric data obtained at the BIMA. The CO moment maps of the BIMA-SONG sample are available from the website[b].

4.2 The Absolute Size of the Molecular Gas Disk

We compare the absolute size of the molecular gas disk (R_{80}) among the three samples. R_{80} is the radius which contains 80 % of the total CO flux (see § 3.1). Using published radial surface brightness profiles of the molecular gas for 38 ETGs in the $\mathrm{ATLAS^{3D}}$ sample (Davis et al., 2013, Figure A1), we estimate R_{80} of the 38 ETGs without accounting for the inclinations and position angles of the galaxies. The inclinations and position angles of the $\mathrm{ATLAS^{3D}}$ galaxies are not publicly available as the CO data. We also estimate R_{80} of 29 LTGs in the BIMA SONG sample as well as the MR sample, using the published integrated intensity maps after correcting for the inclinations and position angles of the galaxies (Helfer et al., 2003, Table 1).

The estimated R_{80} are listed in Table 4.5 and Table 4.7. The histogram of R_{80} for 24 MRs with molecular gas disks, 38 ETGs, and 29 LTGs are shown in Figure 4.1. The R_{80} of the MRs are distributed in two groups, one with $R_{80} < 2$ kpc, and the other with $R_{80} \sim 4$ kpc. The R_{80} of the LTGs are distributed over a wide range between 0.96 kpc and 8.72 kpc. The mean values of R_{80} are 1.61 $\pm$ 0.67 kpc for the MRs, 1.81 $\pm$ 0.92 kpc for the ETGs, and 3.90 $\pm$ 1.76 kpc for the LTGs. A Kolmogorov-Smirnov test (K-S test; see Appendix E) gives P-value = 0.381 for the comparison of the distribution between the MRs and the ETGs, suggesting that the two distributions are not significantly

[b] http://ned.ipac.caltech.edu/level5/March02/SONG/SONG.html

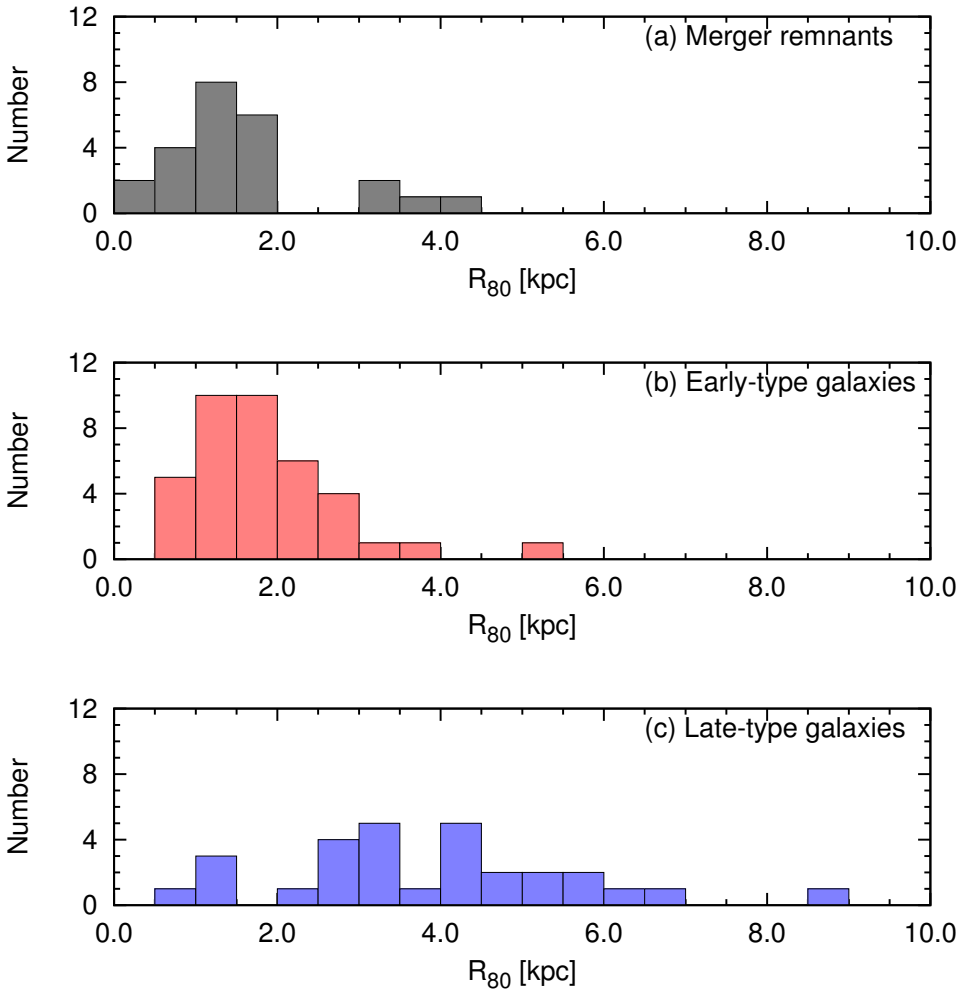

Figure 4.1: Histogram of the absolute size of the molecular gas disk in the 24 MRs (a: upper), 38 ETGs in the ATLAS^{3D} sample (b: middle), and 29 LTGs in the BIMA SONG sample (c: lower).

different. In contrast, the K-S test gives P-value = 0.000 for the comparison between the MRs and the LTGs, suggesting a significant deviation between them. Therefore the MRs have molecular gas disks similar in absolute size to the ETGs rather than the LTGs.

4.3 The Relative Size of the Molecular Gas Disk

We examine the relative size of the molecular gas disk to the stellar spheroidal component among the three samples. Recent numerical simulations suggest that gas forms an extended disk with size larger than the stellar spheroidal component in a MR (see Figure 1.6; Springel & Hernquist, 2005). Our primary goal is to test this theoretical prediction using the three sample population we have compiled. In typical LTGs, the bulge-to-disk size ratio of stellar components is less than unity (Graham & Worley, 2008) and thus the molecular gas disk size is larger than the bulge size because most of the molecular gas is distributed in a disk. In contrast, recent high sensitivity observations reveal the presence of compact molecular gas disks in ETGs (e.g., Young et al., 2008; Crocker et al., 2011).

We estimate the ratio of R_{80} to the K-, (or J-, H-) band effective radius ($R_{\rm eff}$) for the 38 ETGs in the $\rm ATLAS^{3D}$ sample and 29 LTGs in the BIMA-SONG sample in order to investigate the relative size of the molecular gas disk to the stellar spheroidal component. $R_{\rm eff}$ is the radius of the isophote containing half of the total K- (or J-, H-) band luminosity. We use $R_{\rm eff}$ of the ETGs estimated by Cappellari et al. (2011). For the LTGs, we use $R_{\rm eff}$ for 26 out of 29 sources which were estimated also by Cappellari et al. (2011), and we estimate $R_{\rm eff}$ of the remaining three sources in the same way as Cappellari et al. (2011) using the 2MASS data (Jarrett et al., 2003). The ratio between R_{80} and $R_{\rm eff}$ ($R_{\rm ratio}$, hereafter) are listed in Table 4.5 and Table 4.7.

We compare $R_{\rm ratio}$ among the three samples. The histogram of Log $R_{\rm ratio}$ for 24 MRs with molecular gas disks, 38 ETGs, and 29 LTGs are shown in Figure 4.2. The mean values of $R_{\rm ratio}$ are 1.22 ± 0.67 for the MRs, 0.92 ± 0.79 for the ETGs, and 0.89 ± 0.51 for the LTGs. The Log $R_{\rm ratio}$ of the MRs are distributed evenly across the range between -1.11 and 1.22. The Log $R_{\rm ratio}$ of both ETGs and LTGs are concentrated around Log $R_{\rm ratio}$ = 0, which is in contrast to the MRs, where the spread in the distribution is at least two times larger. A K-S test gives P-value = 0.256 for the comparison between the MRs and the ETGs, P-value = 0.139 for the comparison between the MRs and the LTGs, and P-value = 0.194 for the comparison between the ETGs and the LTGs. These results suggest that the relative sizes of the molecular gas disks among the three samples are not significantly different.

Table 4.1: P-values for the Comparison of the Disk Sizes of the Molecular Gas

	MR	ETG	LTG($R_{\rm eff}$)	LTG($R_{\rm bulge}$)
MR	···	0.256	0.139	0.000
ETG	···	···	0.194	0.000
LTG	···	···	···	···

The $R_{\rm eff}$ of the LTGs is determined to be the radius of the isophote containing half of the total K-band luminosity, which consists of a light coming from both bulge and disk. The $R_{\rm eff}$ may not be good for estimating the relative size of the molecular gas disk to the stellar spheroidal component in LTGs. Thus, we estimate the relative size of the molecular gas disk for 25 out of 29 LTGs, using a bulge size ($R_{\rm bulge}$; Fisher et al., 2013) as a substitute for $R_{\rm eff}$. $R_{\rm bulge}$ is defined as a radius at which the bulge surface brightness equals to that of the disk. The ratios between R_{80} and $R_{\rm bulge}$ are listed in Table 4.7. All sources except for NGC 4579 show Log ($R_{80}/R_{\rm bulge}$) larger than zero, indicating that the size of the molecular gas disk is larger than the bulge size. The CO emission in NGC 4579 is concentrated in the nuclear region. The IR imaging of NGC 4579 shows an extended MIR-bright disk (Kennicutt et al., 2003) where gas and dust are thought to be forming new stars. The molecular gas are expected to be distributed there, but the CO emission was undetected probably because of the limited sensitivity or missing flux.

The histogram of Log ($R_{80}/R_{\rm bulge}$) is shown in Figure 4.2 (d). The distribution is significantly different from the distribution of Log ($R_{80}/R_{\rm eff}$). The mean value of $R_{80}/R_{\rm bulge}$ is 6.74 $\pm$ 4.56. The K-S test gives P-value = 0.000 for the comparison between the LTGs and the ETGs. This suggests that the relative size of the molecular gas disk is different. The K-S test also gives P-value = 0.000 for the comparison between the MRs and the LTGs, suggesting a significant difference between them. Therefore, the relative size of the molecular gas disk in the MRs is similar to the relative size of the gas disk in the ETGs rather than the LTGs. These comparisons suggest that the majority of the MRs may evolve into ETGs. Even if some MRs with extended gas disks may become LTGs, they are not a significant fraction and furthermore require mechanisms to expand the size of the molecular gas disk because the disk sizes of these MRs are still smaller than the average value of the LTGs.

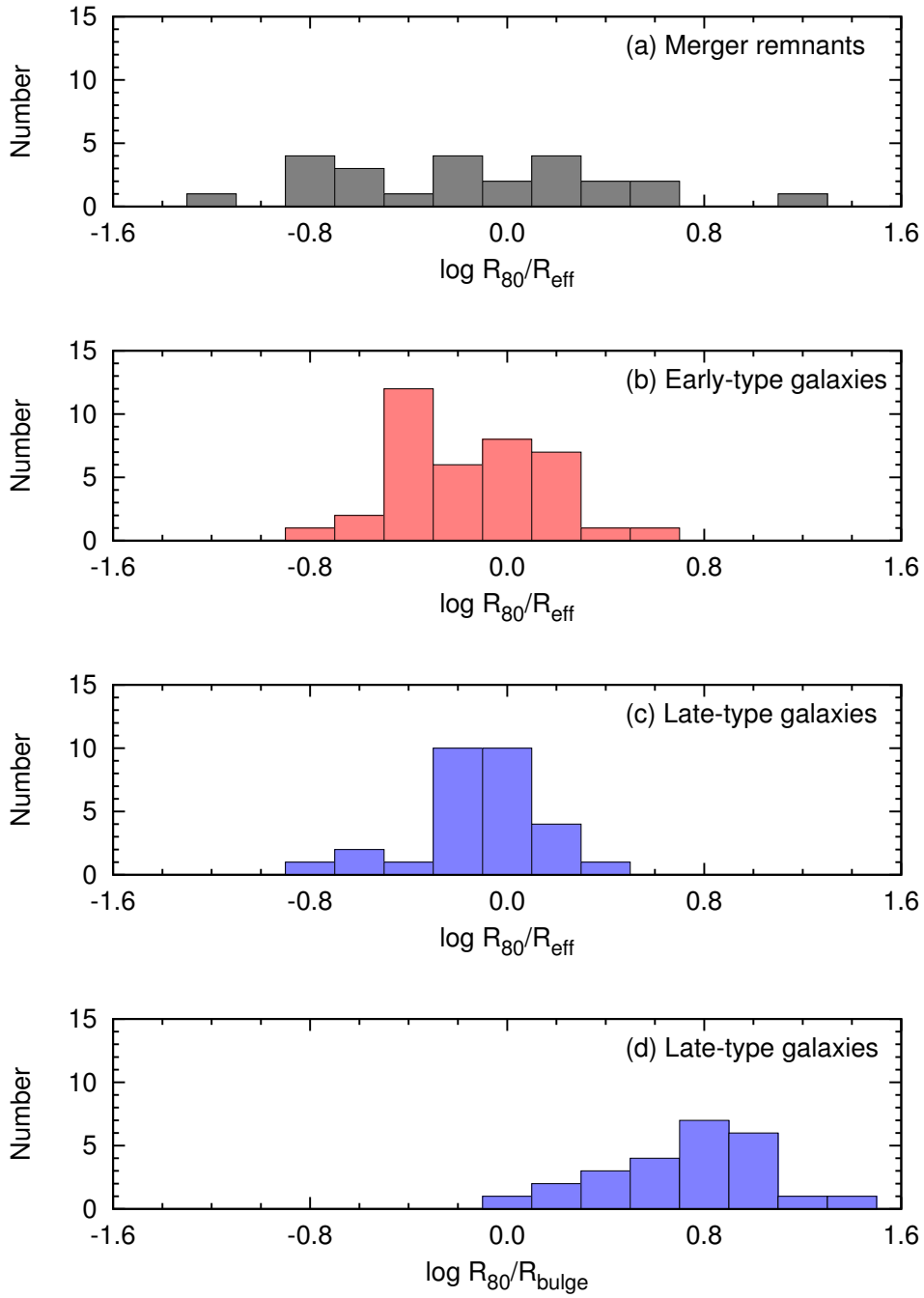

Figure 4.2: Histogram of the relative size of the molecular gas disk in the 24 MRs (a), 38 ETGs in the ATLAS^{3D} sample (b), and 29 LTGs in the BIMA SONG sample (c). The lowest histogram (d) is the same as (c), but the relative size of the molecular gas disk is estimated by a ratio of R_{80} to the bulge size ($R_{\rm bulge}$).

4.4 The Gas Mass Fraction

The gas mass fraction is one of the indicators of galaxy evolution because molecular gas is the fuel for star formation. In general, ETGs are deficient in cold gas than LTGs (Lees et al., 1991). Furthermore, local U/LIRGs and submillimeter galaxies at high-redshift are more gas-rich compared to normal disk galaxies (Sanders et al., 1991; Tacconi et al., 2008). The gas mass fractions are estimated to be 20–80 % in high-redshift galaxies, where active star formation occurs (Tacconi et al., 2010) because a number of massive clumps of stars and gas are formed by gravitational instability in gas-rich disks (Immeli et al., 2004). In addition, Hopkins et al. (2009) predict that mergers with large gas mass fractions yield LTGs.

In this study, we define the gas mass fraction as

$$f_{\rm gas} = \frac{M_{\rm H_2}}{M^*}, \tag{4.1}$$

where $M_{\rm H_2}$ is the molecular gas mass and M^* is the stellar mass. The stellar masses (M^*) of the MR sample are derived from the K-band magnitude (Rothberg & Joseph, 2004) using the mass-to-luminosity relation ($M^*/L_{\rm K}$ = 0.5),

$$M^*[{\rm M}_\odot] = 0.5 \times 10^{-0.4\times(M_{\rm K}-3.28)}, \tag{4.2}$$

where $M_{\rm K}$ is the absolute K-band magnitude (Rothberg & Joseph, 2004, see Table 2.1). The stellar masses are listed in Table 4.3. Most of the MRs have stellar masses of 10^{10} –10^{11} $\rm M_\odot$. The stellar mass of UGC 8058 is 1.1 $\times$ 10^{12} $\rm M_\odot$, which is the most massive in the MR sample. Using these stellar masses and the molecular gas masses, we estimated the gas mass fractions (Table 4.3). The molecular gas masses of 12/37 sources are derived from the single-dish CO data. They are usually called the "total molecular gas mass". The molecular gas masses of the remaining 25/37 sources are estimated using the interferometric CO data, because there are no appropriate data obtained with single-dish telescopes. It is highly possible that the molecular gas mass estimated using the interferometric data is smaller than the total molecular gas mass due to the missing flux.

In addition, we estimate gas mass fractions of the 38 ETGs in the ATLAS$^{\rm 3D}$ sample and the 25 LTGs in the BIMA-SONG sample in order to compare to the gas mass fractions of the MRs. The stellar mass is estimated using the K-band magnitude (Jarrett et al., 2003; Cappellari et al., 2011) and

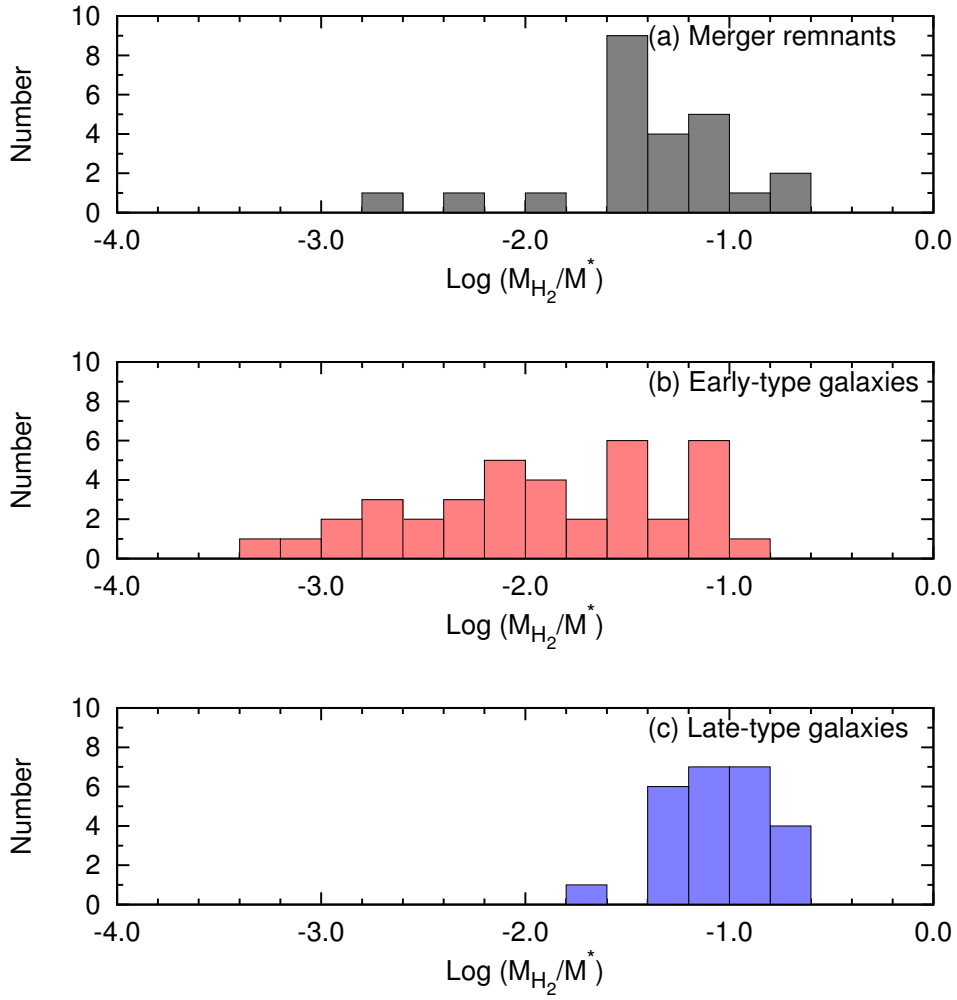

Figure 4.3: Histogram of the gas mass fraction in the 24 MRs (a: upper), 38 ETGs in the $\mathrm{ATLAS}^{3\mathrm{D}}$ sample (b: middle), and 25 LTGs in the BIMA SONG sample (c: lower).

Table 4.2: P-values for the Comparison of the Gas Mass Fractions

	ETG	LTG	ETG + LTG
MR	0.001	0.002	0.174

Equation (4.2). The molecular gas mass is derived from the single-dish CO data (Helfer et al., 2003; Young et al., 2011) using the constant CO-to-H_2 conversion factor ($\alpha_{\rm CO}$ = 4.8; Solomon & Vanden Bout, 2005). The molecular gas mass of one ETG, NGC 4550, is an upper limit, hence the gas mass fraction is also an upper limit.

The histogram of the gas mass fraction for 24 MRs with molecular gas disks, 38 ETGs, and 25 LTGs are shown in Figure 4.3. The majority of the MRs has a gas mass fraction of 1 – 10 %. The gas mass fractions of the LTGs are distributed around 10 %, whereas the gas mass fractions of the ETGs are distributed over a wide range between 0.1 % and 10 %. A K-S test gives P-value = 0.001 for the comparison between the MRs and the ETGs, and P-value = 0.002 for the comparison between the MRs and the LTGs, suggesting that these distributions are different. We compare the distribution between the MR sample and the combined sample of the ETGs with the LTGs. The K-S test gives P-value = 0.174, suggesting that these distributions are not significantly different. It should be noted that the LTG sample is biased towards CO bright sources (Helfer et al., 2003), and the actual molecular gas fraction of typical LTGs are likely to be lower (1-10 %), bringing the distribution of LTGs to a range closer to the MRs. Therefore the P-value between the MRs and ETG/LTGs combined distribution is likely to be a lower limit. These statistics are not inconsistent with the possibility that the MRs include progenitors of both ETGs and LTGs.

4.5 Relation between the size of the gas disk and gas mass fraction

We investigate the properties of the molecular gas in the MRs by comparing the relative sizes of the molecular gas disks ($R_{\rm ratio} = R_{80}/R_{\rm eff}$ and also $R_{\rm ratio} = R_{80}/R_{\rm bulge}$) and gas mass fractions ($f_{\rm gas} = M_{\rm H_2}/M^*$) to ETGs and LTGs. We show the relation between $R_{\rm ratio}$ and $f_{\rm gas}$ of 24 MRs, 38 ETGs, and 21 LTGs in Figure 4.4. All of these sources show rotating molecular gas disks, including rings, spirals, and bar-like structures.

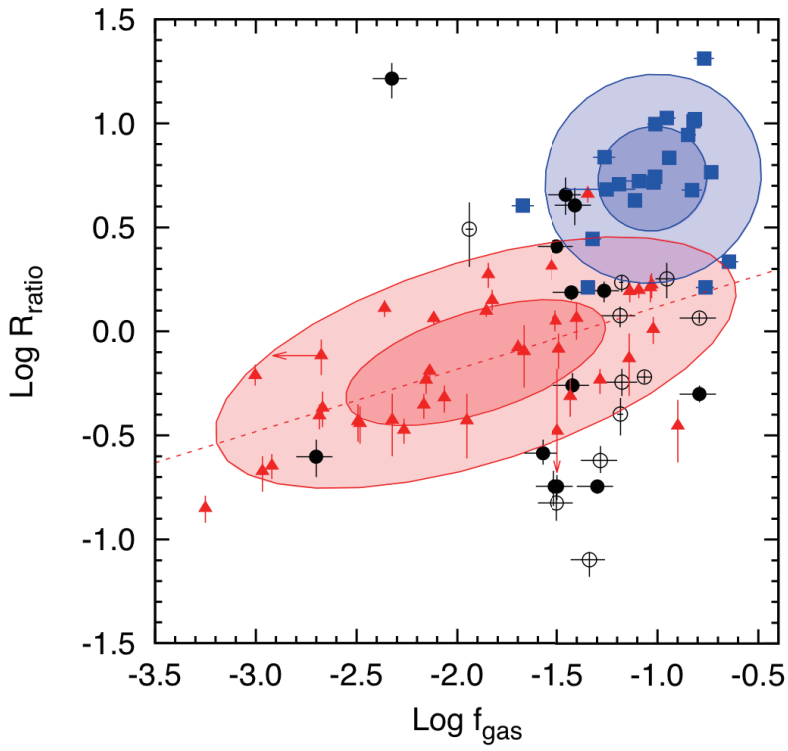

Figure 4.4: Relation between the gas mass fraction and relative size of the molecular gas disk to the stellar spheroidal component. Black filled/open circles show the MRs whose molecular gas mass are estimated using the interferometric/single-dish data, respectively. Red triangles show the ETGs in the ATLAS^{3D} sample. Blue squares show the LTGs in the BIMA-SONG sample. The dark-red and light-red elliptical regions express the contour level inside which the ETG samples are included to within the 1 σ and 2 σ level, respectively. The blue elliptical regions are similar to the red ones, but for the LTG sample. The red dashed line shows a best fit of a correlation between the relative disk size and gas mass fraction for the ETGs.

The important finding from this comparison is that while the ETGs and LTGs occupy two different regions in this plot (Figure 4.4), the MRs show a large scatter and do not follow either population on average. There is no MR in the regions which include 1 σ of the sample of both ETGs and LTGs. About one-third of the MRs lay just in the intermediate region between the ETGs and the LTGs. This possibly suggests that these MRs with molecular gas disks are dynamically evolving transient sources that are ready to evolve into either ETGs or LTGs. In addition, the ETGs show a correlation between the relative disk size and gas mass fraction. The relative disk size becomes larger as the gas mass fraction increases. We estimate the best fit of this correlation using a least-squares fitting and show the result with a red dashed line in Figure 4.4. In contrast, the LTGs are concentrated in a circular region. The mean gas mass fraction of the LTGs is Log $f_{\rm gas}$ = -1.02 $\pm$ 0.25, and the mean disk size of the LTGs is Log $R_{\rm ratio}$ = 0.74 $\pm$ 0.27.

We make the same plots (Figure 4.5), dividing sources by their stellar masses because the gas mass fraction tends to decrease with an increase in the stellar mass according to studies of various galaxies (Tacconi et al., 2013; Narayanan et al., 2012a). The MRs do not show this characteristic. One possibility is the sample selection. The molecular gas mass ranges are narrower, thus this characteristic does not appear in the populations. We find that different types of galaxies occupy different regions in the plot. This feature becomes evident at the stellar mass range of 10.5 $\leq$ Log $M^* <$ 11.0. The majority of the MRs is included in this stellar mass range. They are confined to this stellar mass range during their evolution into ETG/LTGs because changing all of the molecular gas to stars can change the stellar mass only by $\sim$10%. Therefore the MRs will move towards the upper-right or lower-left within this plot if they are to evolve into present-day ETGs and LTGs. We suggest that the MRs need to decrease their gas mass fractions or expand the sizes of the molecular gas disks in a few Gyrs before they become ETG/LTGs.

We now make a simple assumption on star formation, in which the SFR estimated from the FIR luminosity is constant until the molecular gas in a galaxy is consumed completely, assuming that the gas reservoir is not replenished and that all of the molecular gas is used for star formation. Under this assumption, we estimate the gas mass fraction in t yr from the present using the following equation:

$$f_{\rm gas}(t) = \frac{M_{\rm H_2}(t)}{M^*(t)} = \frac{M_{\rm H_2}(0) - \Delta M}{M^*(0) + \Delta M} = \frac{M_{\rm H_2}(0) - {\rm SFR}\Delta t}{M^*(0) + {\rm SFR}\Delta t}, \tag{4.3}$$

where $f_{\rm gas}(t)$ is the gas mass fraction in t yr, ΔM is the amount of mass which changes from the

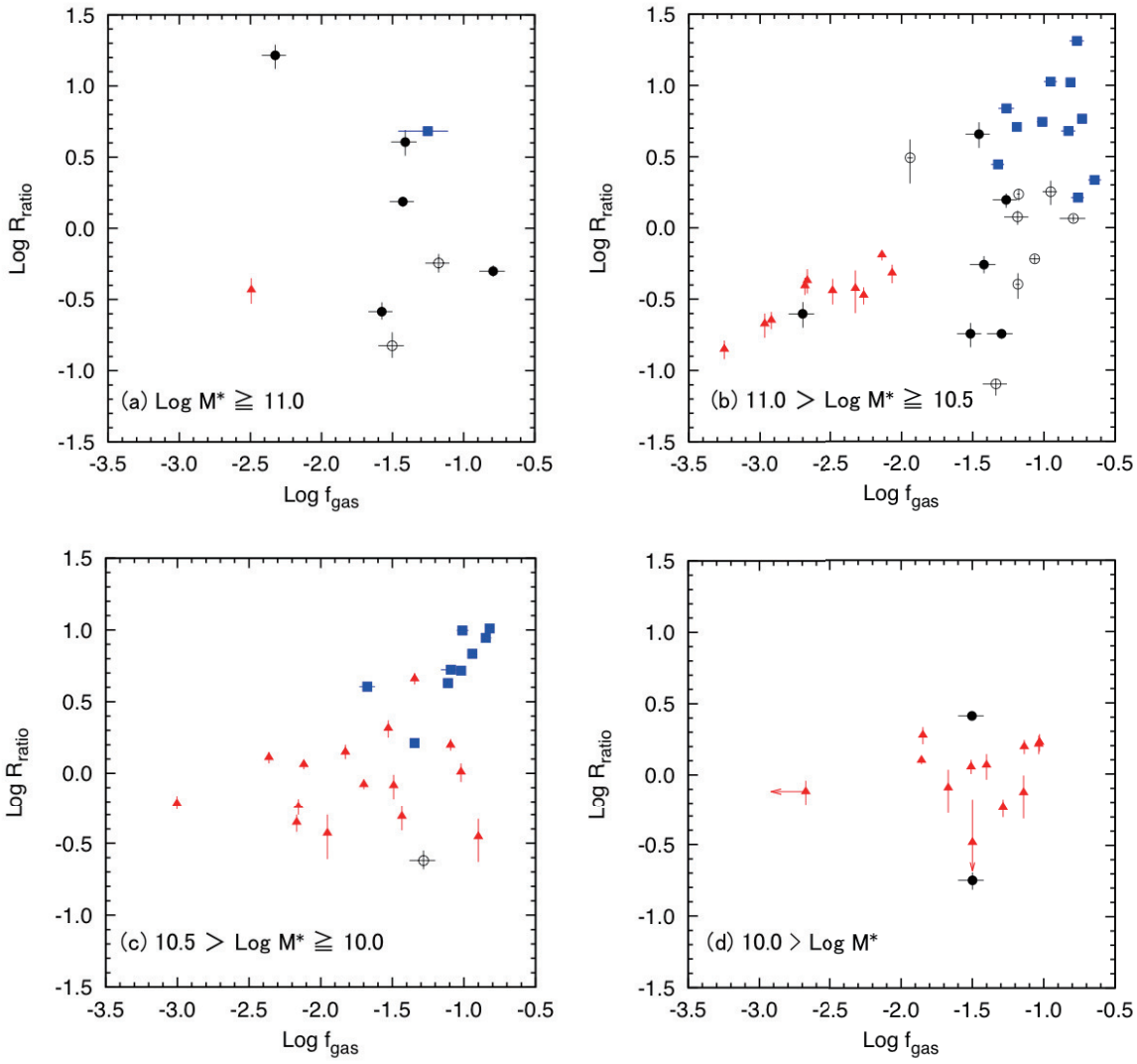

Figure 4.5: The same as Figure 4.4, but divided by the stellar mass. Black filled/open circles show the MRs whose molecular gas mass are estimated using the interferometric/single-dish data, respectively. Red triangles show the ETGs in the ATLAS^{3D} sample. Blue squares show the LTGs in the BIMA-SONG sample.

molecular gas to stars by t yr from the present, $M_{\rm H_2}(0)$ and $M^*(0)$ are the molecular gas mass and stellar mass at the present, respectively. We plot the properties of the 24/37 MRs in 1×10^7 yr with dark-grey circles, 5×10^7 yr with light-grey circles in Figure 4.6, assuming that the $R_{\rm ratio}$ does not change. The galaxies move parallel to the X-axis in the figure.

The seven sources lying in the intermediate region between the ETGs and the LTGs do not move their positions in this plot significantly within 5×10^7 yrs, which indicates that they do not consume their molecular gas as much compared to other MRs with comparable stellar mass. The intermediate region is shown with a green elliptical in Figure 4.6. The average consumption mass of the molecular gas is 1.4×10^8 $M_\odot$. These sources share their properties with the ETG/LTGs. We suggest a scenario that they remain the same position with the current properties or will move slowly toward the average point of the ETG/LTGs in this plot.

In contrast, the majority of the sources lying outside the intermediate region moves significantly, suggesting that they spend a large amount of molecular gas for star formation. The median consumption time of the molecular gas is 7.7×10^7 yr, which corresponds to about half of the average consumption of the other sources. Thus they are likely to use the molecular gas more quickly than the MRs with similar stellar mass which we mentioned above. From this result, we suggest a possible reason why these MRs occupy the same region with the ETG/LTGs that the MRs could move from the current position in a short timescale ($\sim 10^8$ yr) compared to merger timescale and dynamical time of galaxies ($\sim 10^9$ yr).

The $R_{\rm eff}$ is not expected to change significantly because the Sérsic indices of 16/24 sources were determined, suggesting that the stellar components have already undergone dynamical relaxation (Rothberg & Joseph, 2004), and their stellar structure will not change much. For the MRs located at the upper-left of this plot, however the Sérsic index could not be estimated. This implies that the $R_{\rm ratio}$ will (could still) change during their evolution. In addition, it is possible that R_{80} might become smaller due to gas inflow and consumption by star formation. Alternatively, R_{80} might become larger by the retuning of cold gas via tidal tails. Therefore it is highly possible that these MRs in the upper left move parallel to the Y-axis in the figure.

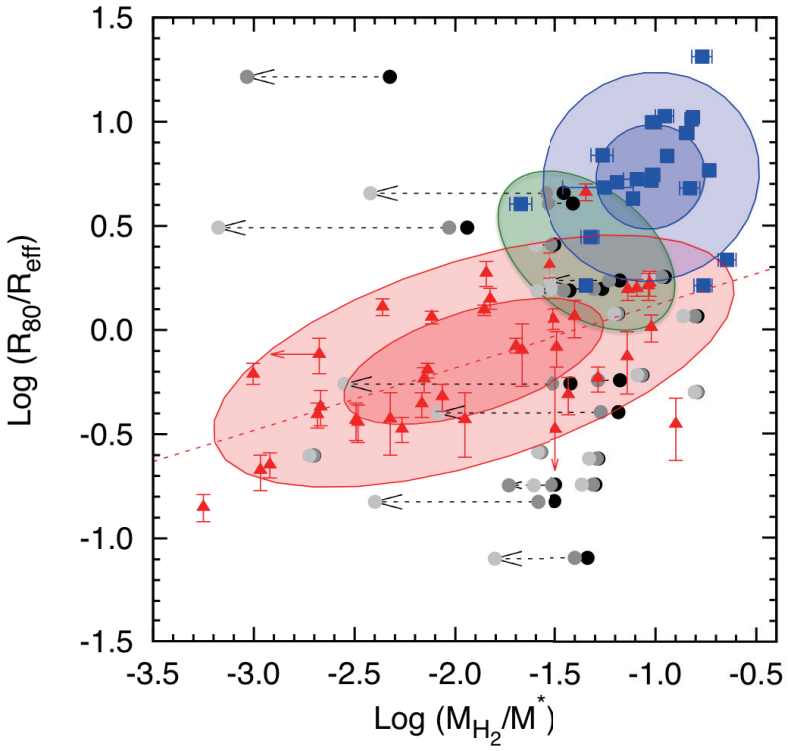

Figure 4.6: The predicted change of the gas mass fraction overlord on the Figure 4.4. The black circles show the MRs at the present. The dark-grey and light-grey circles show the MRs in 1×10^7 yr and 5×10^7 yr, respectively. The green elliptical shows the intermediate region between the ETG and LTG populations.

Table 4.3: Global Properties of the Merger Remnant Sample (2)

Name	M^* [10^{10} $M_\odot$]	Log $f_{\rm gas}$	Classified Type
(1)	(2)	(3)	(4)
UGC 6	4.1	-0.95	A1
NGC 34	7.2	-1.46	A2
Arp 230	0.51	-1.50	A2
NGC 455	7.4	-3.34	C
NGC 828	14	-1.43	A3
UGC 2238	7.0	-1.26	A4
NGC 1210	3.2	-3.23	C
AM 0318-230	11	-2.71	C
NGC 1614	8.1	-1.42	A3
Arp 187	13	-0.79	A4
AM 0612-373	19	-1.57	A3
UGC 4079	3.3	-1.62	C
NGC 2623	5.0	-1.52	A3
NGC 2782	3.1	-1.30	A4
UGC 5101	3.5	-1.41	A2
AM 0956-282	16	-1.50	A3
NGC 3256	7.9	-1.18	A1
NGC 3597	3.2	-0.79	A4
AM 1158-333	1.1	-2.16	B
NGC 4194	2.0	-0.83	B
NGC 4441	1.6	-1.28	A4
UGC 8058	110	-2.33	A2
AM 1255-430	9.6	-1.22	B
AM 1300-233	7.4	-1.34	A3
NGC 5018	12	-3.65	C
Arp 193	5.9	-1.18	A4
AM 1419-263	9.7	-2.41	B
UGC 9829	9.9	-1.33	B
NGC 6052	2.7	-0.83	B
UGC 10675	8.5	-1.94	A2
AM 2038-382	7.8	-1.19	A4
AM 2055-425	11	-1.18	A4
NGC 7135	3.9	-2.91	B
NGC 7252	8.9	-1.06	A4
AM 2246-490	17	-1.50	A3
NGC 7585	10	-3.02	C
NGC 7727	5.0	-2.70	A3

NOTE.—Col.(1): Source name. Col.(2): The stellar mass. Col.(3): The gas mass fraction. This is a logarithm ratio of the molecular gas mass (listed in Table 3.2) to the stellar mass. Col.(4): Type classified according to our definition (see §4.6).

4.6 Evolution of Merger Remnants

According to the properties of the molecular gas, we classify the 37 MRs into the following six types:

- **Type A1:** Sources with a high gas mass fraction and an extended molecular gas disk
- **Type A2:** Sources with a low gas mass fraction and an extended molecular gas disk
- **Type A3:** Sources with a low gas mass fraction and a compact molecular gas disk
- **Type A4:** Sources with a high gas mass fraction and a compact molecular gas disk
- **Type B:** Sources with a clumpy CO structure
- **Type C:** Sources undetected in the CO lines

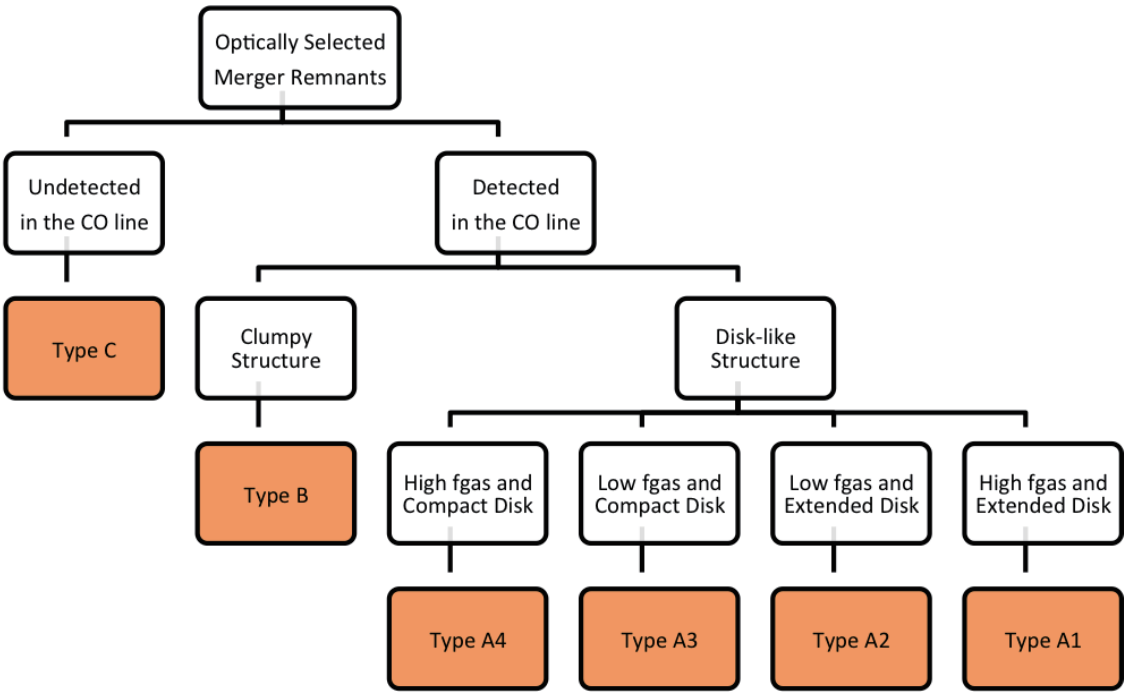

Figure 4.7: Classification chart of the merger remnants.

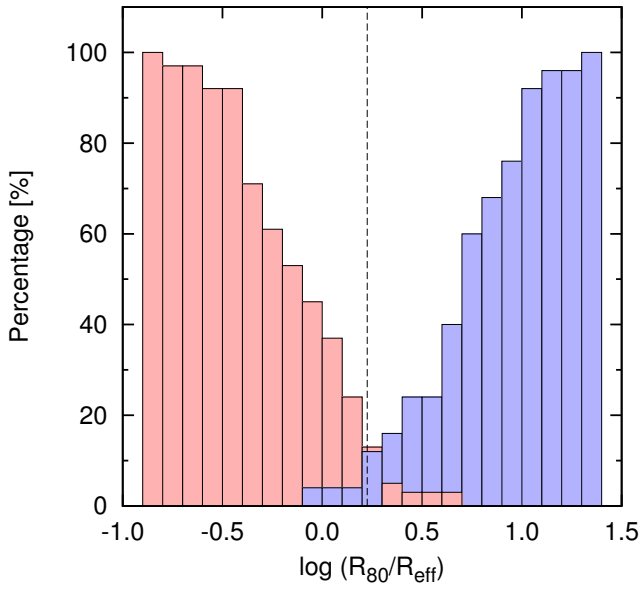

Figure 4.8: The determination of the boundary of the disk size using the distribution of ETGs (red bars) and LTGs (blue bars). The dashed line shows the boundary. The boundary of two distributions are determined by identifying a value which divides ETGs into 88 % : 12 %, and LTGs into 12 % : 88 %.

We set up the boundary of the gas mass fraction and the disk size using the distribution of ETGs and LTGs. The boundary of two distributions are determined by identifying a value which divides ETGs into A : (1-A), and LTGs into (1-A) : A (A = const.) as shown in Figure 4.8. The boundary of the gas mass fraction is Log $f_{\rm gas}$ = -1.30. Mergers with Log $f_{\rm gas}$ $>$ -1.30 are classified as sources with a high gas mass fraction, and mergers with Log $f_{\rm gas}$ $<$ -1.30 are classified as sources with a low gas mass fraction. Similarly, the boundary of the disk size is Log $R_{\rm ratio}$ = 0.215. Mergers with Log $R_{\rm ratio}$ $>$ 0.215 are classified as sources with an extended molecular gas disk, and mergers with Log $R_{\rm ratio}$ $<$ 0.215 are classed as source with a compact molecular gas disk. According to Figure 4.9, where the boundary of the gas mass fraction and the disk size are presented, two galaxies are classified as Type A1, five galaxies are classified as Type A2, eight galaxies are classified as Type A3, and nine galaxies are classified as Type A4. There is no source on the boundary lines. In addition, six galaxies are classified as Type B and seven galaxies are classified as Type C. The average properties (Sérsic index, FIR luminosity, molecular gas mass, stellar mass) of sources in different types are summarized in Table 4.3.

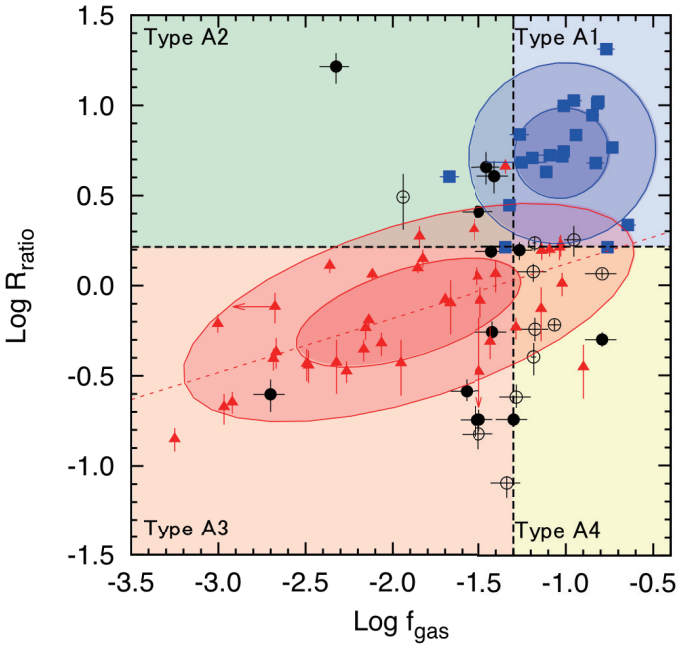

Figure 4.9: Four sub-types of Type A. Black filled/open circles show the MRs whose molecular gas mass are estimated using the interferometric/single-dish data, respectively. Red triangles show ETGs in the ATLAS^{3D} sample. Blue squares show LTGs in the BIMA-SONG sample. The dark-red and light-red elliptical regions express the contour level inside which the ETG samples are included to within the 1 σ and 2 σ level, respectively. The blue elliptical regions are similar to the red ones, but for LTGs. The red dashed line shows a best fit of a correlation between the relative disk size and gas mass fraction for the ETGs.

4.6.1 Type A

Type A is defined as sources whose velocity field of the molecular gas can be modeled by circular motion. 65 % (24/37) of the MR sample are classified as Type A. Furthermore, we divide these 24 sources into four sub-types. We discuss the characteristics of sources classified as different sub-types and the evolution paths of the sources in what follows.

- **Type A1: LTG candidates**

  5 % (2/37) of the MR sample (UGC 6 and NGC 3256) are classified as Type A1, which has a high gas mass fraction (Log $f_{\rm gas}$ > -1.30) and an extended molecular gas disk (Log $R_{\rm ratio}$ > 0.215). Numerical models (Springel & Hernquist, 2005; Hopkins et al., 2009) that predict the occurrence of disk-dominated galaxies require progenitor galaxies with a high gas mass fraction. The gas mass fraction and disk size of all of the MRs are smaller than the average gas

mass fraction and disk size of LTGs ($f_{\rm gas} \sim 11$ % and $R_{\rm ratio} \sim 6.5$). The two galaxies (UGC 6 and NGC 3256) that are close to the boundary between Type A1 and Type A4 lie near the region where the 2 σ level contours of both of ETGs and LTGs overlap (Figure 4.9). UGC 6 has circumnuclear spiral structures seen in the optical (see Figure A.1), whereas the optical morphology of NGC 3256 is still strongly disturbed. It is difficult to statistically discuss the properties due to the small sample size, but a robust result is that they have the largest molecular gas disks ($R_{\rm ratio} \sim 2$). It is highly possible that these galaxies will evolve into LTGs, unless there are further mechanisms to transport the molecular gas toward the central region (e.g., nuclear bar; Bournaud & Combes, 2002) and decrease the size of the molecular gas disk.

- **Type A2: ETG or LTG candidates**

  14 % (5/37) of the MR sample are classified as Type A2, which has a low gas mass fraction (Log $f_{\rm gas} <$ -1.30) and an extended molecular gas disk (Log $R_{\rm ratio} >$ 0.215). The most distinct feature is that the two sources in our sample identified as AGNs (UGC 5101(e.g., Armus et al., 2007) and UGC 8058 (e.g, Lonsdale et al., 2003)) are both classified as this type. In the remaining sources, AGNs are not found, but they have high FIR luminosities (the median $L_{\rm FIR}$ = 11.41; Table 4.4), suggesting active starbursts. The depletion times of the molecular gas are short due to the high SFRs. Assuming that the molecular gas is used for star formation at the current rate, all of the molecular gas in the Type A2 sources except for Arp 230 will be consumed very quickly ($t_{\rm dep} \lesssim 5 \times 10^7$ Gyrs). However, it is possible that a large amount of cold gas settles on an extended gas disk by the return of ejected cold gas via tidal tails (Hibbard & Mihos, 1995) and also cold gas stream/accreation (Dekel et al., 2009).

  The other features of Type A2 sources are that (1) the Sérsic indices of 4/5 sources except for Arp 230 could not be determined by Rothberg & Joseph (2004), indicating strongly disturbed morphology or stellar profiles with a strong excess, (2) the distribution of the molecular gas shows ring-like structures (see the PV-diagrams in Appendix B), some of which may be starburst-rings (König et al., 2013) and (3) they have small C-parameters (the median C-parameter = 0.20 ; Table 4.4), suggesting that the molecular gas is not concentrated in central regions. It is notable that while starburst/AGN activity is taking place in Type A2 sources, they also possess extended molecular gas disks. This is inconsistent with results of numerical simulations (e.g., Mihos & Hernquist, 1996), which require the bulk of the gas to inflow and

concentrate in the central region for starburst/AGN activity to be triggered. Their properties contain possibilities that Type A2 become either ETGs or LTGs.

- **Type A3: ETG candidates**

  22 % (8/37) of the MR sample are classified as Type A3, which has a low gas mass fraction (Log $f_{\rm gas}$ $<$ -1.30) and a compact molecular gas disk (Log $R_{\rm ratio}$ $<$ 0.215). The most noticeable characteristic is that these MRs except for NGC 7727 do not occupy the same regions with either LTG or ETGs in Figure 4.9. If these MRs evolve into present-day ETGs or LTGs, they need to change their gas mass fractions or disk sizes. We expect that it is easy for these MRs to decrease gas mass fraction because their SFRs are high and thus the depletion times of the molecular gas are estimated to be short ($\sim$$10^8$ yr). This is comparable to the timescale of continuous active star formation, but it is shorter than the timescale for tidal features in merger to fade way (a few $\times$ 10^9 yrs). Therefore, the molecular gas reservoir is likely to be used up before the Type A3 sources evolve into ETG/LTGs.

  The other features of Type A3 sources are that (1) the Sérsic indices of most of the sources are 3 $\sim$ 4, which is similar to elliptical galaxies (n = 4), (2) they show large C-parameters (the median C-parameter = 0.43 ; Table 4.4), suggesting nuclear gas concentrations, and (3) they have high FIR luminosities (the median $L_{\rm FIR}$ = 11.35; Table 4.4), but show no presence of AGNs. Their K-band morphology are rather featureless and the Sérsic indices are determined with high confidence (Rothberg & Joseph, 2004). This suggest that the systems have undergone violent relaxation. Since the molecular gas is already concentrated in the nuclear regions as seen in ETGs (e.g., Crocker et al., 2011), it would be difficult to expand the sizes of the molecular gas disks significantly. Therefore, we suggest that Type A3 sources will move from right to left in Figure 4.9 and reach at the sequence of ETGs.

- **Type A4: ETG candidates**

  24 % (9/37) of the MR sample are classified as Type A4, which has a high gas mass fraction (Log $f_{\rm gas}$ $>$ -1.30) and a compact molecular gas disk (Log $R_{\rm ratio}$ $<$ 0.215). Type A4 sources share most of its properties with Type A3. Therefore we suggest that Type A4 sources will also become ETGs, decreasing the molecular gas mass by star formation.

  In addition, we suggest the possibility that two sources (Arp 187 and NGC 3597) will follow a different evolution path from the other sources in Type A4. These two sources have higher

molecular gas mass fraction ($f_{\rm gas}$ = 16 %) than the average of LTGs ($f_{\rm gas} \sim$ 11 %) and low FIR luminosity ($L_{\rm FIR} < 10^{11}$). Arp 187 shows the presence of an AGN activity according to the radio-to-FIR correlation. It is likely that they will move towards the Type A2 region where sources with AGNs are found. NGC 3597 shows a bar (+ spirals) structure in the CO integrated intensity map (Figure 2.2). A bar potential can be one of the mechanisms to trigger gas inflow into the nuclear regions (Bournaud & Combes, 2002). Thus we suggest that the gas mass fraction and disk size will quickly decrease, and it will move toward the lower-left from the present position in the Type-A4 region (Figure 4.9) and then it will follow the same evolution path as the other Type A4 and the Type A3 sources.

4.6.2 Type B: Unclassified

Galaxies in the type B is defined by the velocity field of the molecular gas disk which cannot be modeled by circular motion. 16 % (6/37) of the MR sample are classified as Type B. Their optical morphology shows clumpy structures, but the Sérsic indices were derived properly by Rothberg & Joseph (2004). The median of the stellar mass is about half of the other five types.

The distribution of the molecular gas is either clumpy or complex, and the gas mass fractions are not small compared to the other Types (Table 4.4). A possibility is that these sources are early in the merging process and the molecular gas has not settled in the galactic plane. However, this cannot explain the low stellar mass and the well-determined Sérsic indices, which suggest that the galaxy has experienced dynamical relaxation. These characteristics are not seen in either ETGs or LTGs, therefore the evolution path of Type B sources are not clear.

4.6.3 Type C: ETG candidates

According to our observations using interferometers, Type C sources were not detected in the CO line. 19 % (7/37) of the MR sample are classified as Type C. The 3 σ upper limit of the molecular gas mass are 2 $\times$ 10^{7-8} $M_{\odot}$, which are estimated using the integrated intensity maps with the velocity width of 300 $\rm km\ s^{-1}$. The upper limits of the gas mass fraction are less than 0.2 % (Log $f_{\rm gas} <$ -2.7), which is smaller than the average gas mass fraction of the ETGs. The Type C sources are gas-poor.

Their optical morphology is featureless and the median of the Sérsic indices is 4.12, which is similar to a typical elliptical galaxy (n = 4). The stellar masses of Type C are smaller by a few orders

of magnitude than that of typical supergiant elliptical galaxies (e.g., $M^* \sim 10^{13}$ $M_\odot$ in M87; Weil et al., 1997), which are thought to be formed by major mergers (Naab & Burkert, 2003). Type C has the lowest median of the FIR luminosities in six types and show no evidence of AGN activities. The star formation activity is quiescent (the median of SFR = 0.89; Table 4.4).

Since Type C share properties with ETGs, as the diffuse shells or ripples seen in the optical fade away, we suggest that Type C will evolve into ETGs.

4.7 Summary of the evolution of the merger remnants

In this chapter, we compared the properties of molecular gas and stellar components in the MRs with ETGs and LTGs and discussed the evolution of MRs based on the comparisons. The main motivation of this study is to investigate whether mergers can produce disk galaxies (i.e., LTGs), or mergers all result in spheroid dominated galaxies (i.e., ETGs). We expect MRs to show properties similar to ETG/LTGs, depending on which galaxy type they evolve into. **Overall, we suggest that 65 % of the MRs evolve into ETGs, 5 % into LTGs, 14 % into either ETG/LTGs, and 16 % into galaxies which cannot be classified into ETG or LTGs, including the non-detections.** The specific findings conclusions are as follows:

- The size of the molecular gas disks in MRs is similar to those in the ETGs rather than LTGs. This comparison suggests that more than 60 % of the MRs may evolve into ETGs. Even if 20 % of the MRs with extended gas disks may evolve into LTGs, they are not a significant fraction and furthermore requires a mechanism to expand the size of the molecular gas disk because both gas mass fractions and disk sizes of these MRs are still lower than the average values of the LTGs.

- The majority of the MRs have gas mass fractions of 1 – 10 %. The gas mass fractions of the LTGs are distributed around 10 %, whereas the gas mass fractions of the ETGs are distributed over a wide range between 0.1 % and 10 %. The K-S tests suggest that the distribution of the gas mass fraction are different among the three samples. However, it is suggested that the gas mass fractions between the MRs and a combined distribution of ETG/LTGs is not significantly different (P-value $\geq$ 0.174). These statistics are not inconsistent with the possibility that the MR includes progenitors of both ETGs and LTGs.

- From the comparison between the relative size of the molecular gas disk to the stellar spheroidal component and the gas mass fractions, the MRs do not follow either ETG nor LTG population on average. About one-third (7/24) of the MR sample, which lie between ETGs and LTGs populations in Figure 4.9, do not consume their molecular gas as much within 5×10^7 yrs compared to other MRs with comparable stellar mass. We suggest a scenario that they do not change their properties so much or will change their properties slowly toward the average properties of ETG/LTGs. In contrast, the majority of the sources spend a large amount of molecular gas for star formation, more quickly than the MRs which we mentioned above. The timescale is $\sim 10^8$ yr, which is shorter by an order of magnitude than the merger timescale (Mihos, 1999) or dynamical time of galaxies ($\sim 10^9$ yr).

- According to these analysis of MRs with the molecular gas disks, we suggest that 46 % (17/37; Type A3 + Type A4) of the MR sample will evolve into ETGs which is consistent with the scenario predicted from classical simulations (Toomre, 1977; Barnes & Hernquist, 1992; Naab & Burkert, 2003). In contrast, it is highly possible that 5 % (2/37; Type A1) of the MR sample will evolve into LTGs, unless there are further mechanisms to transport the molecular gas toward the central region (e.g., nuclear bar; Bournaud & Combes, 2002) to decrease the gas disk size. The remaining 14 % (5/37; Type A2) may become either ETGs or LTGs.

- For 16 % (6/37) of the MR sample whose velocity fields cannot be modeled with circular rotation, their clumpy morphology and complex gas structure leads us to speculate that they will evolve into irregular galaxies. In addition, since 19 % (7/37) of the MR sample undetected in the CO line share properties with ETGs, we suggest that they will evolve into ETGs earlier than the MRs with the molecular gas disks, in a time scale ($\sim 10^8$ yr) that is comparable for optical to fade away.

Table 4.4: Average Properties of the Merger Remnants in Different Types

Type	Type A1	Type A2	Type A3	Type A4	Type B	Type C
Number	(2)	(9)	(5)	(8)	(6)	(7)
Stellar Properties						
Morphology					clumpy	featureless
<Sérsic index>	2.17	1.56	3.41	3.03	2.34	4.12
No. (Sérsic n = 10)	1 (50 %)	4 (80 %)	2 (25 %)	1 (11 %)	1 (17 %)	0 (0 %)
<Log M^*> [$M_\odot$]	10.78	10.93	10.89	10.84	10.52	10.87
<$R_{\rm eff}$> [kpc]	1.18	0.38	3.11	2.96	3.58	4.75
Properties of Molecular Gas						
Gas Disk	Yes	Yes	Yes	Yes	No	···
No. (Gas Ring)	1 (50 %)	4 (80 %)	6 (75 %)	7 (78 %)	···	···
<R_{80}> [kpc]	2.04	1.55	1.21	1.47	1.70	···
<$R_{\rm ratio}$>	1.76	4.04	0.22	0.57	0.49	···
<A-parameter>	0.43	0.16	0.27	0.38	···	···
<C-parameter>	0.23	0.20	0.43	0.33	0.55	···
<Log $M_{\rm H_2}$> [$M_\odot$]	9.69	9.40	9.51	9.71	9.54	···
<$f_{\rm gas}$>	8.9 %	3.2 %	3.2 %	6.6 %	5.4 %	···
Star Formation and AGN Activity						
<Log $L_{\rm FIR}$ > [$L_\odot$]	11.21	11.41	11.35	10.80	10.29	9.71
<SFR> [$M_\odot$ yr^{-1}]	35.21	44.55	1.19	10.99	3.45	0.89
<$t_{\rm dep}$> [10^8 yr]	2.09	0.53	1.19	3.85	2.84	···
No. AGN	0 (0 %)	2 (40 %)	0 (0 %)	1 (11 %)	0 (0 %)	0 (0 %)

* Brackets show the median values.

Table 4.5: Properties of the Early-type Galaxies in the $\mathrm{ATLAS^{3D}}$ Sample

Name	Log $L_{\rm FIR}$ [$\mathrm{L_\odot}$]	Log M^* [$\mathrm{M_\odot}$]	Log $M_{\rm H_2}$ [$\mathrm{M_\odot}$]	Log $f_{\rm gas}$	$R_{\rm eff}$ [kpc]	R_{80} [kpc]	$R_{80}/R_{\rm eff}$
(1)	(2)	(3)	(4)	(5)	(6)	(7)	(8)
IC 676	9.70	9.92	8.63	-1.29	2.65	1.56 ± 0.22	0.58 ± 0.08
IC 719	9.41	10.09	8.26	-1.83	3.85	2.53 ± 0.28	1.41 ± 0.16
IC 1024	9.82	9.75	8.61	-1.14	1.12	2.05 ± 0.23	1.56 ± 0.17
NGC 524	9.10	10.89	7.97	-2.92	5.00	1.11 ± 0.16	0.23 ± 0.03
NGC 1222	10.52	10.09	9.07	-1.02	1.90	2.08 ± 0.30	1.02 ± 0.15
NGC 1266	10.45	10.18	9.28	-0.90	2.82	1.04 ± 0.35	0.35 ± 0.12
NGC 2764	10.22	10.29	9.19	-1.09	2.36	3.72 ± 0.34	1.58 ± 0.14
NGC 2768	8.80	10.89	7.64	-3.25	6.40	0.94 ± 0.13	0.14 ± 0.02
NGC 2824	9.68	10.18	8.65	-1.53	1.32	2.95 ± 0.42	2.06 ± 0.29
NGC 3032	9.41	9.81	8.41	-1.40	0.93	1.58 ± 0.32	1.16 ± 0.23
NGC 3182	9.24	10.29	8.33	-1.95	3.41	1.28 ± 0.43	0.37 ± 0.12
NGC 3489	< 8.73	10.21	7.20	-3.00	1.26	0.78 ± 0.09	0.61 ± 0.07
NGC 3607	< 9.28	10.91	8.42	-2.48	4.14	1.51 ± 0.30	0.36 ± 0.07
NGC 3619	9.09	10.44	8.28	-2.16	3.54	1.99 ± 0.28	0.58 ± 0.08
NGC 3626	9.17	10.33	8.21	-2.12	2.44	2.80 ± 0.19	1.15 ± 0.08
NGC 3665	9.89	10.98	8.91	-2.07	4.94	2.38 ± 0.34	0.48 ± 0.07
NGC 4119	8.68	10.05	7.88	-2.17	3.15	1.41 ± 0.20	0.44 ± 0.06
NGC 4150	8.79	9.67	7.82	-1.85	1.17	1.93 ± 0.28	1.88 ± 0.27
NGC 4324	8.69	10.05	8.79	-2.36	1.60	2.06 ± 0.19	1.29 ± 0.12
NGC 4429	< 9.02	10.74	8.05	-2.69	3.43	1.31 ± 0.19	0.39 ± 0.06
NGC 4435	9.22	10.54	7.87	-2.67	2.55	1.07 ± 0.21	0.43 ± 0.08
NGC 4459	9.16	10.57	8.24	-2.32	2.68	1.06 ± 0.35	0.37 ± 0.12
NGC 4476	8.79	9.72	8.05	-1.67	1.30	1.08 ± 0.36	0.80 ± 0.27
NGC 4477	8.64	10.51	7.54	-2.97	3.00	0.66 ± 0.13	0.21 ± 0.04
NGC 4526	9.47	10.86	8.59	-2.27	3.38	1.19 ± 0.17	0.34 ± 0.05
NGC 4550	< 8.97	9.92	< 7.24	< -2.68	1.15	0.89 ± 0.18	0.77 ± 0.15
NGC 4694	8.99	9.87	8.01	-1.86	2.35	2.95 ± 0.16	1.25 ± 0.07
NGC 4710	9.68	10.42	8.72	-1.70	2.51	2.02 ± 0.16	0.84 ± 0.07
NGC 4753	9.70	11.05	8.55	-2.49	5.48	2.01 ± 0.40	0.37 ± 0.07
NGC 5379	< 9.06	9.84	8.33	-1.51	3.04	3.41 ± 0.38	1.12 ± 0.13
NGC 5866	9.63	10.61	8.47	-2.14	2.63	1.69 ± 0.13	0.64 ± 0.05
NGC 6014	9.58	10.21	8.77	-1.43	3.83	1.89 ± 0.38	0.49 ± 0.10
NGC 7465	9.87	10.14	8.79	-1.35	0.95	5.16 ± 0.47	4.58 ± 0.42
PGC 29321	9.61	9.67	8.53	-1.14	1.53	1.14 ± 0.38	0.74 ± 0.25
PGC 58114	9.64	9.64	8.60	-1.04	1.07	1.75 ± 0.25	1.63 ± 0.23
UGC 5408	9.80	9.82	8.32	-1.50	1.53	0.51 ± 0.51	0.33 ± 0.33
UGC 6176	< 9.79	10.07	8.58	-1.49	2.00	1.71 ± 0.34	0.82 ± 0.16
UGC 9519	8.96	9.80	8.77	-1.03	0.90	1.66 ± 0.24	1.67 ± 0.24

NOTE.—Col.(1): Source name. Col.(2) The FIR luminosity. The luminosity is estimated using the IRAS catalog. Col.(3): The stellar mass The mass is estimated from the K-band magnitude (Rothberg & Joseph, 2004). Col.(4): The molecular gas mass estimated using the single-dish CO (1–0) data (Young et al., 2011). Col.(5): The gas mass fraction. This is a logarithm ratio of the molecular gas mass to the stellar mass. Col.(6): The K- (or J-, H-) band effective radius (Rothberg & Joseph, 2004). Col.(7): The radius enclosing 80 % of the total CO flux. Col.(8): The ratio between R_{80} and $R_{\rm eff}$.

Table 4.6: Properties of the Late-type Galaxies in the BIMA SONG Sample (1)

Name	Log $L_{\rm FIR}$ [$L_\odot$]	Log M^* [$M_\odot$]	Log $M_{\rm H_2}$ [$M_\odot$]	Log $f_{\rm gas}$
(1)	(2)	(3)	(4)	(5)
NGC 0628	8.77	10.00	9.54 ± 0.45	-1.02
NGC 1068	10.97	11.01	100 ± 1	-1.01
IC 342	9.59	10.43	...	...
NGC 2903	9.65	10.20	15.3 ± 1.4	-1.01
NGC 3184	9.01	10.00	< 6.81	$<$ -1.17
NGC 3351	9.71	10.35	18.32 ± 2.73	-1.09
NGC 3368	9.57	10.58	< 18.0	$<$ -1.33
NGC 3521	9.76	10.41	29.5 ± 2.1	-0.94
NGC 3627	10.18	10.75	62.4 ± 6.2	-0.95
NGC 3938	9.84	10.35	31.7 ± 2.6	-0.85
NGC 4051	9.89	10.40	...	...
NGC 4258	9.39	10.64	20.9 ± 2.0	-1.32
NGC 4303	10.26	10.64	66.6 ± 3.9	-0.81
NGC 4321	10.23	10.79	91.5 ± 9.8	-0.83
NGC 4414	10.49	10.79	106 ± 12	-0.77
NGC 4535	9.82	10.47	< 35.3	$<$ -0.92
NGC 4569	9.89	10.83	36.8 ± 4.5	-1.26
NGC 4579	9.73	10.87	< 35.9	$<$ -1.31
NGC 4736	9.46	10.24	3.63 ± 0.45	-1.68
NGC 4826	9.26	10.10	5.75 ± 0.30	-1.34
NGC 5005	10.49	11.09	68.9 ± 26.0	-1.25
NGC 5033	10.24	10.77	103 ± 11	-0.76
NGC 5055	9.75	10.48	23.5 ± 1.7	-1.11
NGC 5194	9.88	10.59	71.2 ± 1.8	-0.73
NGC 5248	10.16	10.82	112 ± 12	-0.64
NGC 5247	10.46	10.69	64.5 ± 5.3	-1.01
NGC 5457	9.15	10.54	22.6 ± 1.7	-1.19
NGC 6946	9.70	10.34	33.3 ± 0.9	-0.82
NGC 7331	10.30	10.96	$74.8. \pm 10.0$	1.08

NOTE.—Col.(1): Source name. Col.(2) The FIR luminosity. The luminosity is estimated using the IRAS catalogs. Col.(3): The stellar mass. The mass is estimated using the 2MASS catalog (Jarrett et al., 2003). Col.(4): The molecular gas mass estimated using the single-dish CO (1–0) data (Helfer et al., 2003). Col.(5): The gas mass fraction. This is a logarithm ratio of the molecular gas mass to the stellar mass.

Table 4.7: Properties of the Late-type Galaxies in the BIMA SONG Sample (2)

Name	$R_{\rm eff}$ [kpc]	$R_{\rm bulge}$ [kpc]	R_{80} [kpc]	$R_{80}/R_{\rm eff}$	$R_{80}/R_{\rm bulge}$
(1)	(2)	(3)	(4)	(5)	(6)
NGC 0628	5.00	0.59	3.09 ± 0.05	0.62 ± 0.01	5.20 ± 0.09
NGC 1068	2.31	···	3.06 ± 0.12	1.33 ± 0.05	···
IC 342	7.38[a]	···	1.43 ± 0.03	0.19 ± 0.01	···
NGC 2903	2.60	0.26	2.55 ± 0.05	0.98 ± 0.02	9.93 ± 0.19
NGC 3184	5.19	0.28	3.35 ± 0.06	0.65 ± 0.01	12.1 ± 0.2
NGC 3351	3.55	0.70	3.72 ± 0.08	1.05 ± 0.02	5.28 ± 0.11
NGC 3368	3.42	1.58	4.27 ± 0.08	1.25 ± 0.02	2.69 ± 0.05
NGC 3521	2.10	0.42	2.88 ± 0.06	1.37 ± 0.03	6.82 ± 0.14
NGC 3627	4.27	0.63	6.68 ± 0.09	1.56 ± 0.02	10.6 ± 0.1
NGC 3938	5.97	0.56	4.94 ± 0.12	0.83 ± 0.02	8.81 ± 0.21
NGC 4051	6.70	···	3.45 ± 0.11	0.52 ± 0.02	···
NGC 4258	5.06	0.79	2.21 ± 0.06	0.44 ± 0.01	2.78 ± 0.07
NGC 4303	5.85	0.49	5.09 ± 0.12	0.87 ± 0.02	10.5 ± 0.2
NGC 4321	9.17	1.25	5.97 ± 0.12	0.65 ± 0.01	4.78 ± 0.09
NGC 4414	3.06	0.43	8.72 ± 0.13	2.85 ± 0.04	20.5 ± 0.3
NGC 4535	7.40	0.41	6.37 ± 0.13	0.86 ± 0.02	15.5 ± 0.3
NGC 4569	7.26	0.72	4.98 ± 0.12	0.69 ± 0.02	6.88 ± 0.17
NGC 4579	5.26	1.55	1.39 ± 0.15	0.26 ± 0.03	0.89 ± 0.10
NGC 4736	0.95	0.33	1.31 ± 0.03	1.37 ± 0.03	4.03 ± 0.09
NGC 4826	1.65	0.59	0.96 ± 0.03	0.58 ± 0.02	1.63 ± 0.05
NGC 5005	4.40	0.87	4.17 ± 0.16	0.95 ± 0.04	4.81 ± 0.18
NGC 5033	5.59	2.67	4.35 ± 0.13	0.78 ± 0.02	1.63 ± 0.05
NGC 5055	3.65	0.77	3.28 ± 0.05	0.90 ± 0.01	4.26 ± 0.06
NGC 5194	4.92	0.75	4.35 ± 0.05	0.88 ± 0.01	5.82 ± 0.07
NGC 5248	7.10	1.87	4.05 ± 0.18	0.57 ± 0.02	2.16 ± 0.09
NGC 5247	10.9[a]	1.08	5.95 ± 0.18	0.55 ± 0.02	5.53 ± 0.19
NGC 5457	11.3	0.56	2.87 ± 0.21	0.25 ± 0.01	5.10 ± 0.09
NGC 6946	5.18[a]	0.27	2.73 ± 0.05	0.53 ± 0.01	10.3 ± 0.1
NGC 7331	4.48	···	5.03 ± 0.04	1.12 ± 0.02	···

NOTE.—Col.(1): Source name. Col.(2): The K- (or J-, H-) band effective radius (Cappellari et al., 2011). Col.(3): The bulge size defined as a raids at which the bulge surface brightness equals that of the disk (Fisher et al., 2013). Col.(4): The radius enclosing 80 % of the total CO flux. Col.(5): The ratio between R_{80} and $R_{\rm eff}$. Col.(6): The ratio between R_{80} and $R_{\rm bulge}$.

Chapter 5

Summary and Future Prospects

5.1 Summary

Galaxies is one of the primary components of our observable Universe, and thus revealing the evolution and formation of galaxies is one of the biggest frontiers in understanding our Universe. Since Edwin Hubble discovered LTGs in the first half of the 19th century, the formation mechanism of LTGs, which comprise more than half of all galaxies, has been studied in detail. After half a century of Hubble's discovery, recent numerical simulations have shown that LTGs can form through galaxy mergers. The observational confirmation of this scenario had yet to come.

We have conducted a CO imaging survey of merger remnants (MRs) in the local Universe using millimeter/submillimeter interferometers including ALMA, SMA, and CARMA, and the NRO 45 m single-dish telescope in order to understand the properties of molecular gas and to investigate the evolution of MRs. This study is based on the largest systematic CO imaging survey of MRs to date, enabling, for the first time, a statistical analysis of molecular gas at their final stage of coalescence.

We have revealed, observationally, that merging events in the local Universe are indeed the crossroads of galaxy evolution, reprocessing the otherwise slowly evolving galaxies into a mixture of types including ETGs and LTGs. This result has enormous significance in understanding the evolution of galaxies via galaxy mergers. Furthermore, this study opens up the door to additional studies, for example comparative studies with numerical simulations, and observations of the diffuse gas to confirm the returning of the ejected cold gas via tidal tails and cold gas stream/accretion. Future studies should also be targeted toward high-z galaxies to understand the history of galaxy formation.

This thesis started out by addressing five main questions, each of which were investigated in detail in Chapters 2 – 4. Main conclusions are as follows:

- **What is the distribution and kinematics of cold molecular gas in merger remnants?**
  We investigate interferometric CO maps of 37 optically-selected MRs, including seven sources which were undetected in the CO line. Twenty seven of these galaxies were newly obtained, and 10 are archival data. By fitting the CO velocity field with circular motion, we find that 65 % (24/37) of the sample show kinematical signatures of a rotating molecular gas disk. The sizes of these disks vary significantly from 1.1 kpc to 9.3 kpc. We also find that the emission peaks are clearly shifted from the galactic centers in 75 % (18/24) of the sources with gas disks, suggesting the presence of a ring and/or a bar. We were unable to fit the CO velocity field of other six sources with circular motion. These sources show clumpy distribution and complex velocity fields, indicating that the molecular gas is still strongly disturbed and has not settled. in the galactic plane.

- **Are extended cold molecular gas disks formed in merger remnants, as predicted from recent numerical simulations?**
  We compare the size of the molecular gas disk to the stellar spheroidal component for 24 MRs with CO detection. The size ratios ($R_{\rm eff}$) of the gas disk to the stellar component for 54 % (13/24) of the MRs are less than unity. Six MRs which are bright at infrared wavelengths have compact molecular gas disks, which may have formed by past gas inflow that was triggered by dynamical instability following the merging. On the other hand, **46 % (11/24) of the MRs have gas disks which are extended relative to the stellar component**. We also discover a possible positive correlation between $R_{\rm ratio}$ and the total far-infrared luminosity. This suggests that the physical activities that are responsible for increasing luminosity, namely starburst/AGN, are related to the formation of the extended molecular gas disks. The molecular gas disks in the MRs show various properties, and we conclude that our sample includes MRs at different stages of their evolution, progenitors of galaxies with different characteristics, or different initial conditions.

- **Are the properties of the molecular gas in merger remnants different from early-type and late-type galaxies?**

  The size of the molecular gas disks in MRs is similar to those in the ETGs rather than LTGs. The ratio of molecular gas mass to stellar mass, the gas mass fraction, is found to be in the range 1 – 10 % for MRs. The gas mass fractions of the LTGs are distributed around 10 %, whereas the gas mass fractions of the ETGs are distributed over a wide range between 0.1 % and 10 %. A Kolmogorov-Smirnov test suggests that the distribution of the gas mass fractions are different among the three samples. When the gas mass fractions of ETG/LTGs are combined, however, the MRs are not significantly different. These statistics are not inconsistent with the possibility that the MRs include progenitors of both ETGs and LTGs. In a diagram plotting $R_{\rm ratio}$ versus the gas mass fraction, the distribution of MRs does not overlap with either the ETG or the LTG population. In short, **the molecular gas in MRs is on average similar to ETGs in terms of its disk size, but the MRs are in fact a distinct population with respect to their relation between size and mass relative to the stellar component**.

- **What type of galaxies do merger remnants evolve into?**

  From comparisons of the MRs with ETGs and LTGs regarding their molecular gas and stellar components, **overall, our conclusion is that 65 % of the MRs evolve into ETGs, 5 % into LTGs, 14 % into either ETG/LTGs, and 16 % into galaxies which cannot be classified into ETG/LTGs**. Among the sources with observational signatures of molecular gas disks, we conclude that sources with a compact molecular gas disk will become ETGs regardless of the gas mass fraction, mainly because of the short depletion time of the molecular gas ($\sim 10^8$ yr), and high gas concentration in the nuclear region. On the other hand, we find that sources with an extended molecular gas disk and a large gas mass fraction are likely to result in LTGs, unless there are further mechanisms which transport the molecular gas toward the central region (e.g., nuclear bar) thereby decreasing the disk size. Confirming the evolution path of the sources with an extended molecular gas disk and a low gas mass fraction requires further studies to investigate whether a large amount of cold gas will settle on the extended gas disks by the returning of the ejected cold gas via tidal tails and cold gas accretion. For six MRs whose velocity fields cannot be modeled with circular rotation, their clumpy morphology and complex gas structure

are not seen in either ETG/LTGs. The seven MRs which were not detected in CO will evolve into ETGs earlier than the MRs with the molecular gas disks. This study confirms, observationally, a new scenario that merging events are the crossroads of galaxy evolution, reprocessing them into a mixture of types including ETGs and LTGs.

Finally, we suggest two possibilities. One possibility is that returning the ejected cold gas via tidal tail might be a key to determine the evolution of MRs. The other is that large scale gas inflow is not the only scenario for the triggering of AGN/starburst activity, revealed by the presence of a population of MR with an extended molecular gas disk and AGN/starburst existing together.

5.2 Future Prospects: What's next?

This study is the first step in our series of studies which emphasize the cold molecular gas in MRs, instead of the stellar component which has been the focus of previous studies. We find new insights into the evolution of galaxies via galaxy mergers. There are remaining questions, and additional studies are necessary to completely understand the indications of this thesis study.

- **Where is the location of the star forming region in the extended molecular gas disk?**
  We find clearly extended molecular gas disks in the MRs, while the reformation of an extended disk is a prediction of recent merger simulations. However, we do not know whether the stellar disks will be are formed subsequently from the gas disks. In order to answer this question, we need to know where the star forming regions are located. Are the star forming regions located in the nucleus, throughout the extended disk, or both? To investigate this, we need to image the MRs in dense gas, using HCN/HCO^+ or a higher J transition of CO to compare to the low J emission, i.e., the CO (1–0) line. We will identify where warm and dense gas is distributed in the molecular disk, in other words, regions directly related to star formation. It is important to obtain both the diffuse gas and dense gas for investigating the spatial variation in the excitation or physical conditions as was demonstrated by us using the SMA data of the intermediate-stage merger Antennae galaxies (Ueda et al., 2012). Alternatively, we need new data of star forming tracers in optical/NIR. High-quality optical/NIR imaging can provide the

information of star forming region. Identifying star forming regions in extended molecular gas disk and revealing disk-dominated star formation can strengthen the scenario that mergers will evolve into disk-dominated disk galaxies.

- **Is it possible to expand the sizes of the gas disks by returning ejected cold gas?**
  We find five MRs (Type A2) with extended molecular gas disks and low gas mass fractions. These galaxies either need to acquire gas mass in order to become comparable to LTGs, or decrease the size of its molecular disk to become comparable to ETGs. Confirming the evolution of these MRs, therefore, requires further studies to investigate whether a large amount of cold gas will settle on the extended gas disks by the returning of the ejected diffuse gas via tidal tails and cold gas stream/accretion. The neutral hydrogen (HI) gas is a good tracer of such gas.

  The optically thin HI gas is one of the major components of the ISM in gas-rich galaxies. In our Galaxy, it constitutes about a half of the total gas mass of the ISM. The HI gas traces the loosely bound diffuse extended gas ($n \sim 1$ cm $^{-3}$) and is mainly distributed in the outskirts of the disk. Therefore the HI data allows us to examine the global structure of galaxies, including the properties at the outer regions where the density of the medium is too diffuse for molecular gas to exist. In addition, it is known that tidal interaction can strongly influence the HI distribution and kinematics (Yun et al., 1994), more so than the CO gas which is usually more centrally concentrated (Iono et al., 2004), and traces the higher density (> 10 cm^{-3}) regions.

  Extended gas disks may form by the return of the tidally ejected material (Davis et al., 2011). We will search for kinematic signatures of large-scale infall of the tidally ejected HI gas and examine whether the HI and CO velocity fields share similar structures. If the MRs have HI disks, we will investigate whether the kinematical axis between the HI and CO disks are consistent. If the two alignments are consistent, this suggests the internal origin of the HI disk. On the other hand, if the kinematical axis are misaligned, the HI gas can be of external origin, i.e., infalling gas. We will also estimate the gas mass fraction including the atomic gas for the merger remnants. If kinematic signatures of infall are found, we will additionally investigate whether the infalling HI is massive enough to turn the galaxy into a typical LTG. If the gas mass fraction including the prospective HI is comparable to the gas mass fraction of LTGs, the MR may evolve into LTGs.

Appendix A

Channel Maps

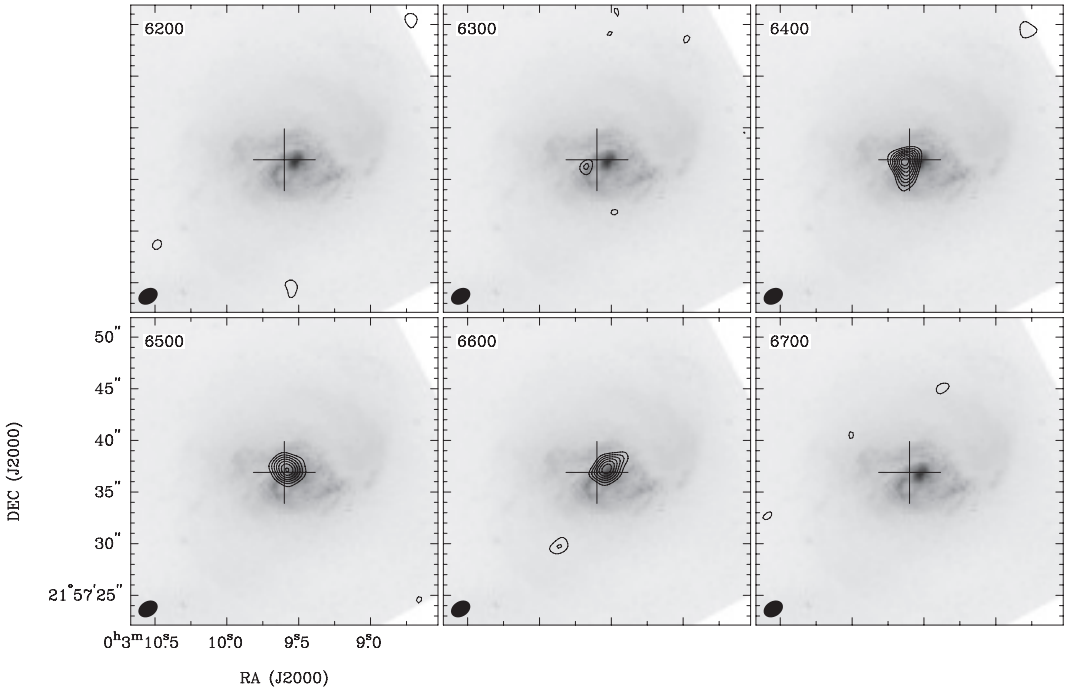

Figure A.1: Channel maps of UGC 6. The plus sign shows the galactic center defined by the K-band image (Rothberg & Joseph, 2004). The contours are 3.37 mJy beam^{-1} $\times$ (3, 4, 5, 6, 7, 8, 9, 10). The background image is the HST/WFPC2 V-band image.

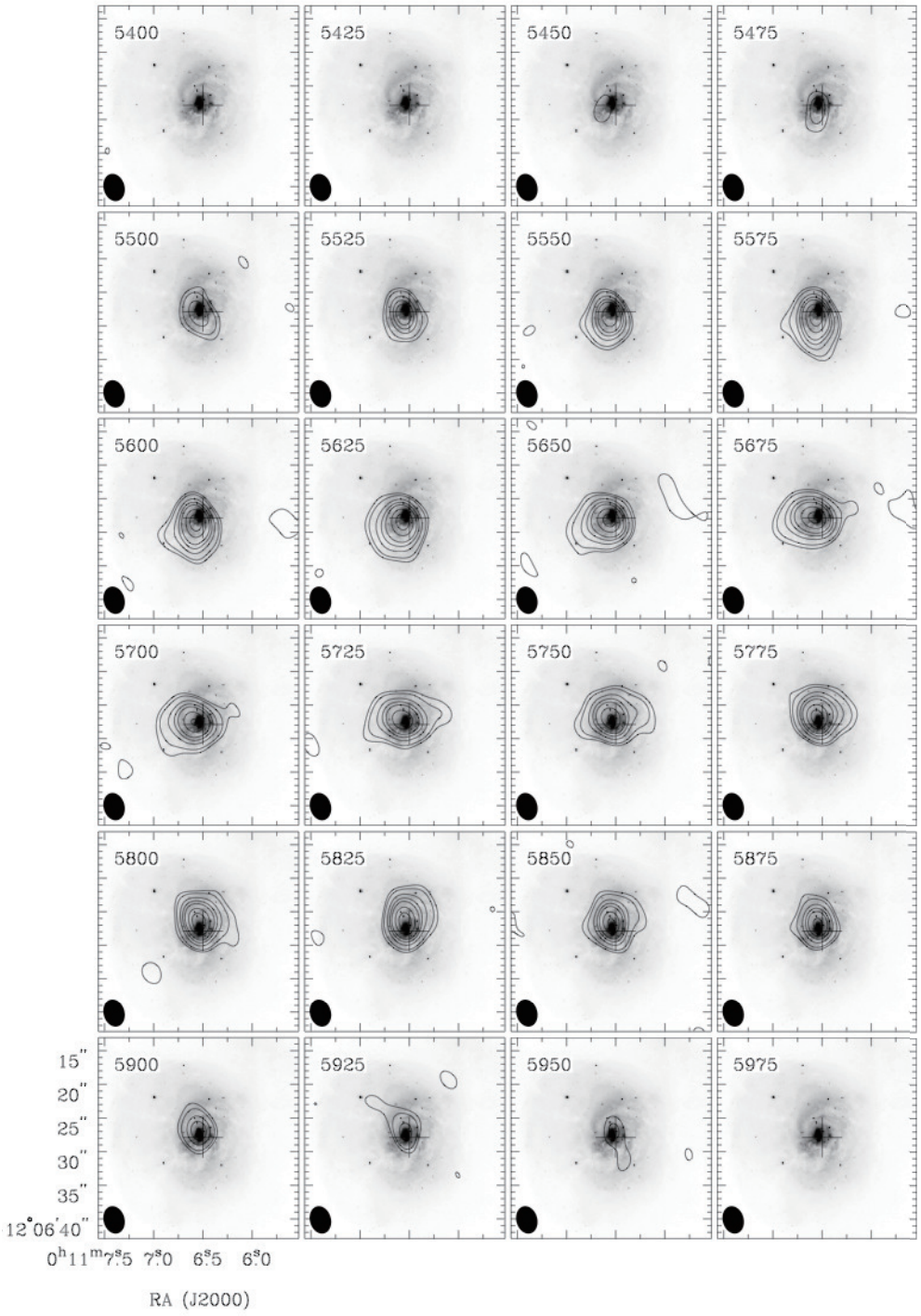

Figure A.2: Same as Figure A.1, but NGC 34. The contours are 14.8 mJy beam^{-1} $\times$ (3, 5, 10, 15, 20, 30, 40). The background image is the HST/ACS B-band image.

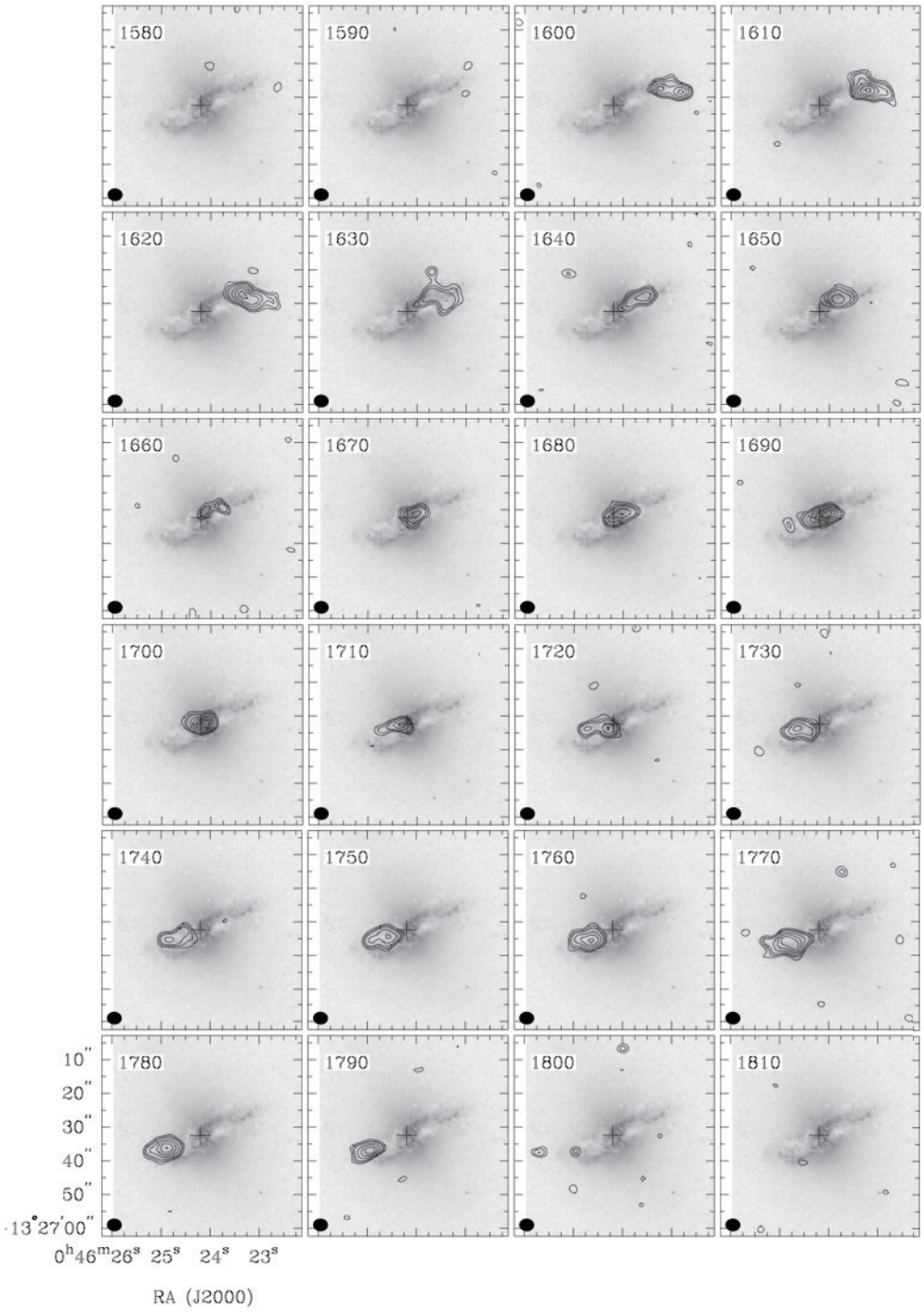

Figure A.3: Same as Figure A.1, but Arp 230. The contours are 4.12 mJy beam^{-1} $\times$ (3, 4, 5, 7, 9, 11, 13). The background image is the HST/WFPC2 V-band image.

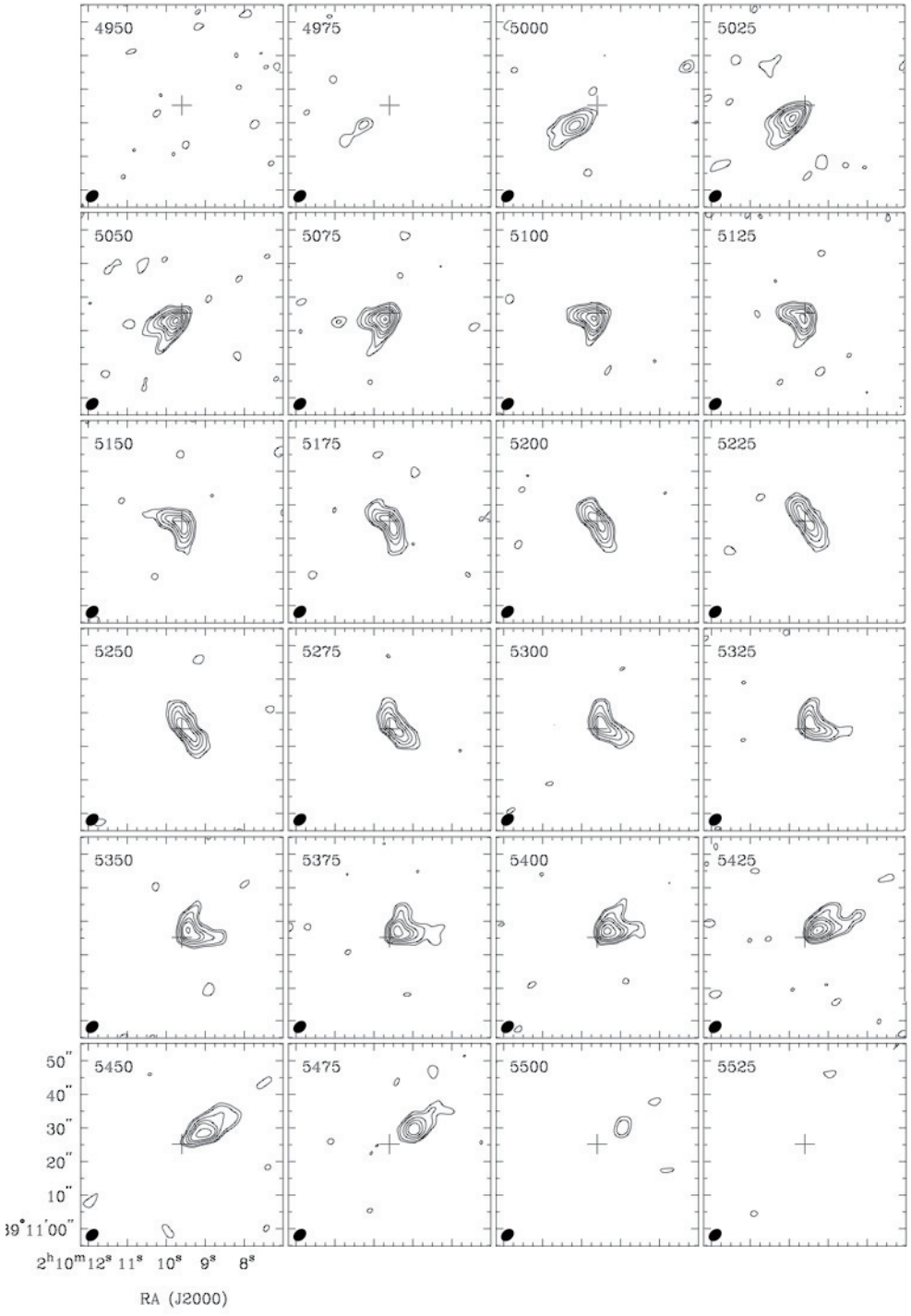

Figure A.4: Same as Figure A.1, but NGC 828. The contours are 22.1 mJy beam^{-1} $\times$ (3, 5, 10, 15, 20, 30, 40, 50).

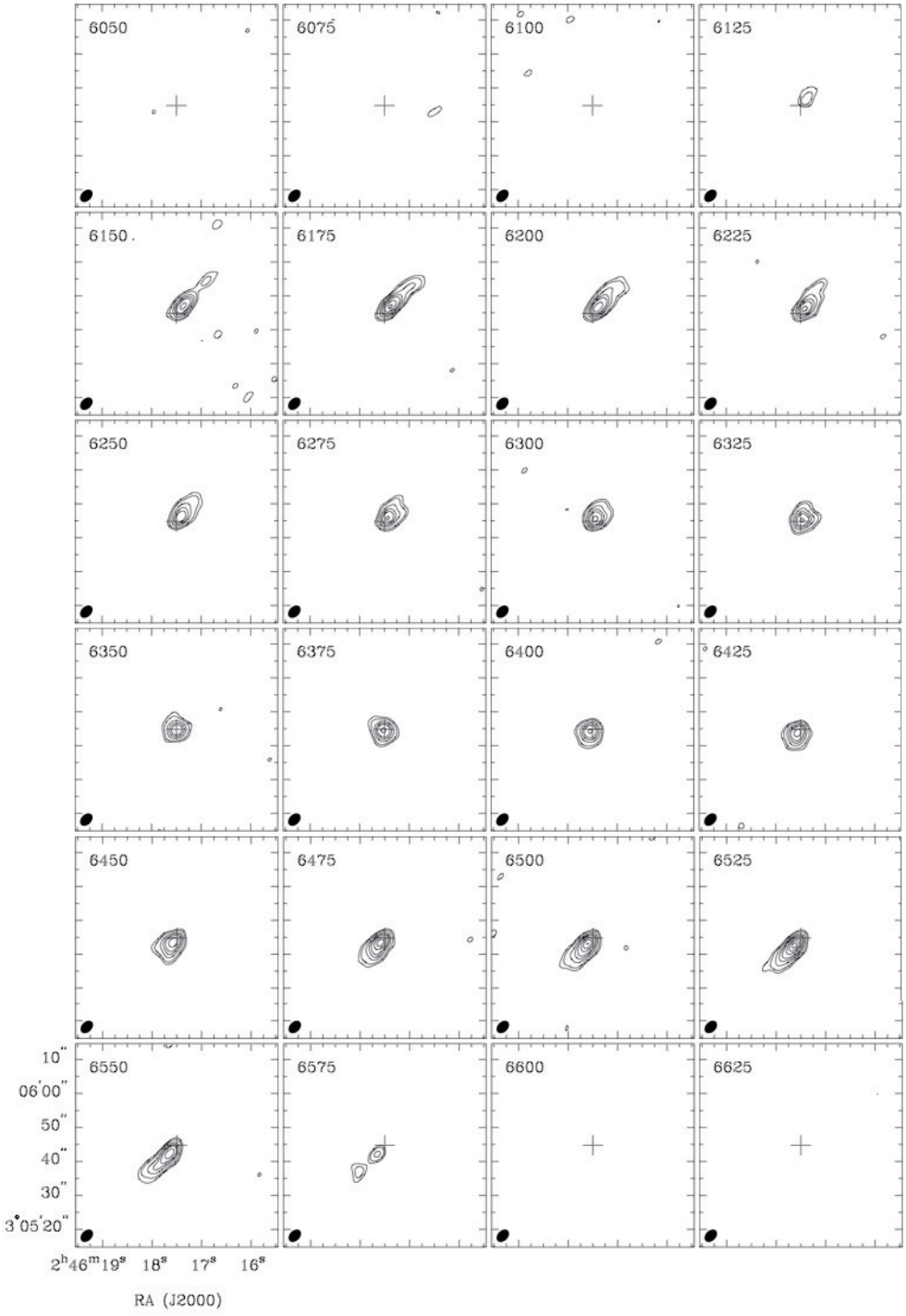

Figure A.5: Same as Figure A.1, but UGC 2238. The contours are 17.7 mJy beam^{-1} $\times$ (3, 5, 10, 15, 20, 30, 40, 50).

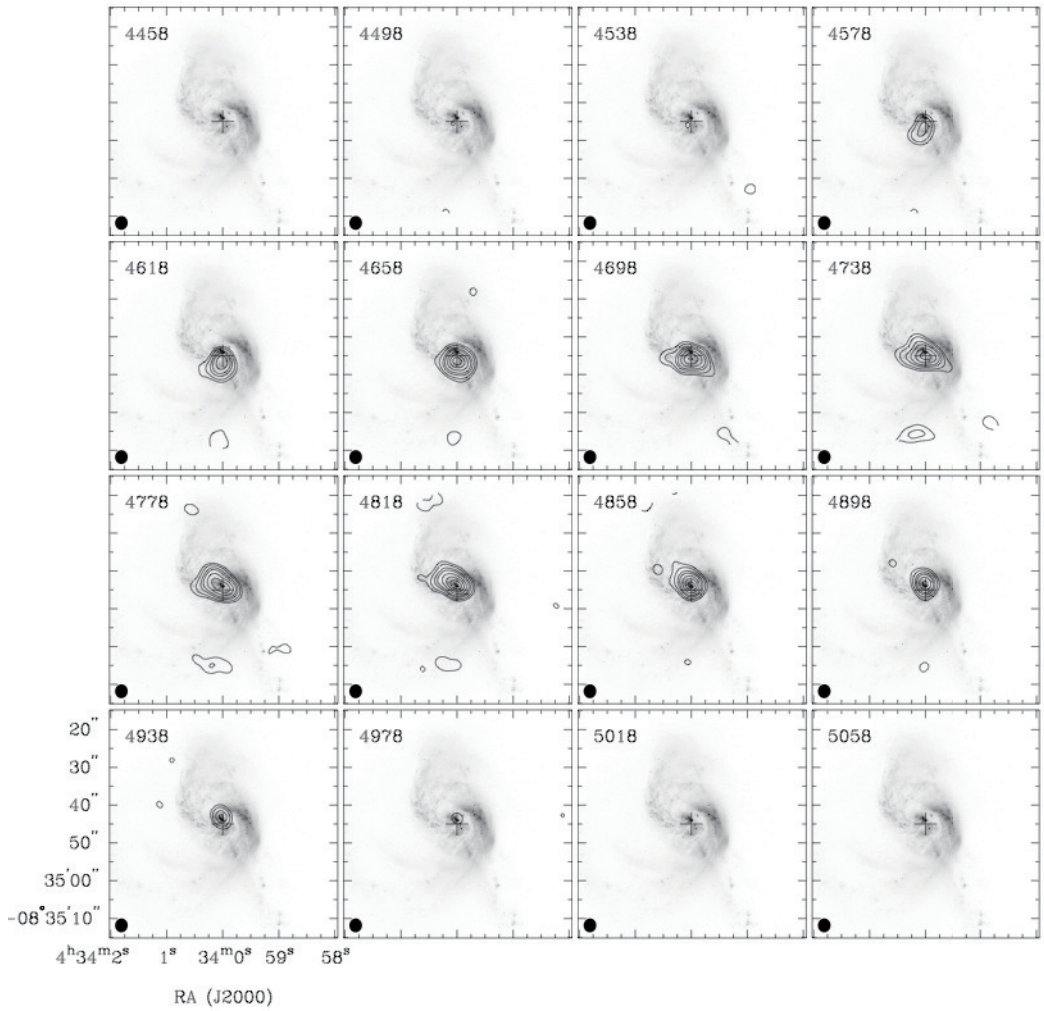

Figure A.6: Same as Figure A.1, but NGC 1614. The contours are 11.2 mJy beam^{-1} $\times$ (5, 10, 20, 30, 50, 75, 100). The background image is the HST/ACS B-band image.

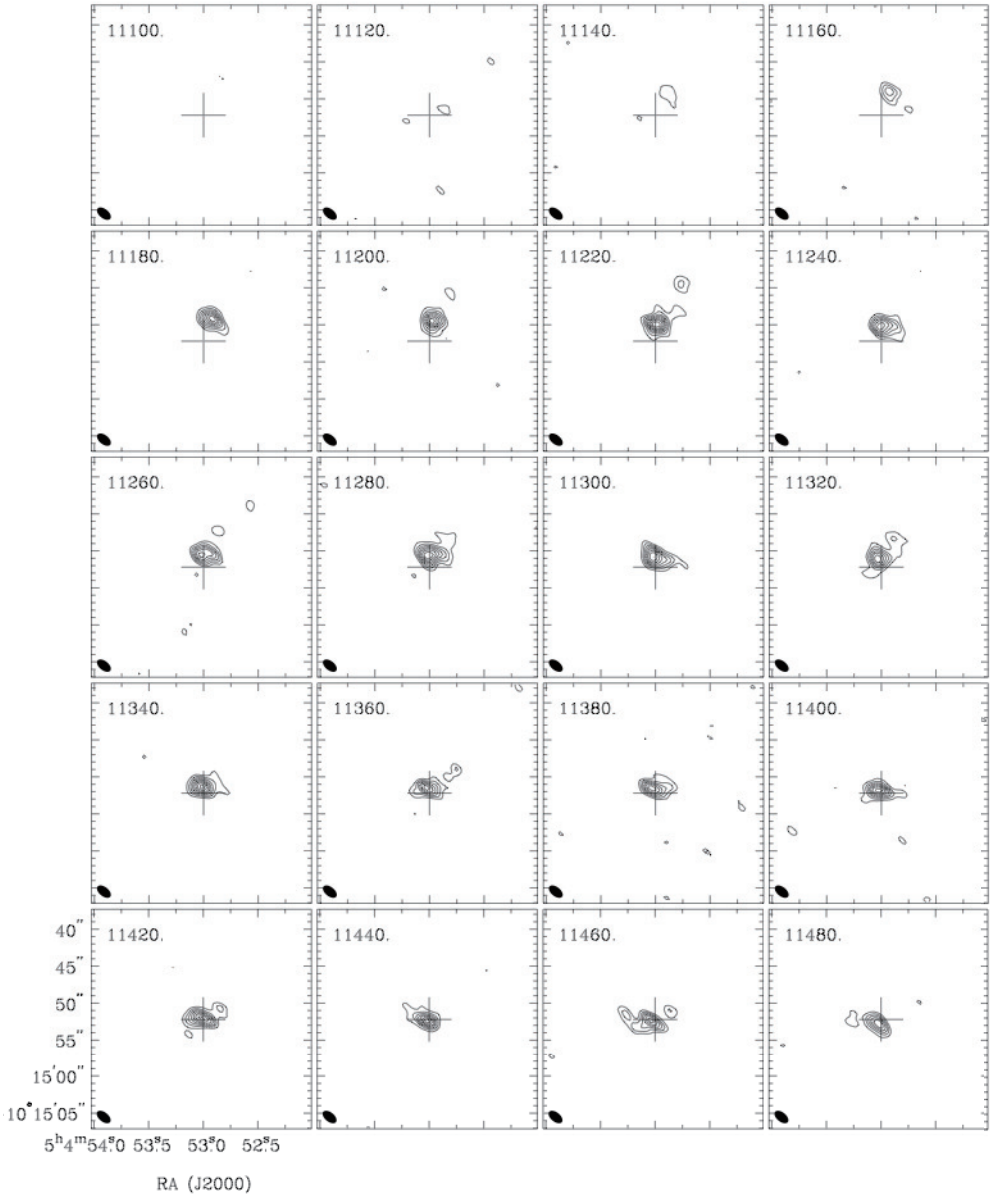

Figure A.7: Same as Figure A.1, but Arp 187. The contours are 2.52 mJy beam^{-1} $\times$ (3, 5, 7, 9, 11, 13, 15, 17).

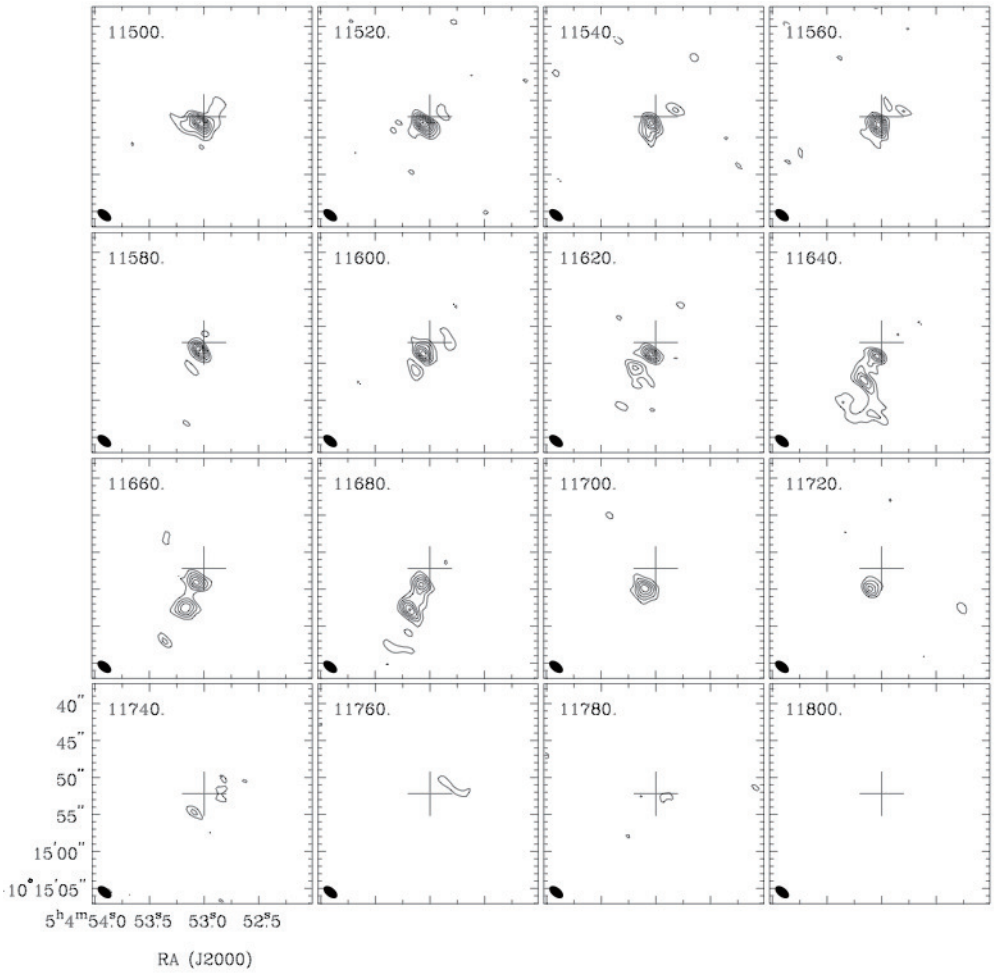

Figure A.7: (Continued.) Same as Figure A.1, but Arp 187. The contours are 2.52 mJy beam^{-1} $\times$ (3, 4, 5, 7, 9, 11, 13, 15, 17).

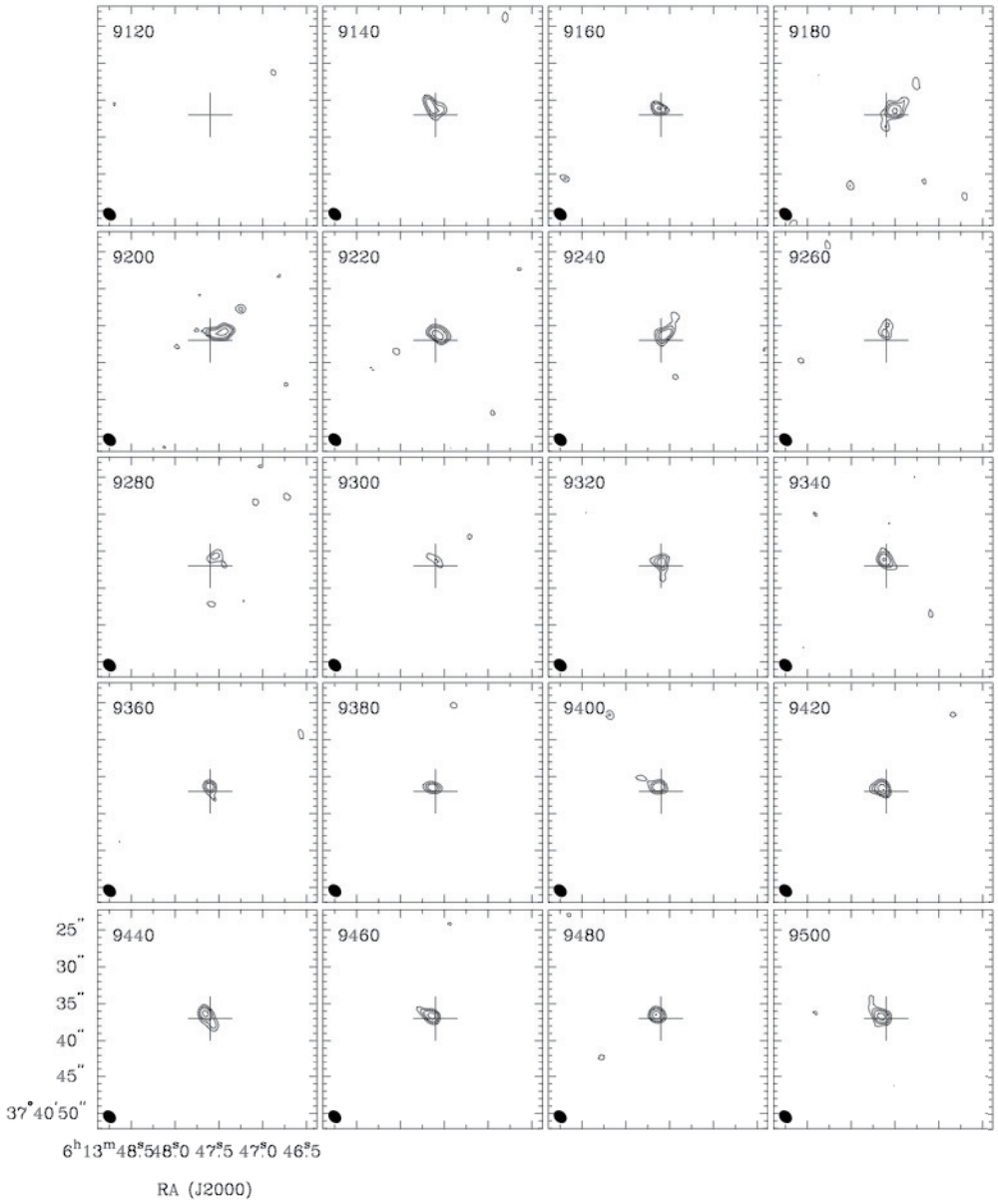

Figure A.8: Same as Figure A.1, but AM 0612-373. The contours are 2.83 mJy beam^{-1} $\times$ (3, 4, 5, 7, 9, 11, 13).

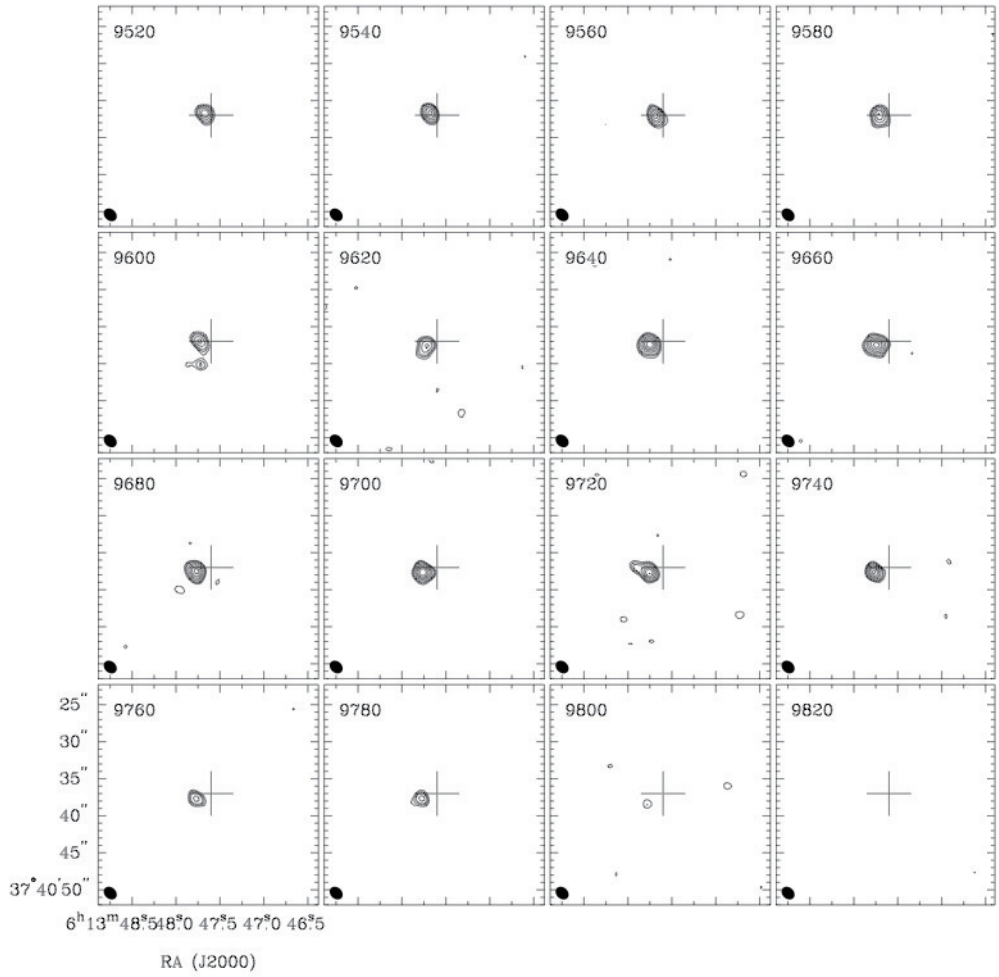

Figure A.8: (Continued.) Same as Figure A.1, but AM 0612-373. The contours are 2.83 mJy beam^{-1} $\times$ (3, 4, 5, 7, 9, 11, 13).

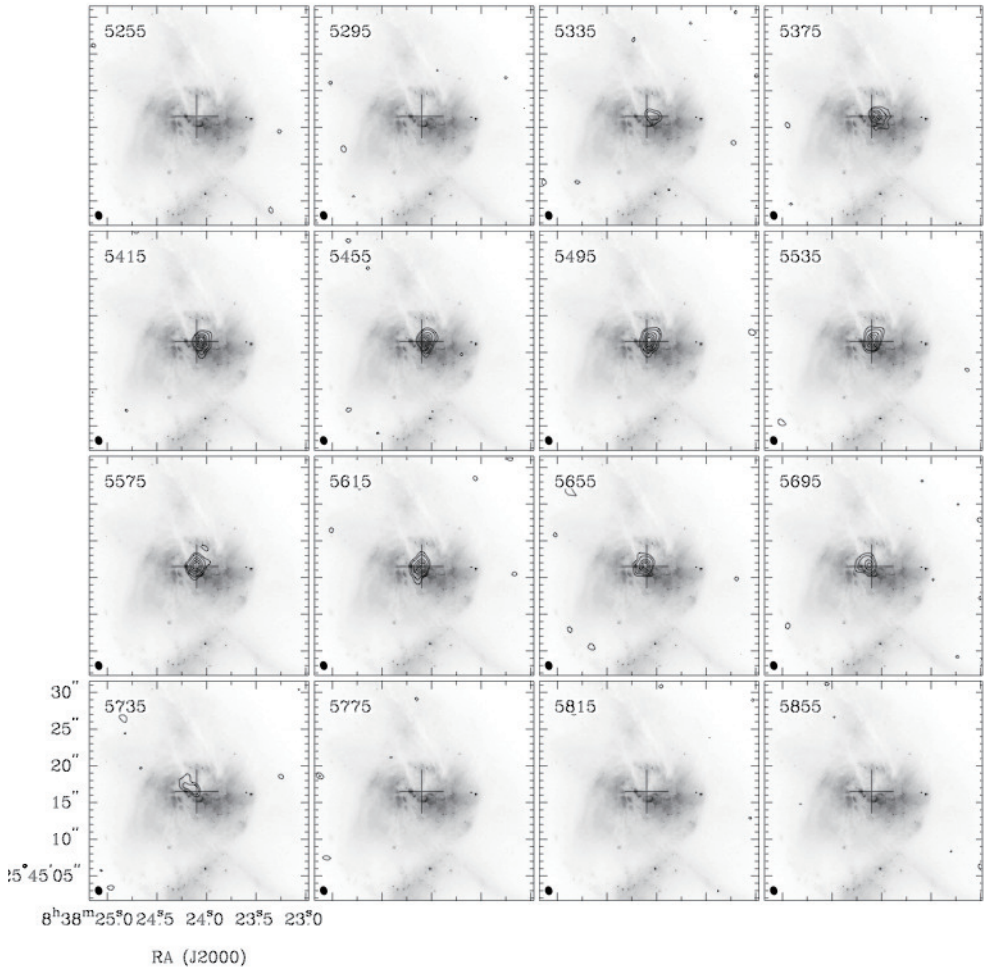

Figure A.9: Same as Figure A.1, but NGC 2623. The contours are 11.6 mJy beam^{-1} $\times$ (3, 5, 10, 15, 20, 25, 30). The background image is the HST/ACS B-band image.

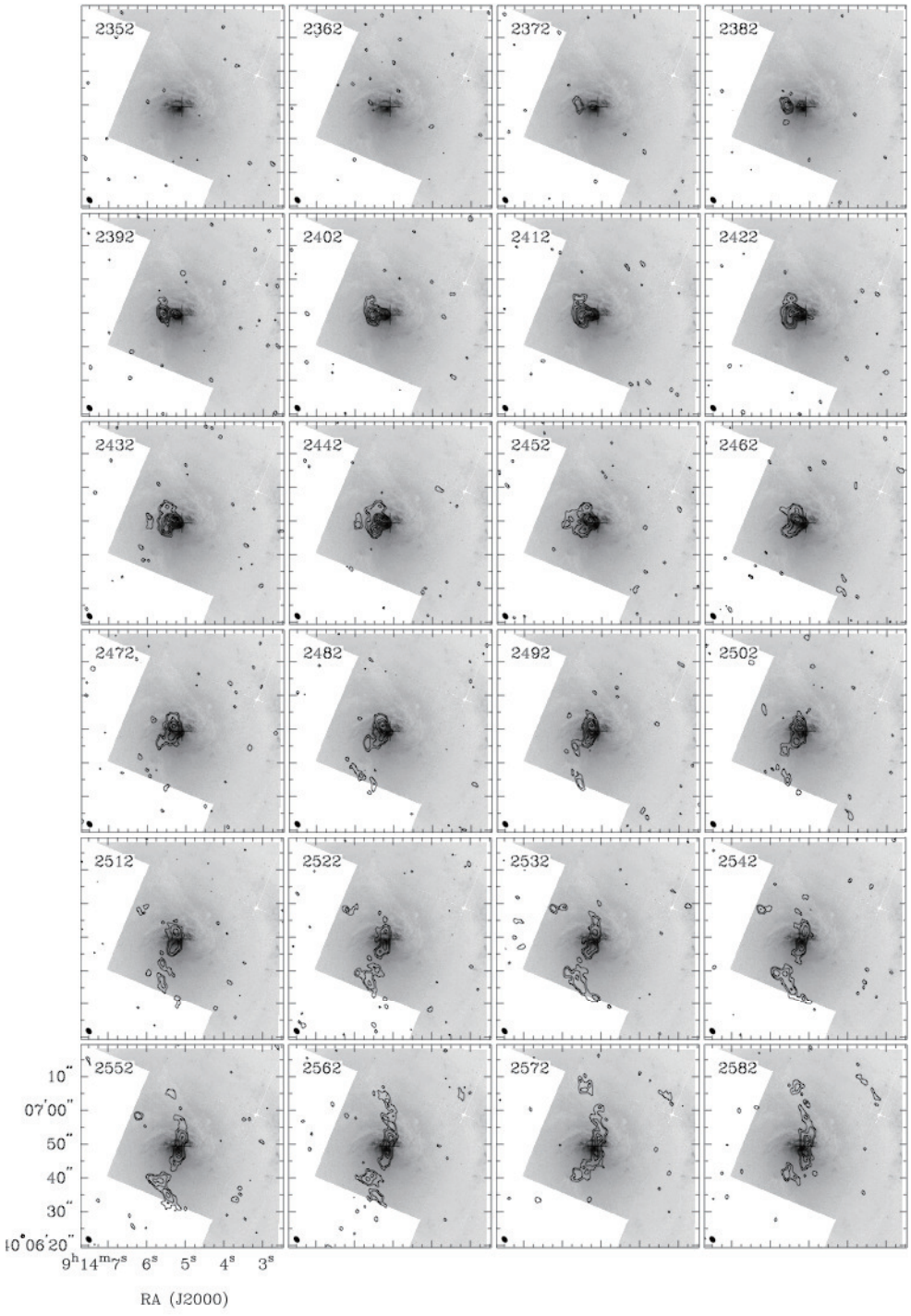

Figure A.10: Same as Figure A.1, but NGC 2782. The contours are 1.94 mJy beam^{-1} $\times$ (3, 5, 10, 15, 20, 30, 40, 50). The background image is the HST/WFPC2 V-band image.

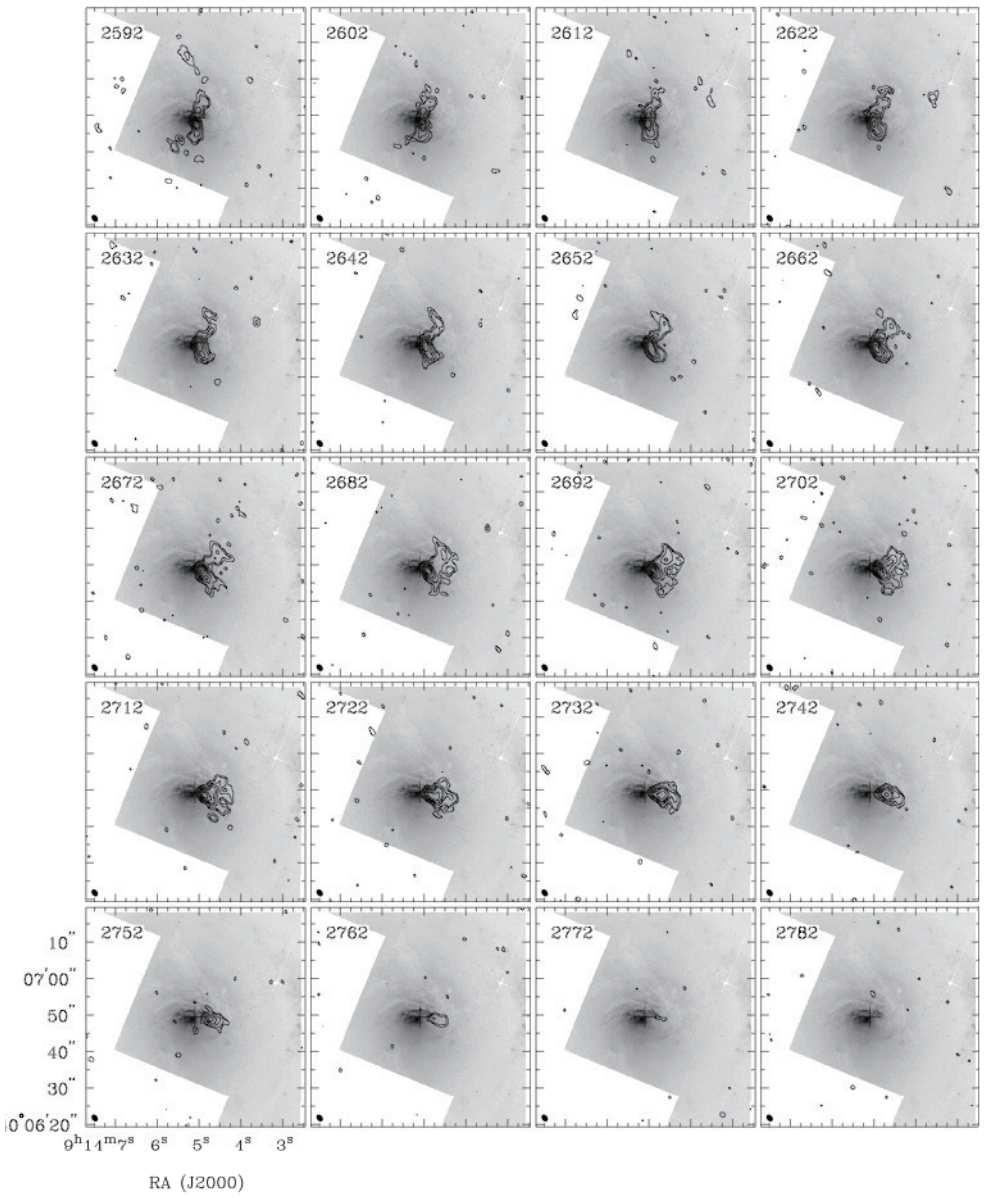

Figure A.10: (Continued.) Same as Figure A.1, but NGC 2782. The contours are 1.94 mJy beam^{-1} $\times$ (3, 5, 10, 15, 20, 30, 40, 50). The background image is the HST/WFPC2 V-band image.

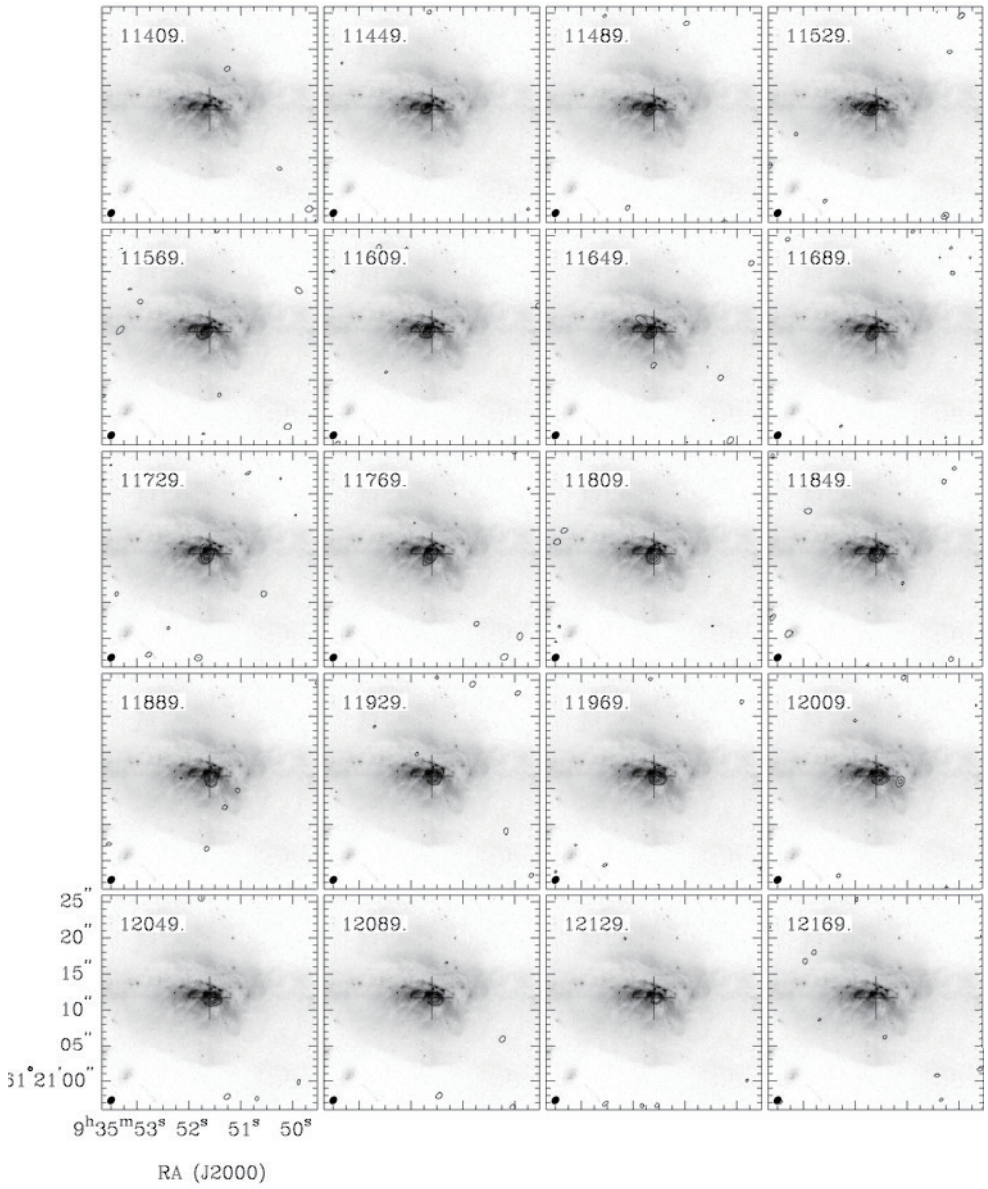

Figure A.11: Same as Figure A.1, but UGC 5101. The contours are 11.9 mJy beam^{-1} $\times$ (3, 5, 10, 15, 20, 25). The background image is the HST/ACS B-band image.

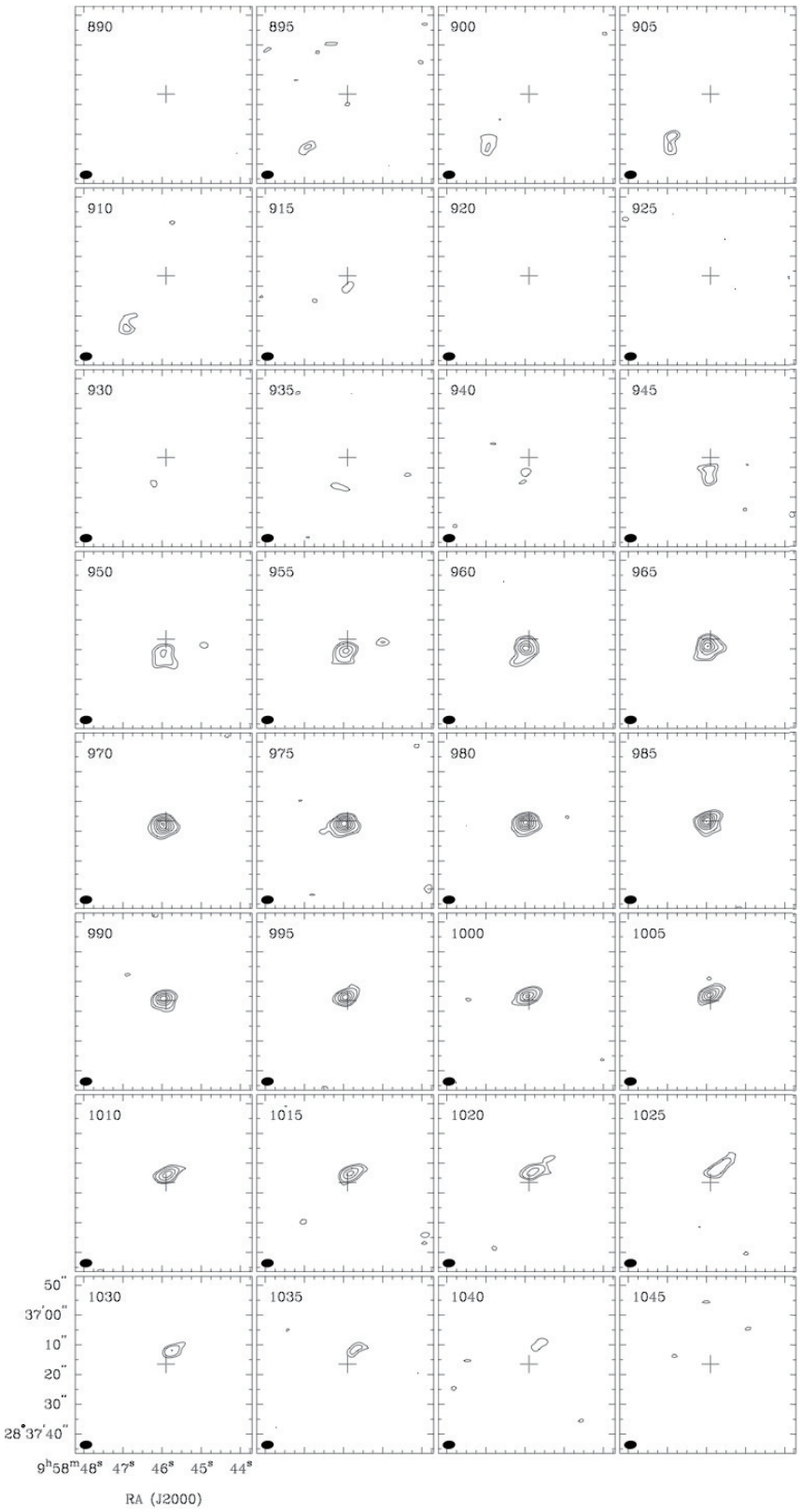

Figure A.12: Same as Figure A.1, but AM 0956-282. The contours are 5.71 mJy beam^{-1} $\times$ (3, 5, 10, 15, 20, 25, 30).

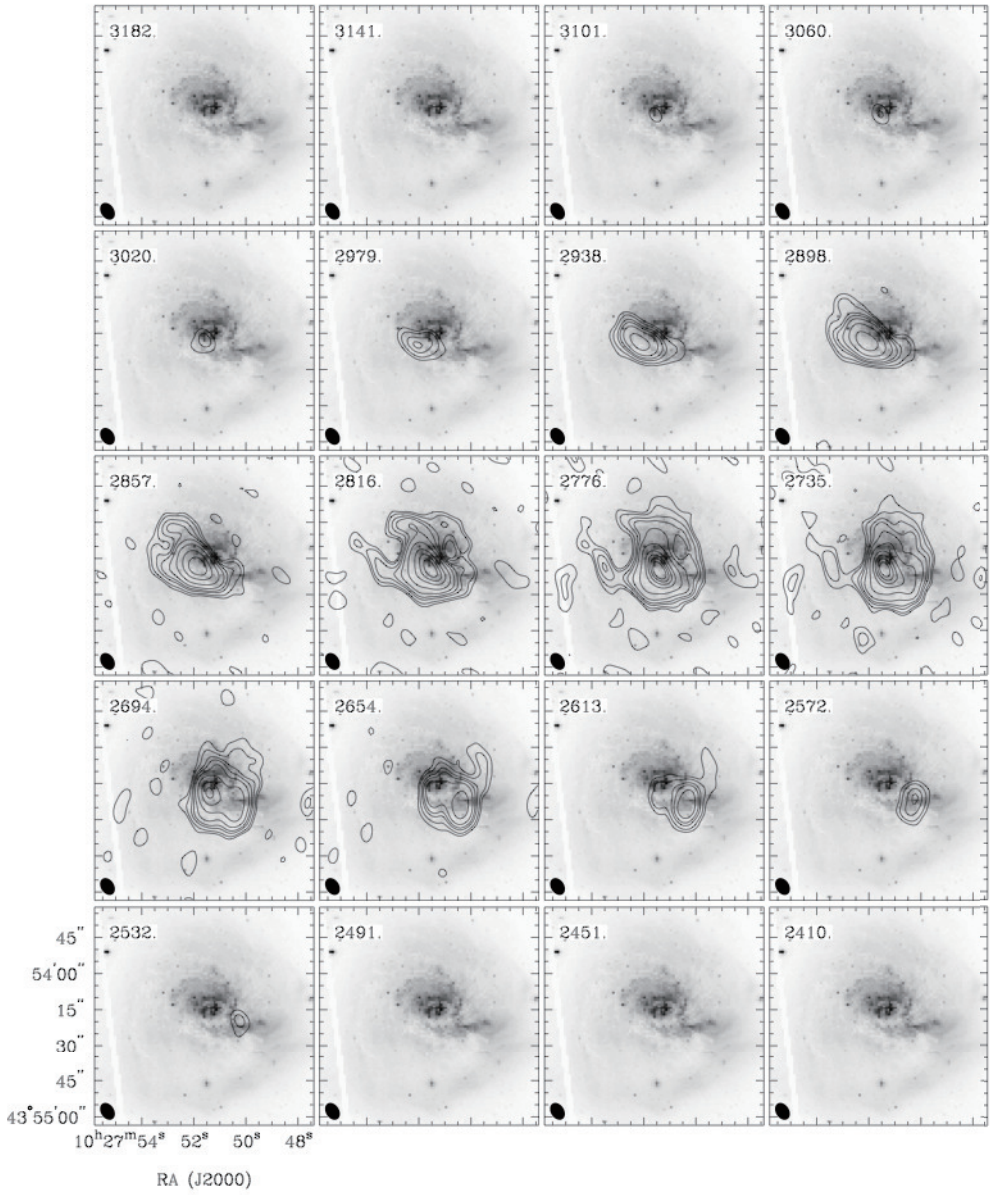

Figure A.13: Same as Figure A.1, but NGC 3256. The contours are 3.87 mJy beam^{-1} (3 σ) $\times$ (5, 10, 20, 30, 50, 100, 200, 300, 400, 500). The background image is the HST/ACS B-band image.

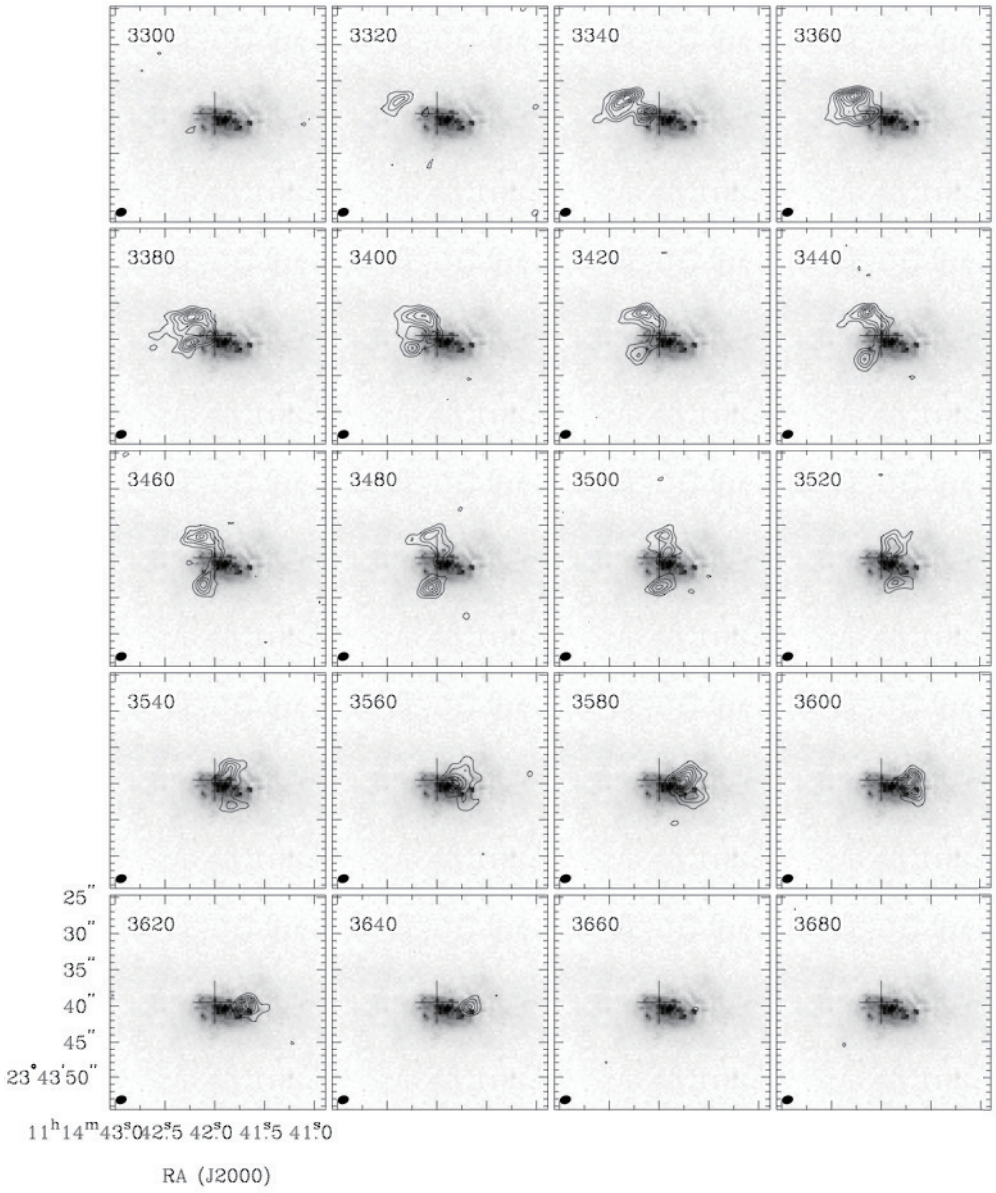

Figure A.14: Same as Figure A.1, but NGC 3597. The contours are 3.87 mJy beam^{-1} $\times$ (3, 6, 9, 12, 15, 18, 21, 24). The background image is the HST/WFPC2 V-band image.

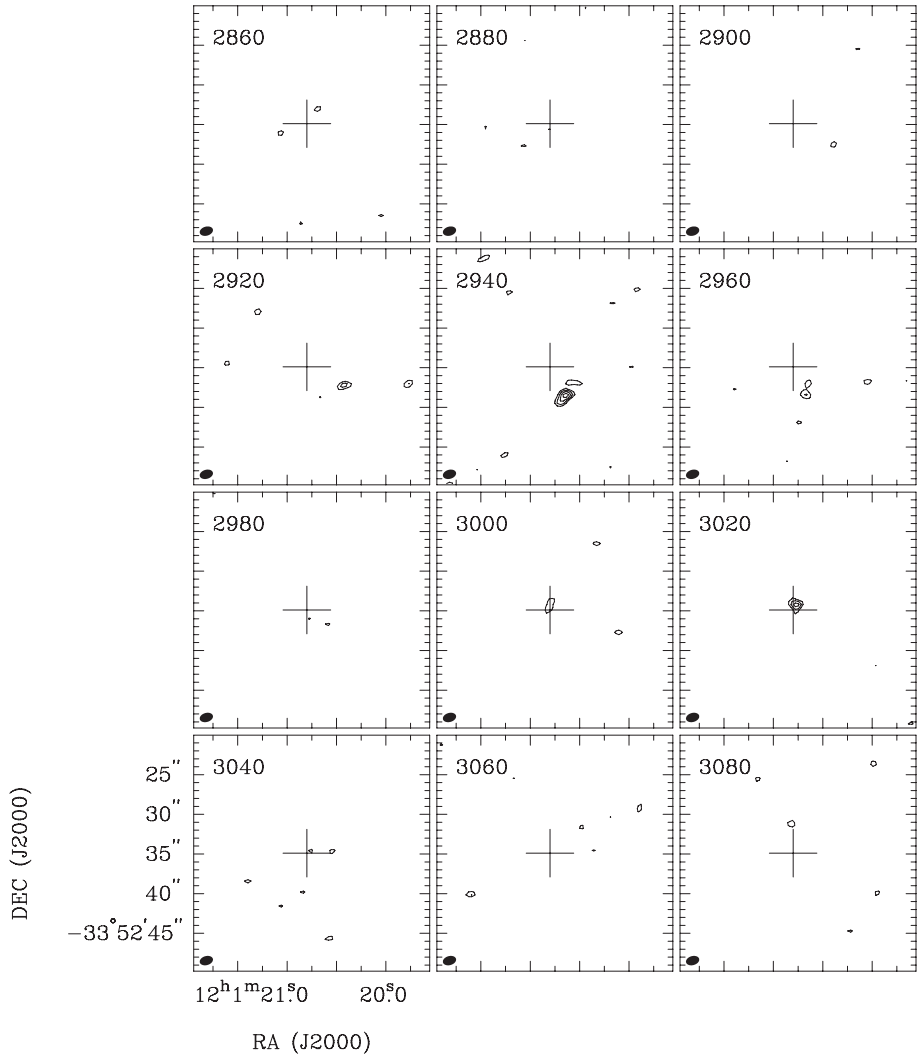

Figure A.15: Same as Figure A.1, but AM 1158-333. The contours are 4.60 mJy beam^{-1} $\times$ (3, 4, 5, 6).

Figure A.16: Same as Figure A.1, but NGC 4194. The contours are 34.7 mJy beam^{-1} $\times$ (3, 5, 7, 9, 11, 13, 15).

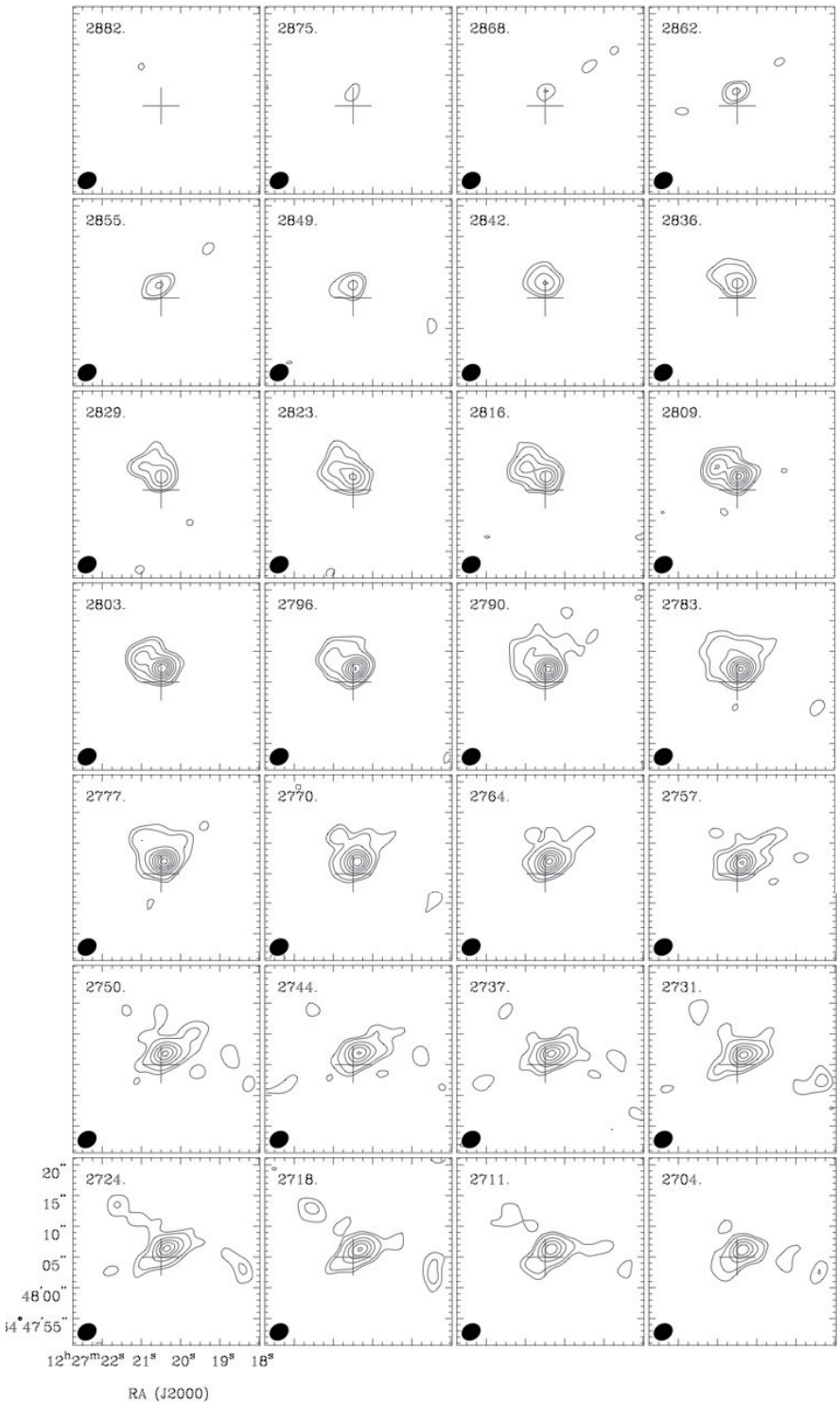

Figure A.17: Same as Figure A.1, but NGC 4441. The contours are 2.92 mJy beam^{-1} $\times$ (3, 5, 10, 15, 20, 25, 30, 35).

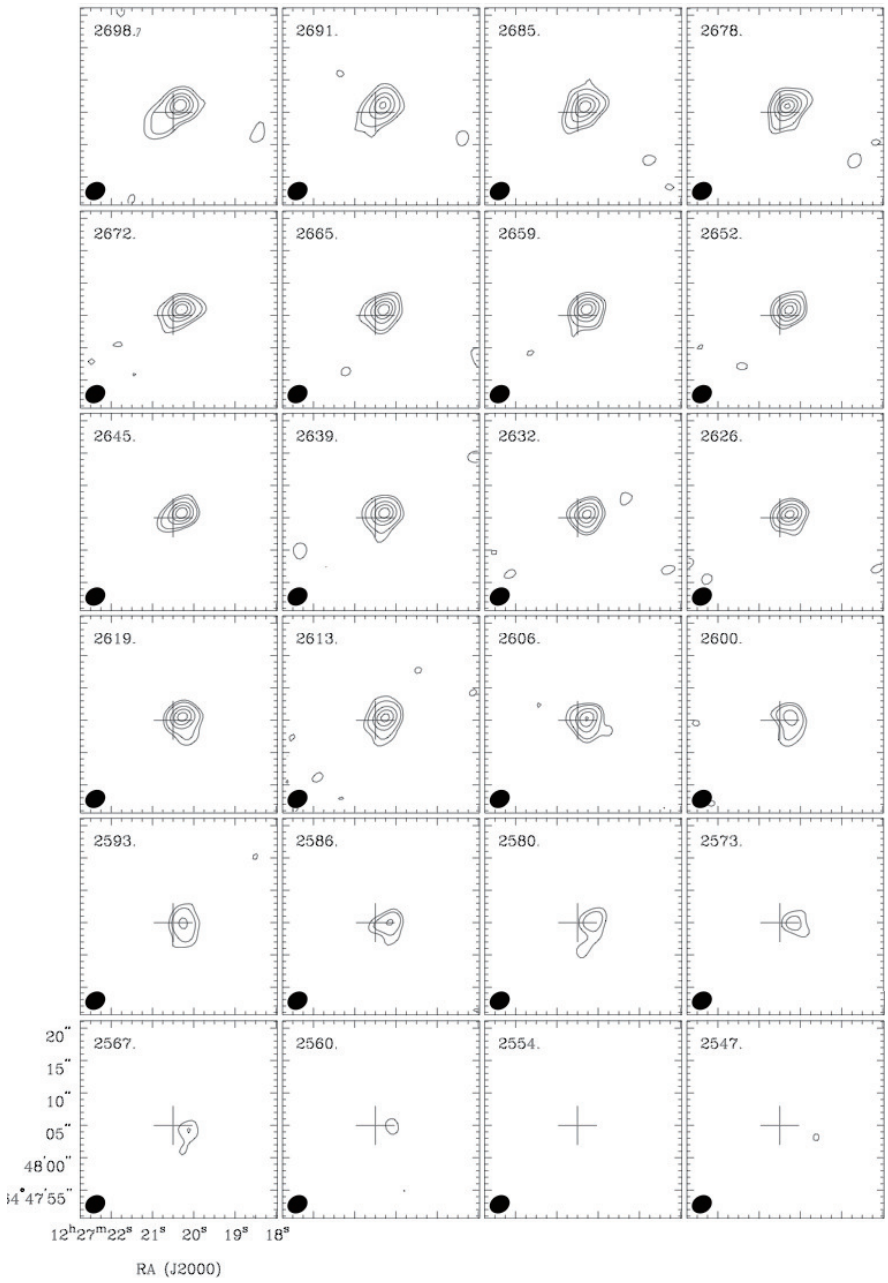

Figure A.17: (Continued.) Same as Figure A.1, but NGC 4441. The contours are 1.94 mJy beam^{-1} $\times$ (3, 5, 10, 15, 20, 25, 30, 35).

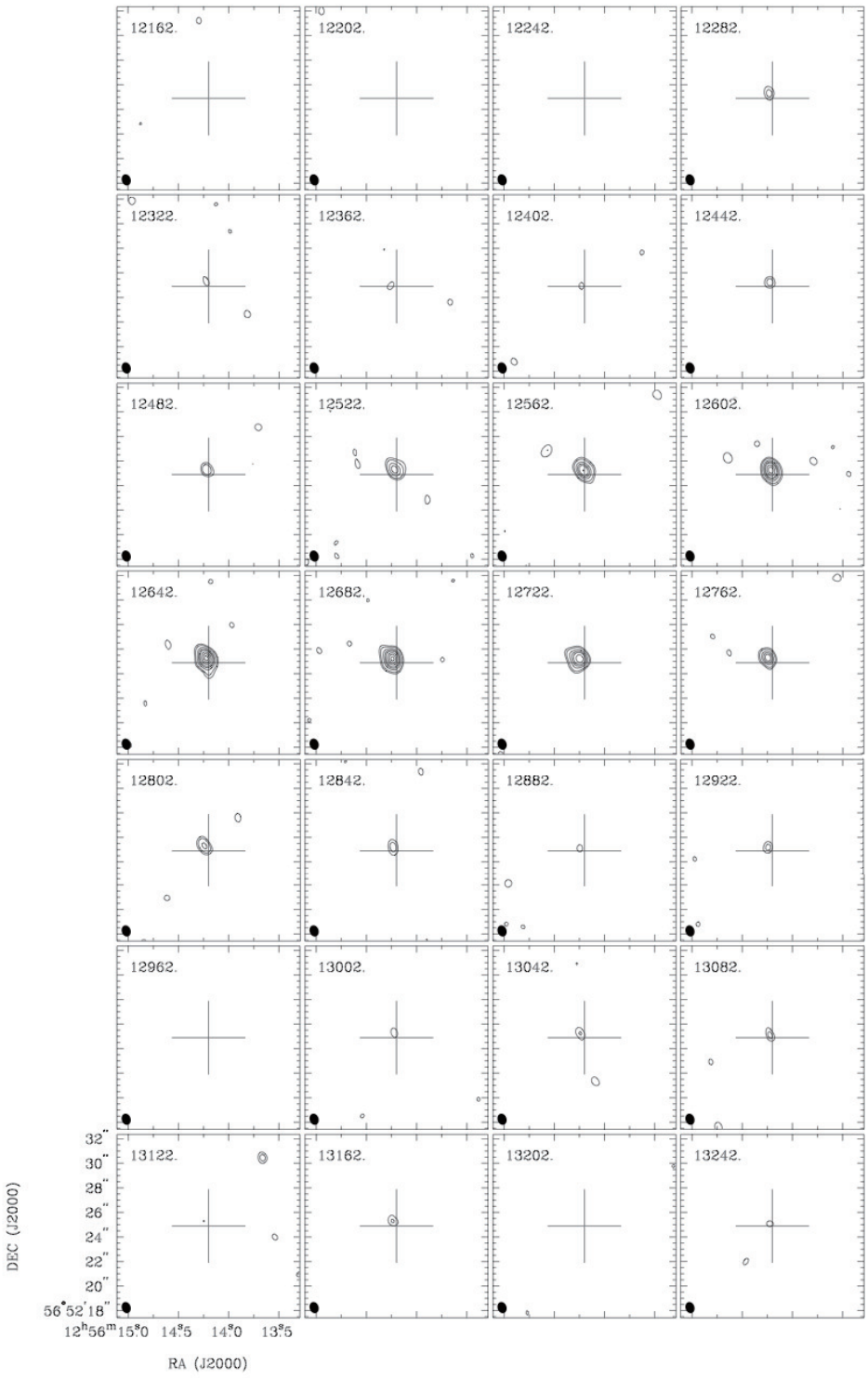

Figure A.18: Same as Figure A.1, but UGC 8058. The contours are 19.8 mJy beam^{-1} $\times$ (3, 5, 10, 15, 20, 30, 40, 50).

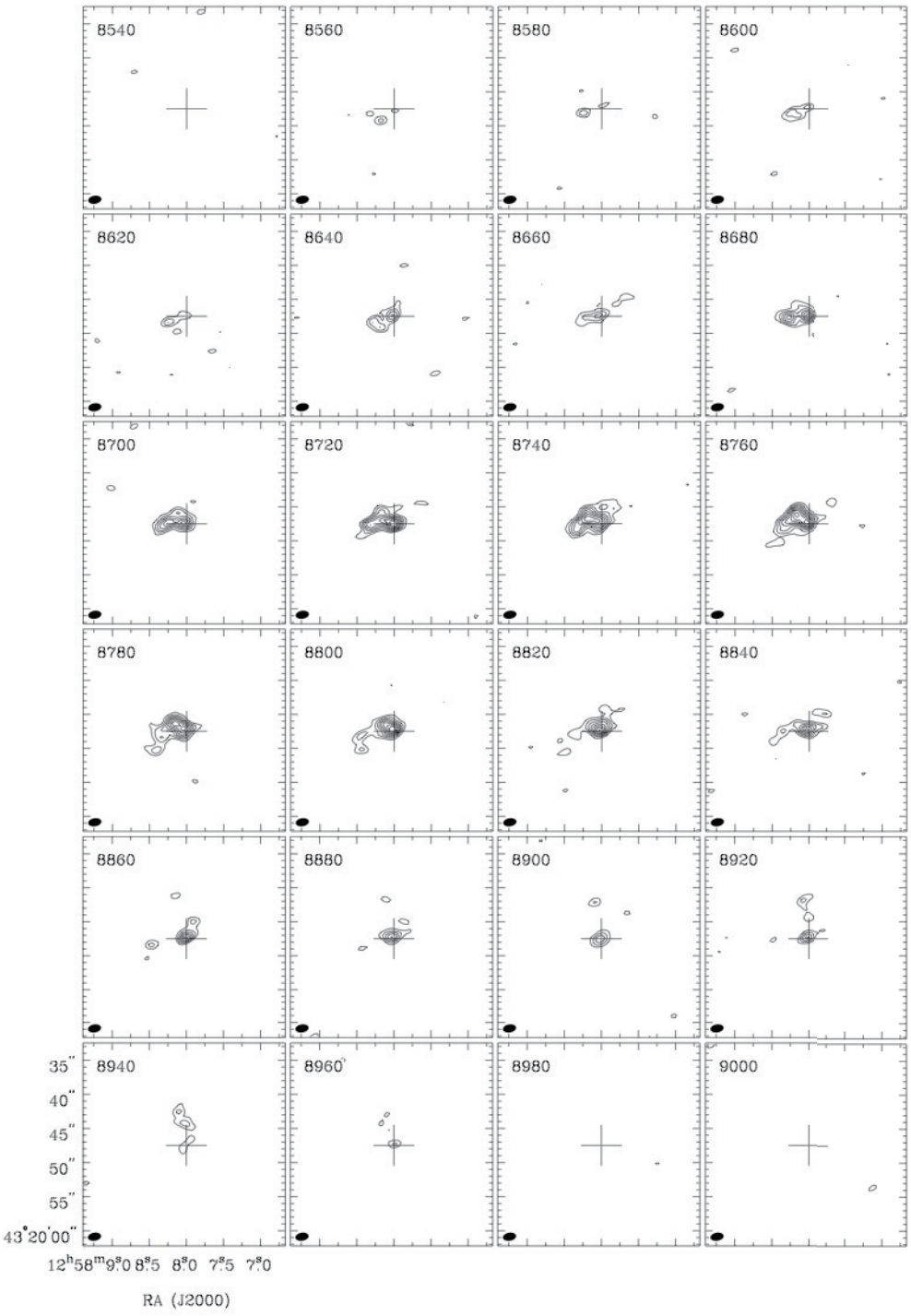

Figure A.19: Same as Figure A.1, but AM 1255-430. The contours are 1.78 mJy beam^{-1} $\times$ (3, 5, 7, 9, 11, 13, 15, 17).

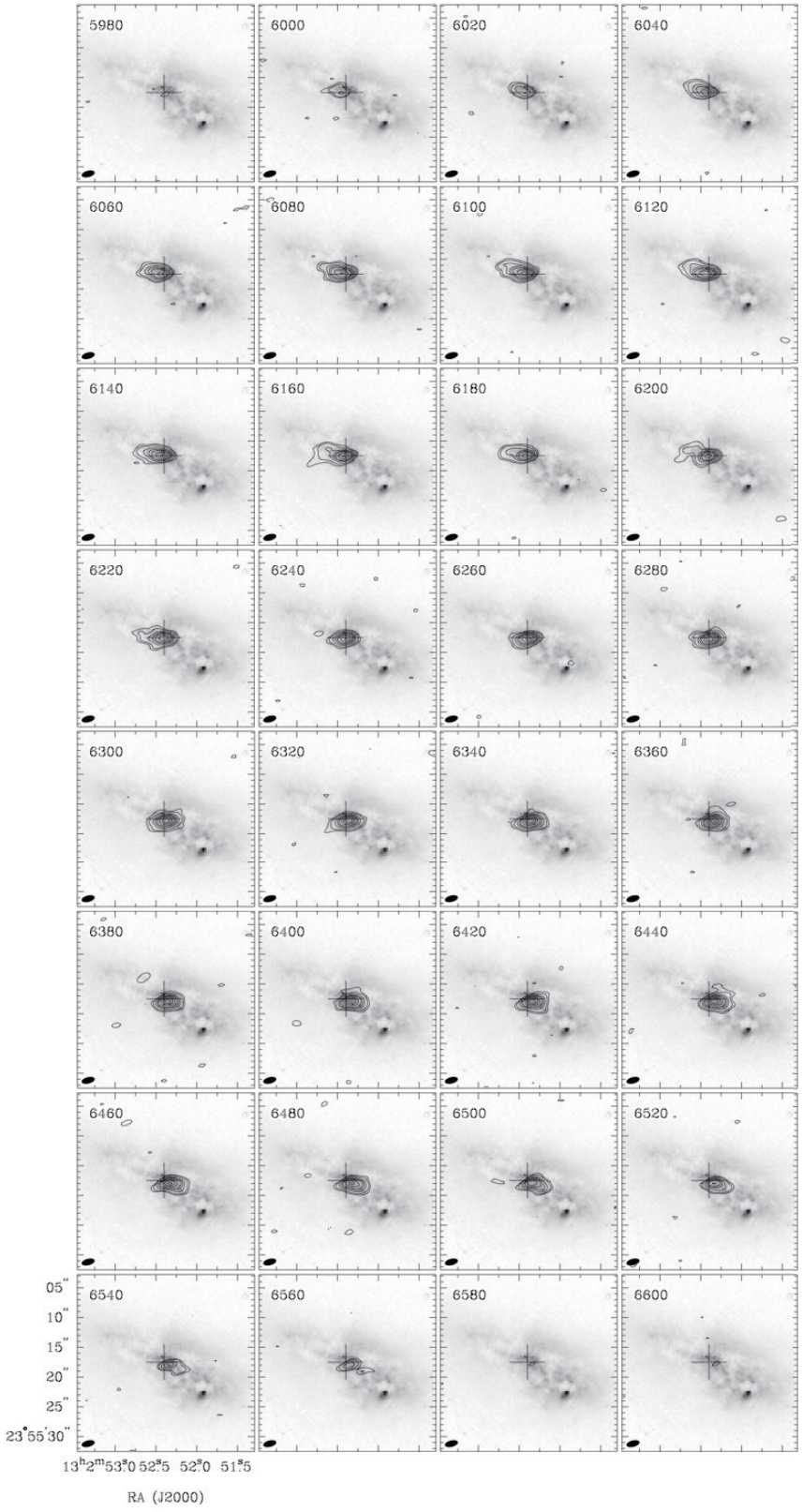

Figure A.20: Same as Figure A.1, but AM 1300-233. The contours are 2.06 mJy beam^{-1} $\times$ (3, 5, 10, 15, 20, 30, 40, 50). The background image is the HST/ACS B-band image.

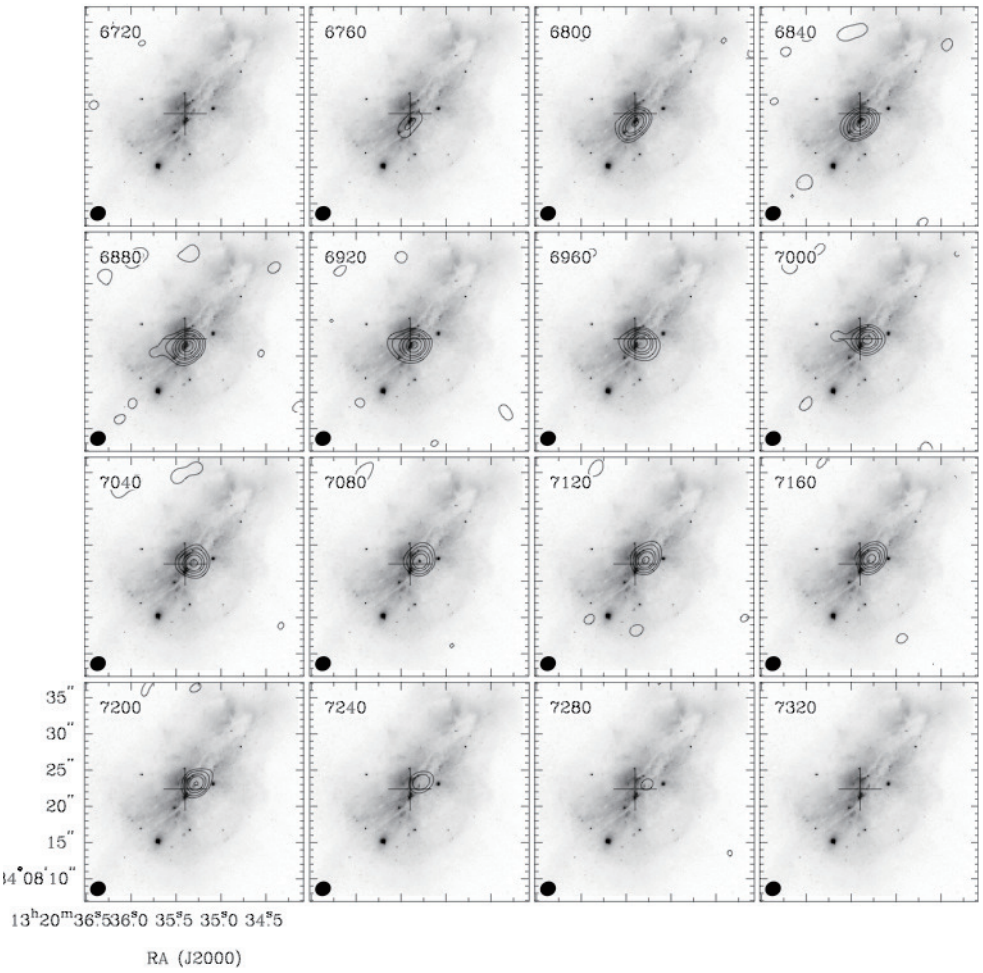

Figure A.21: Same as Figure A.1, but Arp 193. The contours are 23.0 mJy beam^{-1} $\times$ (5, 10, 20, 30, 50, 75). The background image is the HST/ACS B-band image.

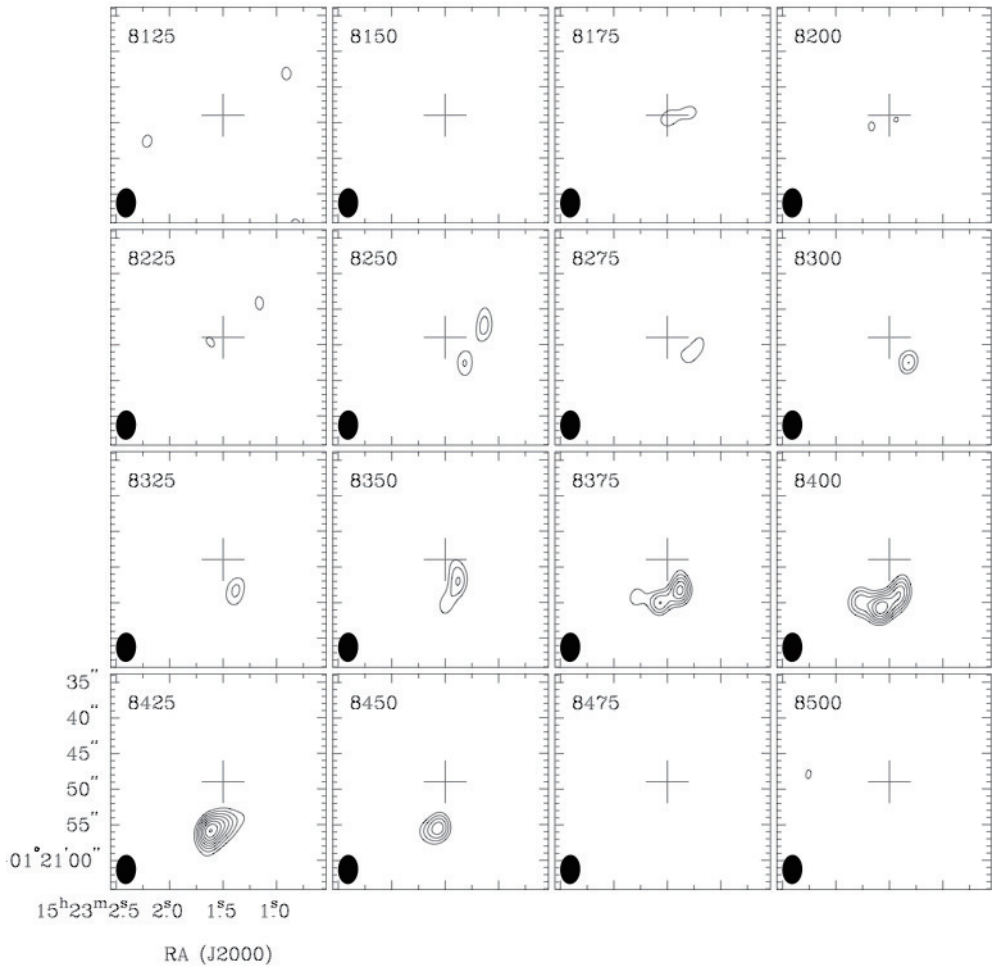

Figure A.22: Same as Figure A.1, but UGC 9829. The contours are 24.4 mJy beam^{-1} $\times$ (3, 4, 5, 6, 7, 8, 9, 10).

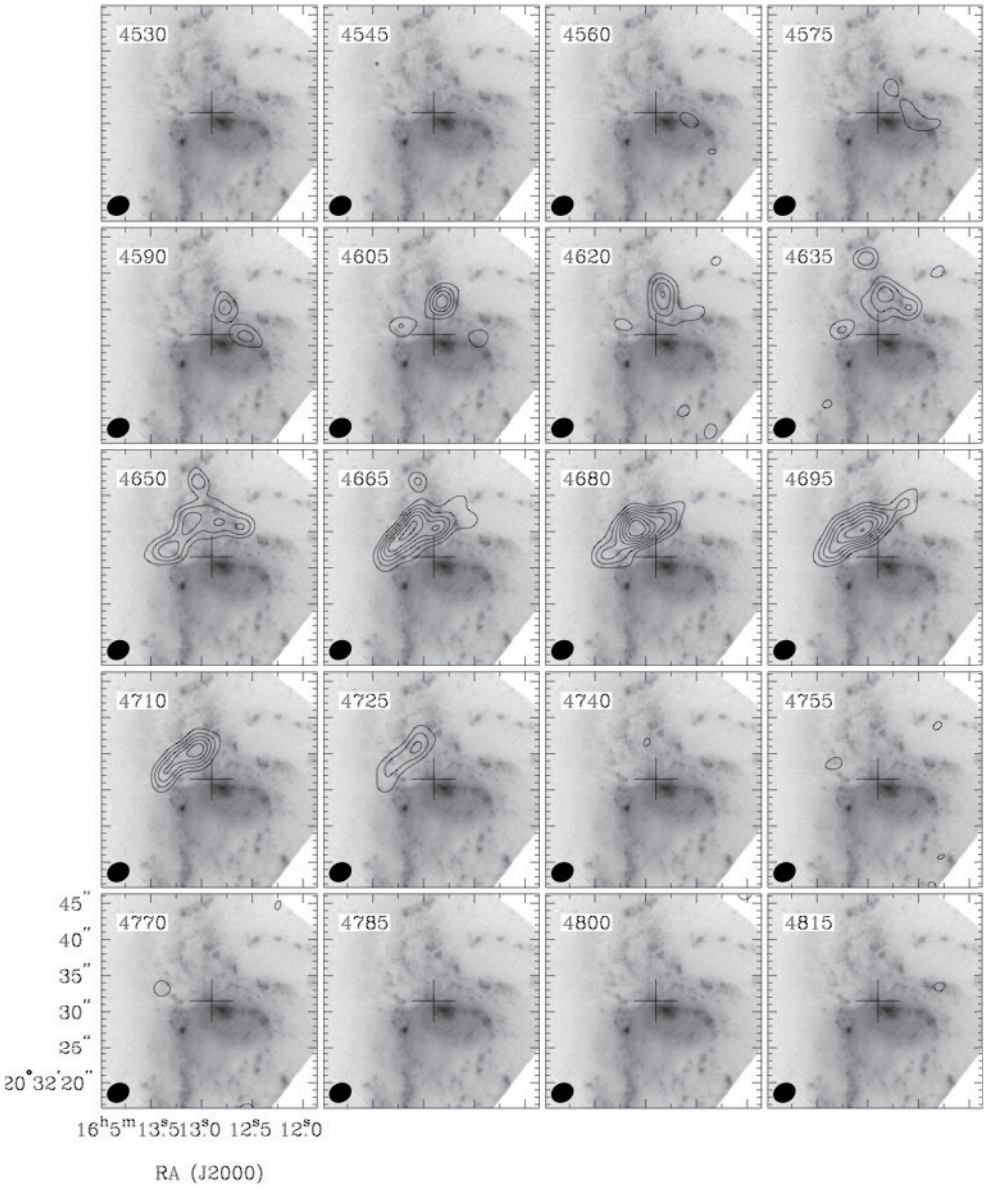

Figure A.23: Same as Figure A.1, but NGC 6052. The contours are 21.4 mJy beam^{-1} $\times$ (3, 5, 7, 9, 11, 13, 15). The background image is the HST/WFPC2 V-band image.

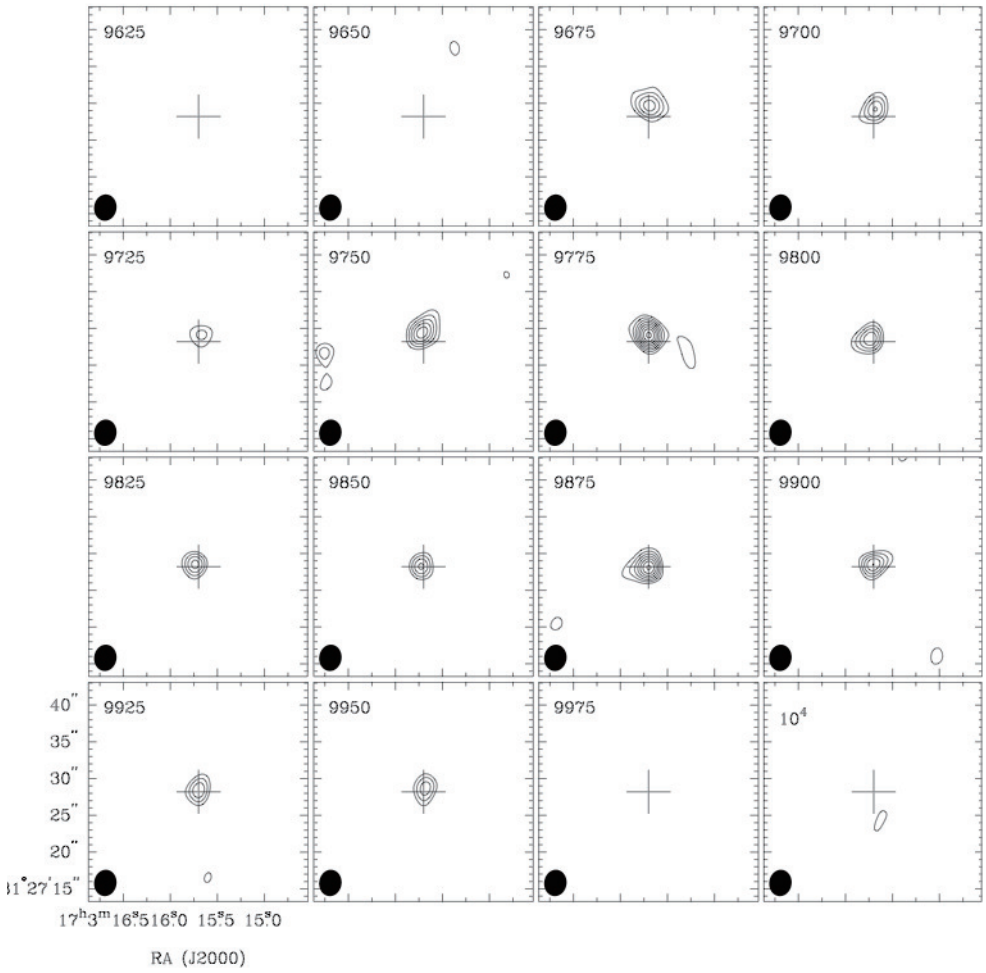

Figure A.24: Same as Figure A.1, but UGC 10675. The contours are 18.0 mJy beam^{-1} $\times$ (3, 4, 5, 6, 7, 8, 9, 10).

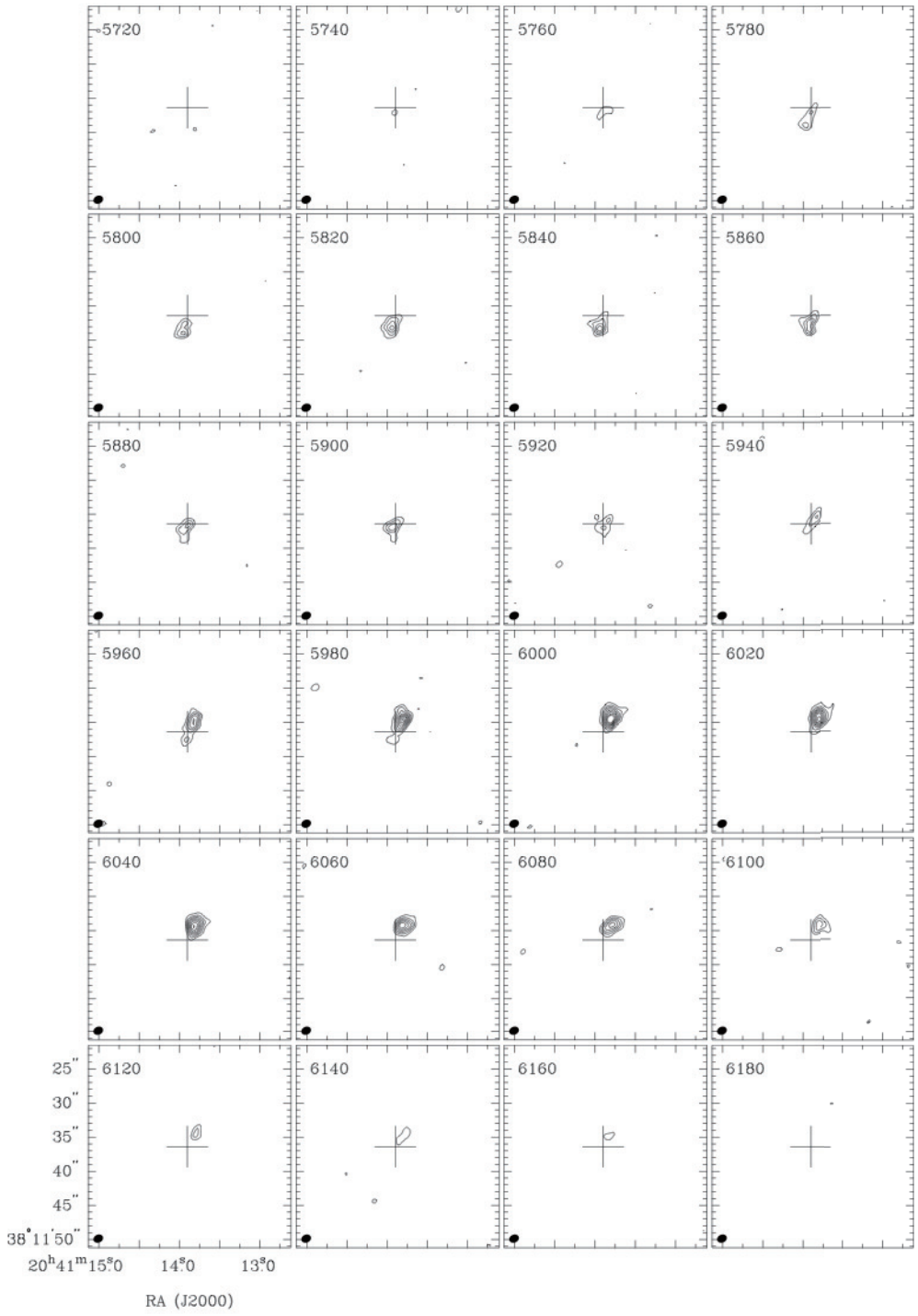

Figure A.25: Same as Figure A.1, but AM 2038-382. The contours are 2.97 mJy beam^{-1} $\times$ (3, 5, 7, 9, 11, 13, 15, 17).

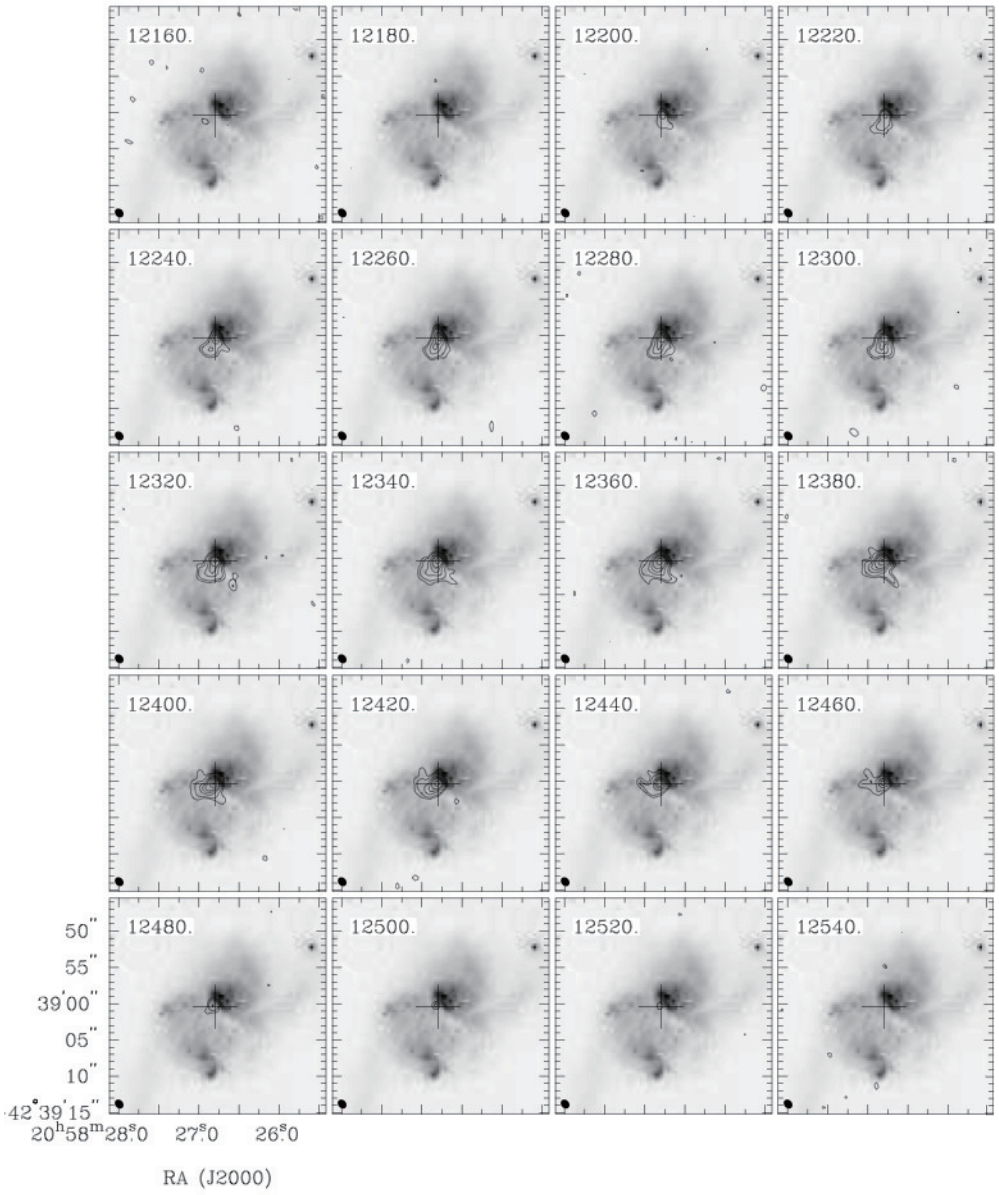

Figure A.26: Same as Figure A.1, but AM 2055-425. The contours are 2.34 mJy beam^{-1} $\times$ (3, 5, 10, 15, 20, 30, 40). The background image is the HST/ACS B-band image.

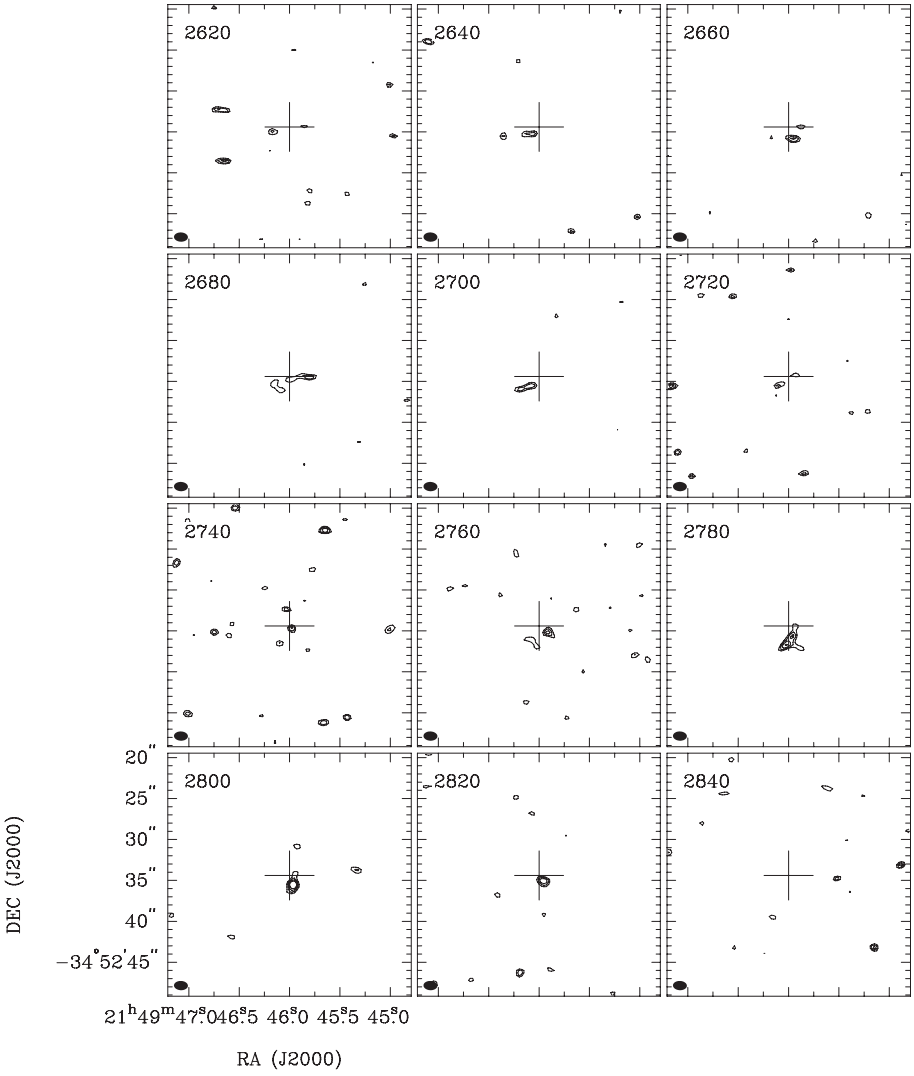

Figure A.27: Same as Figure A.1, but NGC 7135. The contours are 3.99 mJy beam^{-1} $\times$ (2.5, 3, 3.5, 4).

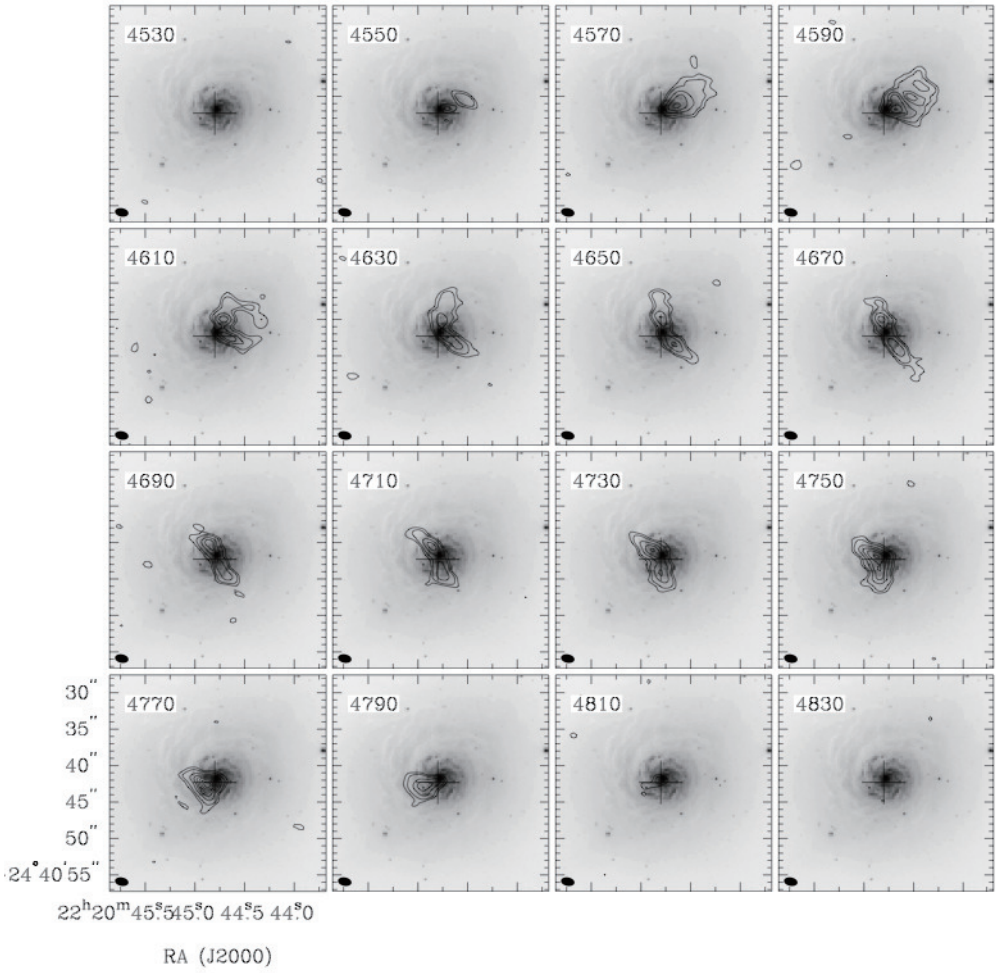

Figure A.28: Same as Figure A.1, but NGC 7252. The contours are 3.36 mJy beam^{-1} $\times$ (3, 5, 10, 15, 20, 25, 30, 35). The background image is the HST/WFPC3 B-band image.

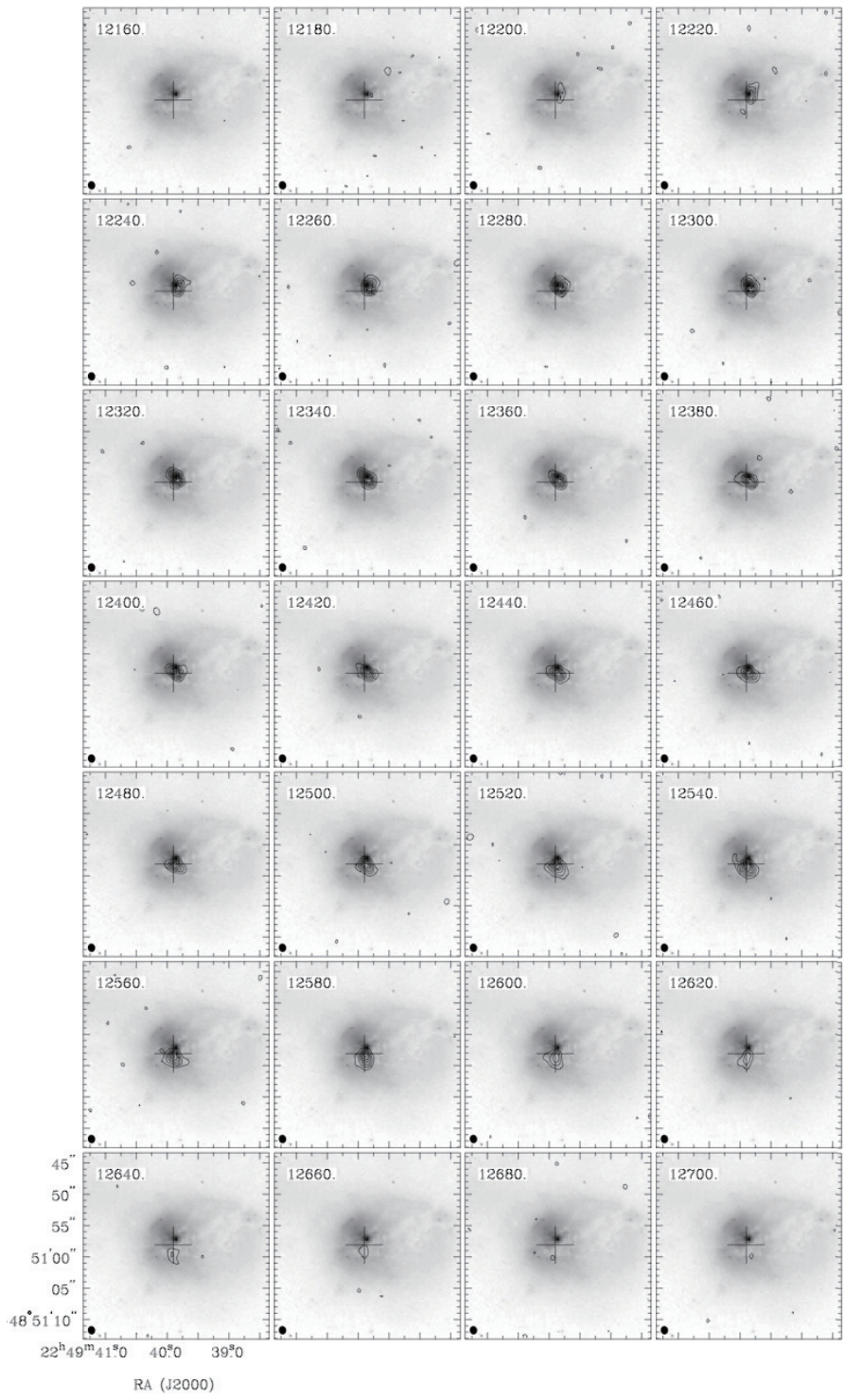

Figure A.29: Same as Figure A.1, but AM 2246-490. The contours are 2.24 mJy beam^{-1} $\times$ (3, 6, 9, 12, 15, 18, 21, 24). The background image is the HST/ACS B-band image.

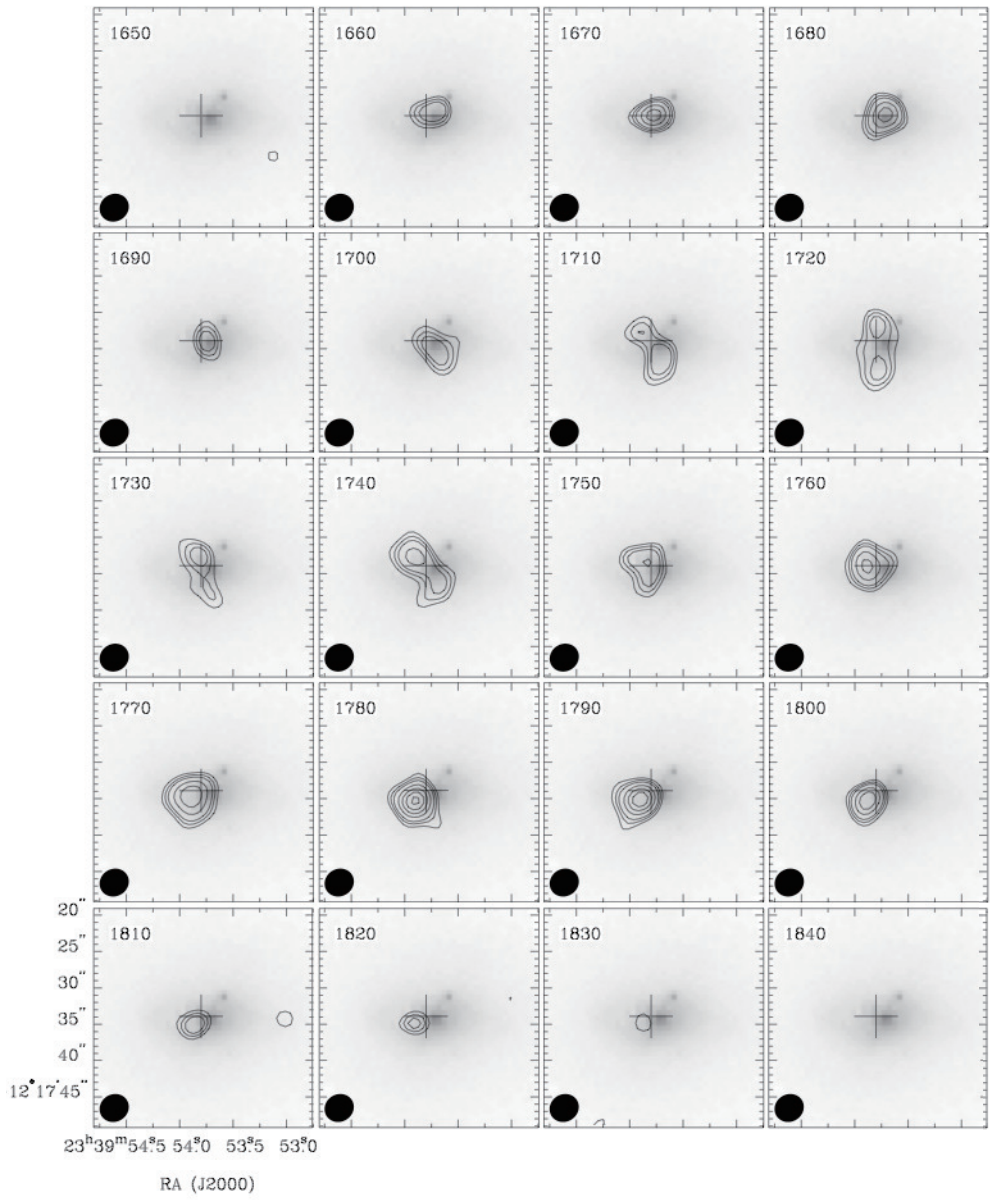

Figure A.30: Same as Figure A.1, but NGC 7727. The contours are 3.08 mJy beam^{-1} $\times$ (3, 4, 5, 7, 9, 11, 13). The background image is the HST/WFPC2 V-band image.

Appendix B

Position-Velocity Diagram

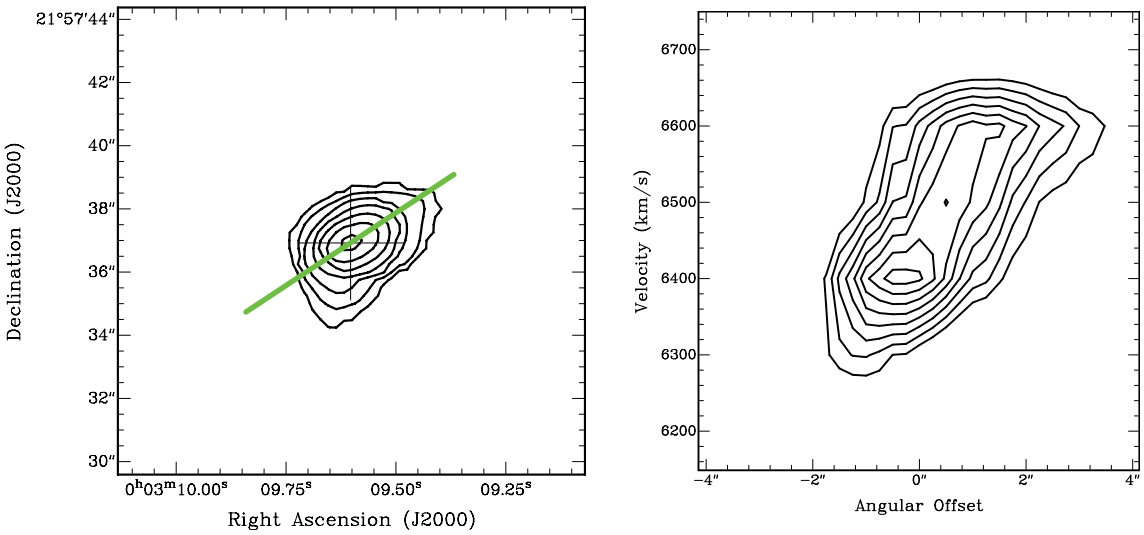

Figure B.1: The right figure is the Position-Velocity diagram of UGC 6 along the green cut line shown in the moment 0 map (left figure), which is the kinematical major axis defined by fitting the CO velocity field. The plus sign in the left figure shows the galactic center defined by the K-band image (Rothberg & Joseph, 2004). The contours in the left figure are 1.2 Jy km s$^{-1}\times$ (1, 2, 3, 4, 5, 6, 7) and the contours in the right figure are 3.37 mJy beam^{-1} $\times$ (3, 4, 5, 6, 7, 8, 9, 10).

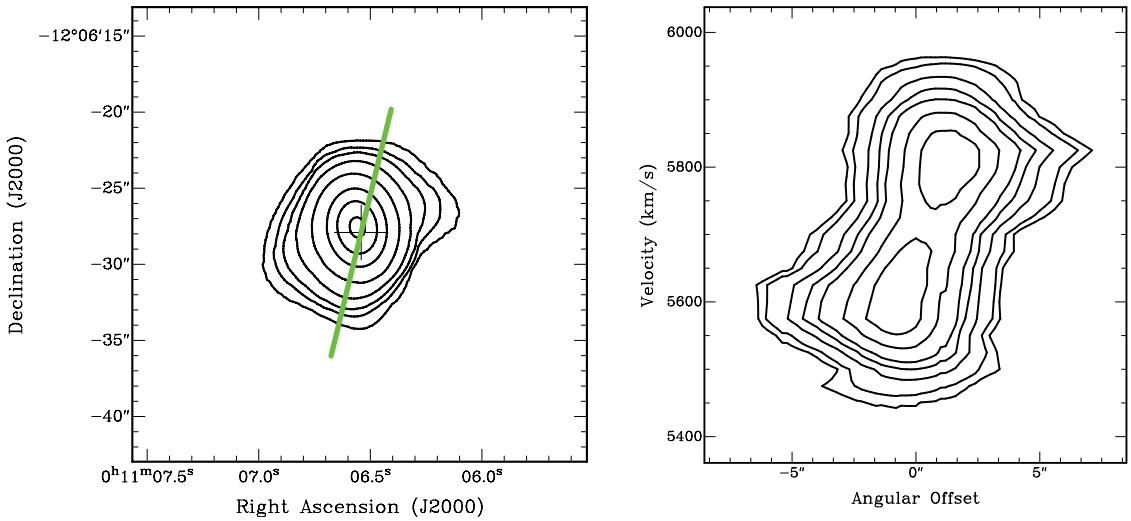

Figure B.2: Same as Figure B.1, but NGC 34. The contours in the right figure are 5.6 Jy km s$^{-1}\times$ (1, 2, 3, 5, 10, 20, 30, 40) and the contours in the right figure are 14.8 mJy beam^{-1} $\times$ (3, 5, 10, 15, 20, 30, 40).

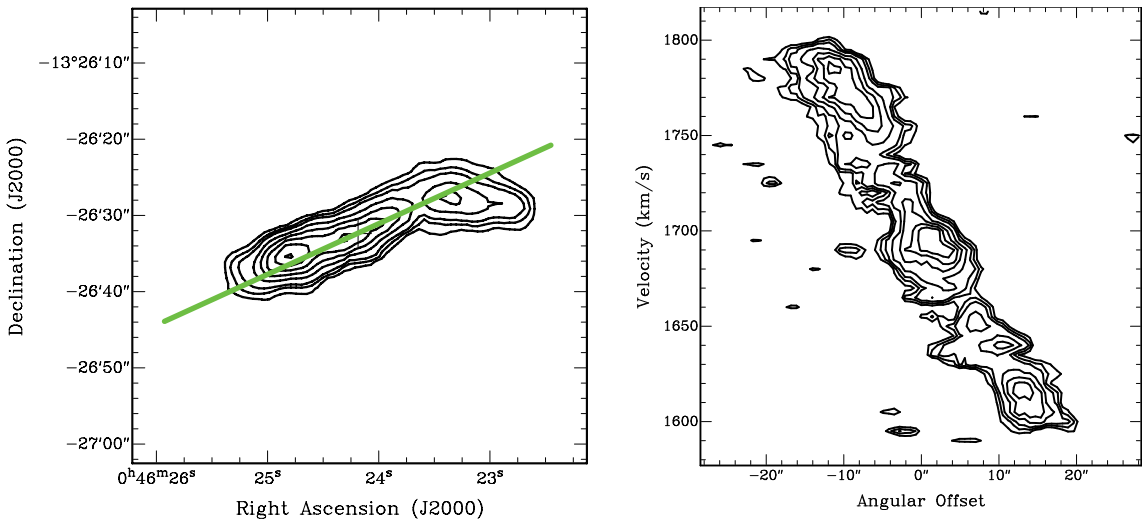

Figure B.3: Same as Figure B.1, but Arp 230. The contours in the right figure are 0.23 Jy km s$^{-1}\times$ (1, 2, 3, 5, 7, 9, 11, 13) and the contours in the right figure are 4.12 mJy beam^{-1} $\times$ (3, 4, 5, 7, 9, 11, 13).

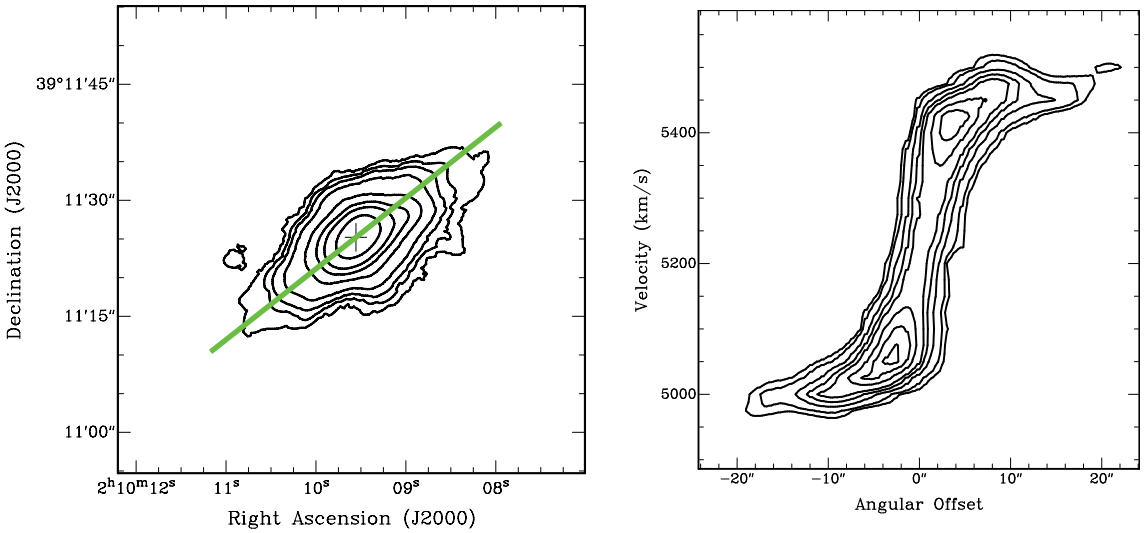

Figure B.4: Same as Figure B.1, but NGC 828. The contours in the left figure are 4.3 Jy km s$^{-1}\times$ (1, 2, 3, 5, 10, 20, 30, 40) and the contours in the right firegu are 22.1 mJy beam^{-1} $\times$ (3, 5, 10, 15, 20, 30, 40, 50).

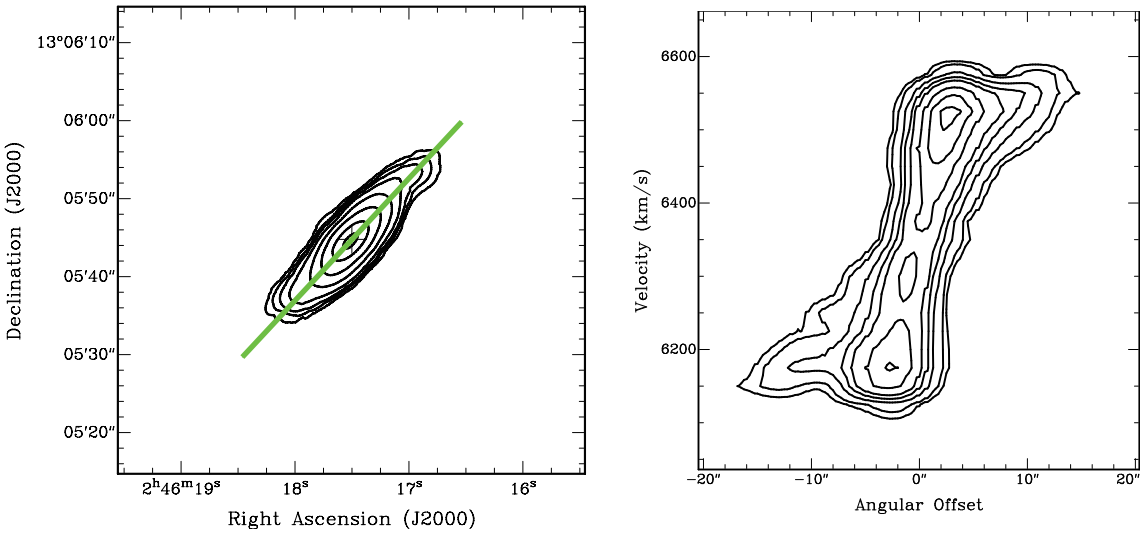

Figure B.5: Same as Figure B.1, but UGC 2238. The contours in the left figure are 3.0 Jy km s^{-1} (1, 2, 3, 5, 10, 20, 40, 60) and the contours in the right figure are 17.7 mJy beam^{-1} $\times$ (3, 5, 10, 15, 20, 30, 40, 50).

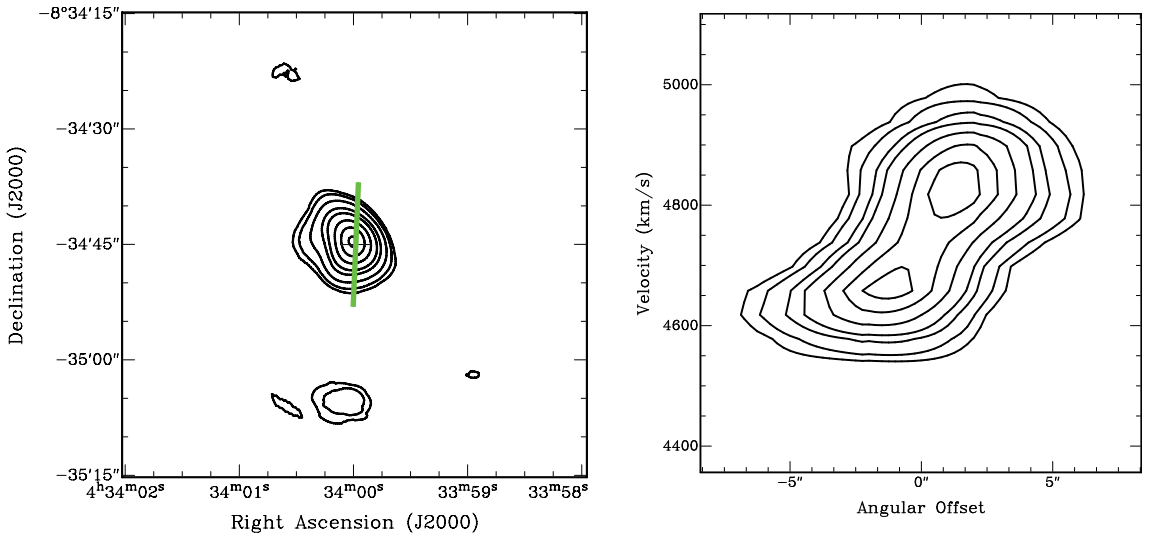

Figure B.6: Same as Figure B.1, but NGC 1614. The contours in the left figure are 3.0 Jy km s$^{-1}\times$ (1, 2, 3, 5, 10, 25, 50, 75, 100) and the contours in the right figure are 11.2 mJy beam^{-1} $\times$ (5, 10, 20, 30, 50, 75, 100).

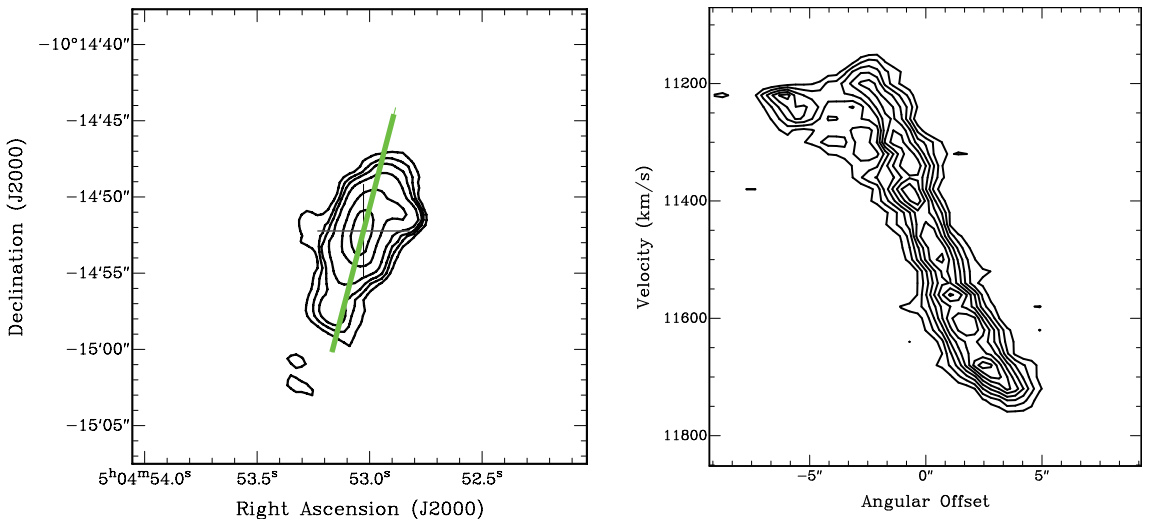

Figure B.7: Same as Figure B.1, but Arp 187. The contours in the left figure are 0.46 Jy km s$^{-1}\times$ (1, 2, 3, 5, 10, 15, 20) and the contours in the right figure are 2.52 mJy beam^{-1} $\times$ (3, 5, 7, 9, 11, 13, 15, 17).

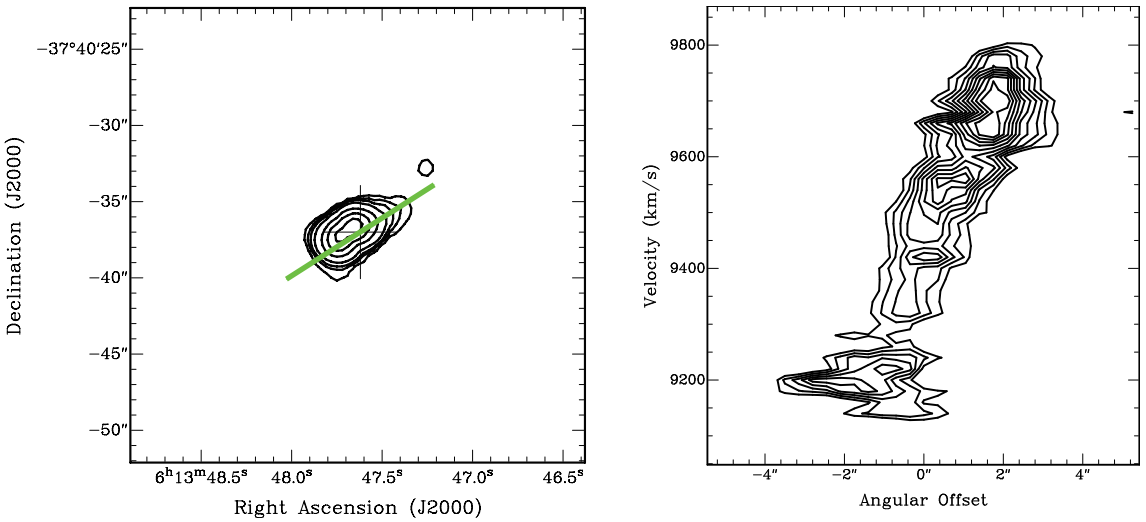

Figure B.8: Same as Figure B.1, but AM 0612-373. The contours in the left figure are 0.38 Jy km s$^{-1}\times$ (1, 2, 3, 5, 10, 15, 20) and the contours in the right figure are 2.83 mJy beam^{-1} $\times$ (3, 4, 5, 6, 7, 8, 9, 10, 11).

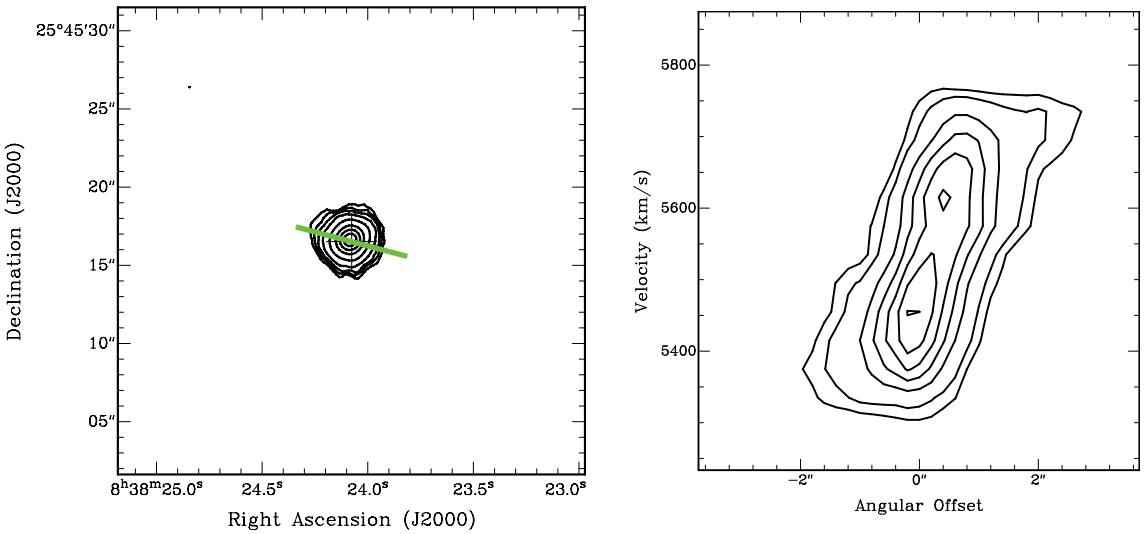

Figure B.9: Same as Figure B.1, but NGC 2623. The contours in the left figure are 2.0 Jy km s$^{-1}\times$ 1, 2, 3, 5, 10, 20, 30, 40) and the contours in the right figure are 11.6 mJy beam^{-1} $\times$ (3, 5, 10, 15, 20, 25, 30).

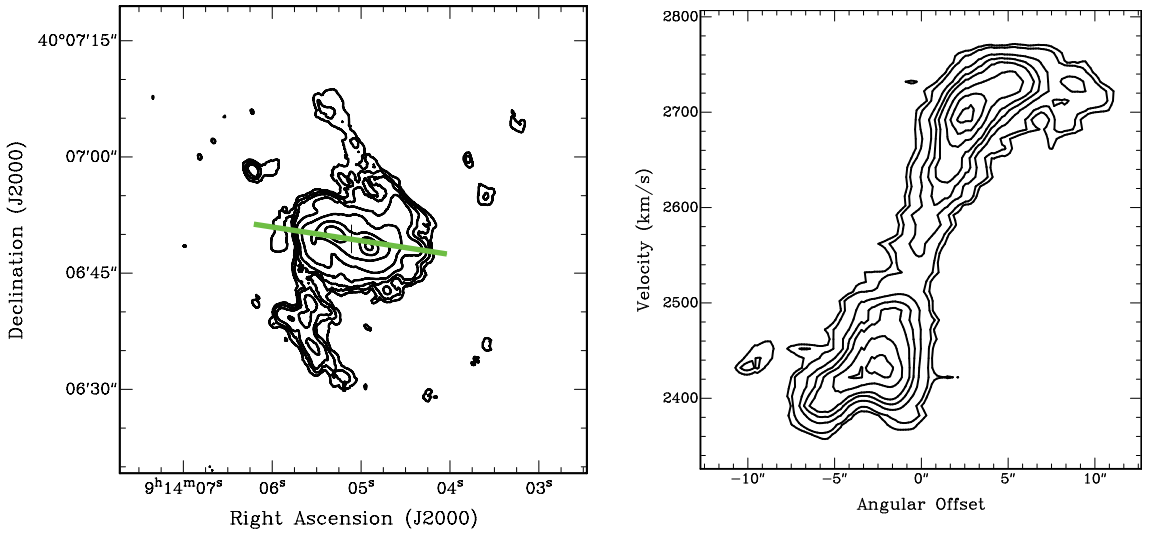

Figure B.10: Same as Figure B.1, but NGC 2782. The contours in the left figure are 0.19 Jy km s$^{-1}\times$ (1, 2, 3, 5, 10, 20, 30, 40) and the contours in the right figure are 1.94 mJy beam^{-1} $\times$ (3, 5, 10, 15, 20, 30, 40, 50).

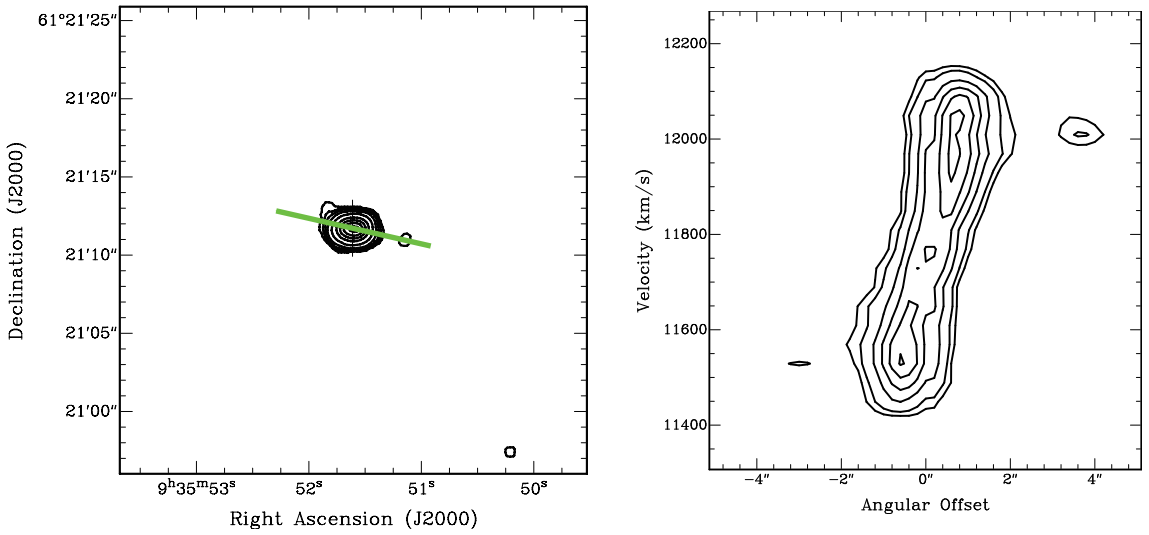

Figure B.11: Same as Figure B.1, but UGC 5101. The contours in the left figure are 2.3 Jy km s$^{-1}\times$ (1, 2, 3, 5, 10, 25, 50) and the contours in the right figure are 11.9 mJy beam^{-1} $\times$ (3, 5, 10, 15, 20, 25).

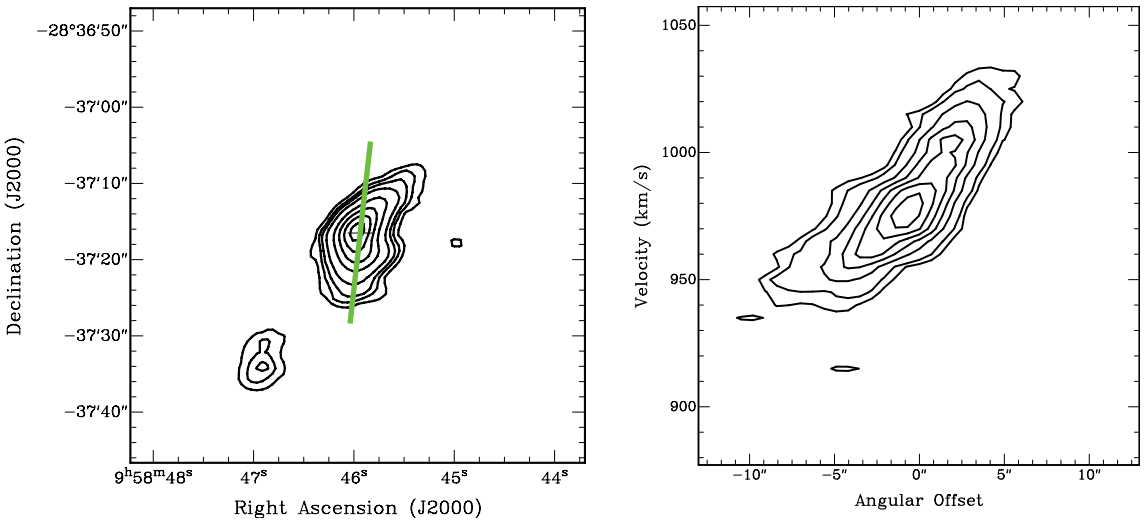

Figure B.12: Same as Figure B.1, but AM 0956-282. The contours in the left figure are 0.22 Jy km s$^{-1}\times$ (1, 2, 3, 5, 10, 15, 20, 25) and the contours in the right figure are 5.71 mJy beam^{-1} $\times$ (3, 5, 10, 15, 20, 25, 30).

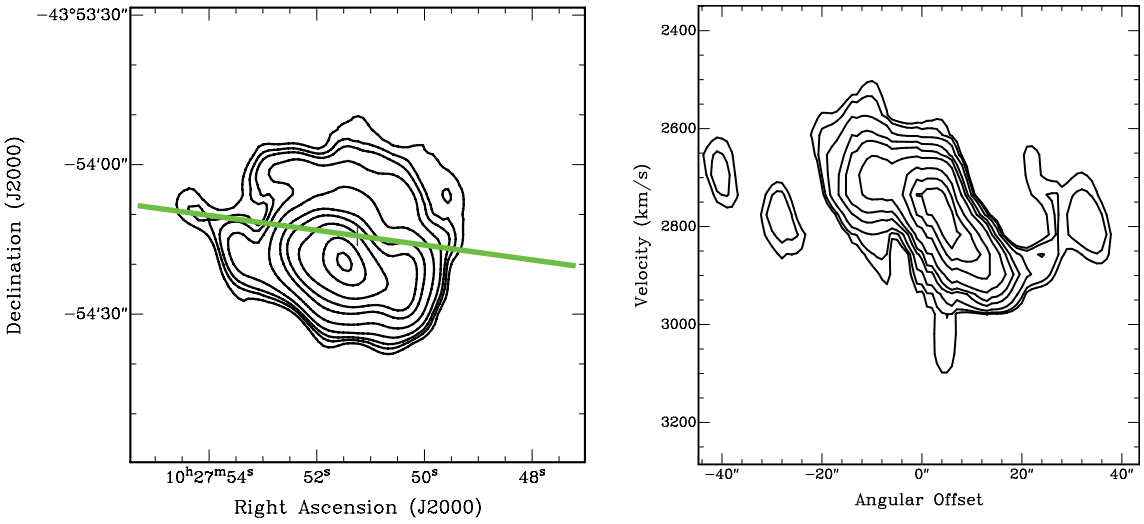

Figure B.13: Same as Figure B.1, but NGC 3256. The contours in the left figure are 2.0 Jy km s$^{-1}\times$ (1, 2, 3, 5, 10, 20, 30, 50, 100, 150) and the contours in the right figure are 3.87 mJy beam^{-1} (3 σ) $\times$ (3, 5, 10, 20, 30, 50, 100, 150, 200).

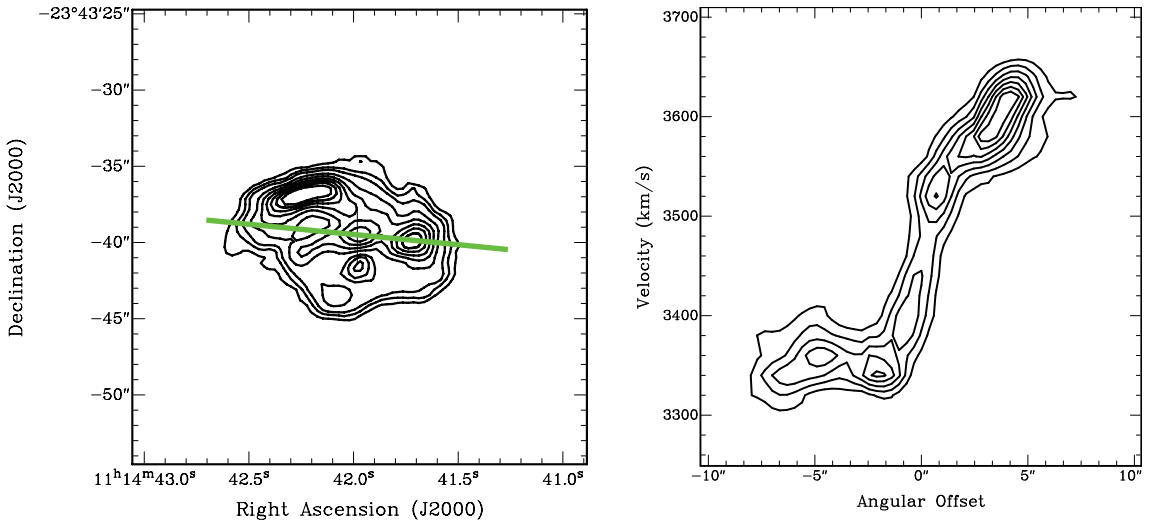

Figure B.14: Same as Figure B.1, but NGC 3597. The contours in the left figure are 0.46 Jy km s$^{-1}\times$ (1, 2, 3, 5, 7, 9, 11, 13, 15) and the contours in the right figure are 3.87 mJy beam^{-1} $\times$ (3, 6, 9, 12, 15, 18, 21, 24).

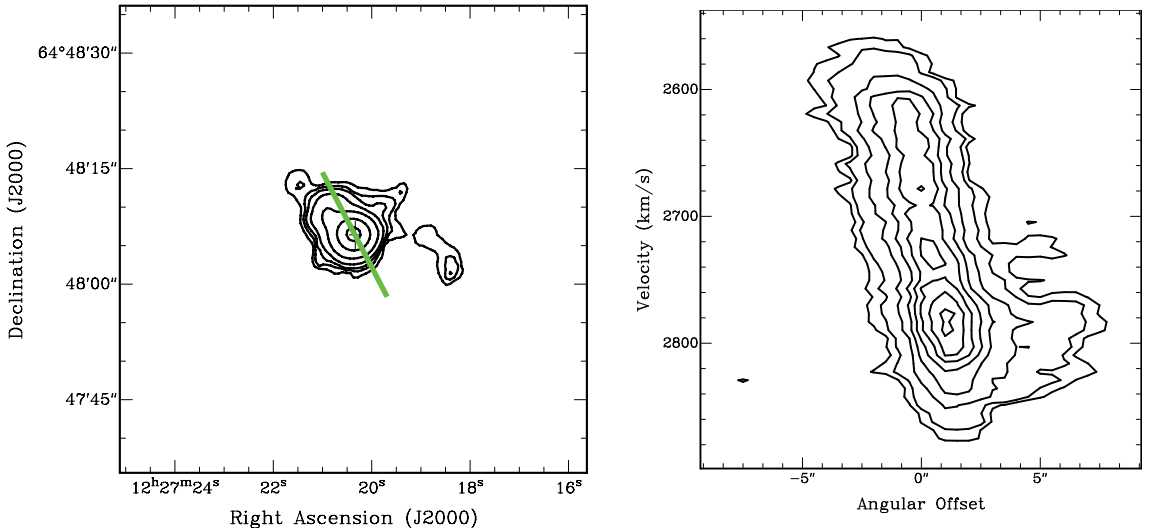

Figure B.15: Same as Figure B.1, but NGC 4441. The contours in the left figure are 0.28 Jy km s$^{-1}\times$ (1, 2, 3, 5, 10, 25, 50) and the contours in the right figure are 2.92 mJy beam^{-1} $\times$ (3, 5, 10, 15, 20, 25, 30, 35).

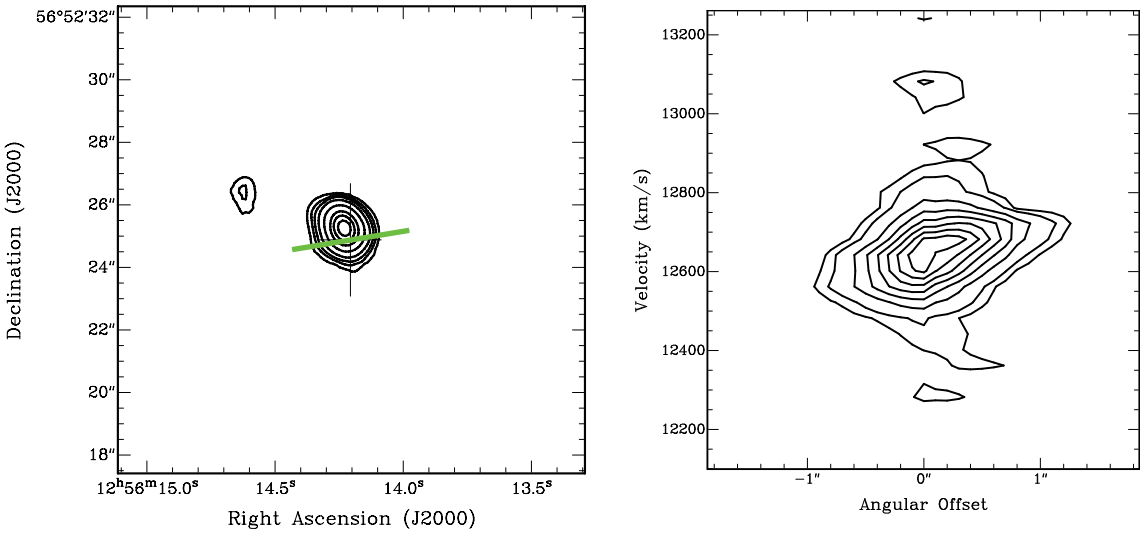

Figure B.16: Same as Figure B.1, but UGC 8058. The contours in the left figure are 5.8 Jy km s$^{-1}\times$ (1, 2, 3, 5, 10, 20, 30, 40) and the contours in the right figure are 19.8 mJy beam^{-1} $\times$ (3, 5, 10, 15, 20, 25, 30, 35).

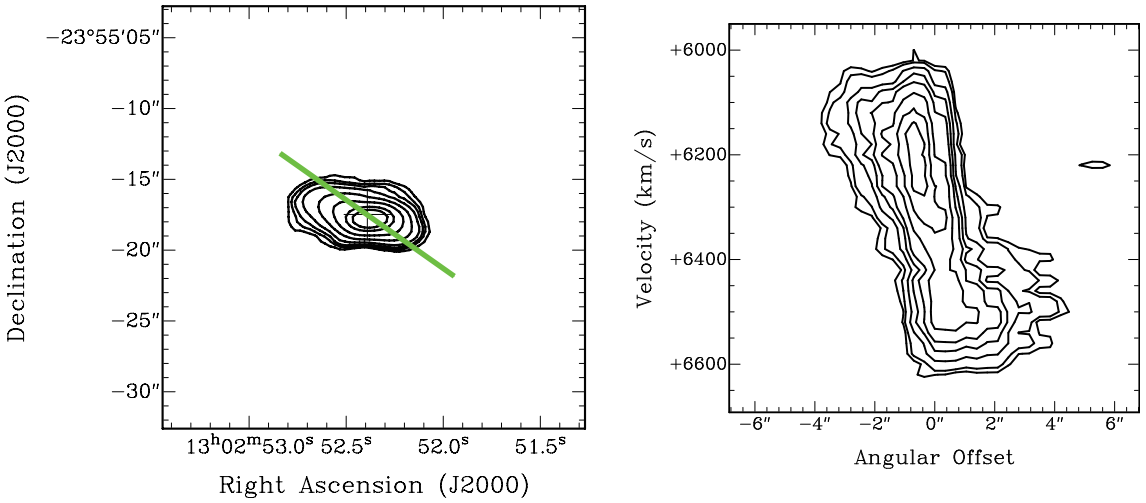

Figure B.17: Same as Figure B.1, but AM 1300-233. The contours in the left figure are 0.39 Jy km s$^{-1}\times$ (1, 2, 3, 5, 10, 20, 40, 60) and the contours in the right figure are 2.06 mJy beam^{-1} $\times$ (3, 5, 10, 15, 20, 30, 40, 50).

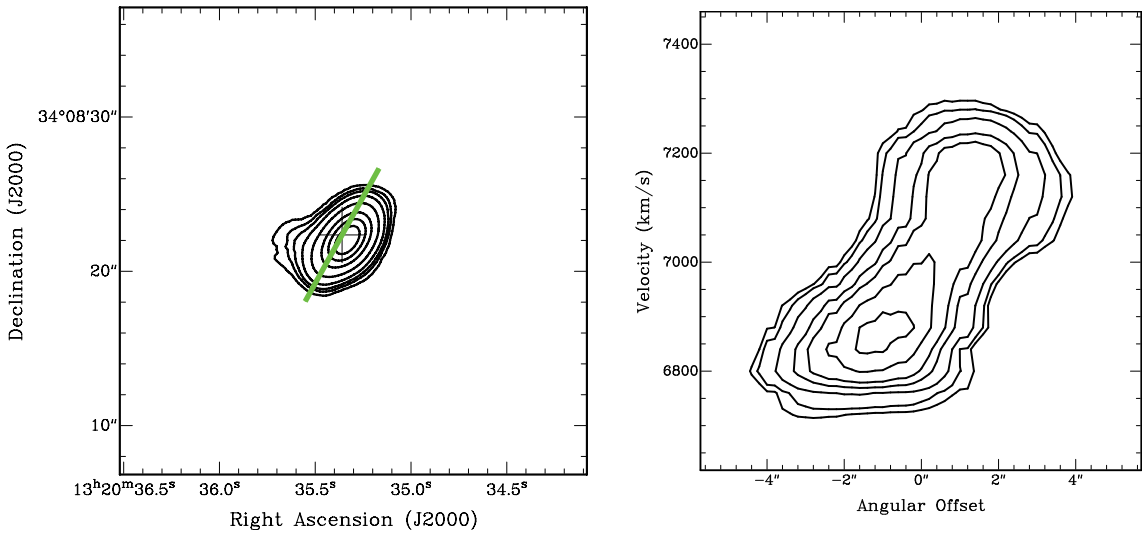

Figure B.18: Same as Figure B.1, but Arp 193. The contours in the left figure are 10 $\mathrm{Jy\ km\ s^{-1}}\times$ (1, 2, 3, 5, 10, 20, 30, 40) and the contours in the right figure are 23.0 mJy beam^{-1} $\times$ (3, 5, 10, 20, 30, 50, 75).

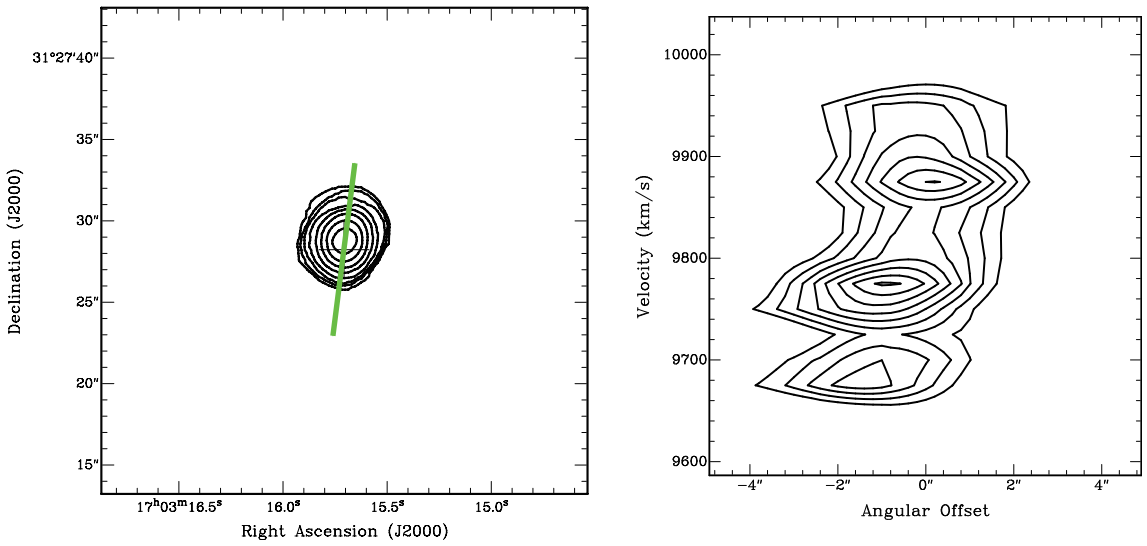

Figure B.19: Same as Figure B.1, but UGC 10675. The contours in the left figure are 2.4 $\mathrm{Jy\ km\ s^{-1}}\times$ (1, 2, 3, 4, 5, 6, 7, 8) and the contours are 18.0 mJy beam^{-1} $\times$ (3, 4, 5, 6, 7, 8, 9, 10).

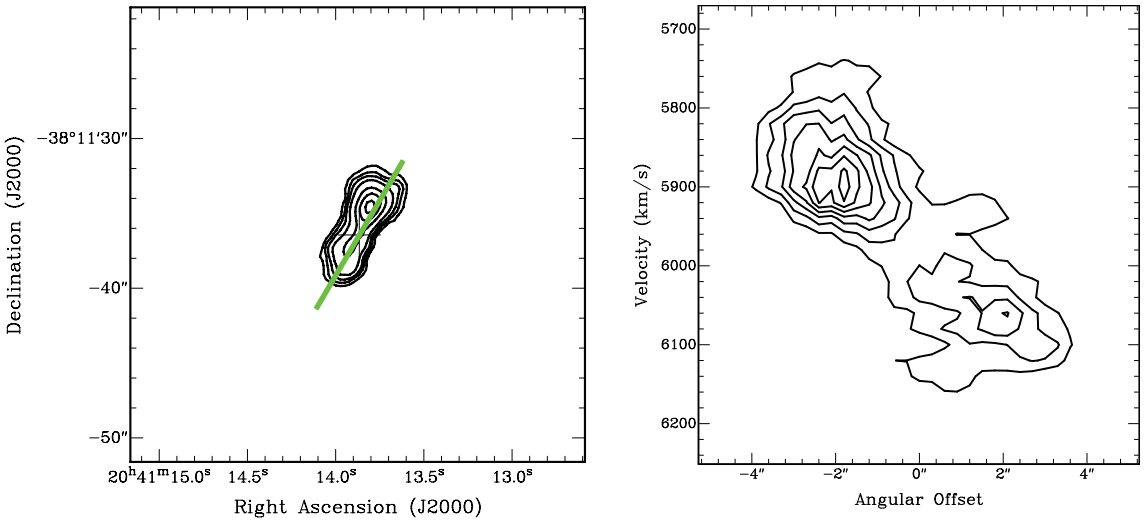

Figure B.20: Same as Figure B.1, but AM 2038-382. The contours in the left figure are 0.37 Jy km s$^{-1}\times$ (1, 2, 3, 5, 10, 15, 20) and the contours in the right figure are 2.97 mJy beam^{-1} $\times$ (3, 5, 7, 9, 11, 13, 15).

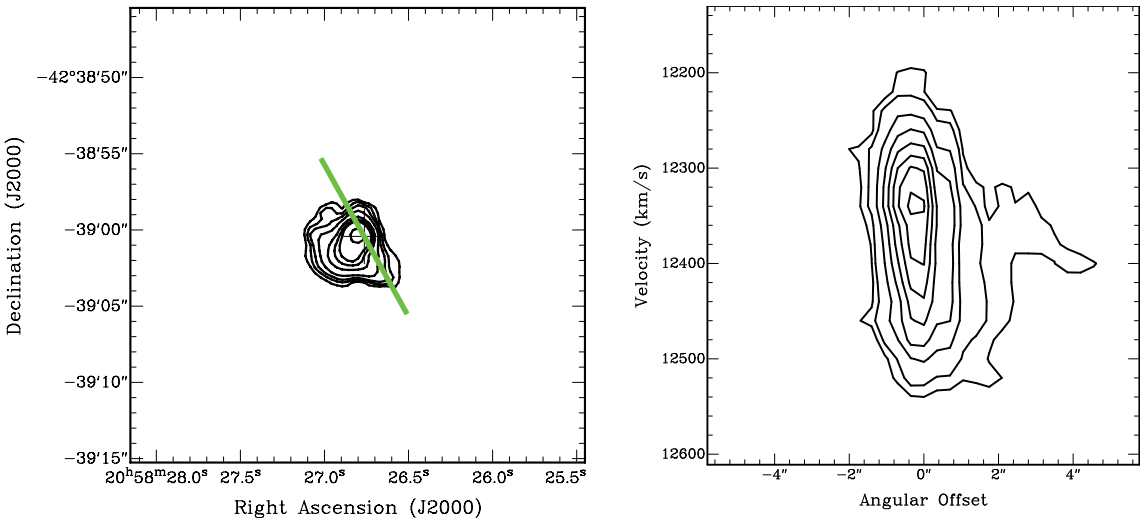

Figure B.21: Same as Figure B.1, but AM 2055-425. The contours in the left figure are 0.31 Jy km s$^{-1}\times$ (1, 2, 3, 5, 10, 15, 20, 30) and the contours in the right figure are 2.34 mJy beam^{-1} $\times$ (3, 5, 10, 15, 20, 25, 30, 35).

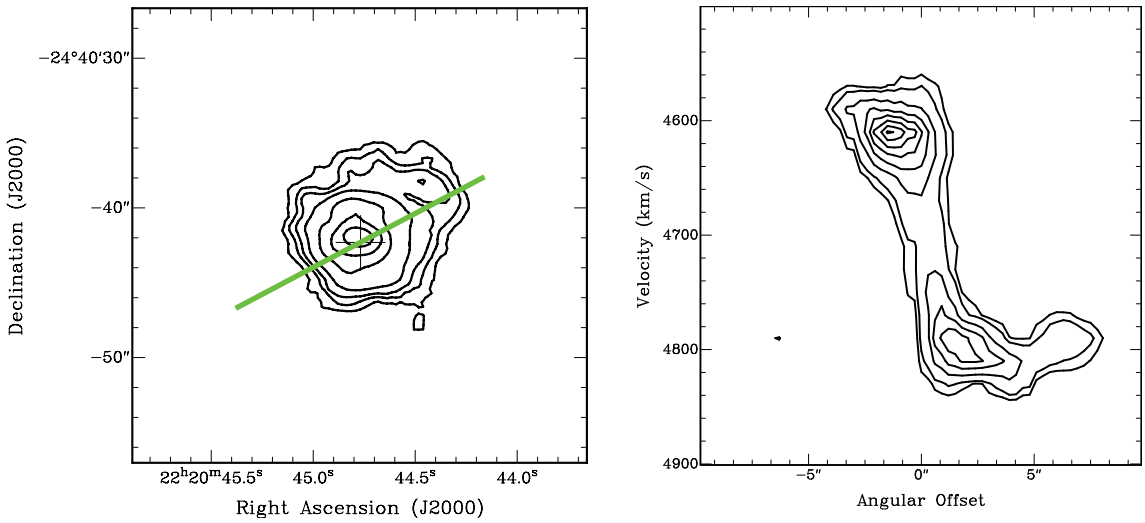

Figure B.22: Same as Figure B.1, but NGC 7252. The contours in the left figure are 0.37 Jy km s$^{-1}\times$ (1, 2, 3, 5, 10, 15, 20) and the contours in the right figure are 3.36 mJy beam^{-1} $\times$ (3, 5, 10, 15, 20, 25, 30, 35).

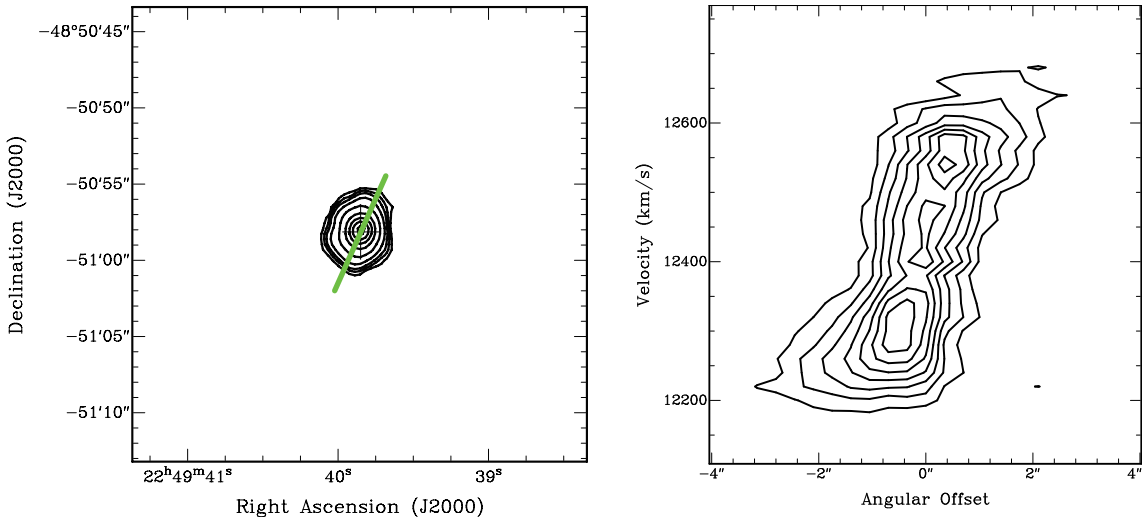

Figure B.23: Same as Figure B.1, but AM 2246-490. The contours in the left figure are 0.30 Jy km s$^{-1}\times$ (1, 2, 3, 5, 10, 20, 30, 40, 50) and the contours in the right figure are 2.34 mJy beam^{-1} $\times$ (3, 6, 9, 12, 15, 18, 21).

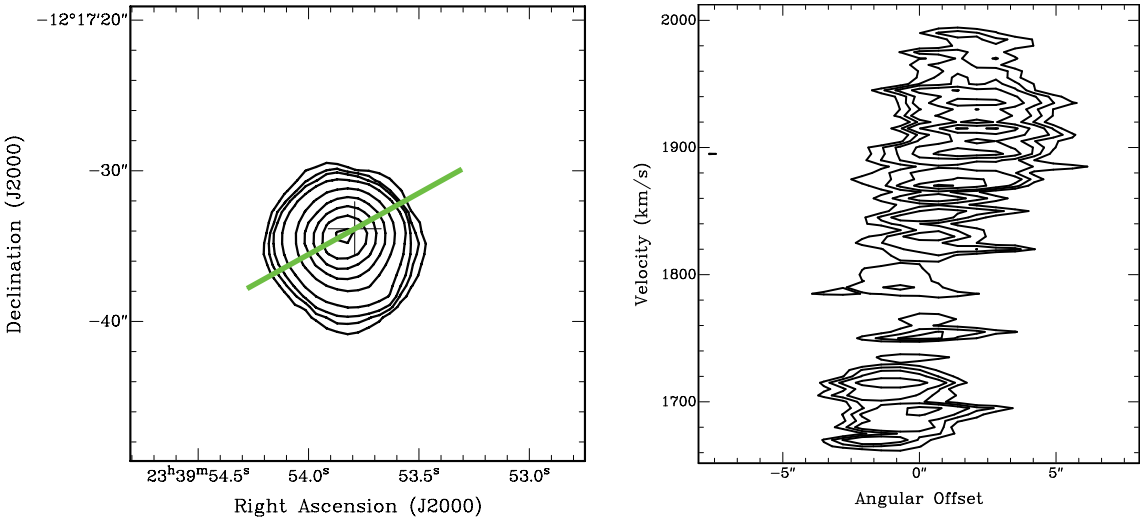

Figure B.24: Same as Figure B.1, but NGC 7727. The contours in the left figure are 0.22 $\mathrm{Jy\ km\ s^{-1}}\times$ (1, 2, 3, 5, 10, 15, 20, 25, 30) and the contours in the right figure are 4.36 mJy beam^{-1} $\times$ (3, 4, 5, 7, 9, 11).

Appendix C

Fitting and Modeling Tests for the Reproducibility of Velocity Fields

We have conducted three tests for the reproducibility of velocity fields under different conditions, using the AIPS's tasks. AIPS is a software package for calibration, imaging, and data analysis on astronomical data. We use two AIPS's tasks, GAL and MODVF, to quantify velocity fields. The task GAL reads a velocity field and calculates parameters specifying the orientation and the rotation curve of the object. If the velocity field consists of N data points, the parameters are determined by GAL using a nonlinear least squares fitting to N data points. The task MODVF creates a modeled velocity field based on the result from GAL, or information given by the user. The user inputs four initial parameters of the reference disk; (1) the radii, (2) the rotation velocities at the radiii, (3) the warp angle, and (4) the twisting angle.

C.1 TEST 1: Initial Values

The AIPS's task GAL estimates the rotation curve of a input galaxy. The users needs to assign the initial values of these parameters. A good combination of initial values speeds up the procedure, whereas a bad one will cause the fit to diverge and result in failure. In order to investigate the initial value dependence of the final estimates, we have conducted a test to determine the five basic input parameters (central coordinates (X, Y), inclination θ, position angle ϕ, and systemic velocity $V_{\rm sys}$) of a galaxy velocity field, using 32 combinations of the initial values.

First, we create a simple velocity field of a galactic gas disk with circular motion, using the parameters listed in Table C.1 and assuming that the rotational velocity monotonically increases at the radius $r < 6''$and it is constant at $r \geq 6''$ (The maximum radius $r_{\rm max}$ is $15''$; hereafter MODEL 1). The velocity field and the rotation curve of MODEL 1 are presented in Figure C.1. We assume sets of initial values which are close to the parameters of MODEL 1, and then ran the task GAL, using a constant rotational velocity over the whole galaxies ($0''\leq r \leq 15''$).

Table C.1: Basic Parameters of MODEL 1

central coordinate in coordinates	($0^{\rm h}0^{\rm m}0^{\rm s}$, $0°0'0''$)
central coordinate in pixels	(50.0, 50.0)
position angle of the disk	0.0°
inclination of the disk	30.0°
systemic velocity	1000.0 km s^{-1}
maximum rotation velocity	300.0 km s^{-1}
pixel scale	$1''$/ 1 pix

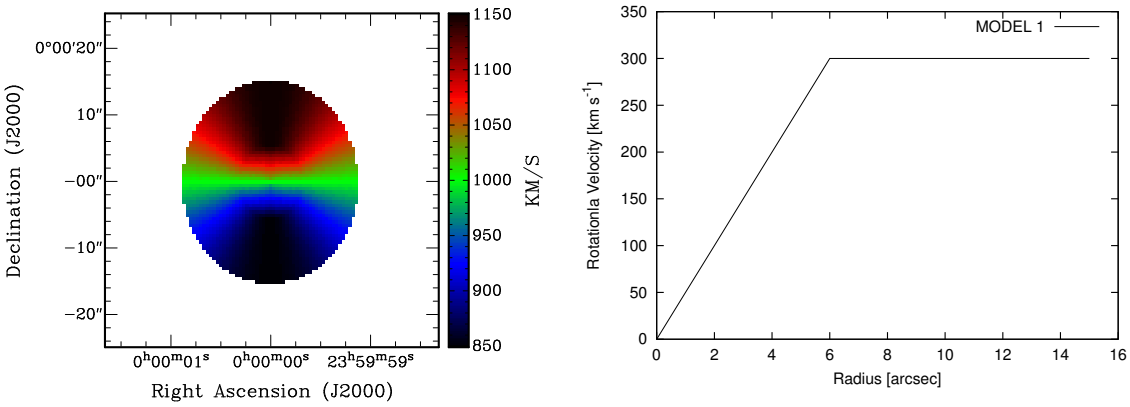

Figure C.1: The velocity field (left) and rotation curve (right) of MODEL 1.

The fitting results are shown in Table C.2. The central coordinates are determined to be 50.0 ± 1.1. The position angle is accurately estimated in all cases. The inclination is estimated to range between 28.°9 and 29.°9, which are slightly smaller than the true inclination of MODEL 1. The systemic velocities are determined to be 1000.0 ± 0.5 km s^{-1}. In case of choosing initial values which are close

Table C.2: Fitting Results for the initial value dependence

	initial values					fitting results					
	X	Y	ϕ	θ	V_{sys}	X	Y	ϕ	θ	V_{sys}	V_{max}
ID	[pix]	[pix]	[deg]	[deg]	[km s^{-1}]	[pix]	[pix]	[deg]	[deg]	[km s^{-1}]	[km s^{-1}]
1	55.0	55.0	5.0	35.0	1050.0	50.2	50.0	0.0	29.9	1000.0	289.0
2	45.0	55.0	5.0	35.0	1050.0	49.8	50.0	0.0	29.9	1000.0	289.0
3	55.0	45.0	5.0	35.0	1050.0	50.2	50.0	0.0	29.9	1000.0	289.2
4	55.0	55.0	355.0	35.0	1050.0	50.2	50.0	0.0	29.9	1000.0	289.0
5	55.0	55.0	5.0	25.0	1050.0	50.2	50.0	0.0	29.9	1000.0	289.1
6	55.0	55.0	5.0	35.0	950.0	50.2	50.0	0.0	29.9	1000.0	289.0
7	45.0	45.0	5.0	35.0	1050.0	49.8	50.0	0.0	29.9	1000.0	289.2
8	45.0	55.0	355.0	35.0	1050.0	49.8	50.0	0.0	29.9	1000.0	289.2
9	45.0	55.0	5.0	25.0	1050.0	49.8	50.0	0.0	29.9	1000.0	289.2
10	45.0	55.0	5.0	35.0	950.0	49.8	50.0	0.0	29.9	1000.0	289.0
11	55.0	45.0	355.0	35.0	1050.0	50.2	50.0	0.0	29.9	1000.0	289.2
12	55.0	45.0	5.0	25.0	1050.0	50.2	50.0	0.0	29.9	1000.0	289.3
13	55.0	45.0	5.0	35.0	955.0	50.2	50.0	0.0	29.9	1000.0	289.2
14	55.0	55.0	355.0	25.0	1050.0	50.2	50.0	0.0	29.9	1000.0	289.2
15	55.0	55.0	355.0	35.0	950.0	50.2	50.0	0.0	29.9	1000.0	289.0
16	55.0	55.0	5.0	25.0	950.0	50.2	50.0	0.0	29.9	1000.0	289.1
17	45.0	45.0	355.0	35.0	1050.0	48.9	50.1	0.0	29.0	1000.3	296.7
18	45.0	45.0	5.0	25.0	1050.0	49.8	50.0	0.0	29.9	1000.0	289.2
19	45.0	45.0	5.0	35.0	955.0	49.8	50.0	0.0	29.9	1000.0	289.2
20	45.0	55.0	355.0	25.0	1050.0	49.8	50.0	0.0	29.9	1000.0	289.1
21	45.0	55.0	355.0	25.0	950.0	49.8	50.0	0.0	29.9	1000.0	289.2
22	45.0	55.0	5.0	25.0	950.0	49.8	50.0	0.0	29.9	1000.0	289.2
23	55.0	35.0	345.0	25.0	1050.0	50.2	50.0	0.0	29.9	1000.0	289.2
24	55.0	45.0	355.0	35.0	1050.0	50.2	50.0	0.0	29.9	1000.0	289.2
25	50.0	55.0	355.0	25.0	950.0	50.2	50.0	0.0	29.9	1000.0	289.3
26	55.0	55.0	355.0	25.0	950.0	50.2	50.0	0.0	29.9	1000.0	289.2
27	45.0	45.0	355.0	25.0	1050.0	48.9	49.9	0.0	28.9	999.5	296.8
28	45.0	45.0	355.0	35.0	950.0	48.9	50.1	0.0	29.0	1000.3	296.7
29	45.0	45.0	5.0	25.0	950.0	48.9	50.1	0.0	29.0	1000.2	296.5
30	45.0	55.0	355.0	25.0	950.0	49.8	50.0	0.0	29.9	1000.0	289.1
31	55.0	45.0	355.0	25.0	950.0	51.1	50.1	0.0	29.0	1000.2	296.6
32	45.0	45.0	355.0	25.0	950.0	48.9	49.9	0.0	28.9	999.5	296.8

NOTE—(X, Y): the central coordinate in pixels, θ: position angle, ϕ: inclination, V_{sys}: systemic velocity, V_{max}: the maximum rotational velocity.

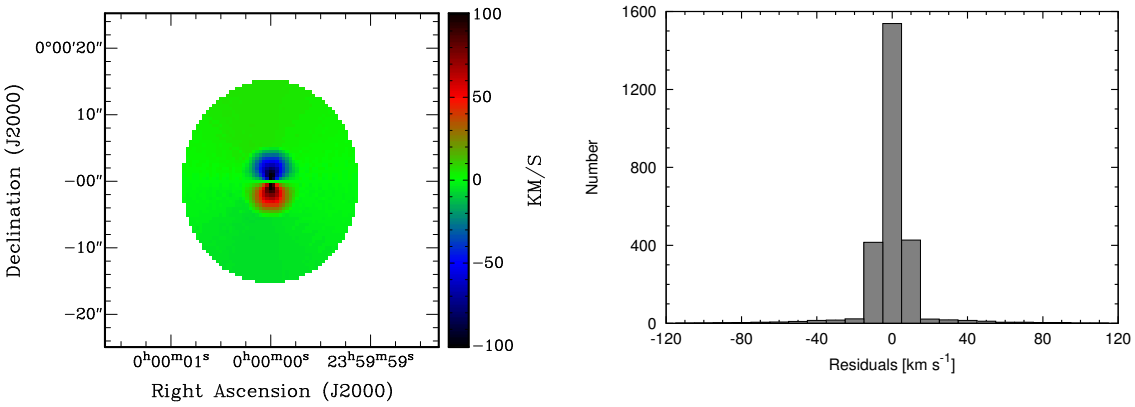

Figure C.2: (left) The residual map created by subtracting the model of the fitting result (ID = 1; see Table C.2) from MODEL 1. (right) Number distribution of the residuals seen in the residual map.

to the true values of an input velocity field, there is no significant difference between the estimated values by fitting and the true values. However, if we choose initial values which are far from the true values of an input velocity field, the fitting program fails to determine the fitting parameters.

We create a velocity field model using the fitting results with the AIPS's task MODVF to verify the accuracy of the fitting. We subtract the velocity field model from MODEL 1 and make a residual map. The residual map and number distribution of the residuals in the case of ID = 1 (see Table C.2) are shown in Figure C.2. Though large residuals are seen in the inner region ($r < 6''$), 95.5 % (2σ) of residuals are distributed in the range of $\pm$ 29 $\mathrm{km\ s^{-1}}$. The residuals in the outer region ($r \geq 6''$) are less than $\pm$ 10 $\mathrm{km\ s^{-1}}$. The residual maps and the number distribution of residuals in other cases (ID = 2–32) are quite similar to those in the case of ID = 1. This is expected, as the central region ($r < 6''$) is fit by a constant rotational velocity where it is in fact rigid rotation.

We also present the maximum rotational velocity ($\mathrm{V_{max}}$) estimated by fitting in Table C.2. The estimated $\mathrm{V_{max}}$ is approximately 10 km $\mathrm{s^{-1}}$ smaller than the true $\mathrm{V_{max}}$ of MODEL 1. We run the fitting program, assuming a constant rotational velocity over the whole galaxies ($0'' \leq r \leq 15''$), but the rotational velocity of MODEL 1 is not constant. The rotational velocity of MODEL 1 at $r < 6''$ is smaller than the constant rotational velocity seen in the outer region ($r \geq 6''$) and large residuals are seen in the inner region ($r < 6''$) as shown in Figure C.2. Thus it is expected that the underestimations of $\mathrm{V_{max}}$ are caused by this non-constant rotational velocity in the inner region.

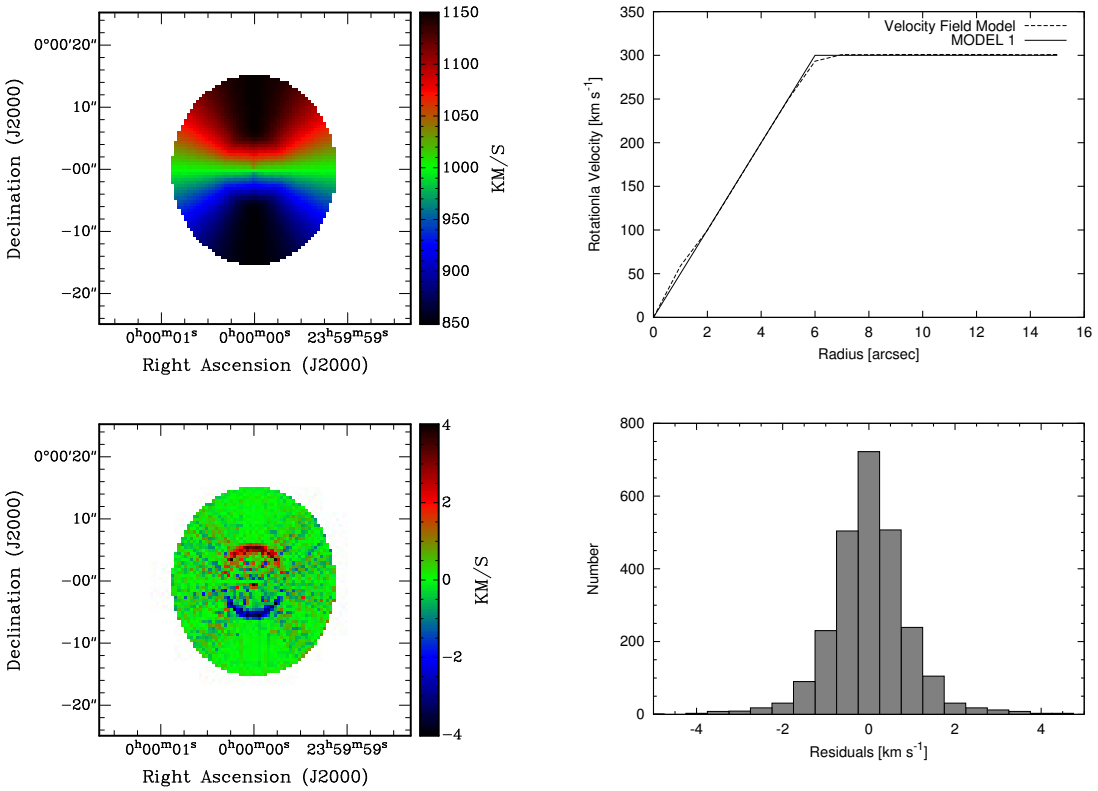

Figure C.3: Fitting results of TEST 2. (upper-left) The velocity field model created based on the fitting result. (upper-right) The rotation curves of the velocity field model (upper-left) and MODEL 1. (bottom-left) The residual map created by subtracting the velocity field model (upper-left) from MODEL 1. (bottom-right) Number distribution of the residuals seen in the residual map.

C.2 TEST 2: Fitting with Concentric Rings

As shown in TEST 1 (Figure C.2), large residuals are seen in the inner region of the gas disk, when we run the fitting program, assuming that the rotational velocity is constant over the whole galaxy. In order to decrease the residuals, we use a different fitting program. The task GAL can divide the velocity field into a number of concentric rings with an equal width of a ring, and then determine rotational velocities, assuming a constant velocity within each concentric ring. We fit the velocity field of MODEL 1 with concentric rings ($\Delta\, r$ = 1″) using the fitting results (ID=1; Table C.2) as new initial values. This time, we fix the initial values and only estimate the rotational velocities.

The rotation curve estimated by the fitting are shown in Figure C.3 (upper-right), and the velocity field model created based on the fitting result is shown in Figure C.3 (upper-left). They are similar to the rotation curve and velocity field of MODEL 1. In addition, we find that the residuals decrease in the residual map (Figure C.3 (bottom-left)), compared to the residual map of TEST 1 (Figure C.2), though slightly large, nearly symmetric residuals are seen at the radius of $6''$. As shown in the number distribution of the residuals (Figure C.3 (bottom-right)), 95.5 % (2σ) of residuals are distributed in the range of $2\ \mathrm{km\,s^{-1}}$ and the maximum residual is 4.7 $\mathrm{km\,s^{-1}}$. Therefore, we use a two-step fitting procedure. Firstly, we run a fitting program to determine the geometry of an input galaxy, such as a position angle and inclination, assuming that the rotational velocity is constant over the whole galaxy, a procedure identical to TEST 1. Secondly, we run a fitting program with concentric rings to determine the rotation curve as in TEST 2, in order to make out fitting robust.

C.3 TEST 3: Non-Elliptical Structure

We investigate whether a fitting program is successful when we apply it to velocity fields with non-elliptical structure such as clumpy structures. We create three types of velocity fields (MODEL 2A, 2B, 2C), which are part of MODEL 1. MODEL 1 is a velocity field of a gas disk in a galaxy. The velocity fields of MODEL 2A, 2B, 2C are shown in Figure C.4 (left column). These velocity field models show circular motion, but their shapes are neither circles nor ellipticals.

- **MODEL 2A:** The velocity field consists of one gas component. The majority of the gas comes from the north part of the galactic disk. The gas is associated with the galactic center.

- **MODEL 2B:** The velocity field consists of two gas components. The larger component is located at the north part of the galactic disk (high-velocity), and the smaller component is located at the south part (low-velocity). The gas is associated with the galactic center.

- **MODEL 2C:** The velocity field consists of two gas components. This velocity field is similar to MODEL 2B, but the gas is not associated with the galactic center.

The fitting programs are successful when we apply them to MODEL 2A, 2B, 2C, but the accuracy of the fitting parameters are different in each model.

- **MODEL 2A:** The accuracy of the fitting parameters is the highest of three models, but it is lower compared to TEST 2. The galactic center is determined to be a point shifted $1''$ towards the north from the true galactic center, suggesting that the determination of a center position is affected by the distribution of components. The position angle and inclination are estimated to be $2\overset{\circ}{.}2$ and $37\overset{\circ}{.}0$, respectively. The maximum rotational velocity is estimated to be smaller than the true value of MODEL 2A due to a high inclination estimated by the first fitting. The residual map shows negative residuals in the majority of the component.

- **MODEL 2B:** The accuracy of the fitting parameters is lower compared to MODEL 2A. The galactic center is accurately estimated, but the deviation of the estimated position angle and inclination from the true values become large. The position angle and inclination are estimated to be $354\overset{\circ}{.}1$ (= $-5\overset{\circ}{.}9$) and $48\overset{\circ}{.}6$, respectively. As is the case with MODEL 2A, the maximum rotational velocity is estimated to be smaller than the true value of MODEL 2B due to a high inclination. The effect of the bad estimation of the position angle is seen in the residual maps.

- **MODEL 2C:** The accuracy of the fitting parameters is the lowest of three models. The galactic center is set to a point shifted $6''$towards the north-west from the true galactic center, which lies in the larger component. It seems that it is difficult to determine correctly the position of a galactic center in the case where the gas is not associated with the galactic center. The position angle and inclination are estimated to be $8\overset{\circ}{.}1$ and $11\overset{\circ}{.}2$, respectively. The maximum rotational velocity is estimated to be significantly larger ($\sim$840 $\mathrm{km\ s^{-1}}$) than the true value of MODEL 2C (300 $\mathrm{km\ s^{-1}}$) due to a very low inclination estimated by the first fitting. In this case, the kinematic parameters are tentatively estimated by the fitting programs, but these parameters are far from the true values of MODEL 2C.

According to the tests for the reproducibility of velocity fields, we conclude the following:

(1) It is better that we use a two-step fitting to estimate the kinematical parameters. The first step is to run a fitting program, assuming that the rotational velocity is constant over the whole galaxy. From this, we can determine the geometry of galaxies such as position angles and inclinations. The second step is to run a fitting program with concentric rings in order to determine the rotation curve. This fitting method is used by Koda et al. (2002).

(2) It is important to choose initial values which are close to the true values of an input velocity

field. In such a case, there is no significant difference between the estimated values and the true values. However, if we choose initial values which are far from the true values of an input velocity field, the fitting program fail to determine the fitting parameters.

(3) The determination of a galactic center is affected by the distribution of the gas, and it might be difficult to determine correctly a position of a galactic center in the case where the gas is not associated with the galactic center. Thus it is better to assume the galactic center coordinates determined from other observations, and that the molecular gas rotate around it.

(4) Estimation of inclination is more difficult than position angles. The estimation of an inclination may contain large errors, especially in the case where input velocity fields are not simple.

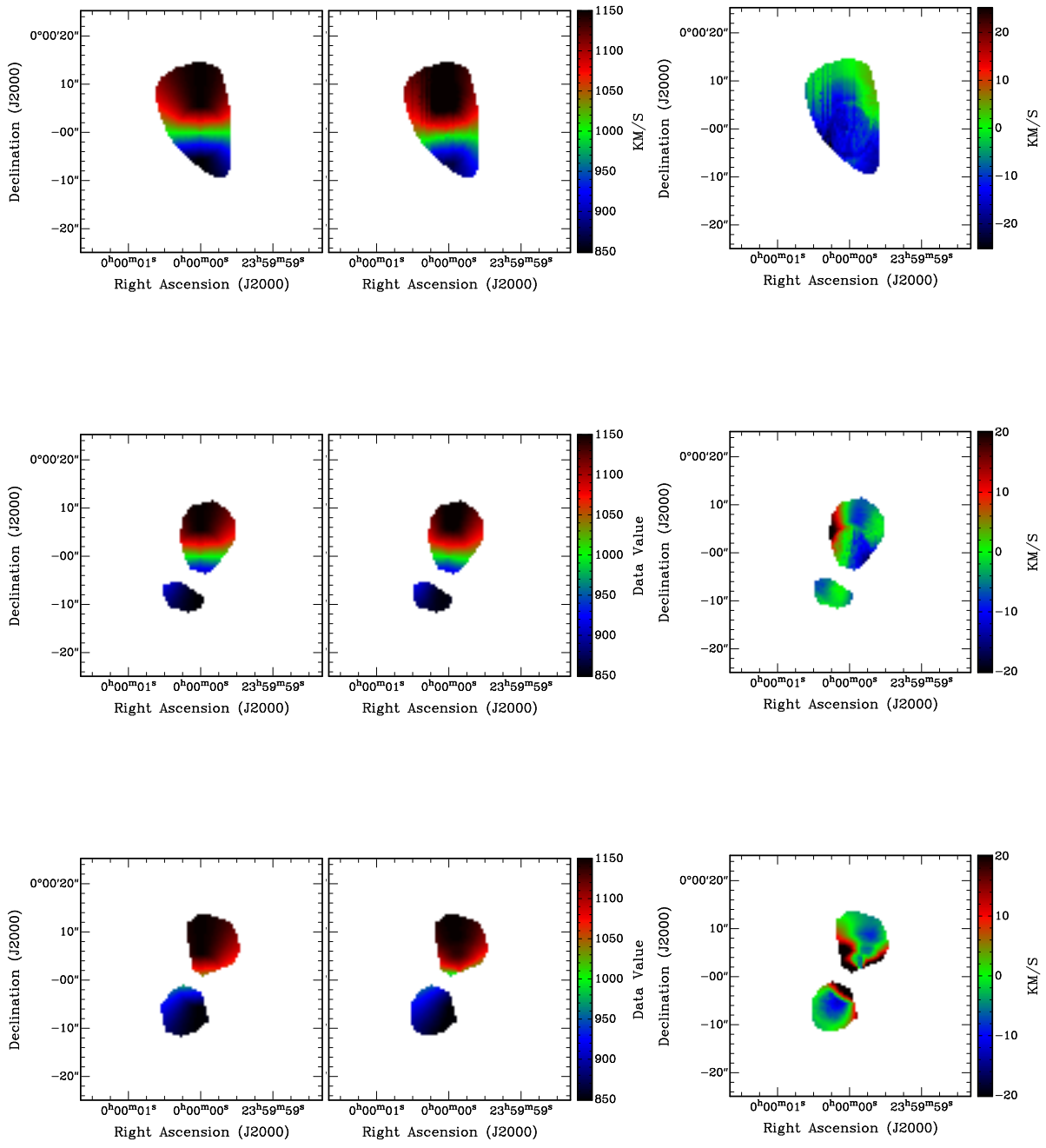

Figure C.4: Fitting results of TEST 3 (upper: MODEL 2A, middle: MODEL 2B, bottom: MODEL 2C). (left-column) The velocity fields of MODELs. (middle-column) The velocity field models created based on the fitting result. (right-column) The residual maps created by subtracting the velocity field model (middle) from MODELs (left).

Appendix D

Basic Definitions

D.1 Intensity and Flux Density

Electromagnetic radiation in the radio windows is a wave phenomenon, but we consider that the radiation travels in straight lines called $rays$ when the scale of the system greatly exceeds the wavelength. We consider an infinitesimal $d\sigma$ normal to the direction of the given ray (**n**). The infinitesimal power dE crossing $d\sigma$ in the frequency range $d\nu$ and in the elements of solid angle $d\Omega$ during the time interval dt is given by

$$dE = I_\nu \cos\theta \; d\sigma \; dt \; d\Omega \; d\nu, \tag{D.1}$$

where θ is the angle between the direction normal to $d\sigma$ and the direction to $d\Omega$, and I_ν is the **specific intensity**, simply **intensity**, or **brightness**. The dimensions of the specific intensity are erg s^{-1} cm^{-2} Hz^{-1} sr^{-1} or W m^{-2} Hz^{-1} sr^{-1} (1 erg = 10^{-7} W·s). The specific intensity depends on location in space, on direction, and on frequency.

The **flux density** (simply **flux**) is the amount of radiant energy transferred across unit area in unit frequency interval in unit time. The differential amount of flux (dS_ν) from the solid angle $d\Omega$ is

$$dS_\nu = I_\nu \cos\theta \; d\Omega. \tag{D.2}$$

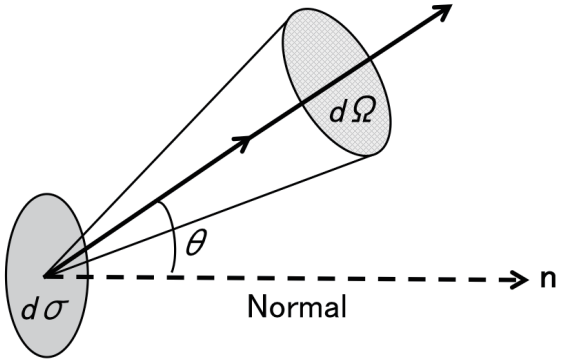

Figure D.1: Schematic diagram to illustrate the definition of the specific intensity.

Thus, the total flux S_ν is obtained by integrating Equation (D.2) over all solid angles:

$$S_\nu = \int I_\nu \cos\theta \, d\Omega. \tag{D.3}$$

The dimensions of the flux density are erg s^{-1} cm^{-2} Hz^{-1} or W m^{-2} Hz^{-1}. In radio astronomy, the flux density is usually measured in units of the Jansky [Jy], which is defined as

$$1 \text{ Jy} = 10^{-26} \text{ W m}^{-2} \text{ Hz}^{-1} = 10^{-23} \text{ erg s}^{-1} \text{ cm}^{-2} \text{ Hz}^{-1}. \tag{D.4}$$

We consider a sphere with an uniform brightness I_ν and a radius R. According to Equation (D.3), the total flux received by an observer at a distance r is

$$S_\nu = \int_{\Omega_s} I_\nu \cos\theta \, d\Omega = I_\nu \int_0^{2\pi} d\phi \int_0^{\theta_c} \sin\theta \cos\theta \, d\theta \tag{D.5}$$

where $\sin\theta_c = R/r$ is the angle at which a ray from an observer is tangent to the sphere. Then we obtain

$$S_\nu = \pi \, I_\nu \sin^2\theta_c = I_\nu \frac{\pi R^2}{r^2}. \tag{D.6}$$

We define $\Delta\Omega = \pi R^2/r^2$ as the area subtended by a sphere at a distance r, which is the $solid\ angle$. It follows that

$$S_\nu = I_\nu \, \Delta\Omega \tag{D.7}$$

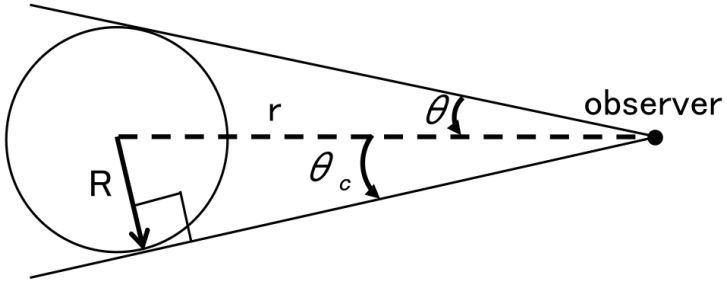

Figure D.2: Total flux from an uniformly bright sphere

D.2 Brightness Temperature

The spectral distribution of the radiation of a blackbody in thermodynamic equilibrium is given by the Planck law

$$B_\nu(T) = \frac{2h\nu^3}{c^2}\frac{1}{e^{\frac{h\nu}{kT}}-1}, \tag{D.8}$$

where c is the speed of light, h is the Planck constant, and k is the Boltzmann constant. This function gives the emitted power per unit frequency interval. The dimensions of the spectral distribution are the same as the specific intensity. Assuming $h\nu \ll kT$, the exponential can be expanded

$$e^{\frac{h\nu}{kT}} \cong 1 + \frac{h\nu}{kT} + \cdots \tag{D.9}$$

In this case, Equation (D.8) results in

$$\begin{aligned} B_\nu(T) &= \frac{2h\nu^3}{c^2}\frac{1}{e^{\frac{h\nu}{kT}}-1} \\ &\simeq \frac{2h\nu^3}{c^2}\frac{1}{1+\frac{h\nu}{kT}-1} \\ &= \frac{2h\nu^2}{c^2}kT. \end{aligned} \tag{D.10}$$

This is the **Rayleigh-Jeans law**, which can apply at low frequencies (in radio range).

The specific intensity of an extended source at a certain frequency is measured the thermodynamic temperature of the blackbody having the same brightness at that frequency. Thus we define the **brightness temperature** $T_b(\nu)$ linked by the relation:

$$B_\nu(T_b) = I_\nu. \tag{D.11}$$

This relation is useful in radio astronomy, where the Rayleigh–Jeans law is usually applicable. Inserting the Rayleigh-Jeans law (Equation (D.10)) into Equation (D.11), the brightness temperature is

$$T_b = \frac{c^2}{2k}\frac{1}{\nu^2}I_\nu. \tag{D.12}$$

Using Equation (D.7), we have

$$S_\nu = \frac{2k\nu^2}{c^2}T_b\Delta\Omega. \tag{D.13}$$

This equation shows the relation between the flux density S_ν and the brightness temperature T_b.

D.3 The CO Line Luminosity

The CO line luminosity can be expressed in several ways. From energy conservation law, the relation between monochromatic CO line luminosity $L_{\rm CO}(\nu_{\rm rest})$ and observed flux density $S(\nu_{\rm obs})$ is given by

$$\nu_{\rm rest}\ L_{\rm CO}(\nu_{\rm rest}) = 4\pi\ D_{\rm L}^2\ \nu_{\rm obs}\ S(\nu_{\rm obs}), \tag{D.14}$$

where $\nu_{\rm rest}$ is the rest frequency, $\nu_{\rm obs}$ is the observing frequency (= $\nu_{\rm rest}(1+z)^{-1}$), and $D_{\rm L}$ is the luminosity distance. Integrating both sides of Equation (D.14) with respect to $\nu_{\rm rest}$ and $\nu_{\rm obs}$, respectively, we have

$$\begin{aligned}
L_{\rm CO} &= \int L_{\rm CO}(\nu_{\rm rest})\ d\nu_{\rm rest} \\
&= \int 4\pi\ D_{\rm L}^2\ S(\nu_{\rm obs})\ d\nu_{\rm obs} \\
&= 4\pi\ D_{\rm L}^2 \int S\ \frac{\nu_{\rm obs}}{c} dv \\
&= 4\pi\ D_{\rm L}^2 \int S\ \frac{\nu_{\rm rest}}{(1+z)c} dv \\
&= \frac{4\pi}{c}\ \nu_{\rm rest}\ (1+z)^{-1}\ D_{\rm L}^2 \int S\ dv \\
&= \frac{4\pi}{c}\ S_{\rm CO}\ \Delta v\ \nu_{\rm rest}\ (1+z)^{-1}\ D_{\rm L}^2 \\
&= 1.04\times10^{-3}\Big[\frac{S_{\rm CO}\ \Delta v}{\rm Jy\ km\ s^{-1}}\Big]\Big[\frac{\nu_{\rm rest}}{\rm GHz}\Big]\Big[\frac{D_{\rm L}}{\rm Mpc}\Big]^2(1+z)^{-1}\ [L_\odot],
\end{aligned} \tag{D.15}$$

The CO line luminosity is often expressed in units of K km s^{-1} pc^2 as

$$L'_{\rm CO} = T_{\rm b}\Delta v\ \Omega_{\rm s} D_{\rm A}^2, \tag{D.16}$$

where $T_{\rm b}\ \Delta v$ is the velocity-integrated brightness temperature, $\Omega_{\rm s}$ is the solid angle subtended by the source, and $D_{\rm A}$ is the angular size distance (= $D_{\rm L}(1+z)^{-2}$). "$\Omega_{\rm s}\cdot D_{\rm A}^2$" corresponds to the source area. The observed integrated line intensity is given by

$$I_{\rm CO} = \int T_{\rm mb}\ {\rm d}v = T_{\rm mb}\Delta v, \tag{D.17}$$

where $T_{\rm mb}$ is the main beam brightness temperature, which decreases with redshift of a source. Thus we have to correct $I_{\rm CO}$ by the following equation:

$$T_{\rm b}\Delta v\ \Omega_{\rm s} = I_{\rm CO}\Omega_{\rm s\star b}(1+z), \tag{D.18}$$

where $\Omega_{\rm s\star b}$ is the solid angle of the source convolved with the telescope beam, because the photon energy is proportional to the frequency ($E = h\nu$) and the rest frequency is given by $\nu_{\rm rest} = \nu_{\rm obs}$ (1+z). Then the CO line luminosityis expressed as

$$\begin{aligned} L'_{\rm CO} &= T_{\rm b}\Delta v\ \Omega_{\rm s} D_{\rm A}^2 \\ &= I_{\rm CO}\Omega_{\rm s\star b}(1+z)D_{\rm A}^2 \\ &= I_{\rm CO}\Omega_{\rm s\star b}D_{\rm L}^2(1+z)^{-3} \\ &= 23.5\Big[\frac{\Omega_{\rm s\star b}}{\rm arcsec^2}\Big]\Big[\frac{D_{\rm L}}{\rm Mpc}\Big]^2\Big[\frac{I_{\rm CO}}{\rm K\ km\ s^{-1}}\Big](1+z)^{-3} \quad [{\rm K\ km\ s^{-1}}]. \end{aligned} \tag{D.19}$$

If a source is much smaller than the beam size, $\Omega_{\rm s\star b} \approx \Omega_b$.

The relation between the main beam temperature $T_{\rm mb}$ [K] and the flux density S [Jy] is

$$T_{\rm mb} = \frac{c^2}{2k\nu_{\rm obs}^2\Omega_{s\star b}}S. \tag{D.20}$$

The CO line luminosity can be also expressed for a source of any size, using Equations (D.16), (D.17) and (D.18),

$$\begin{aligned} L'_{\rm CO} &= T_{\rm b}\Delta v\Omega_{\rm s}D_{\rm A}^2 \\ &= I_{\rm CO}\Omega_{\rm s\star b}(1+z)D_{\rm A}^2 \\ &= T_{\rm mb}\Delta v\Omega_{\rm s\star b}D_{\rm L}^2(1+z)^{-3} \\ &= \frac{c^2}{2k}S_{\rm CO}\Delta v\nu_{\rm obs}^{-2}D_{\rm L}^2(1+z)^{-3} \\ &= 3.25\times10^7\Big[\frac{S_{\rm CO}\Delta v}{\rm Jy\ km\ s^{-1}}\Big]\Big[\frac{\nu_{\rm obs}}{\rm GHz}\Big]^{-2}\Big[\frac{D_{\rm L}}{\rm Mpc}\Big]^2(1+z)^{-3}\ [{\rm km\ s^{-1}pc^2}]. \end{aligned} \tag{D.21}$$

D.4 The CO Luminosity-to-H_2 Mass Conversion Factor

The CO luminosity-to-H_2 mass conversion factor $X_{\rm CO}$ is defined as

$$X_{\rm CO}\ [{\rm cm^{-2}\ (K\ km\ s^{-1})^{-1}}] = \frac{N_{\rm H_2}}{W_{\rm CO}}, \tag{D.22}$$

where $N_{\rm H_2}$ is the molecular gas column density and $W_{\rm CO}$ is the CO line integrated intensity measured in K km s^{-1}. Alternatively, the conversion factor $\alpha_{\rm CO}$ can be defined as the ratio of the molecular gas mass to the CO line luminosity:

$$\alpha_{\rm CO}\ [{\rm M_\odot\ pc^{-2}\ (K\ km\ s^{-1})^{-1}}] = \frac{M_{\rm gas}}{L_{\rm CO}}, \tag{D.23}$$

where $M_{\rm gas}$ is the molecular gas mass. These conversion factors, $X_{\rm CO}$ and $\alpha_{\rm CO}$, are related via

$$X_{\rm CO} = 6.3 \times 10^{19}\ \alpha_{\rm CO} \tag{D.24}$$

The conversion factor has been a controversial issue for a long time. Solomon & Barrett (1991) find that the conversion factor is roughly constant in the Milky Way and nearby spiral galaxies, and suggest that the conversion factor is $X_{\rm CO}$ = 2.2 $\times$ 10^{20} cm^{-2} (K km s^{-1})$^{-1}$, corresponding to $\alpha_{\rm CO}$ = 4.8 M$_\odot$ pc^{-2} (K km s^{-1})$^{-1}$. However, the conversion factor in gas-rich galaxies at high-z and local U/LIRGs is lower than the standard value in the Milk Way (e.g., $\alpha_{\rm CO} \sim$ 0.6–0.8; Downes & Solomon, 1998; Papadopoulos et al., 2012). In addition, the conversion factor in low-metallicity environments is larger than the standard value in the Milky Way (e.g., Wilson, 1995; Genzel et al., 2012)

Appendix E

The Kolmogorov-Smirnov Test

The Kolmogorov-Smirnov test (KS-test) determines whether two samples differ significantly. It is a method of hypothesis testing whether a one-dimensional probability distribution of a sample differs from a reference probability distribution (one-sample KS-test), or whether two one-dimensional probability distributions of samples differ (two-sample KS-test).

The two-sample KS-test is one of the most useful and general nonparametric methods for comparing two samples because it is sensitive to differences in both location and shape of the cumulative distribution functions of the two samples. The Kolmogorov-Smirnov statistic quantifies the distance between the cumulative distribution functions of two samples. The maximum deviation is defined as

$$D = \max|S_1(x) - S_2(x)| \tag{E.1}$$

where $S_1(x)$ and $S_2(x)$ are the cumulative distributions of the two sample. The significance probability (P) under null hypothesis (H_0) that the two samples are from the same parent population is given by

$$P(D) = Q\left(D\sqrt{\frac{n_1 n_2}{n1 + n_2}}\right) \tag{E.2}$$

$$Q(K) = 2\sum_{i=1}(-1)^{i-1}\exp(-2i^2K^2) \tag{E.3}$$

where n_1 and n_2 are the numbers of elements in the two samples. If $P(D)$ is less than a given level of statistical significance, the null hypothesis is rejected at level K.

Bibliography

Aalto, S., Johansson, L. E. B., Booth, R. S., & Black, J. H. 1991, A&A, 249, 323

Alatalo, K., Davis, T. A., Bureau, M., et al. 2013, MNRAS, 432, 1796

Albrecht, M., Chini, R., Krügel, E., Müller, S. A. H., & Lemke, R. 2004, A&A, 414, 141

Albrecht, M., Krügel, E., & Chini, R. 2007, A&A, 462, 575

Alloin, D., & Duflot, R. 1979, A&A, 78, L5

Andreani, P., Casoli, F., & Gerin, M. 1995, A&A, 300, 43

Annibali, F., Bressan, A., Rampazzo, R., Zeilinger, W. W., & Danese, L. 2007, A&A, 463, 455

Armus, L., Charmandaris, V., Bernard-Salas, J., et al. 2007, ApJ, 656, 148

Arp, H. 1966, Atlas of peculiar galaxies (Pasadena: California Inst. Technology, 1966)

Arp, H. C., & Madore, B. 1987, A catalogue of southern peculiar galaxies and associations (Cambridge ; New York : Cambridge University Press, 1987.)

Balick, B., Faber, S. M., & Gallagher, J. S. 1976, ApJ, 209, 710

Barger, A. J., Aragon-Salamanca, A., Ellis, R. S., et al. 1996, MNRAS, 279, 1

Barnes, J. E. 2002, MNRAS, 333, 481

Barnes, J. E., & Hernquist, L. 1992, ARA&A, 30, 705

Barnes, J. E., & Hernquist, L. E. 1991, ApJ, 370, L65

Beichman, C. A., Neugebauer, G., Habing, H. J., Clegg, P. E., & Chester, T. J., eds. 1988, Infrared astronomical satellite (IRAS) catalogs and atlases. Volume 1: Explanatory supplement, Vol. 1

Bender, R., Burstein, D., & Faber, S. M. 1992, ApJ, 399, 462

Berentzen, I., Shlosman, I., Martinez-Valpuesta, I., & Heller, C. H. 2007, ApJ, 666, 189

Bertram, T., Eckart, A., Krips, M., Staguhn, J. G., & Hackenberg, W. 2006, A&A, 448, 29

Boquien, M., Duc, P.-A., Wu, Y., et al. 2009, AJ, 137, 4561

Borne, K. D., & Richstone, D. O. 1991, ApJ, 369, 111

Bottinelli, L., Gouguenheim, L., Fouque, P., & Paturel, G. 1990, A&AS, 82, 391

Bottinelli, L., Durand, N., Fouque, P., et al. 1993, A&AS, 102, 57

Bournaud, F., & Combes, F. 2002, A&A, 392, 83

Bournaud, F., Combes, F., & Jog, C. J. 2004, A&A, 418, L27

Bournaud, F., Jog, C. J., & Combes, F. 2007, A&A, 476, 1179

Boylan-Kolchin, M., Springel, V., White, S. D. M., Jenkins, A., & Lemson, G. 2009, MNRAS, 398, 1150

Brassington, N. J., Ponman, T. J., & Read, A. M. 2007, MNRAS, 377, 1439

Bridge, C. R., Carlberg, R. G., & Sullivan, M. 2010, ApJ, 709, 1067

Brightman, M., & Nandra, K. 2011, MNRAS, 414, 3084

Brown, M. J. I., Jannuzi, B. T., Floyd, D. J. E., & Mould, J. R. 2011, ApJ, 731, L41

Bundy, K., Fukugita, M., Ellis, R. S., et al. 2009, ApJ, 697, 1369

Cappellari, M., Emsellem, E., Krajnović, D., et al. 2011, MNRAS, 413, 813

Casoli, F., Dupraz, C., & Combes, F. 1992, A&A, 264, 55

Chien, L.-H., & Barnes, J. E. 2010, MNRAS, 407, 43

Chitre, A., & Jog, C. J. 2002, A&A, 388, 407

Cicone, C., Maiolino, R., Sturm, E., et al. 2013, ArXiv e-prints, arXiv:1311.2595

Condon, J. J., Anderson, M. L., & Helou, G. 1991, ApJ, 376, 95

Condon, J. J., Cotton, W. D., & Broderick, J. J. 2002, AJ, 124, 675

Condon, J. J., Cotton, W. D., Greisen, E. W., et al. 1998, AJ, 115, 1693

Condon, J. J., Helou, G., Sanders, D. B., & Soifer, B. T. 1990, ApJS, 73, 359

—. 1996, ApJS, 103, 81

Cox, A. L., & Sparke, L. S. 2004, AJ, 128, 2013

Crabtree, D. R., & Smecker-Hane, T. 1994, in Bulletin of the American Astronomical Society, Vol. 26, American Astronomical Society Meeting Abstracts, #107.14

Crocker, A. F., Bureau, M., Young, L. M., & Combes, F. 2011, MNRAS, 410, 1197

Dasyra, K. M., Tacconi, L. J., Davies, R. I., et al. 2006, ApJ, 651, 835

Davis, T. A., Alatalo, K., Sarzi, M., et al. 2011, MNRAS, 417, 882

Davis, T. A., Alatalo, K., Bureau, M., et al. 2013, MNRAS, 429, 534

Deeg, H.-J., Brinks, E., Duric, N., Klein, U., & Skillman, E. 1993, ApJ, 410, 626

Dekel, A., Birnboim, Y., Engel, G., et al. 2009, Nature, 457, 451

Denisiuk, E. K., Lipovetskii, V. A., & Afanasev, V. L. 1976, Astrofizika, 12, 665

Deo, R. P., Crenshaw, D. M., Kraemer, S. B., et al. 2007, ApJ, 671, 124

Dicke, R. H., Peebles, P. J. E., Roll, P. G., & Wilkinson, D. T. 1965, ApJ, 142, 414

Djorgovski, S., & Davis, M. 1987, ApJ, 313, 59

Downes, D., & Solomon, P. M. 1998, ApJ, 507, 615

Epinat, B., Amram, P., Marcelin, M., et al. 2008, MNRAS, 388, 500

Evans, A. S., Mazzarella, J. M., Surace, J. A., et al. 2005, ApJS, 159, 197

Fernández, X., van Gorkom, J. H., Schweizer, F., & Barnes, J. E. 2010, AJ, 140, 1965

Finkelstein, S. L., Papovich, C., Dickinson, M., et al. 2013, ArXiv e-prints, arXiv:1310.6031

Fisher, D. B., Bolatto, A., Drory, N., et al. 2013, ApJ, 764, 174

Fort, B. P., Prieur, J.-L., Carter, D., Meatheringham, S. J., & Vigroux, L. 1986, ApJ, 306, 110

Franceschini, A., Braito, V., Persic, M., et al. 2003, MNRAS, 343, 1181

Gallego, J., Zamorano, J., Rego, M., Alonso, O., & Vitores, A. G. 1996, A&AS, 120, 323

Garland, C. A., Pisano, D. J., Williams, J. P., Guzmán, R., & Castander, F. J. 2004, ApJ, 615, 689

Garland, C. A., Williams, J. P., Pisano, D. J., et al. 2005, ApJ, 624, 714

Genzel, R., Tacconi, L. J., Rigopoulou, D., Lutz, D., & Tecza, M. 2001, ApJ, 563, 527

Genzel, R., Tacconi, L. J., Combes, F., et al. 2012, ApJ, 746, 69

Georgakakis, A., Hopkins, A. M., Caulton, A., et al. 2001, MNRAS, 326, 1431

Gonçalves, A. C., Véron-Cetty, M.-P., & Véron, P. 1999, A&AS, 135, 437

Goudfrooij, P., Hansen, L., Jorgensen, H. E., & Norgaard-Nielsen, H. U. 1994, A&AS, 105, 341

Graham, A. W., & Worley, C. C. 2008, MNRAS, 388, 1708

Haan, S., Surace, J. A., Armus, L., et al. 2011, AJ, 141, 100

Hattori, T., Yoshida, M., Ohtani, H., et al. 2004, AJ, 127, 736

Helfer, T. T., Thornley, M. D., Regan, M. W., et al. 2003, ApJS, 145, 259

Helou, G., Khan, I. R., Malek, L., & Boehmer, L. 1988, ApJS, 68, 151

Helou, G., Soifer, B. T., & Rowan-Robinson, M. 1985, ApJ, 298, L7

Hernquist, L. 1989, Nature, 340, 687

Hibbard, J. E., Guhathakurta, P., van Gorkom, J. H., & Schweizer, F. 1994, AJ, 107, 67

Hibbard, J. E., & Mihos, J. C. 1995, AJ, 110, 140

Holmberg, E. 1941, ApJ, 94, 385

Holtzman, J. A., Watson, A. M., Mould, J. R., et al. 1996, AJ, 112, 416

Hopkins, P. F., Cox, T. J., Younger, J. D., & Hernquist, L. 2009, ApJ, 691, 1168

Hopkins, P. F., Somerville, R. S., Hernquist, L., et al. 2006, ApJ, 652, 864

Horellou, C., & Booth, R. 1997, A&AS, 126, 3

Howell, J. H., Armus, L., Mazzarella, J. M., et al. 2010, ApJ, 715, 572

Hubble, E. 1958, The realm of the nebulae (New York: Dover, 1958)

Hubble, E. P. 1936, Realm of the Nebulae (New Haven: Yale University Press, 1936)

Huchtmeier, W. K., & Tammann, G. A. 1992, A&A, 257, 455

Hunt, L. K., Combes, F., García-Burillo, S., et al. 2008, A&A, 482, 133

Imanishi, M. 2006, AJ, 131, 2406

Imanishi, M., Nakagawa, T., Shirahata, M., Ohyama, Y., & Onaka, T. 2010, ApJ, 721, 1233

Imanishi, M., Terashima, Y., Anabuki, N., & Nakagawa, T. 2003, ApJ, 596, L167

Immeli, A., Samland, M., Gerhard, O., & Westera, P. 2004, A&A, 413, 547

Iono, D., Yun, M. S., & Mihos, J. C. 2004, ApJ, 616, 199

Iono, D., Wilson, C. D., Yun, M. S., et al. 2009, ApJ, 695, 1537

Iwasawa, K., Sanders, D. B., Teng, S. H., et al. 2011, A&A, 529, A106

James, P., Bate, C., Wells, M., Wright, G., & Doyon, R. 1999, MNRAS, 309, 585

Jarrett, T. H., Chester, T., Cutri, R., Schneider, S. E., & Huchra, J. P. 2003, AJ, 125, 525

Ji, L., Chen, Y., Huang, J. H., Gu, Q. S., & Lei, S. J. 2000, A&A, 355, 922

Jog, C. J., & Chitre, A. 2002, A&A, 393, L89

Jogee, S., Miller, S. H., Penner, K., et al. 2009, ApJ, 697, 1971

Jütte, E., Aalto, S., & Hüttemeister, S. 2010, A&A, 509, A19

Kennicutt, Jr., R. C. 1998, ARA&A, 36, 189

Kennicutt, Jr., R. C., Armus, L., Bendo, G., et al. 2003, PASP, 115, 928

Kereš, D., Katz, N., Weinberg, D. H., & Davé, R. 2005, MNRAS, 363, 2

Kewley, L. J., Heisler, C. A., Dopita, M. A., & Lumsden, S. 2001, ApJS, 132, 37

Kim, D.-W., Jura, M., Guhathakurta, P., Knapp, G. R., & van Gorkom, J. H. 1988, ApJ, 330, 684

Knapen, J. H. 2005, A&A, 429, 141

Koda, J., Sofue, Y., Kohno, K., et al. 2002, ApJ, 573, 105

König, S., Aalto, S., Muller, S., Beswick, R. J., & Gallagher, J. S. 2013, A&A, 553, A72

Koribalski, B. S., Staveley-Smith, L., Kilborn, V. A., et al. 2004, AJ, 128, 16

Kormendy, J., & Bender, R. 1996, ApJ, 464, L119

Laine, S., van der Marel, R. P., Rossa, J., et al. 2003, AJ, 126, 2717

Lake, G., & Dressler, A. 1986, ApJ, 310, 605

Larson, R. B., & Tinsley, B. M. 1978, ApJ, 219, 46

Lees, J. F., Knapp, G. R., Rupen, M. P., & Phillips, T. G. 1991, ApJ, 379, 177

Lin, L., Patton, D. R., Koo, D. C., et al. 2008, ApJ, 681, 232

Longhetti, M., Rampazzo, R., Bressan, A., & Chiosi, C. 1998, A&AS, 130, 267

Lonsdale, C. J., Lonsdale, C. J., Smith, H. E., & Diamond, P. J. 2003, ApJ, 592, 804

Maiolino, R., Ruiz, M., Rieke, G. H., & Papadopoulos, P. 1997, ApJ, 485, 552

Malin, D. F., & Carter, D. 1983, ApJ, 274, 534

Manthey, E., Aalto, S., Hüttemeister, S., & Oosterloo, T. A. 2008, A&A, 484, 693

Mao, R.-Q., Schulz, A., Henkel, C., et al. 2010, ApJ, 724, 1336

Marino, A., Iodice, E., Tantalo, R., et al. 2009, A&A, 508, 1235

Márquez, I., Masegosa, J., Moles, M., et al. 2002, A&A, 393, 389

Martini, P., Regan, M. W., Mulchaey, J. S., & Pogge, R. W. 2003, ApJS, 146, 353

McGaugh, S. S., & Bothun, G. D. 1990, AJ, 100, 1073

Mihos, C. 1999, Ap&SS, 266, 195

Mihos, J. C., & Bothun, G. D. 1998, ApJ, 500, 619

Mihos, J. C., Bothun, G. D., & Richstone, D. O. 1993, ApJ, 418, 82

Mihos, J. C., & Hernquist, L. 1996, ApJ, 464, 641

Miller, B. W., Whitmore, B. C., Schweizer, F., & Fall, S. M. 1997, AJ, 114, 2381

Minkowski, R. L., & Abell, G. O. 1963, The National Geographic Society-Palomar Observatory Sky Survey (the University of Chicago Press), 481

Mirabel, I. F., Booth, R. S., Johansson, L. E. B., Garay, G., & Sanders, D. B. 1990, A&A, 236, 327

Mirabel, I. F., & Sanders, D. B. 1988, ApJ, 335, 104

Moshir, M., Kopman, G., & Conrow, T. A. O. 1992, IRAS Faint Source Survey, Explanatory supplement version 2 (Pasadena: Infrared Processing and Analysis Center, California Institute of Technology, 1992, edited by Moshir, M.; Kopman, G.; Conrow, T. a.o.)

Moshir, M., Kopan, G., Conrow, T., et al. 2008, VizieR Online Data Catalog, 2275, 0

Mulchaey, J. S., Wilson, A. S., & Tsvetanov, Z. 1996, ApJS, 102, 309

Murray, N., & Rahman, M. 2010, ApJ, 709, 424

Naab, T., & Burkert, A. 2001, in Astronomical Society of the Pacific Conference Series, Vol. 249, The Central Kiloparsec of Starbursts and AGN: The La Palma Connection, ed. J. H. Knapen, J. E. Beckman, I. Shlosman, & T. J. Mahoney, 735

Naab, T., & Burkert, A. 2003, ApJ, 597, 893

Naab, T., Johansson, P. H., & Ostriker, J. P. 2009, ApJ, 699, L178

Naab, T., Khochfar, S., & Burkert, A. 2006, ApJ, 636, L81

Nagao, T., Taniguchi, Y., & Murayama, T. 2000, AJ, 119, 2605

Nakajima, T., Sakai, T., Asayama, S., et al. 2008, PASJ, 60, 435

Nakanishi, H., & Sofue, Y. 2006, PASJ, 58, 847

Narayanan, D., Bothwell, M., & Davé, R. 2012a, MNRAS, 426, 1178

Narayanan, D., Cox, T. J., & Hernquist, L. 2008, ApJ, 681, L77

Narayanan, D., Groppi, C. E., Kulesa, C. A., & Walker, C. K. 2005, ApJ, 630, 269

Narayanan, D., Krumholz, M. R., Ostriker, E. C., & Hernquist, L. 2012b, MNRAS, 421, 3127

Neugebauer, G., Habing, H. J., van Duinen, R., et al. 1984, ApJ, 278, L1

Nicholson, R. A., Bland-Hawthorn, J., & Taylor, K. 1992, ApJ, 387, 503

Nilson, P. 1973, Uppsala general catalogue of galaxies (Acta Universitatis Upsaliensis. Nova Acta Regiae Societatis Scientiarum Upsaliensis - Uppsala Astronomiska Observatoriums Annaler, Uppsala: Astronomiska Observatorium, 1973)

Osterbrock, D. E., & Martel, A. 1993, ApJ, 414, 552

Papadopoulos, P. P., van der Werf, P., Xilouris, E., Isaak, K. G., & Gao, Y. 2012, ApJ, 751, 10

Peeples, M. S., & Martini, P. 2006, ApJ, 652, 1097

Penzias, A. A., & Wilson, R. W. 1965, ApJ, 142, 419

Poggianti, B. M., & Wu, H. 2000, ApJ, 529, 157

Quinn, P. J., Hernquist, L., & Fullagar, D. P. 1993, ApJ, 403, 74

Rampazzo, R., Plana, H., Longhetti, M., et al. 2003, MNRAS, 343, 819

Rampazzo, R., Marino, A., Tantalo, R., et al. 2007, MNRAS, 381, 245

Regan, M. W., Thornley, M. D., Helfer, T. T., et al. 2001, ApJ, 561, 218

Richter, O.-G., Sackett, P. D., & Sparke, L. S. 1994, AJ, 107, 99

Rigopoulou, D., Lawrence, A., White, G. J., Rowan-Robinson, M., & Church, S. E. 1996, A&A, 305, 747

Risaliti, G., Maiolino, R., Marconi, A., et al. 2006, MNRAS, 365, 303

Robertson, B. E., & Bullock, J. S. 2008, ApJ, 685, L27

Rothberg, B., & Fischer, J. 2010, ApJ, 712, 318

Rothberg, B., & Joseph, R. D. 2004, AJ, 128, 2098

—. 2006a, AJ, 131, 185

—. 2006b, AJ, 132, 976

Sanders, D. B., & Mirabel, I. F. 1996, ARA&A, 34, 749

Sanders, D. B., Scoville, N. Z., & Soifer, B. T. 1991, ApJ, 370, 158

Schiminovich, D. 2001, in Astronomical Society of the Pacific Conference Series, Vol. 240, Gas and Galaxy Evolution, ed. J. E. Hibbard, M. Rupen, & J. H. van Gorkom, 147

Schiminovich, D., van Gorkom, J. H., & van der Hulst, J. M. 2013, AJ, 145, 34

Schombert, J. M., Wallin, J. F., & Struck-Marcell, C. 1990, AJ, 99, 497

Schweizer, F. 1982, ApJ, 252, 455

Schweizer, F. 1983, in IAU Symposium, Vol. 100, Internal Kinematics and Dynamics of Galaxies, ed. E. Athanassoula, 319–326

—. 1986, Science, 231, 227

Schweizer, F. 1990, in Dynamics and Interactions of Galaxies, ed. R. Wielen, 60–71

—. 1996, AJ, 111, 109

Schweizer, F., & Seitzer, P. 1992, AJ, 104, 1039

—. 2007, AJ, 133, 2132

Sekiguchi, K., & Wolstencroft, R. D. 1993, MNRAS, 263, 349

Shier, L. M., & Fischer, J. 1998, ApJ, 497, 163

Simien, F., & Prugniel, P. 1997, A&AS, 122, 521

Sliwa, K., Wilson, C. D., Petitpas, G. R., et al. 2012, ApJ, 753, 46

Smirnova, A., & Moiseev, A. 2010, MNRAS, 40, 307

Smith, D. A., Herter, T., Haynes, M. P., Beichman, C. A., & Gautier, III, T. N. 1996, ApJS, 104, 217

Smith, E. P., & Hintzen, P. 1991, AJ, 101, 410

Smith, H. E., Lonsdale, C. J., & Lonsdale, C. J. 1998, ApJ, 492, 137

Smoot, G. F., Bennett, C. L., Kogut, A., et al. 1992, ApJ, 396, L1

Solomon, P. M., & Barrett, J. W. 1991, in IAU Symposium, Vol. 146, Dynamics of Galaxies and Their Molecular Cloud Distributions, ed. F. Combes & F. Casoli, 235

Solomon, P. M., Downes, D., Radford, S. J. E., & Barrett, J. W. 1997, ApJ, 478, 144

Solomon, P. M., & Vanden Bout, P. A. 2005, ARA&A, 43, 677

Springel, V., Di Matteo, T., & Hernquist, L. 2005, ApJ, 620, L79

Springel, V., & Hernquist, L. 2005, ApJ, 622, L9

Springob, C. M., Haynes, M. P., Giovanelli, R., & Kent, B. R. 2005, ApJS, 160, 149

Struck, C. 1999, Phys. Rep., 321, 1

Tacconi, L. J., Genzel, R., Smail, I., et al. 2008, ApJ, 680, 246

Tacconi, L. J., Genzel, R., Neri, R., et al. 2010, Nature, 463, 781

Tacconi, L. J., Neri, R., Genzel, R., et al. 2013, ApJ, 768, 74

Takeuchi, T. T., Buat, V., Heinis, S., et al. 2010, A&A, 514, A4

Taniguchi, Y., & Noguchi, M. 1991, AJ, 101, 1601

Theureau, G., Bottinelli, L., Coudreau-Durand, N., et al. 1998, A&AS, 130, 333

Tielens, A. G. G. M. 2005, The Physics and Chemistry of the Interstellar Medium (Cambridge, UK: Cambridge University Press, 2005)

Toomre, A. 1977, in Evolution of Galaxies and Stellar Populations, ed. B. M. Tinsley & R. B. G. Larson, D. Campbell, 401

Toomre, A., & Toomre, J. 1972, ApJ, 178, 623

Ueda, J., Iono, D., Petitpas, G., et al. 2012, ApJ, 745, 65

Veilleux, S., Kim, D.-C., Sanders, D. B., Mazzarella, J. M., & Soifer, B. T. 1995, ApJS, 98, 171

Vorontsov-Velyaminov, B. A. 1959, in Atlas and catalog of interacting galaxies (1959), 0

Vorontsov-Velyaminov, B. A. 1977, A&AS, 28, 1

Walker, I. R., Mihos, J. C., & Hernquist, L. 1996, ApJ, 460, 121

Wang, Z., Schweizer, F., & Scoville, N. Z. 1992, ApJ, 396, 510

Wang, Z., Scoville, N. Z., & Sanders, D. B. 1991, ApJ, 368, 112

Weil, M. L., Bland-Hawthorn, J., & Malin, D. F. 1997, ApJ, 490, 664

Whitmore, B. C., Lucas, R. A., McElroy, D. B., et al. 1990, AJ, 100, 1489

Whitmore, B. C., Miller, B. W., Schweizer, F., & Fall, S. M. 1997, AJ, 114, 1797

Whitmore, B. C., Schweizer, F., Leitherer, C., Borne, K., & Robert, C. 1993, AJ, 106, 1354

Wiklind, T., Combes, F., & Henkel, C. 1995, A&A, 297, 643

Wilson, C. D. 1995, ApJ, 448, L97

Wilson, C. D., Petitpas, G. R., Iono, D., et al. 2008, ApJS, 178, 189

Wright, A., & Otrupcek, R. 1992, Bulletin d'Information du Centre de Donnees Stellaires, 41, 47

Yamamura, I., Makiuti, S., Ikeda, N., et al. 2010, VizieR Online Data Catalog, 2298, 0

Yao, L., Seaquist, E. R., Kuno, N., & Dunne, L. 2003, ApJ, 588, 771

Young, J. S., Xie, S., Tacconi, L., et al. 1995, ApJS, 98, 219

Young, L. M., Bureau, M., & Cappellari, M. 2008, ApJ, 676, 317

Young, L. M., Bureau, M., Davis, T. A., et al. 2011, MNRAS, 414, 940

Yuan, T.-T., Kewley, L. J., & Sanders, D. B. 2010, ApJ, 709, 884

Yun, M. S., Ho, P. T. P., & Lo, K. Y. 1994, Nature, 372, 530

Yun, M. S., Reddy, N. A., & Condon, J. J. 2001, ApJ, 554, 803

Zhu, M., Seaquist, E. R., Davoust, E., Frayer, D. T., & Bushouse, H. A. 1999, AJ, 118, 145

Zhu, M., Seaquist, E. R., & Kuno, N. 2003, ApJ, 588, 243

Acknowledgment

First of all, I would like to thank my thesis adviser, Daisuke Iono for his contributions to all aspects of my work. He is a great scientist, educator, and adviser, who provided a lot of advice and idea for this work. This work would not have been possible without his contribution and guidance. He was always a good adviser for me through good times and bad times. I appreciate very much the support from him, and would like to give him a champagne cork like the ones he gave to his advisers.

I am deeply grateful to my supervisor, Ryohei Kawabe for giving me a valuable opportunity to study radio astronomy for these past five years. He always encouraged me to reach for my goals and did not say no to my ideas and plans. I was happy to be his student.

I would like to thank my advisors and colleagues, Min Yun, Desika Narayanan, Alison Crocker, Daniel Espada, Bunyo Hatsukade, Hiroyuki Kaneko, and Yoichi Tamura. I would like to give special thanks to Min for his continuous support from our previous study on the Antennae galaxies.

I would like to thank my Predoctoral Research Review Committee at the Harvard-Smithsonian Center for Astrophysics, David Wilner, Giovanni Fazio, Zhong Wang, and Mark Gurwell. I would like to give special thanks to David for giving me a great opportunity to study at the CfA and to experience observations using the SMA. I was very glad when our proposals were successful.

I am greatly thankful to the scientists, post-docs and grad students at the National Astronomical Observatory of Japan, the Nobeyama Radio Observatory, the CfA, and University of Tokyo. I would like to give special thanks to Shinya Komugi for teaching knowledge of Astronomy and English and checking my presentations and scientific papers. I would also like to give special thanks to Akihiko Hirota and Takashi Tsukagoshi for their technical supports. I am very grateful to members of Professor Kawabe's laboratory, Chihomi, Toshiki, and Minju for chatting with me during work breaks. I was very happy to enjoy my gradstudent life.

I am very grateful to my friends for keeping in touch and cheering me up when I was down. I would like to list your names, but the list is long. I have never forgotten the good memories with you. I would like to give special thanks to Yuta for having given a lot of emotional supports to me in what has been an extremely difficult time since we are high school students.

Finally, I thank my parents, my sister, Hat, and the extended family for being very supportive throughout my studies. Last but not least, I would like to send my colleagues and myself the words, "Galaxies are like people. The better we get to know them, the more interesting they seem to be."
I would like to thank you!

I would like to thank Eva Jütte, Leslie K. Hunt, and Santiago García-Burillo for kindly providing their published data and Barry Rothberg and Robert D. Joseph for allowing me to use their K-band images. I would like to express my gratitude to the ALMA[a], SMA[b], and CARMA[c] staff members for making the new observations possible. This study has made use of the following ALMA data: ADS/JAO.ALMA#2011.0.00099.S and ALMA Science Verification data: ADS/JAO.ALMA#2011.0.00002.SV.

[a]ALMA is a partnership of ESO (representing its member states), NSF (USA) and NINS (Japan), together with NRC (Canada) and NSC and ASIAA (Taiwan), in cooperation with the Republic of Chile. The Joint ALMA Observatory is operated by ESO, AUI/NRAO and NAOJ.

[b]The Submillimeter Array is a joint project between the Smithsonian Astrophysical Observatory and the Academia Sinica Institute of Astronomy and Astrophysics and is funded by the Smithsonian Institution and the Academia Sinica.

[c]Support for CARMA construction was derived from the Gordon and Betty Moore Foundation, the Kenneth T. and Eileen L. Norris Foundation, the James S. Mc-Donnell Foundation, the Associates of the California Institute of Technology, the University of Chicago, the states of California, Illinois, and Maryland, and the National Science Foundation. Ongoing CARMA development and operations are supported by the National Science Foundation under a cooperative agreement, and by the CARMA partner universities.